Applications of Infrared Imaging Interferometry: Binaries, Rapid Rotators, and Hot Jupiters

by

Ming Zhao

A dissertation submitted in partial fulfillment
of the requirements for the degree of
Doctor of Philosophy
(Astronomy and Astrophysics)
in The University of Michigan
2009

Doctoral Committee:

Associate Professor John D. Monnier, Chair
Professor Fred C. Adams
Professor Charles R. Cowley
Professor Lee Hartmann
Professor Mario L. Mateo

To my parents, and my brother

Acknowledgments

First, I would like to thank my thesis advisor Prof. John Monnier for his instruction and mentoring during the past 6 years. It has been a great pleasure and privilege to work with him. His dedication and enthusiasm for science, professional computing, experimental and organizing skills, and endless of great ideas always inspire and motivate me. I would like to thank him for his support on every aspect. He is always available for consulting and discussing any problems that I had, and has given me invaluable hands-on instructions on research, presentation skills, and academic writing. Prof. Monnier is not only a great mentor but also a great friend in personal life. I have enjoyed lots of fun and enlightening conversations with him, especially those regarding Apple gadgets.

I also would like to thank other members of my thesis committee: Prof. Fred Adams, Prof. Charles Cowley, Prof. Lee Hartmann, and Prof. Mario Mateo for their time and valuable advice for my thesis. I appreciate Prof. Cowley for answering lots of my questions about hot stars, Prof. Hartmann for reading and commenting my proposal, and Prof. Mateo for discussing and giving suggestions to my observation. I also want to acknowledge my collaborators Dr. Ettore Pedretti, Dr. Nathalie Thureau, and Dr. David Berger for their help on observations and discussions on questions regarding interferometry and computing. I very much appreciate Prof.

Douglas Gies and Dr. Willie Torres for their help and elaborate comments for our papers. It has been very enjoyable to work with them. I have also enjoyed the warm welcome from Prof. Gies at Georgia State University and have enjoyed my visit there. I also would like to thank Prof. Hal McAlister for allocating us the observing times of CHARA (Georgia State University), without which I cannot complete this thesis. I also greatly appreciate the observing support from the whole CHARA crew on Mt. Wilson, CA., and particularly I would like to thank PJ Goldfinger for her music and delicious pancakes during those long observing nights. In addition, I would like to thank Prof. Hugh Aller for his help and support in the first year of my graduate study. It was an pleasure to work with him, and I got lots of experience on radio interferometry and synthesis imaging.

I would like to say thank you to my fellow graduate students in the Astronomy Department in Michigan, especially to my six-year officemate Catherine Espaillat, and as well as Ajay Tannirkulam, Tom Brink, Scott Cameron, Sarah Ragan and Zhaohuan Zhu for their great help in the past years. All of them have been very good friends. Tom has given me lots of tutorials and guide on football, basketball, baseball, American culture, as well as observations. I always bother Tom and Catherine with a lot of language related questions and they are always available for answers. I have had lots of discussions with Ajay on research related problems and he always provides good thoughts and ideas. I have enjoyed every single conversation and discussion with all of them. Furthermore, I also want to thank the support from the staff in the department for their great help with administrative things.

My six years of life in Ann Arbor has been really joyful. I have made lots of friends and I especially would like to thank Li Zhang, Zhixi Wan, Sijian Wang and Bo Huang for their great help in my personal life. They have always been very supportive to me. Finally, I would like to say a big “Thank You” to my parents and my brother. Without their strong support, I would not make this far.

This thesis was financially supported by the Michelson Graduate Fellowship program, organized by NASA and the the former Michelson Science Center, and NASA grant NNG 04GI33G. Chapter 3, 4, 5 are mostly based on publications in the Astrophysical Journal (Zhao et al., 2007; Monnier et al., 2007; Zhao et al., 2009), the Astrophysical Journal Letters (Zhao et al., 2008), and proceedings of the Society of Photographic Instrumentation Engineers (SPIE) (Zhao et al., 2008b).

Contents

Chapter

List of Figures

Figure

List of Tables

Table

List of Appendices

Appendix

List of Abbreviations

BCL	Beam Combination Laboratory
BSF	Beam Synthesis Facility
CHARA	Center for High Angular Resolution Astronomy
HR	Hertzsprung-Russell
IR	infrared
IRFM	InfraRed Flux Method
IOTA	Infrared Optical Telescope Array
GSU	Georgia State University
MACIM	The Markov Chain Imager for Optical Interferometry
mas	milli-arcsecond
MEM	Maximum Entropy Method
OPD	Optical Path Difference
OPLE	Optical Path Length Equalization
POP	Pipes of Pan
PTI	Palomar Testbed Interferometer
SED	Spectral Energy Distribution
UD	Uniform Disk
VLTI	Very Large Telescope Interferometer

Abstract

Long baseline optical inerferometers now have the power to resolve objects as small as 0.5 milliarcseconds in the near-IR and possess the capability of conducting real aperture synthesis imaging, allowing us to study stars and their environments in unprecedented detail. As a fundamental property of stars, rotation affects stars' luminosities, effective temperatures, and their evolution. Since most of hot stars are rapid rotators, understanding the effects of rotation will shed light on critical areas of stellar evolution and basic astrophysics. Using the CHARA array and the MIRC combiner, we resolved the surfaces of three rapid rotators, α Cep, α Oph and Altair. We reconstructed an image for α Cep, and modeled the surface brightness distribution for all three stars, allowing us to confirm the "gravity darkening" phenomenon and investigate the impact of rapid rotation on their locations in the H-R diagram. Our modeling of rapid rotators also allowed us to propose a new way of measuring masses of stars.

We also studied binary stars with IR interferometers. We conducted combined interferometric and spectroscopic study of the metallic-lined A star λ Vir, permitting us to determine its orbital and physical properties to high accuracy. The determination of masses of the system also allowed us to compare observations with stellar evolution models, in which reasonable matches were found. In addition, using CHARA-MIRC we also made the first resolved images of the well-known interacting and eclipsing binary system β Lyrae, which also allowed us to obtain its full orbital parameters and estimate the masses of its components.

Lastly, we present our efforts toward direct detection of nearby hot Jupiters using precision closure phases obtained with long baseline interferometer. We present closure phase simulations, preliminary observations on the hot Jupiter system υ And, as well as calibration studies and test observations of a high contrast binary ϵ Per. We conclude that with all the ongoing improvements, it is feasible to achieve the goal of detecting hot Jupiters with CHARA-MIRC.

Chapter 1

Introduction

Optical/IR interferometry has made wide range of great impacts to astrophysics in the past two decades, including precise determination of fundamental stellar properties and characterizing circumstellar environments. It is also starting to be recognized as an important tool to resolve and characterize extra-solar planets. In this chapter I will discuss the scientific background of interferometric studies, and their importance and contributions to astrophysics.

1.1 Interferometry in stellar astrophysics

1.1.1 Effective temperatures and stellar radii

Stars are the basic elements of galaxies and the observing universe. Understanding their properties and structures can greatly help us to understand their formation, evolution, distribution, etc., and can also shed light on galaxy evolution. Stellar structure and evolution models were first developed in the 1950's by (Schwarzschild, 1958) and (Henyey et al., 1959), which helped us to understand many physical processes in star formation and evolution. During the last two decades, the fast development of powerful computers has advanced numerical computation of stellar models. The accuracy of observational data have also been greatly increased due to the improvement of photometry and spectrascopy, allowing stringent test and validation of evolution models and helping enriching the input physics to stellar models (Lebreton, 2000). The success of stellar evolution theory has helped us to understand the Hertzsprung-Russell (HR) diagram of stars, the most fundamental diagram for a stellar astrophysicist, especially the stellar distrbution of stars in globular and open clusters (Cassisi, 2009).

Luminosity and effective temperature are two of the most basic properties of stars. The H-R diagram characterizes stars by mapping these two quantities, which also allows us to get the stellar radii. The free input parameters of stellar models, either observational (e.g., mass, chemical composition) or physical (e.g., opacity, equation of state, nuclear reaction rates, mixing length of convection, overshooting, atomic diffusion) eventually reflect themselves on stellar luminosity, effective temperature, radius, and oscillation frequencies, etc. Therefore, a large number of precise measurements of luminosities, effective temperatures and/or stellar radii will allow us to test the input physics of stellar models and give more precise values of free parameters, and may even reveal the necessity of including processes previously neglected (Lebreton, 2000).

Test of stellar models requires precise measurements of stellar luminosity and temperature. Integration of multi-band photometry gives the bolometric flux of a star, and thus its luminosity if the distance is known. Determination of the effective temperature of a star, however, is not that straightforward. Typical ways of determine a stellar effective temperature includes multi-band photometry measurements and spectroscopic measurements. In particular, photometric methods include the InfraRed Flux Method (IRFM) (Blackwell & Lynas-Gray, 1994) which uses the total integrated flux (assuming an atmosphere model) and the observed IR flux of a star to estimate the T_{eff}, the surface brightness method (Barnes et al., 1978) which performs a (T$_{eff}$, V-K) calibration based on hundreds of stars, and multi-parameter empirical determination of T$_{eff}$ which calculates T$_{eff}$ as a function of color indices and gravity (Alonso et al., 1996). Spectroscopic determination of T$_{eff}$ is based on analysis of certain spectral lines that are sensitive to temperature (e.g., Boden et al., 2005). However, these determination methods largely rely on atmosphere models and in other ways on calibrations, which undoubtedly introduce large uncertainties in the measured temperatures. The effective temperature of a star is defined as

$$T_{eff} \equiv (\frac{L}{4\pi\sigma R^2})^{\frac{1}{4}} = (\frac{4f_{bol}}{\sigma\theta_{LD}^2})^{\frac{1}{4}}, \tag{1.1}$$

where L is the luminosity of the star, R is the stellar radius, f$_{bol}$ is the bolometric flux, and σ is the Stefan-Boltzmann constant. Therefore, the most direct and model-independent way of determine effective temperature is to combine bolometric fluxes with angular diameter measurements, which in turn requires precise measurements of stellar angular sizes.

There are only a few ways of measuring stellar angular diameters directly, including light curve and radial velocity studies of detached eclipsing binaries (Andersen, 1991), lunar oculation (LO), and long baseline interferomtry. The advance of long baseline interferometers in the past decade has allowed us to reach baselines as long as 300 meters, permitting us to determine stellar diameter with unprecedented precision which has trumped the other two methods (see, e.g., Quirrenbach, 2001). The first extensive set of angular diameter measurements of 32 A and B type stars obtained by Hanbury Brown et al. (1974) using the Narrabri Intensity Interferometer still serves as the best diameters and effective temperatures of A and B stars. Previously interferometric measurements were mostly for giants and hot stars. The current generation of interferometers now allow us to extend the diameter measurements to later spectral types, such as K and M stars (e.g., Berger et al., 2006; Baines et al., 2008), increasing the sample of stars that have precise effective temperature estimates. In addition, systematic differences among different methods have been seen (Quirrenbach, 2001). The direct determination of effective temperature of stars can therefore be used to test for the systematic errors of other methods, which is particularly important for studies of pulsators among peculiar stars and low-metallicity stars (Cunha et al., 2007).

In addition to the determination of effective temperatures of stars, interferometric measurements of stellar diameters also have importance for other aspects of stellar astrophysics. With precision of only a few percent, other effects such as limb darkening, pulsation and rotation become important. The high resolution of interferometric measurements can therefore be used to test limb darkening models (e.g., Perrin et al., 2004). Also,due to the wavelength dependance of opacity, some cool stars have very strong variation of their angular diameters with wavelengths. For instance, the coolest Mira stars have monochromatic diameters which may differ at the same pulsational phase by a factor of ∼2 (Hofmann et al., 1998). Direct interferometric measurements of radii are therefore very important in characterizing these stars.

Interferometric measurements of stellar diameters can also help asteroseismology to constrain models of pulsating stars, and characterizing pulsaton modes through phase measurements if the surface structure is resolved (Cunha et al., 2007). For the classic pulsator Cepheids, their Period-Luminosity (P-L) relation is of great importance to the cosmological distance ladder. If the calibration of the cepheid P-L relation is biased, the whole cosmological distance scale would be biased as well. Interferometry permits a new version of the Baade-Wesselink method (BW) (Baade, 1926; Wesselink, 1946) to precisely and independently calibrate the P-L relation, which does not need the measurement of stellar temperature but only the stellar diameter instead (Mérand et al., 2005).

For rapidly rotating stars, rotation will not only change their interior and their evolutionary status, but also change their apparent temperatures and luminosities depending upon their inclination to the line of sight. Measuring their sizes at different angles on the sky, and even resolve their surface brightness distribution will greatly help us to characterize these stars and hence determine their true temperatures and luminosities. With multiple baselines and efficient good spatial coverage provided by the current interferometers, we can even characterize stars by directly imaging their surface. The first image of the surface of a star other than the Sun was made by Burns et al. (1997) using the COAST interferometer, while the first such image of a main-sequence star was made by Monnier et al. (2007) using the CHARA interferometer. In Chapter 3, we will discuss our most recent studies of 3 rapid rotators and imaging of two of them. (Monnier et al., 2007; Zhao et al., 2009), and will discuss our determination of their temperatures and luminosities as well.

1.1.2 Stellar mass

Stellar mass is the most fundamental property of a star. The initial mass, along with chemical abundance, can in principle determine all other properties of a star as a function of age. The mass of a star can typically only be measured through the orbit of a binary system. Nevertheless, one still usually has to combine two or more techniques to determine the orbit of a binary, such as spectroscopy and visual/astrometric measurements, or spectroscopy and interferometric measurements. Spectroscopic measurements can provide most of the orbital elements of a binary except the position angle of the ascending node and the inclination which is coupled with mass (M $\sin^3 i$) and semi-major axis (a $\sin i$) of the system. Although visual or astrometric orbits can provide the inclination, the overlap of the two types of orbits is not very common, since spectroscopic binaries are generally biased to close-orbit systems that are hard to resolve. High resolution interferometric observations have the capability of resolving close binary systems, and thus have great advantage and are of great importance in determining masses of stars. In addition to masses of binaries, interferometric orbit measurement of spectroscopic binaries can also provide an independent determination of distance, also known as the “orbital parallax”, which can be used as another mean of calibrating other types of observations such as luminosity, absolute stellar radius, etc.

Because of the importance of interferometry in binary study, observations of spectroscopic binaries have been conducted extensively by many interferometers, and currently there are more than 40 binaries been measured (Cunha et al., 2007). Andersen (1991) has pointed out that stellar mass has to be determined within an accuracy of 1% - 2% in order to provide useful test of stellar models. The current generation of interferometers are already able to provide such high accuracies of stellar masses, allowing stringent test of stellar evolution models (e.g., Hummel et al., 2001; Boden et al., 2005, 2006). We will talk about an example of such observations in §4.1 as well.

Tests of stellar models conducted by Andersen (1991) also show that main sequence models for stars with masses in the range of ∼1 - ∼10 $M_\odot$ and chemical abundances close to that of the Sun agree with observations very well. However, models for chemical abundances much different from the Sun are not very well tested and calibrated by observations due to a lack of suitable systems and lack of accurate measurements. Similarly, stellar structure and evolution models of pre-main sequence (PMS) stars are among the areas where our understanding of stellar structure is most uncertain, particularly for low mass systems (Palla & Stahler, 2001; Hillenbrand & White, 2004). Interferometric observations can thus provide great insight in these areas, and observations have already been starting to cover rare type stars and all regions of the HR diagram to allow a comprehensive test of stellar models (e.g., Boden et al., 2006, 2009).

In addition, the great resolving power of current generation interferometers have allowed us to study and even image extremely close binaries and interacting binaries. For instance, Raghavan et al. (2009) resolved the 1.1 period binary HD 146361, which is the shortest-period binary to date. In §4.2, we will discuss the study and imaging of the interacting binary β Lyr, which has a separation of only 1 milliarcsec and is the smallest binary system ever resolved.

1.2 Interferometry in studies of circumstellar environments

In addition to the basic parameters of stars, current interferometers are also able to resolve the circumstellar environments, including mass loss and stellar winds (e.g., Millan-Gabet et al., 1999; Tuthill et al., 1999; Monnier, 1999), H_α emissions and circumstellar disks around hot stars (e.g., Quirrenbach et al., 1994; Gies et al., 2007; Tycner et al., 2008), dust shells of evolved stars (e.g., Danchi et al., 1994; Weigelt et al., 1998; Monnier et al., 2000a,b,c), and shed light on YSOs and disks around young stars, especially the innermost part of those disks (e.g., Tuthill et al., 2001; Monnier & Millan-Gabet, 2002; Monnier et al., 2008; Tannirkulam et al., 2008). (Please refer to Monnier (2003) and Quirrenbach (2001) for details)

1.3 Interferometry in detecting extra-solar planets

Precise determination of the radii of exoplanets is critical to our interpretation of their atmospheres and construction of detailed evolutionary and structural models (Charbonneau et al., 2007). The only way to date to determine planetary radii is through detections of planets transiting their host stars (Charbonneau et al., 2007). The fit to their transit light curves gives a constraint on the ratio of planetary radius to host star radius, i.e., R_{pl}/R_*. However, fits to such data show a fundamental degeneracy among the quantities, R_{pl}, R_* and inclination of the system (i) (Winn et al., 2005; Charbonneau et al., 2006). Although the value of i can be determined with high precision multi-color light curves together with a fit to the limb-darkening coefficients of the star (Knutson et al., 2007), the value of R_* cannot be determined in a straightforward way unless we introduce other quantities such as the mass of the star and stellar evolution tracks (Cody & Sasselov 2002, Noyes et al., 2008).

Long baseline interferometry can provide direct determination of radii of the planet host star, and thus gives an independent measurement of planet radii. This method has already been applied to a selection of ∼36 planet host stars (Baines et al., 2008, 2009), and the radius of the planet HD 189733b has already been independently measured (Baines et al., 2007).

In addition to planet radius, optical interferometers are also being used to probe the thermal emission from giant close-in extra-solar planets by resolving the planetary system, which can yield the flux ratio of the system and the inclination, permitting us to characterize the atmosphere of the planet and determine its mass. Active progress is being made in this field. We will discuss more about this topic in Chapter 5.

Furthermore, with improving sensitivity, very high accuracy can be achieved in ground- based differential astrometric measurements between stars separated by at most a few tens of arcseconds on the sky. With specially designed instruments, interferometric astrometry can even reach a precision of tens of micro-arcseconds, allowing us to detect extra-solar planets and their orbits. Such effort has also being actively pursued and results are expected soon (Pott et al., 2008).

1.4 Overview of the thesis

This thesis discusses about several imaging studies using the CHARA array and the MIRC combiner. In Chapter 2 I first give a brief introduction of the basics of optical/IR interferometry, including the astrophysical quantities we use in our modeling and imaging, i.e., visibilities and closure phases. I then briefly introduce the common aperture synthesis algorithms. After that I list the current interferometers in operation and give a short introduction to the CHARA array and the MIRC combiner.

In Chapter 3, I discuss studies of three nearby rapid rotators, α Cep, α Oph and Altair, including their gravity darkening modeling and imaging of two of them. I also present the determination of their real effective temperatures and luminosities, as well as their locations on the HR diagram. After that I present a new method of determining masses of single stars.

In Chapter 4, I discuss two different binary systems, a chemical peculiar binary λ Vir and an interacting binary β Lyrae. For λ Vir, I combine spectroscopic data and interferometric data to determine its orbital parameters, and hence the masses of the system and test of stellar evolution models. For β Lyrae, I present its first resolved images at five different epochs, and determine its orbital parameters and masses as well.

In Chapter 5, I present the efforts toward direct detection of hot Jupiters using precision closure phases, including closure phase simulations, preliminary observations of υ And, calibration studies, and test observation of high contrast binary ϵ Per.

Chapter 2

Basics of Optical/IR Interferometry

2.1 Basic principles

This chapter will briefly review the basic concepts of stellar interferometry. More details can be found in Monnier (1999), Quirrenbach (2001), Monnier (2003), the notes of the Michelson Summer School (Lawson, 2000), and references therein.

The simplest example of interferometry is the famous Young's Double Slit experiment. In this experiment, light from a point source in the distance passes through two slits. Because of the wave nature of light, the two beams of light come through the slits interfere with each other like waves on water and form fringe patterns on a screen, as shown in the first panel of Figure 2.1. This experiment illustrates the basic principle behind an interferometer. Interferometers combine light from distant objects using multiple telescopes and measure the interference of the light. The monochromatic intensity of the fringe pattern is a sinusoidal wave ($I = I_0(1 + cos(2\pi\theta b/\lambda)$, ignoring the size of the slits), and the fringe spacing is λ/b radians, where b is the baseline between the two slits (or telescopes) and λ is the wavelength of the light. If we have another point source, the second set of fringes will shift slightly on the screen, and two sets of fringes will superpose together, as illustrated in the second panel of Figure 2.1. If the two sources are separated by an angular distance of $\lambda/(2b)$

radians, the fringe patterns will be canceled out and the intensity on the screen will become uniform, as shown in the right panel of Figure 2.1.

Clearly, the fringe spacing depends only on the baseline of the two telescopes when the wavelength of the light is fixed. Similarly, in the case of a single aperture telescope, light passes through a circular aperture will form diffraction patterns on the image plane. The width between the first nulls of the diffraction pattern is $2.44\frac{\lambda}{D}$ rad, where D is the diameter of the aperture. The resolution of a single aperture is defined as $1.22\frac{\lambda}{D}$ according to the "Rayleigh Criterion", which is half of the size between the first nulls. Therefore, we can also define the resolution of an interferometer in the same way as half of the size between two fringe nulls, i.e.,

$$\theta_{resolution} = \frac{\lambda}{2B}\, rad, \tag{2.1}$$

where B is the longest baseline of the interferometer.

2.2 Fringe Visibilities

The fringes detected by an interferometer can be quantified as fringe visibility, which is basically the contrast of the fringes:

$$V = \frac{I_{max} - I_{min}}{I_{max} + I_{min}} = \frac{Fringe\ amplitude}{Average\ fringe\ intenity}, \tag{2.2}$$

where I_{max} and I_{min} denote the maximum and minimum fringe intensities.

The fringe visibility also directly relates to the Fourier transform of the brightness distribution within a small field, which is known as the van Cittert-Zernike theorem (see Thompson et al., 1986; Born, 1999, for details):

$$V(\frac{(\Delta x, \Delta y)}{\lambda}) = \iint I(l,m) e^{-2\pi i(\Delta x l + \Delta y m)/\lambda} dl dm, \tag{2.3}$$

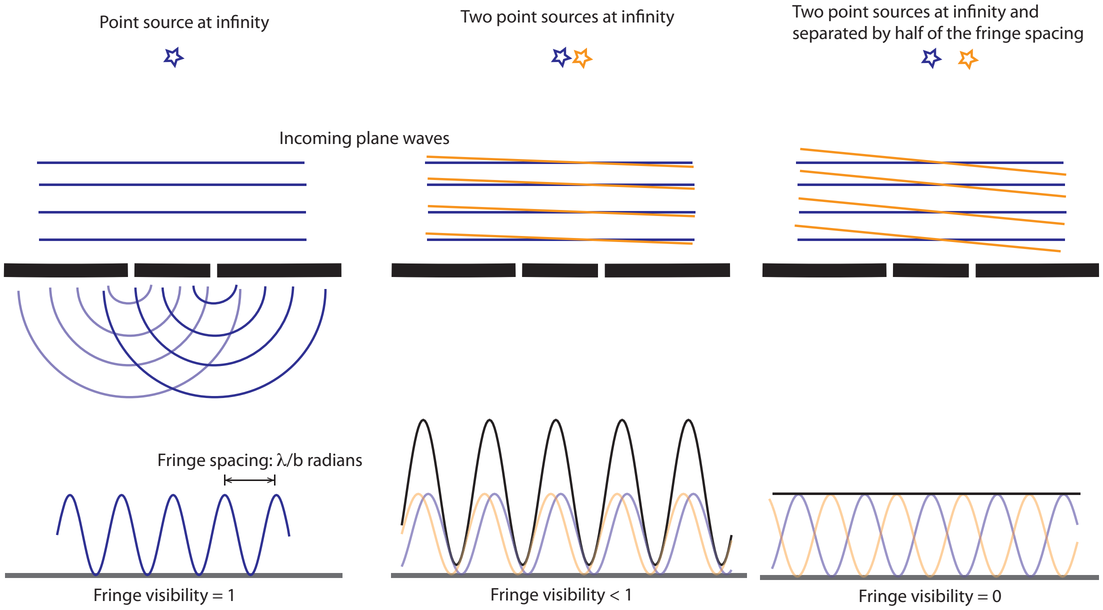

Figure 2.1 Young's double-slit experiment for monochromatic light. The left panel shows the case for the single point source, the middle panel shows the example of a double point-source, and the right panel shows the case when two point sources are separated by one fringe spacing.

where l and m denote the relative position to the phase center on the sky in radians, $I(l,m)$ denotes the intensity distribution of the source, and $(\Delta x, \Delta y)$ denotes the baseline vector projected onto the plane of the sky. This quantity is also known as the *complex visibility*. Generally, $\frac{(\Delta x, \Delta y)}{\lambda}$ is also written in units of wavelength as (u,v), and the corresponding plane is called the UV plane (which is also the Fourier plane of the source brightness). Therefore, each complex visibility relates to a point on the UV plane. As the Earth rotates, each projected baseline will form a track on the UV plane, allowing us to sample a series of visibilities at various spatial frequencies. For a multiple baseline interferometer array with N telescopes, there are $C_2^N = (N(N-1))/2$ independent baselines, thus we can have (N(N-1))/2 different tracks on the UV plane. Figure 2.2 shows 3 examples of baseline tracks on the UV plane. Because each baseline has a point-symmetric counterpart on the UV plane (e.g., baseline 1-2 vs. 2-1), we therefore see 6 baseline tracks for 3 independent baselines in each example.

Figure 2.3 shows some examples of visibilities and the corresponding UV plane. The top panels show the case of a uniform disk, whose visibility is a first order Bessel function of the first kind. The middle panels show the case of an equal unresolved binary, which shows periodic visibility changes. The bottom panels show the case of two equal gaussian eclipses with an axial ratio of 2:1. Note the horizontal dimension of the Gaussians points are larger than their vertical dimension, therefore in the UV plane the corresponding vertical dimension has more high frequency power than the horizontal dimension.

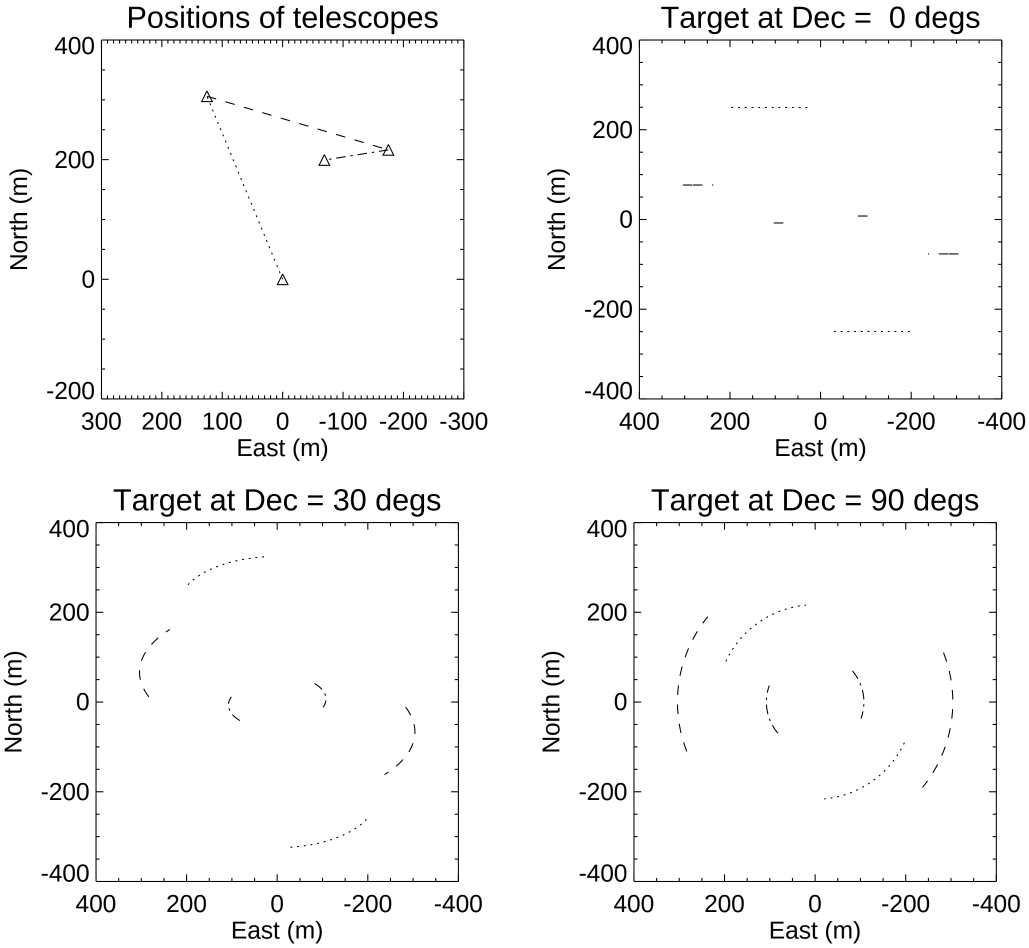

Figure 2.2 Baseline tracks on the UV plane due to the diurnal motion of the Earth. Four telescopes and three baselines at a latitude of 30^o are used in these examples. The top left panel shows the relative positions of the telescopes and the lines connecting them indicate the baselines we use. The top right panel shows the UV tracks at declination of 0^o, the bottom left panel shows the tracks at declination of 30^o, and the bottom right panel is at 90^o. Each track corresponds to 4 hours of motion, from hour angle of -2 hrs to +2 hrs. Each baseline is shown by a different line style. Each track has a point-symmetric counterpart, thus we see 6 UV tracks in total in each plot.

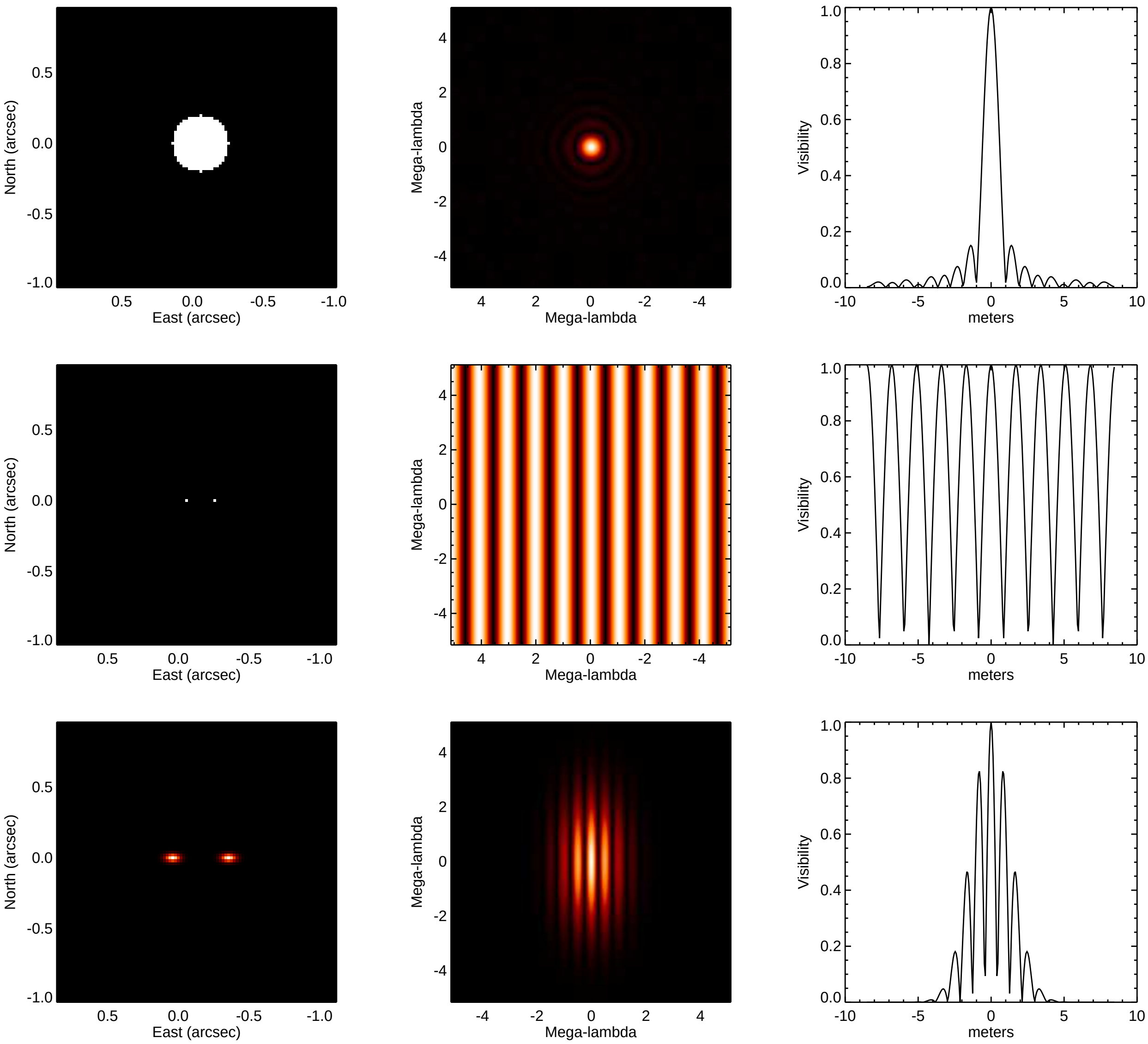

Figure 2.3 Simulated visibilities for 3 types of sources. The first column shows the sources, the middle column shows the 2-D visibility distribution, and the third column shows a slice of the middle panels along the east-west direction. The visibilities are simulated at a wavelength of 1.65 microns.

2.3 Closure Phases

The complex visibility contains both amplitude and phases. Phase is an important quantity in that it carries information about the brightness distribution of the source. However, the phase of the light wave coming from a distant source is always corrupted as atmospheric turbulence always induces random and extra phase shifts, as illustrated by the left panel of Figure 2.4. This makes the phases of complex visibilities useless.

Nevertheless, we can combine 3 telescopes in a closed triangle, and the extra phase seen by each telescope can be canceled in a closed form. As indicated in the right panel of Figure 2.4, the observed phase of baseline 1-2, 2-3 and 3-1 can be written as the combination of the intrinsic phase Φ_o and the extra phase $\Delta\Phi$:

$$\Phi(1-2) = \Phi_o(1-2) + [\Delta\Phi(2) - \Delta\Phi(1)], \tag{2.4}$$

$$\Phi(2-3) = \Phi_o(2-3) + [\Delta\Phi(3) - \Delta\Phi(2)], \tag{2.5}$$

$$\Phi(3-1) = \Phi_o(3-1) + [\Delta\Phi(3) - \Delta\Phi(1)], \tag{2.6}$$

these extra phases can be canceled out if we sum the phases from 3 telescopes in a closed triangle:

$$Closure\ Phase = \Phi(1{-}2)+\Phi(2{-}3)+\Phi(3{-}1) = \Phi_o(1{-}2)+\Phi_o(2{-}3)+\Phi_o(3{-}1) \tag{2.7}$$

This phase closure, or closure phase, carries some intrinsic phase information of the target (see Monnier (2003) for details). It is immune to any phase shifts induced by the atmosphere and many other systematic errors as well. Because of this, it was widely applied to very long baseline interferometry in radio to compensate poor phase

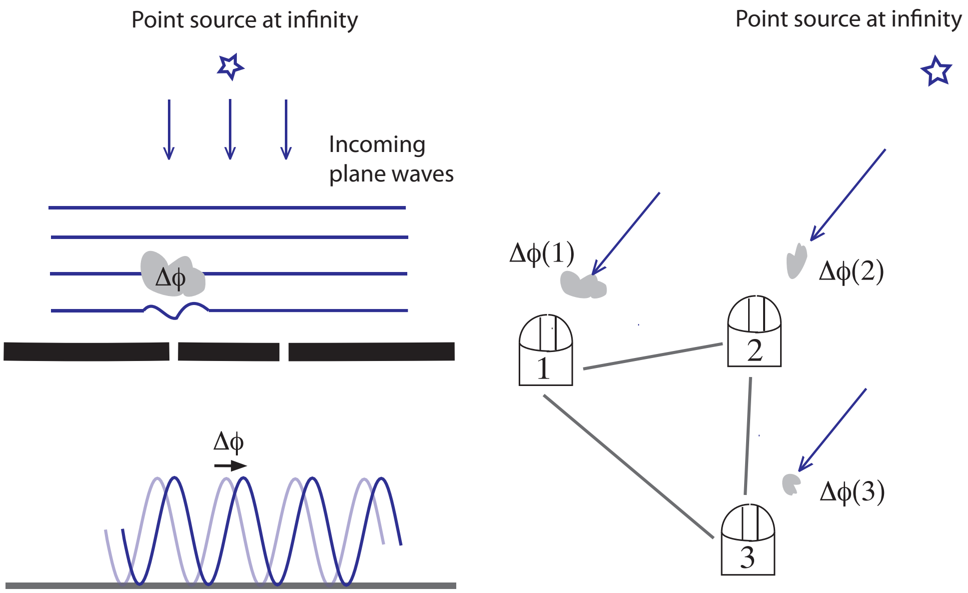

Figure 2.4 The two panels illustrate how a phase delay above an aperture causes a phase shift in the detected fringe pattern - phase errors introduced at any telescope causes equal but opposite phase shifts, which are canceled out in a closed phase triangle, i.e., the closure phase.

stability. Closure phase is also a good quantity for stable and precise measurements. It is widely used in aperture synthesis imaging for phase calibration. In our studies presented in the next few chapters, our modeling will mostly rely on closure phases. Closure phase is very sensitive to asymmetric brightness distributions. For unresolved sources or sources with point-symmetry, the closure phases are either 0^o or 180^o. For a simple resolved binary, the closure phases are proportional to its brightness ratio.

To obtain closure phases, one needs at least three telescopes to form a closed triangle. For N telescopes, there are $C_3^N = N(N-1)(N-2)/6$ possible closed triangles, but only $C_2^{N-1} = ((N-1)(N-2))/2$ independent ones. Therefore a 4 telescope array can have 3 independent closure phases and a 6 telescope can have 10 independent closure phases.

2.4 Aperture Synthesis Imaging

Using visibilities and closure phases, one can construct models for a stellar object. However, a model-independent image is also very useful and can provide more straightforward information of the object.

As shown in Eq. 2.3, the complex visibility is the Fourier transform of the intensity distribution of the object. Thus, the intensity distribution can be inverted by inverse Fourier transform:

$$I(l,m) = \iint V(u,v) e^{2\pi i(ul+vm)} du dv \tag{2.8}$$

However, due to sparse and discrete sampling of the UV plane, our information of the complex visibility is very limited, and thus this inversion process is not straightforward. One needs a reasonable number of samplings to get enough information of the original intensity distribution. A large number of sample points at various frequencies in the UV plane can greatly help the reconstruction of the image.

Because of the limited visibility and phase information, the image reconstruction always have many possible solutions. Thus some reasonable constraints are applied to regulate the solution, for instance, limiting the field-of-view of the image, making the imaging as smooth as possible, and providing a *priori* information to constrain the image.

Popular image reconstruction algorithms include CLEAN and MEM. CLEAN was first introduced by Högbom (1974), and is widely used in radio interferometry (VLA, VLBA, VLBI). In the CLEAN method, the Fourier transform of the spatial frequency sampling function (equals to 1 at places where has visibility measurements, and equals to 0 elsewhere) is called the "dirty beam", which is in fact similar to the point spread function of a continuous aperture but much noisier and has many sidelobes. The Fourier transform of the 2-D visibility image (equals to 0 at places with no data) is used as an estimate of the true image, which is called the "dirty image". In this case, reconstructing the true image is a process of deconvolving the dirty map with the dirty beam (see Clark (1980), Cornwell et al. (1999), Briggs et al. (1999) for more details about CLEAN).

The Maximum Entropy Method (MEM) is more commonly adopted in optical/IR interferometry. MEM defines the entropy of the image as $S = -\sum_i f_i \ln(f_i/I_i)$ after the thermodynamic quantity, where I_i is the user specified image prior, f_i is the fraction of the total flux in pixel i. MEM maximizes the entropy of the reconstructed image while minimizing the corresponding χ^2 of the data. While the smoothness of the image is maintained by MEM, the image also contains some spatial information beyond the diffraction limit, which is known as "super-resolution". Thus the resolution of a MEM image is generally higher than that using CLEAN. More discussions of MEM can be found in Narayan & Nityananda (1986), Monnier (2003), and references therein.

The above algorithms only work for Fourier amplitudes and phases. As already mentioned in the previous section, the phase information is always corrupted by the turbulent atmosphere, and only the closure phase is maintained and immune to the atmospheric phase corruption. Thus, we can use the closure phases to estimate the Fourier phases. This process is known as "Self-Calibration" and is widely adopted in both CLEAN and MEM imaging reconstructions. More details about self-calibration can be found in Cornwell & Wilkinson (1981) and Monnier (1999).

Another method of reconstructing an image is the Monte-Carlo Markov chain imaging developed by Ireland et al. (2006). This algorithm uses a simulated annealing method to limit the probability of converging to local minima as can occur when traditional imaging methods are used on data with limited phase information. The corresponding program is known as MACIM. It uses the maximum entropy as one of the regularizers, and uses the statistical properties from Monte-Carlo Markov chains of images to place statistical limits on image features. More details can be found in Ireland et al. (2006).

In this thesis, most of our images are reconstructed using the MACIM package. Some images are also made by the MEM-based BSMEM (Buscher, 1994) software for cross check.

2.5 Current Optical/IR Interferometers

Since the 1980's, more than 14 optical/IR interferometers have been constructed. A few of them have already been closed in recent years, including Mark III, GI2T, IOTA, COAST and PTI. Currently 7 facilities are still in operation, and are summarized in Table 2.1.

In addition to the current running facilities, three other future facilities are planned. The Large Binocular Telescope Interferometer (LBTI) is expected to start science operations in late 2010. The Magdalena Ridge Observatory Interferometer (MROI) is currently under construction. The Optical Hawaiian Array for Nanoradian Astronomy (OHANA), which will connect several Mauna Kea telescopes with

Table 2.1. Current optical/IR interferometers

Acronym	Telescope Number	Telescope Size(m)	Maximum baseline (m)	Wavelength coverage
CHARA	6	1.0	331	Visible, near-IR
ISI	3	1.65	85	Mid-IR
Keck-I	2	10.0	85	Near-IR, mid-IR
MIRA-I	2	0.25	30	Visible
NPOI	6	0.5	99	Visible
SUSI	2	0.14	160	Visible
VLTI	4(UT), 4(AT)	8.2(UT), 1.8(AT)	202	Near-IR, mid-IR

CHARA	Center for High Angular Resolution Astronomy
ISI	Infrared Spatial Interferometer
Keck-I	Keck Interferometer
MIRA-I	Mitake Infrared Array
NPOI	Navy Prototype Optical Interferometer
SUSI	Sydney University Stellar Interferometer
VLTI	VLT Interferometer

[a] This table is based on Table 3. in Monnier (2003), and the information is up-to-date.

single-mode fibers, is being developed and initial experiments have been carried out.

2.6 The CHARA Array and the MIRC Combiner

2.6.1 The CHARA Array

The CHARA Array, designed and built by Georgia State University's Center for High Angular Resolution Astronomy (CHARA), consists of six 1-meter telescopes and is located on the top of Mount Wilson, California (ten Brummelaar et al., 2005). The array is arranged in a Y-shaped configuration (see Figure 2.5), with 2 telescopes in each arm and separated by different distances to form 15 non-redundant baselines and 20 closed triangles for closure phase measurements. The lengths of CHARA baselines range from 34m to 331m, making it the largest operating optical/IR interferometer array in the world, and providing resolutions up to ~ 0.2 mas at the V band, $\sim$0.5 mas at the H band, and ~ 0.7mas at the K band (resolution defined by the first visibility null of an equal binary, i.e., $\frac{\lambda}{2B}$).

Figure 2.5 shows the layout of the CHARA array atop Mt. Wilson. Light from distant stars are collected by the six Coudé telescopes and transported into six vacuum beam transport tubes. The beams are then brought into the Beam Synthesis Facility, which is isolated from the outside structure to minimize vibration and a relatively constant and uniform temperature is maintained to minimize air turbulence. Inside the Beam Synthesis Facility, the six beams are first reflected into the Optical Path Length Equalization (OPLE) system to eliminate the optical path difference between each pair of beams. The full OPLE system consists of two stages. The first stage happens inside the vacuum tubes, which are also referred to as the "Pipes of Pan" (PoP). The PoPs have five different fixed optical delay intervals, ranging from

0m to 143.1m (ten Brummelaar et al., 2005). The beams coming out of the Pops and the vacuum system are then injected into the second part of the OPLE - the movable delay carts. The carts are designed to move on precision-aligned steel tracks with a full length of $\sim$ 46m, providing 92m of delay compensation. A servo controlled laser metrology system is used to precisely track the positions of the delay carts to allow real-time compensation of the changing optical path differences of all beams during observations. After the delay system, the beams are arranged by a Beam Sampling System which can provide various beam orders for different instruments and observing programs. Lastly, the outgoing beams are split by dichroic splitters into visible part and infrared part. Part of the visible beams are used for the tip-tilt tracking system which serves as a simple "AO" system to partially compensate the atmospheric seeing, while the rest can be used visible beam combiners such as VEGA (Mourard et al., 2008). The infrared part of the beams are brought into other beam combiners where interference fringes form and interferometric observables (visibilities, closure phases) are measured, including MIRC (Monnier et al., 2004), FLOUR (Mérand et al., 2006), NIRO (ten Brummelaar et al., 2005), and PAVO (Ireland et al., 2008), etc. (See ten Brummelaar et al. (2005) and references therein for more details of the CHARA array.)

Figure 2.6 shows the simulated UV coverage for a star at declination of 30^o and 60^o. Four telescopes of the CHARA array, S1-E1-W1-W2, are used in the plots. The good UV coverage of CHARA allows real aperture synthesis imaging with the highest resolution in optical/IR.

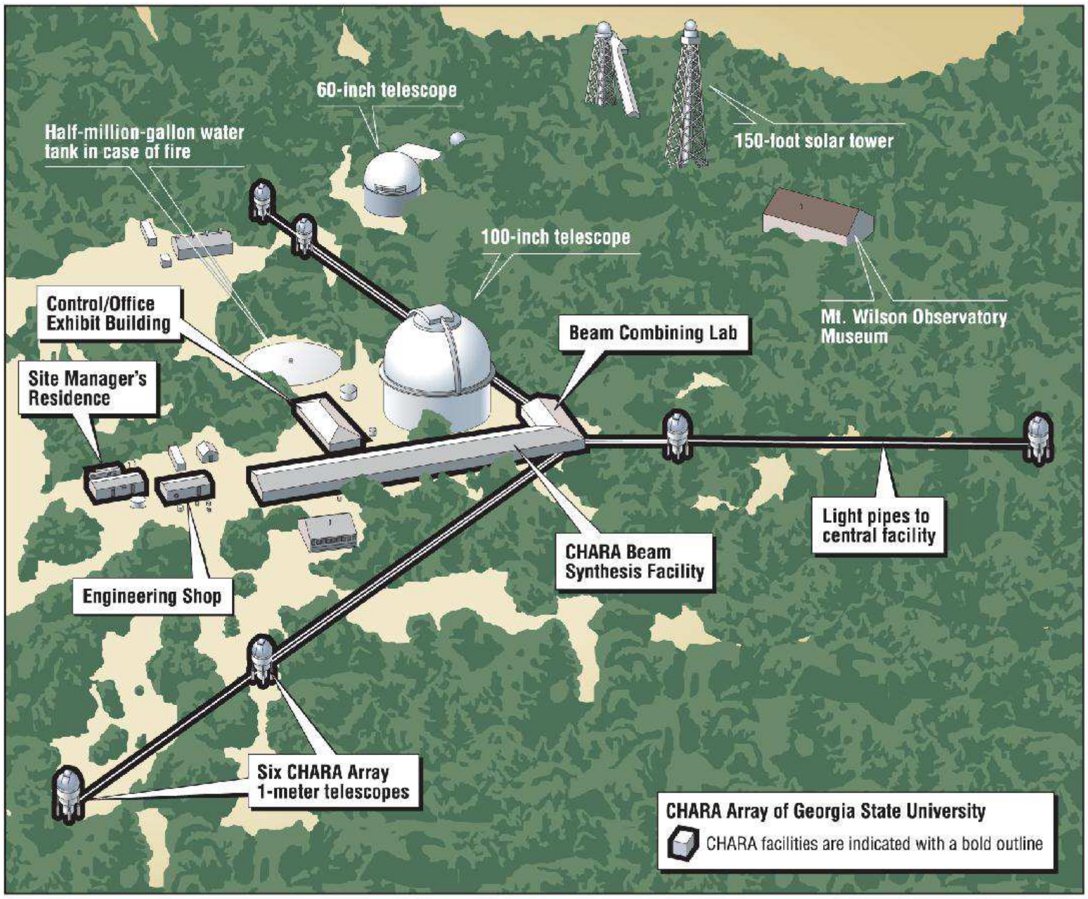

Figure 2.5 The layout of the CHARA array atop Mount Wilson (Picture by GSU Office of University Relations).

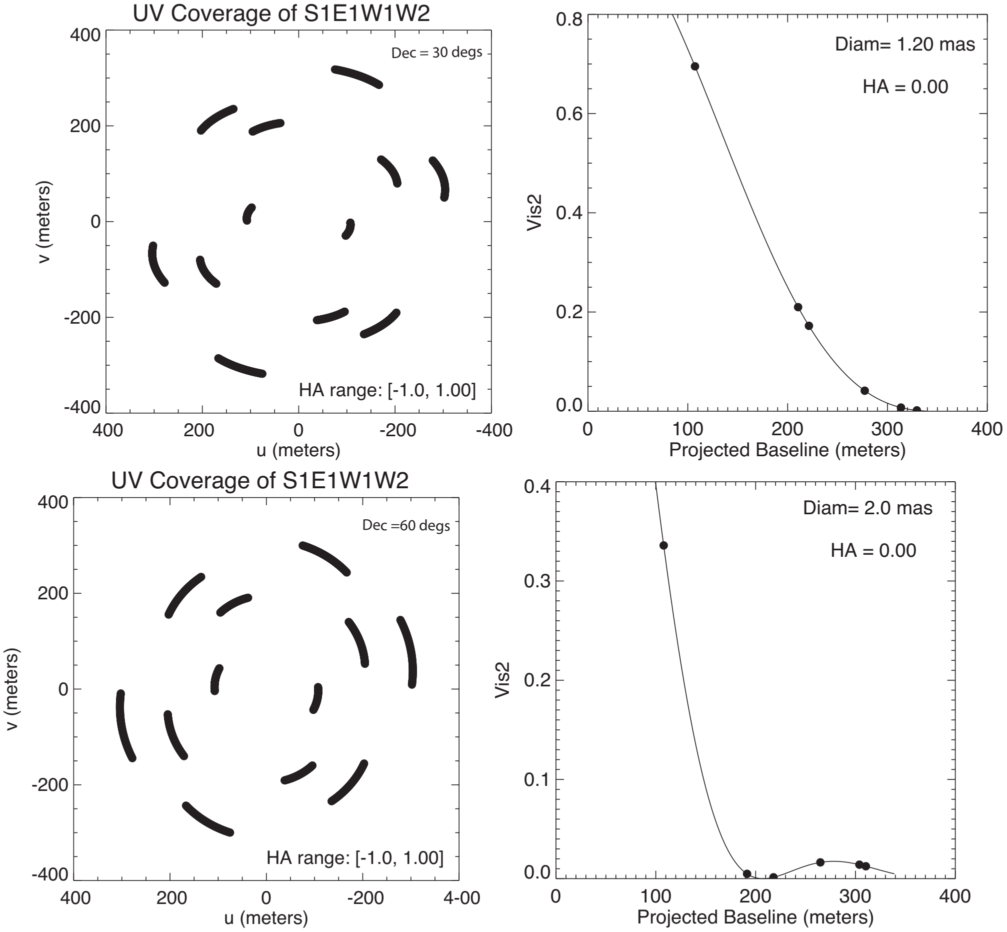

Figure 2.6 CHARA UV coverage and corresponding squared-visibilities. The plots are for telescopes S1-E1-W1-W2. The top panels are for a target at a declination of 30^o. The diameter of the target is 1.20 milliarcsec. The bottom panels show the case for a target at a declination of 60^o, and the diameter of the target is 2.0 milliarcsec. In the top panels, the squared-visibility of the longest baseline just reaches the first null, while in the bottom panels 3 long baselines are already on the second lobe of the squared-visibilitty curve.

2.6.2 MIRC

The Michigan Infra-Red Combiner (MIRC) is an "imaging" combiner designed and built by Prof. John Monnier at the University of Michigan to combine multiple CHARA telescopes together for true interferometric imaging in the *H* and *K* band. MIRC has the capability of combining all six telescopes of CHARA together. Currently it combines 4 telescopes, providing 6 visibilities, 4 closure phases and 4 triple amplitudes simultaneously in 8 narrow spectral channels (see Monnier et al., 2004, 2006, for details). MIRC is designed for stable calibrations and precise closure phase measurements. It uses single mode fibers to spatially filter the light coming from the CHARA beams. Figure 2.7 shows the layout of MIRC. Beams coming out from the CHARA delay system are reflected to off-axis parabolas where they are focused into single mode fibers. The fibers are brought together by a V-groove array in a non-redundant pattern, as shown in the bottom panel of Figure 2.7. The outgoing fiber beams are then collimated by a lenslet array and are focused by a spherical mirror to form an interference pattern, which consists of six overlapping fringes with non-redundant spatial frequencies. The fringes are focused again by a cylindrical lens into a "line" of fringes and are dispersed by low spectral resolution prisms with R $\sim$ 50. Figure 2.8 shows the white light fringes before and after the cylindrical lens, and the fringes dispersed by the prism. The dispersed fringes are finally detected by a PICNIC camera in the cryogenic dewar, where they fall onto 8 spectral channels spanning the *H* band (λ=1.5 - 1.8 μm) (Monnier et al., 2004, 2006). Alternatively, a spectral resolution of R $\sim$ 150 or 400 can also be reached using grisms installed inside the dewar. The first fringes of MIRC are shown in Figure 2.9. A detailed description of the MIRC control system and related software can be found in Pedretti et al. (2009).

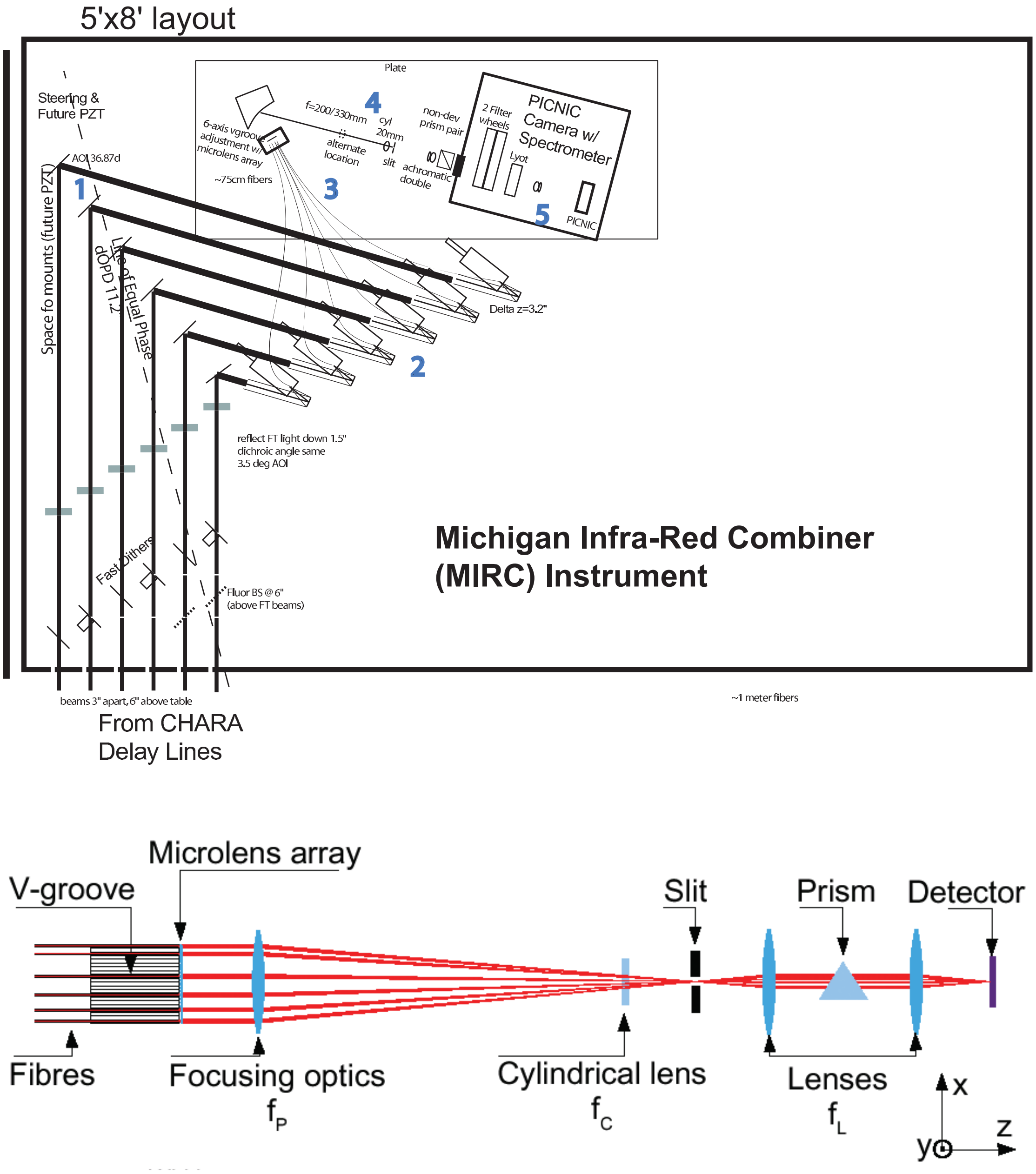

Figure 2.7 Layout of MIRC. *Top* : The layout of the MIRC beam combiner. 1: reflecting mirrors; 2: off-axis parabolas; 3: single-mode fibers and the V-groove that combines the fibers together; 4: the rest of the optics (also shown in the bottom panel); 5: the cryogenic dewar that contains the camera and spectrometer. *Bottom* : the V-groove, microlens array and the rest of the optics. (Images are taken from Monnier et al. (2004))

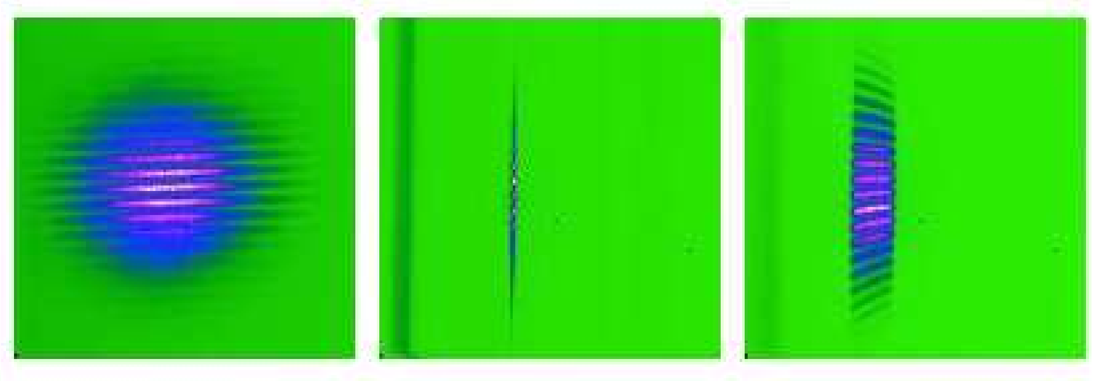

Figure 2.8 MIRC lab fringes. MIRC white light fringes, fringes after the cylindrical lens, and fringes dispersed by the prism. (Images are taken from Monnier et al. (2006))

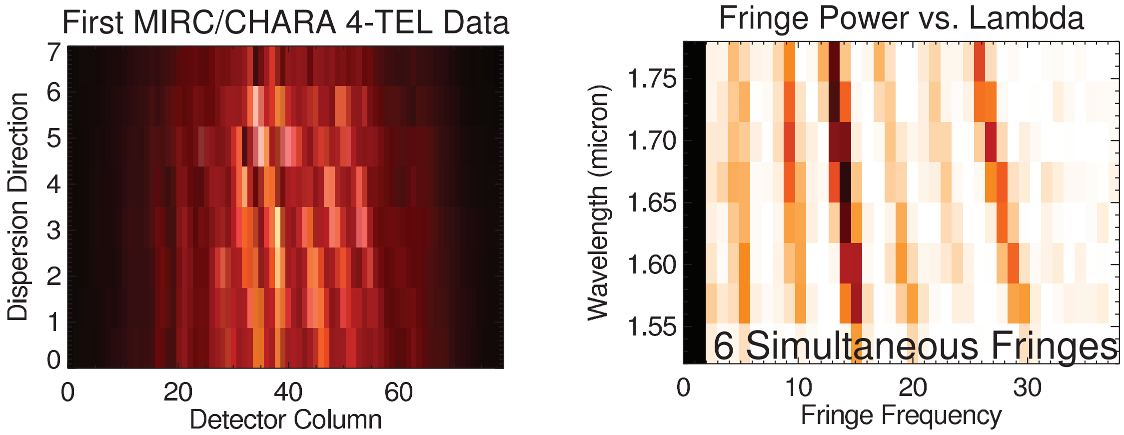

Figure 2.9 First fringes of MIRC. The left panel shows the detected fringes using 4 telescopes simultaneously. This is the same as what we can see in real-time on the MIRC control software. The right panel shows the power spectrum of the 6 fringes, spread onto 8 wavelength channels in the vertical direction. (Images are taken from Monnier et al. (2006))

Chapter 3

Rapid Rotators

Abstract[1]**:** We present sub-milliarcseond resolution observations of three nearby rapid rotators α Cephei, α Ophiuchi, and Altair, obtained with the CHARA array - the largest optical/IR interferometer in the world. Incorporating a gravity darkening model, we are able to determine the inclination, the polar and equatorial radius and temperature, as well as the fractional rotation speed of the three stars with unprecedented precision. The polar and equatorial regions of the three stars have ~1500-2000K temperature gradient, causing their apparent temperatures and luminosities to be dependent on their viewing angles. Our modeling allows us to determine the true effective temperatures and luminosities of all three stars, permitting us to investigate their true locations on the H-R diagram. These properties in turn give us estimates of their masses and ages within a few percent of error using stellar evolution models. Also, based on our gravity darkening modeling, we propose a new method to estimate the masses of single stars in a more direct way through Vsin i measurements and precise geometrical constraint. Lastly, we investigate the degeneracy between the inclination and the gravity darkening coefficient, which especially affects the modeling of α Oph. Although incorporating Vsin i has lifted the

---

[1] This chapter is mostly based on Zhao et al. (2009) and my contributions in Monnier et al. (2007)

degeneracy to some extent, higher resolution observations are still needed to further constrain the parameters independently.

3.1 Introduction

In the past few years, optical interferometers have resolved the elongated photospheres of rapidly-rotating stars for the first time. The emergence of these high angular resolution observations of hot stars has shined a spotlight on critical areas of stellar evolution and basic astrophysics that demand our attention. For decades, stellar rotation was generally overlooked in stellar models and was regarded to have a trivial influence on stellar evolution because most stars are slow rotators, such as the Sun (Maeder & Meynet, 2000). Although the effects of rotation on solar type stars are indeed relatively mild, they are more prominent on hot stars. Studies have shown that a large fraction of hot stars are rapid rotators with rotational velocities more than 120 $\mathrm{km\,s^{-1}}$(Abt & Morrell, 1995; Abt et al., 2002). Virtually all the emission-line B (Be) stars are rapid rotators with rotational velocities of $\sim$ 90% of breakup (Frémat et al., 2005). Stars that are rapidly rotating have many unique characteristics. The centrifugal force from rapid rotation distorts their photospheres and causes them to be oblate. This distortion causes their surface brightness and T_{eff} to vary with latitude, and their equatorial temperatures are predicted to be much cooler than their polar temperatures, a phenomenon known as "Gravity Darkening" (von Zeipel, 1924a,b). Recent stellar models that took rotation into account showed that rapid rotation also affects stars' luminosity, abundance (Pinsonneault, 1997; Yoon et al., 2008), evolution, and increases their lifetime (Kiziloglu & Civelek, 1996; Talon et al., 1997; Meynet & Maeder, 2000). It is also linked to stellar wind, mass loss (e.g., Maeder et al., 2007), and even Gamma-Ray bursts (MacFadyen & Woosley, 1999; MacFadyen et al., 2001; Burrows et al., 2007a).

The development of long baseline optical interferometry in recent years has provoked observations on several nearby rapid rotators. Using the Palomar Testbed Interferometer, van Belle et al. (2001) measured the photospheric elongation of the star Altair and found one of its dimension is $\sim 14\%$ larger than the other. Observations using the CHARA array (Aufdenberg et al., 2006) and the Navy Prototype Optical Interferometer (NPOI) (Peterson et al., 2006) both found that the photometric standard star Vega is actually a nearly pole-on rapid rotator, which explained the mystery that Vega looks brighter than the mean A0 V star based on nearby star clusters. In addition to Altair and Vega, several other nearby rapid rotators have also been studied and are found to be oblate, including Achernar, Alderamin (α Cephei) and Regulus (Domiciano de Souza et al., 2003; van Belle et al., 2006; McAlister et al., 2005; Kervella & Domiciano de Souza, 2006; Monnier et al., 2007). These studies confirmed the general picture of von Zeipel's gravity darkening law, but also raised discrepancies between observations and the widely adopted standard von Zeipel model (i.e., $T_{eff} \propto g_{eff}^{\beta}$, where β is the gravity darkening coefficient, and $\beta = 0.25$ for fully radiative envelopes). For instance, using the CHARA array Monnier et al. (2007) reconstructed a model-independent image for Altair and found a darker-than-expected equator compared to their gravity darkening model. This suggests for the first time from observations that the standard gravity darkening law may work only at a basic level and other mechanisms need to be introduced to account for the extra darkening. To address this issue, more detailed studies and model-independent images of rapid rotators are needed.

In this chapter, we present our study of the three nearby rapid rotator α Cephei, α Ophiuchi, and Altair, all observed with the CHARA long baseline optical/IR interferometer array and the MIRC beam combiner. The star α Cephei (α Cep , Alderamin, HR 8162, V=2.46, H=2.13, d=14.96pc) is the eighth nearest A star in the sky. It was classified as an A7 IV-V star in early studies, but was recently classified as an A8V main sequence star by Gray et al. (2003). It is one of the few A stars (including Altair) that are found to have chromosphere activities (Walter et al., 1995; Simon & Landsman, 1997; Simon et al., 2002). The Vsin i measurements of α Cep show large scatter, spanning from $\sim 180km\ s^{-1}$ to $\sim 245km\ s^{-1}$ (Bernacca & Perinotto, 1973; Uesugi & Fukuda, 1970; Royer et al., 2007; Abt & Morrell, 1995). Recently, van Belle et al. (2006) studied α Cep using the CHARA array and found it is rotating close to break-up, and its photosphere is elongated due to rapid rotation.

The star α Ophiuchi (α Oph , Rasalhague, HR 6556, $V = 2.09$, H=1.66, d=14.68pc) is a nearby subgiant binary system (Wagman, 1946; Lippincott & Wagman, 1966), and is the seventh nearest A star in the sky. The primary is a A5IV sub-giant which was first identified as a class III star but was later corrected to class IV by Augensen & Heintz (1992) and Gray et al. (2001). Several groups have tried to study the orbit of the system (McAlister & Hartkopf, 1984; Kamper et al., 1989; Mason et al., 1999; Augensen & Heintz, 1992; Gatewood, 2005, etc.), and it was lately determined to have a period of $\sim$ 8.6 yrs and a semi-major axis between 0.4" - 0.5". The mass determination of the primary has large scatter, ranging from $2M_{\odot}$ to $4.9M_{\odot}$ (e.g, Kamper et al., 1989; Augensen & Heintz, 1992; Gatewood, 2005). The companion, which is approximately a K2V star, is thought to have a mass of 0.5-1.2$M_\odot$(Kamper et al., 1989; Augensen & Heintz, 1992; Gatewood, 2005), and is observed to be 3.5 mag fainter than the primary in the K band (Boccaletti et al., 2001). The size of the primary was estimated to be $\sim$ 1.6 - 1.7 $R_\odot$(Barnes et al., 1978; Blackwell et al., 1980). Its rotational velocity V$\sin i$ ranges from 210km s^{-1}to 240km s^{-1}(Bernacca & Perinotto, 1973; Uesugi & Fukuda, 1970; Abt & Morrell, 1995; Royer et al., 2002), implying α Oph is spinning at a significant fraction of its break-up speed of $\sim$ 270 km s^{-1}.

The star Altair (α Aquilae, α Aql, HR 7557, V = 0.77, H = 0.102, d=5.14 pc) is an A7IV-V type star in the northern sky. It is the second nearest A star and the twelfth brightest star in the sky, and is a member of the famous “Summer Triangle” (the other two stars are Vega and Deneb). Altair shows very large projected velocity, varying from 200km s^{-1}(Abt & Morrell, 1995), 217km s^{-1}(Royer et al., 2002), to 242km s^{-1}(Uesugi & Fukuda, 1982). Using the Palomar Testbed Interferometer, van Belle et al. (2001) found that Altair is elongated and one dimension is $\sim$ 14% larger than the other. Using the Navy Prototype Optical Interferometer, Ohishi et al. (2004) found that Altair has asymmetric surface brightness distribution and its pole is brighter than other parts of the star. Using the same data, Peterson et al. (2006) modeled Altair using the gravity darkening model and confirmed the oblateness and asymmetric structure of Altair due to rapid rotation. The most recent breakthrough was achieved by Monnier et al. (2007), who reconstructed a model-independent image for Altair using the CHARA array - the first image of a main-sequence star rather than the Sun, and found deficiencies in the von Zeipel model. In this chapter we only report the modeling part of this study. The details about imaging Altair can be found in Monnier et al. (2007).

This chapter is organized as follows. We report our observations and data reduction schemes in §3.2. We discuss our aperture synthesis imaging for α Cep and α Oph in §3.3 and present gravity darkening models for all three stars in §3.4. In §3.5, we present their temperatures, luminosities, and their locations on the H-R diagram. Based on our modeling, we propose a new method to estimate the mass of a star in §3.6. Finally, we discuss our results in §3.7 and present our conclusions in §3.8.

3.2 Observations and data reduction

Our observations were conducted at the Georgia State University (GSU) Center for High Angular Resolution Astronomy (CHARA) interferometer array along with the MIRC combiner. Details of the CHARA array and MIRC have already been discussed in §2.6.1 and §2.6.2.

Our use of single mode fibers makes the systematic visibilities of MIRC relatively stable. However, the atmospheric turbulence changes faster than the 5.5ms readout speed of the camera, causing decoherence of the fringes that needs to be calibrated. We therefore observe several calibrators adjacent to our targets over each observing night. For the purpose of bias subtraction and flux calibration, each set of fringe data is bracketed with measurements of background (i.e., data taken with all beams closed), shutter sequences (i.e., data taken with only one beam open at a time to

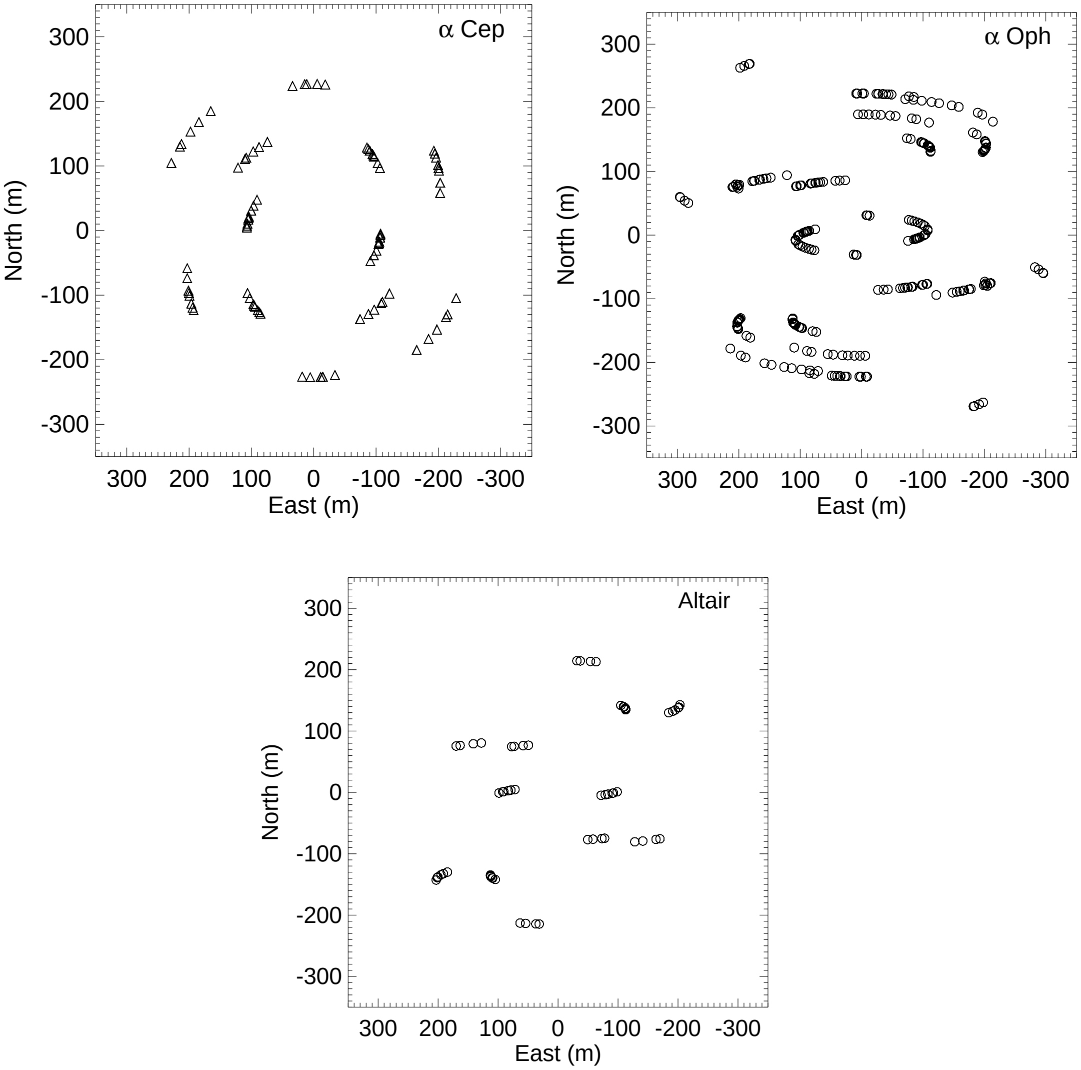

Figure 3.1 Baseline coverages for α Cep and α Oph. The longest baselines in the observations are 251m, 329m, and 248m for α Cep, α Oph, and Altair, corresponding to resolutions of 0.68mas, 0.52mas, 0.69mas, respectively. The UV coverage can be obtained by dividing these plots by corresponding wavelengths.

estimate the amount of light coming from each beam), and foreground (i.e., data taken with all beams open but without fringes) (Pedretti et al., 2009). Each object is observed for multiple sets. During the period of taking fringe data, a group-delay fringe tracker is used to track the fringes (Thureau et al., 2006). In order to track the flux coupled into each beam in “real time” to improve the visibility measurements, we use spinning choppers to temporally modulate the light going into each fiber simultaneously with fringe measurements. The chopper speeds were set to 25Hz, 30Hz, 35Hz and 40Hz in 2006 and were increased to 55Hz, 65Hz, 75Hz and 85Hz in 2007 to avoid overlap of modulating frequencies caused by chopper drifts.

We observed α Cep on 4 nights in 2006 and observed α Oph on 8 nights in 2006 and 2007, using various array configurations optimized for equal Fourier coverage in all directions for good imaging. We observed Altair on the nights of 2006 Aug 31 and 2006 Sep 01 using the smaller array configuration of CHARA (S2-E2-W1-W2). The detailed log of our observations is listed in Table 3.1. Figure 3.1 shows the overall baseline coverage of our observations of α Cep, α Oph, and Altair.

The data reduction process follows the pipeline outlined by Monnier et al. (2007), which was validated using data on the binary ι Peg. In brief, after frame-coadding, background subtraction and Fourier transformation of the raw data, fringe amplitudes and phases are used to form squared-visibilities and triple products. Raw squared-visibilities are then estimated from the power spectrum after foreground bias subtraction. After the fiber coupling efficiencies are estimated using either the chopping signal or direct fit to the fiber profiles, we obtain uncalibrated squared-visibilities and complex triple amplitudes. Finally, calibrators with known sizes are

Table 3.1. Observation logs for α Oph and α Cep

Target	Obs. Date	Telescopes	Calibrators	Chopper
α Oph	UT 2006Jun20	W1-W2-S1-S2	α Sge	no
	UT 2006Jun21	W1-W2-S1-S2	ζ Oph, γ Ser	no
	UT 2006Aug28	S2-E2-W1-W2	υ Peg	no
	UT 2006Aug29	S2-E2-W1-W2	γ Lyr, υ Peg	no
	UT 2006Aug30	S2-E2-W1-W2	γ Lyr	yes
	UT 2006Aug31	S2-E2-W1-W2	γ Lyr, υ Peg	yes
	UT 2007May10	S1-E1-W1-W2	ζ Oph, τ Aql	yes
	UT 2007May12	S1-E1-W1-W2	ζ Oph, τ Aql	yes
α Cep	UT 2006Oct09	S2-E2-W1-W2	29 Peg, υ And, ζ Per	yes
	UT 2006Oct11	S2-E2-W1-W2	υ And, ζ Per	yes
	UT 2006Oct12	S2-E2-W1-W2	29 Peg, ζ Per	yes
	UT 2006Oct16	S2-E2-W1-W2	29 Peg, υ And	yes
Altair	UT 2006Aug31	S2-E2-W1-W2	γ Lyr, υ Peg	yes
	UT 2006Sep01	S2-E2-W1-W2	γ Lyr	yes

used to calibrate the drifts in overall system response before we obtain the calibrated squared-visibilites, closure phases, and complex triple amplitudes. The adopted sizes of our calibrators are listed in Table 3.2. Corresponding errors of the data are estimated by combining both the scatter of the data and calibration errors.

3.3 Aperture Synthesis Imaging

We employed the publicly-available application "Markov-Chain Imager for Optical Interferometry (MACIM)" (Ireland et al., 2006) to reconstruct images for α Cep and α Oph. The application applies the Maximum Entropy Method (MEM) (Narayan & Nityananda, 1986) widely used in radio synthesis imaging, and has been validated on other test data (Lawson et al., 2006). Since the photosphere of a star has a sharp emission cut-off at the edge, which is imprinted in the highest spatial frequencies that

Table 3.2. Calibrator diameters

Calibrator	UD diameter (mas)	Reference
α Sge	1.32 ±0.02	Uniform-disk fit to PTI archive data[a]
ζ Oph	0.51 ± 0.05	Hanbury Brown et al. (1974)
γ Ser	1.21± 0.05	Uniform-disk fit to PTI archive data
γ Lyr	0.74 ±0.10	Leggett et al. (1986)
υ Peg	1.01 ± 0.04	Blackwell & Lynas-Gray (1994)
τ Aql	1.10 ± 0.01	Mérand et al. (2005, 2006)
29 Peg	1.0 ± 0.1	MIRC measurement
υ And	1.17 ± 0.02	Boden 2008[b]
ζ Per	0.67 ± 0.03	getCal[c]

[a] available at http://mscweb.ipac.caltech.edu/mscdat-pti

[b] SED fit, private communication

[c] http://mscweb.ipac.caltech.edu/gcWeb/gcWeb.jsp

cannot be observed, we constrain the field of view of the images within an ellipse to avoid spreading-out of the flux by the MEM procedure at the edge of the star. This constraint is appropriate for α Cep and α Oph due to their lack of any circumstellar emission outside of their photospheres. The details of this approach can be found in Monnier et al. (2007). The ellipse prior is found by conducting MACIM imaging on a grid of $\sim$ 400 different ellipses with uniform surface brightness, spanning a range of possible sizes, axial ratios, and position angles. To ensure the smoothness of the image, we also de-weighted the high resolution data by convolving with a 0.3 milliarcsec beam, an approach usually applied in radio synthesis imaging. The image with the global maximum entropy is then taken as the final result. We treated each wavelength channel as providing a distinct set of (u, v) plane coverage, ignoring any wavelength-dependence of the image itself. This assumption is well justified for α Cep and α Oph since the brightness profiles of their photospheres are almost identical in all channels in the H band.

Figure 3.2 shows the reconstructed image of α Cep (${\chi_\nu}^2 = 1.10$). Its photosphere is well resolved and appears elongated along the east-west direction. The bright region at the bottom with T_{eff} above 7000K (left panel) is later identified close to the pole and the dark belt below 6500K is the equator - a direct confirmation of the gravity darkening effect. The image implies the pole of α Cep is medium inclined. The very top of the image becomes bright again since the photosphere is brighter toward the poles. The right panel of Fig.3.2 shows the orientation of α Cep based on the model in §3.4. It shows that the bright spot in the image is in fact above the pole as the pole of α Cep is limb-darkened. The squared-visibilities, closure phases, and triple amplitudes derived from the image are compared with the data in Figure 3.3, 3.4, and 3.5.

Although we have tried intensively to reconstruct an image for α Oph, we are unable to find a unique solution for it. This is because the brightness distribution of a stellar surface is mainly imprinted in our closure phases. The closure phase is only sensitive to asymmetric structures of the object, while a symmetric object only gives either 0^o or 180^o closure phases. The squared-visibilities of our data are less constraining due to their relatively large errors. The near equator-on inclination of α Oph (see §3.4.2) makes its brightness distribution nearly symmetric, providing too few non-zero closure phase signatures to constrain the image. Therefore, we could not obtain a reliable solution for α Oph in the image reconstruction. We have also pursued other imaging programs such as MIRA (Thiébaut, 2008), and obtained similar results in our preliminary efforts (Thiébaut 2008, private communication).

Thus we only present the model of α Oph in this paper. As we will see in §3.4.2, the lack of non-zero closure phase signatures of α Oph also brings similar issues to our modeling, causing high degeneracy to the inclination and the gravity darkening coefficient.

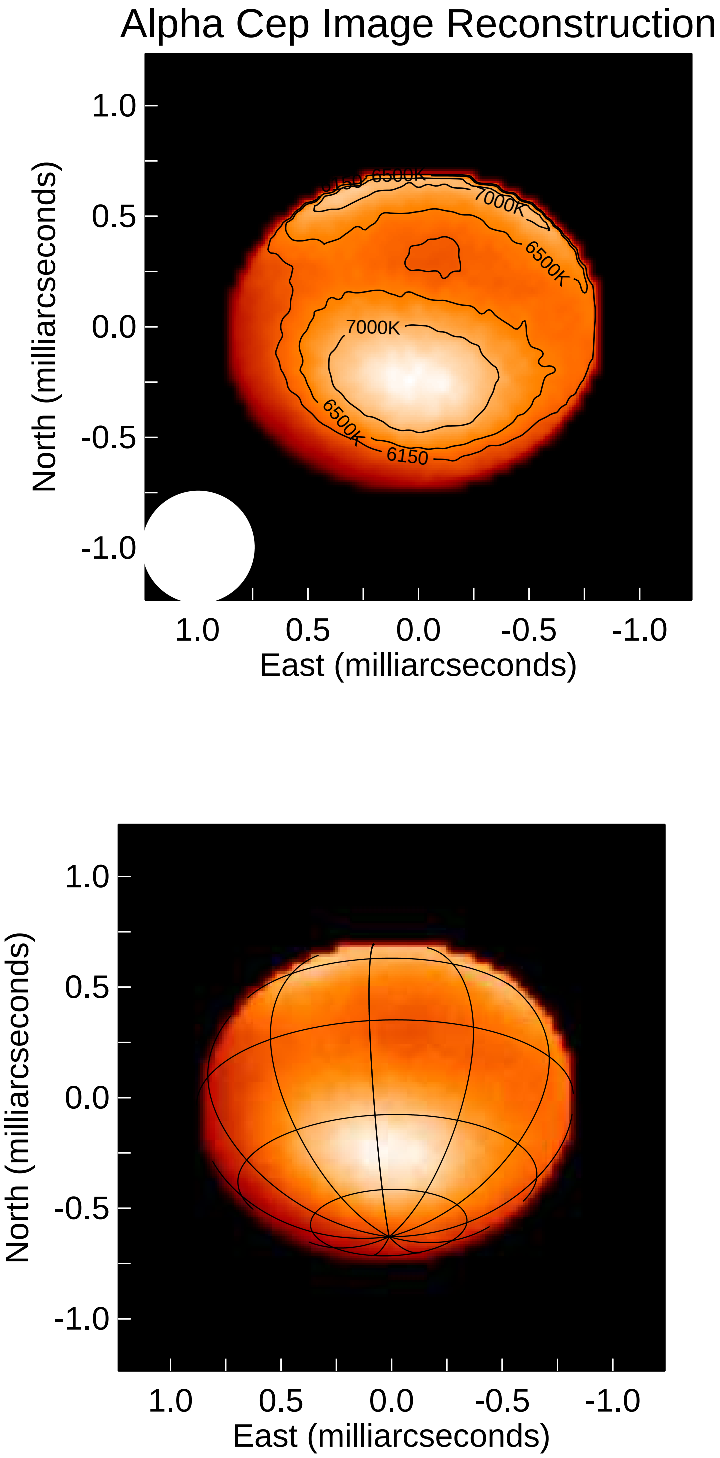

Figure 3.2 Reconstructed MACIM image of α Cep. The left panel shows the contours of local brightness temperature. To help visualize the geometry of α Cep, the right panel shows its latitude and longitude using the positions from the standard model discussed in §3.4. The white circle at the bottom-left corner of the left panel shows the size of the convolving beam that we use for the image reconstruction. The total χ^2_ν of the image is 1.10. The resolution of the image is 0.68 milliarcsec.

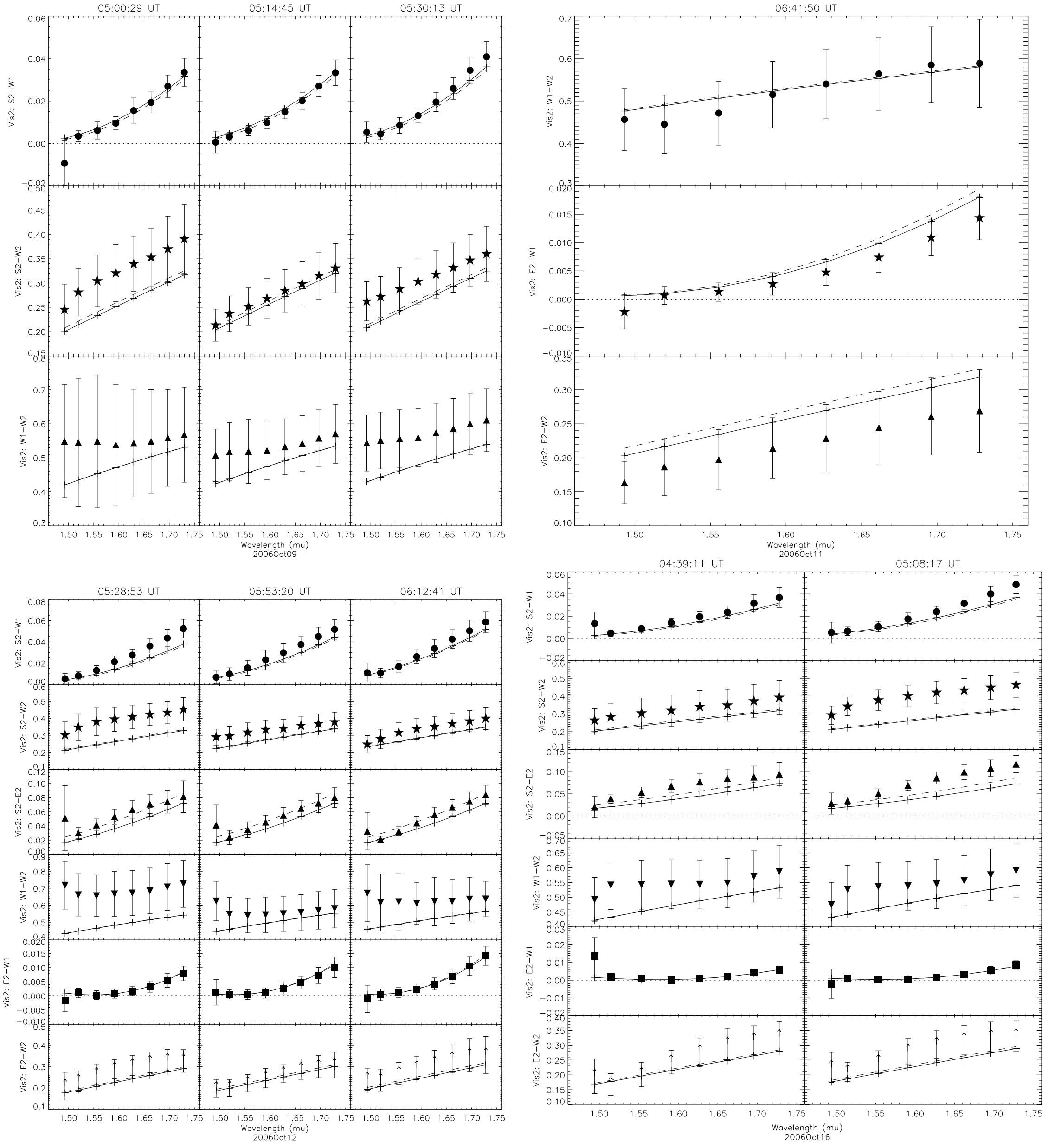

Figure 3.3 Squared visibilities of α Cep. α Cep squared-visibilities from the MACIM image (solid lines) and the gravity darkening model ($\beta = 0.216$, dashed lines) vs. data (filled points with error bars) for the night of 2006Oct 09, 2006Oct11, 2006Oct12, and 2006Oct16. The overall χ^2_ν of the image's squared-visibilities is 0.87, while that of the model is 0.80. Each row stands for a different baseline, while the columns indicate different times of observation. The eight data points in each panel indicate the eight spectral channels of MIRC across the H band. (Please refer to the electronic edition if the type size is too small.)

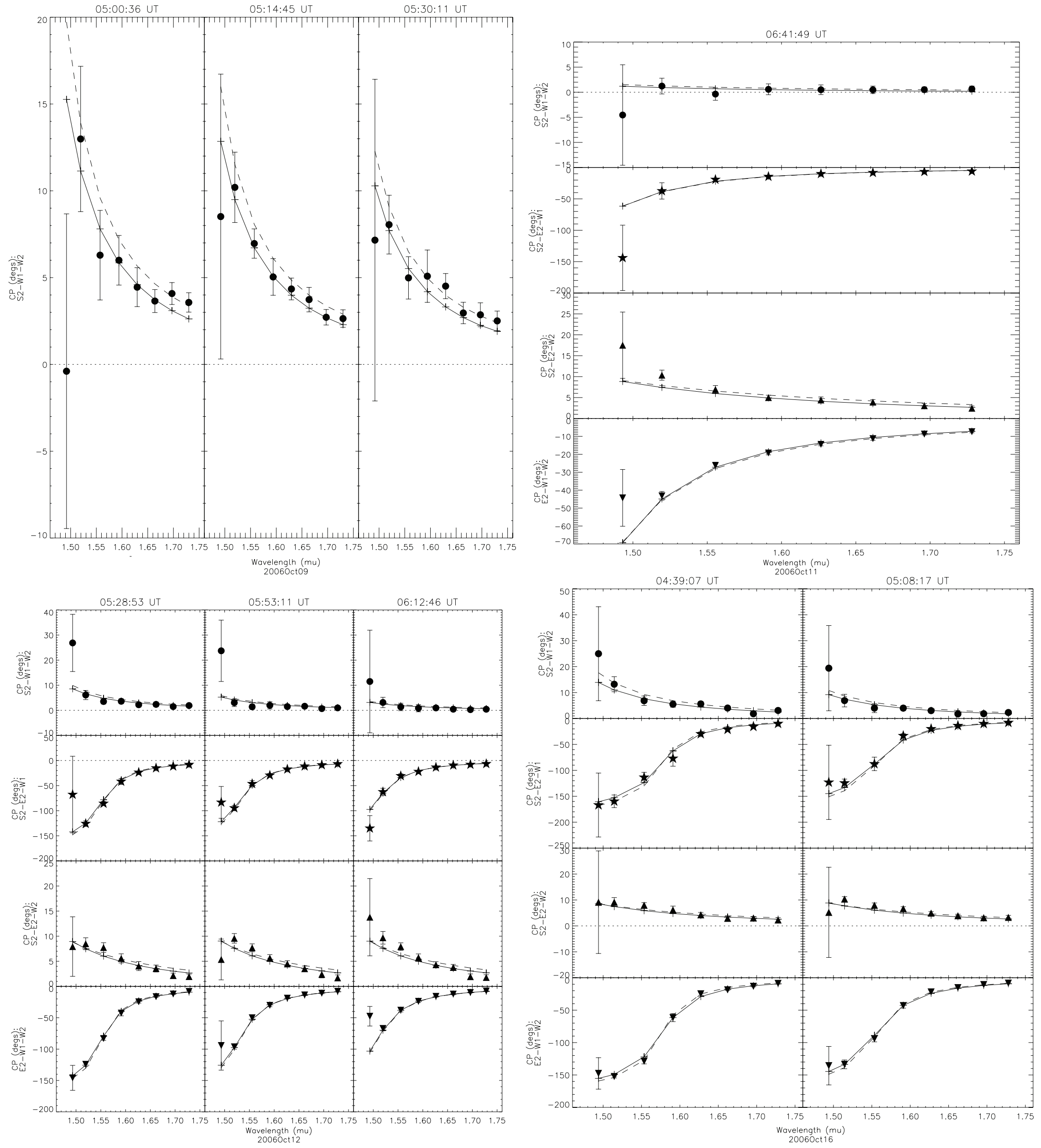

Figure 3.4 Closure phases of α Cep. Similar to Fig.3.3 but showing the closure phases for α Cep for the night of 2006 Oct 09, 2006Oct11, 2006Oct12, and 2006Oct16. The solid lines stand for the closure phases of the MACIM image, and the dashed lines stand for the model. Each row stands for a different telescope triangle. The overall χ^2_ν of the image's closure phases is 0.95, while that of the model is 1.27.

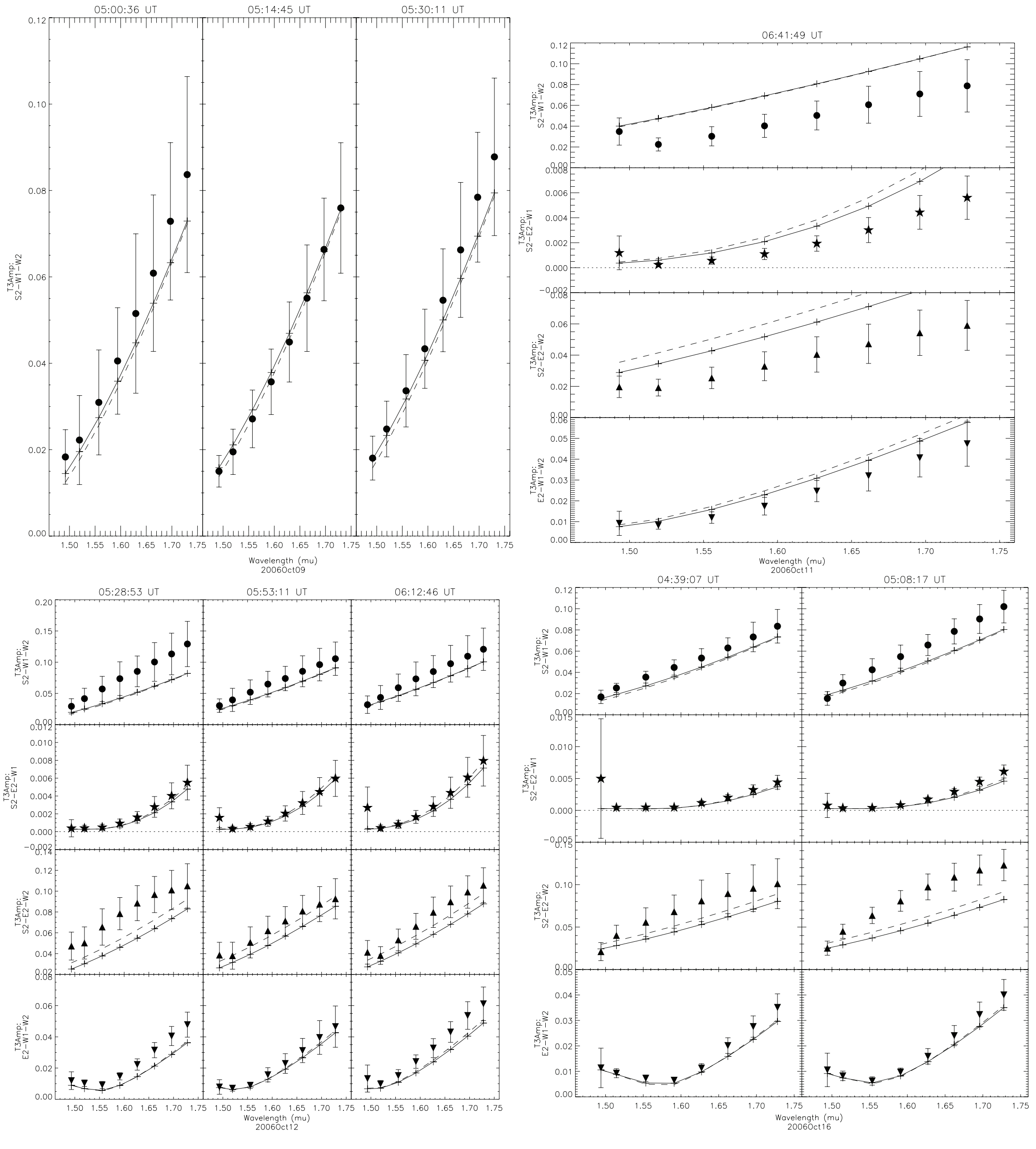

Figure 3.5 Triple amplitudes of α Cep. Similar to Fig.3.3 but showing the triple amplitudes for α Cep for the night of 2006 Oct 09, 2006Oct11, 2006Oct12, and 2006Oct16.

3.4 Surface Brightness Modeling

In addition to synthesis imaging, we construct rapid rotator models to fit the data of all three stars, following the prescription described in Aufdenberg et al. (2006) and references therein. Specifically, we assume a Roche potential (point mass) and solid body rotation in our model, and use the von Zeipel gravity darkening law (von Zeipel, 1924a,b) to characterize the latitudinal temperature profile. Six parameters are used to define the models, including the stellar radius and temperature at the pole, the angular rotation rate as a fraction of breakup (ω), the gravity darkening coefficient (β), the inclination angle, and the position angle (east of north) of the star. To ensure accuracy of the models, we construct them at four different wavelength channels across the H band. The intensity and limb darkening at each point of the stellar surface is interpolated using the stellar atmosphere models of Kurucz (Kurucz, 1993) as a function of local temperature, gravity, viewing angle, and wavelength. The 3D surfaces of the models are generated using patches with uniform surface areas to avoid over-sampling at the poles or under-sampling at the equators, and also to speed up the computation. A direct Fourier transform is then used to convert the projected intensity model to squared-visibilities, closure phases and triple amplitudes. We have validated our model by comparing with another independent model from Jason Aufdenberg (private communication, 2007) on the data of Vega from Aufdenberg et al. (2006) (see Figure 3.6). We also compared the model using Kurucz limb darkening with one using PHOENIX limb darkening and found the difference is negligible.[2]. In addition, we also force our model to match the V and H band photometric fluxes obtained from the literature (see Tables 3.3, 3.4) to constrain the temperature range.

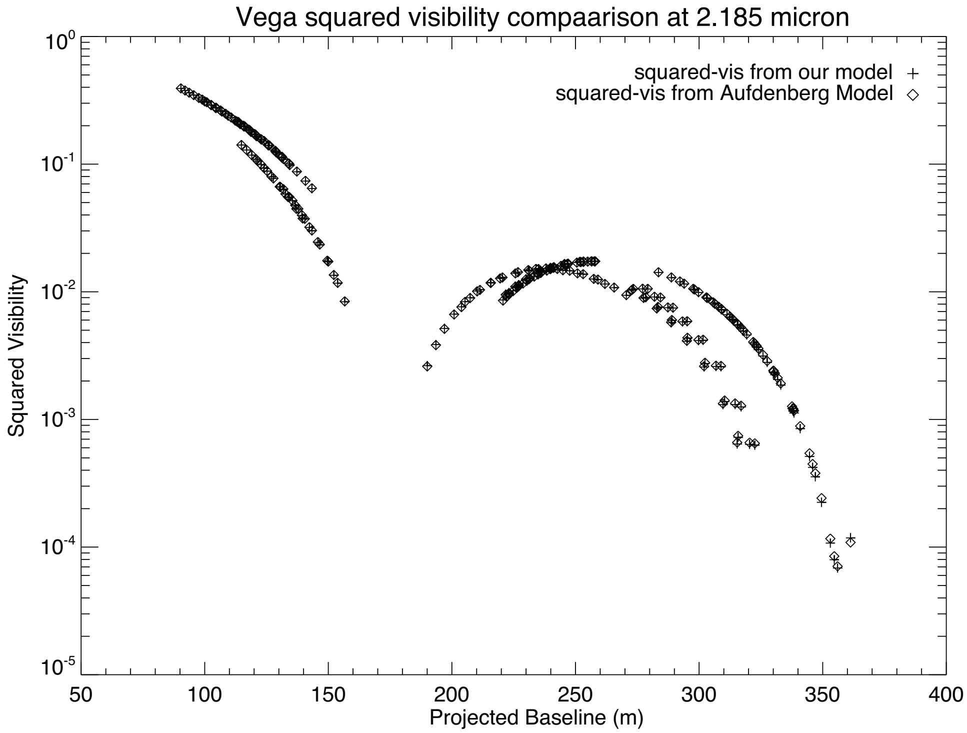

Figure 3.6 Comparison of gravity darkening models. The crosses indicate the squared visibilities from our model, while the diamonds indicate those from the model of Aufdenberg et al. (2006). Both models are using the PHOENIX stellar atmosphere grids. The two gravity darkening models resemble with each other very well and only have slight differences close to the visibility nulls.

3.4.1 α Cep

We first fit the data of α Cep with the standard von Zeipel gravity darkening model for fully radiative envelopes (i.e., $T_{eff} \propto g_{eff}^{\beta}$, where $\beta = 0.25$; hereafter, the standard model). The Levenberg-Marquardt algorithm is applied for the least-square minimization and the parameter spaces are extensively searched in the fit. We as-

---

[2] The data and models used for the comparison are available at http://www.astro.lsa.umich.edu/∼mingzhao/rapidrot.php

sume M = 2.0 $M_\odot$(van Belle et al., 2006), distance = 14.96 pc (Perryman et al., 1997), and metallicity $[Fe/H] = 0.09$ (Gray et al., 2003) in the model. The left panel of Figure 3.7 shows the best-fit standard model of α Cep, with an overall goodness of fit χ_ν^2 of 1.21. The model shows the photosphere of α Cep is elongated, with a bright polar region at the bottom and a dark equator above it - generally consistent with the synthesized image in Fig.3.2. Our standard model yields an inclination of $64.9^o \pm 4.1^o$ and a position angle of $-178.3^o \pm 4.1^o$, consistent with the ellipse fit of van Belle et al. (2006, hereafter VB06), which gave a position angle of -177^o (or 3^o depending on the definition). However, both the inclination and the position angle of their gravity darkening model ($i = 88.2^o, P.A. = 17^o \; or \; -163^o$) differ from our results, as we have better UV coverage and also closure phase information which is very sensitive to asymmetric structures. Our model indicates α Cep is rotating very fast, at 92.6% of its break-up speed. The temperature at the poles is ∼2400K higher than at the equator, while its radius at the equator is 26% larger than at the poles. The best-fit parameters of the standard model are listed in the second column of Table 3.3. Since the calibration error of the data varies from night to night, we estimate the error of each parameter by bootstrapping different nights of data while treating each night as a whole. We then fit the new set of data and iterate this procedure for hundreds of times. The resulting standard deviations of the bootstrapped distributions are then taken as the errors of the model parameters.

In addition to our data, we also combine the squared-visibilities from VB06 (here after "Classic data") into our fit. The combined fit gives a slightly higher inclination, and all parameters are still consistent with our previous fit. The total ${\chi_\nu}^2$ of the combined fit is 1.25. However, the ${\chi_\nu}^2$ of the Classic data (${\chi_\nu}^2$=2.0) is very large although it is slightly better than the original result of VB06 (${\chi_\nu}^2$ =2.16), implying that either the Classic data have additional un-calibrated errors or the model needs more degrees of freedom. We first look into a free β in the model. Indeed, the von Zeipel theory suggests that the standard gravity darkening coefficient ($\beta = 0.25$) only applies to pure radiative envelopes. However, it is uncertain if α Cep is pure radiative or not. The atmosphere models of Kurucz (1979) suggest that, for an atmosphere with T$_{eff} > 7500K$ and $\log g \sim 4$, like the polar areas of α Cep, convection should have very little or no effect. But it starts to play a role when temperature and $\log g$ drop below those numbers. In addition, the evolution models of β calculated by Claret (1998, 2000) also indicate that, for a 2-2.5M$_\odot$ star, convection starts to take place once T$_{eff}$ is below ~7900K. For the case of α Cep, although its T$_{eff}$s at the polar areas are higher than 8000K, they drop to only ~6700K in the equator, implying that convection may have effects in the equatorial areas and β may deviate from the standard value. Therefore as a preliminary effort, we extend the standard von Zeipel law to a free β.

The new combined β-free fit gives a ${\chi_\nu}^2$ of 2.11 to the Classic data, similar to the original VB06's result. But it prefers a β of 0.22 rather than the 0.08 value of VB06. To address this issue, we tried to fit the combined data at a fixed β of 0.08 instead, but only obtained a total ${\chi_\nu}^2$ of ~ 6.5, much worse than the previous result. In addition, we also fit the Classic data only but found it is too hard to constrain the model due to the small amount of data and lack of phase information. Therefore, due to possible uncertainties of the Classic data, we applied the β-free model to the

MIRC measurements only, and the results are shown in the third column of Table 3.3. The best-fit model is shown in the right panel of Figure 3.7. The squared-visibilities, closure phases and triple amplitudes of the β-free model are compared with the data in Figures 3.3, 3.4, and 3.5, respectively.

The right panel of Figure 3.7 shows that the β-free model is more consistent with the synthesized image in Fig.3.2 than the standard model. The ${\chi_\nu}^2$ of closure phase is significantly improved in the new best-fit although the ${\chi_\nu}^2$ of the triple amplitude is slightly larger. Figure 3.8 illustrates the χ^2_ν space of inclination and β for α Cep, showing the value of β is well constrained in the new model and is slightly lower than the standard value of 0.25. We also test the corresponding Vsini of the models in Fig.3.8. The peak of the χ^2_ν space falls inside the green box, consistent with the observed range of Vsini. The new model prefers a lower inclination of $55.70^o \pm 6.23^o$, a higher rotational speed of 94% of break-up, and a similar position angle. The new best-fit temperatures at the poles and the equator are both cooler than those of the previous standard model.

In addition to using an average β throughout the stellar surface as applied above, we are also pursuing fitting β as a function of latitude. This approach will be presented in a future work with higher resolution data.

Table 3.3. Best-fit and physical parameters of α Cep

Model Parameters	Standard ($\beta = 0.25$)	Non-standard (β-free)*
Inclination (degs)	64.91 ± 4.11	55.70 ± 6.23
Position Angle (degs)	-178.26± 4.10	-178.84 ± 4.28
T_{pol} (K)	8863± 260	8588 ± 300
R_{pol} ($R_\odot$)	2.199 ± 0.035	2.162 ± 0.036
T_{eq} (K)	6707 ± 200	6574 ± 200
R_{eq} ($R_\odot$)	2.739± 0.040	2.740 ± 0.044
ω	0.926 ± 0.018	0.941 ±0.020
β	0.25 (fixed)	0.216± 0.021
Model V Magnitude[a]	2.45	2.45
Model H Magnitude[b]	1.92	1.91
Model v sin i (km/s)	237	225
Total χ^2_ν	1.21	1.18
Vis^2 χ^2_ν	0.79	0.80
CP χ^2_ν	1.43	1.27
T3amp χ^2_ν	1.71	1.76
Other Physical Parameters		
True $T_{eff}(K)$	7690 ± 150	7510 ± 160
True Luminosity ($L_\odot$)	20.1 ± 1.6	18.1 ± 1.8
Apparent $T_{eff}(K)$	-	7510
Apparent Luminosity ($L_\odot$)	-	17.9
Mass ($M_\odot$)[c]	-	1.92 ± 0.04
Age (Gyrs)[c]	-	0.99 ± 0.07
$[Fe/H]$[d]	0.09	
Distance (pc)[e]	14.96	

*The β-free model is adopted as the final model, see text of §3.4.1 for detail.

[a] V magnitude from literature: 2.456 ± 0.002 (Perryman et al., 1997)

[b] H magnitude from literature: 2.13 ± 0.18 (Cutri et al., 2003)

[c] Based on the Y^2 stellar evolution model (Demarque et al., 2004).

[d] Gray et al. (2003)

[e] Perryman et al. (1997)

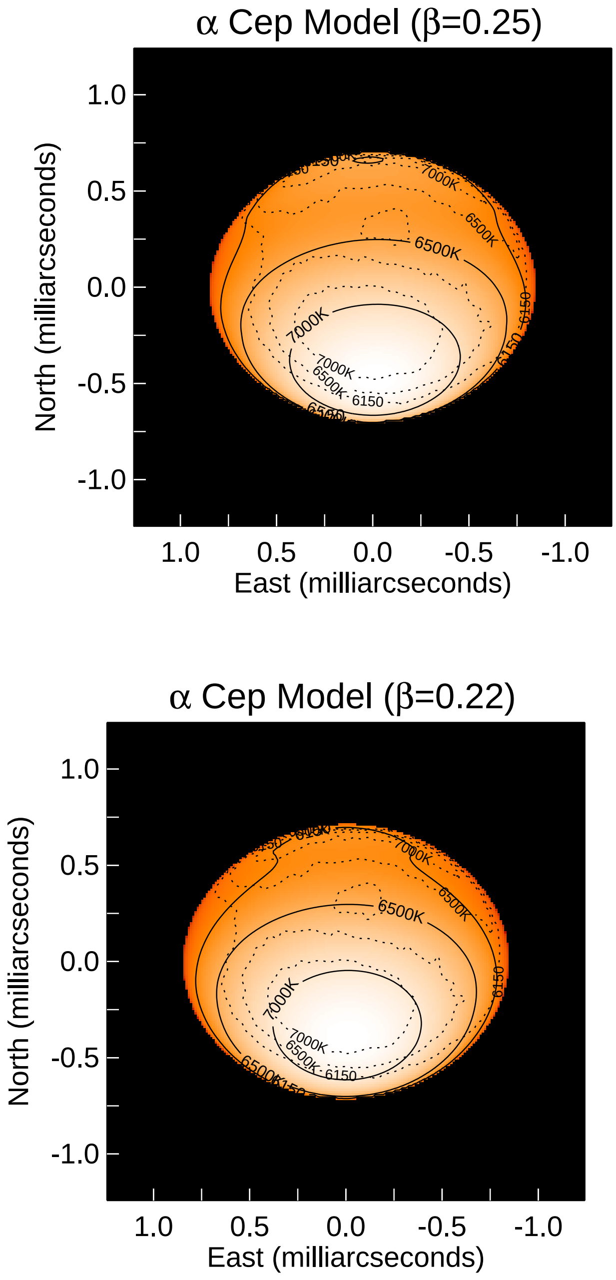

Figure 3.7 The gravity darkening models of α Cep . The contours indicate the local brightness temperatures on the surface of the star. The left panel shows the best-fit standard gravity darkening model ($\beta = 0.25$) overplotted with the temperature contours from Figure 3.2. The total χ^2_ν of the standard model is 1.21. The right panel shows the best-fit β-free model, also overplotted with the temperature contours from Figure 3.2, and has a total χ^2_ν of 1.18. The resolution of the data is 0.68 milliarcsec.

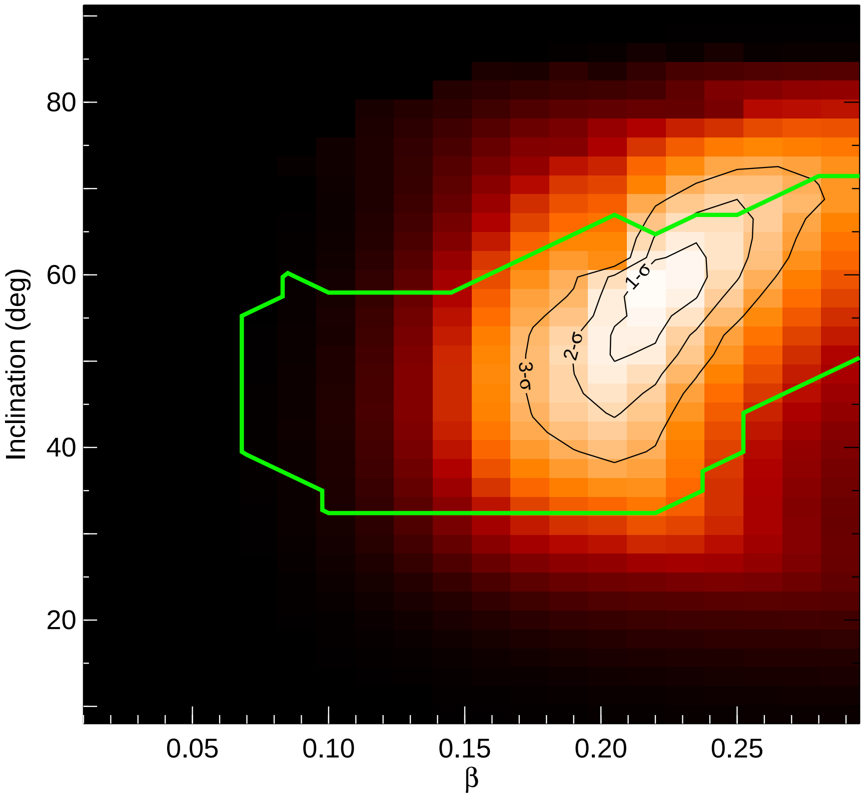

Figure 3.8 The χ^2_ν surface of β and inclination for α Cep. The corresponding probability peaks at $\beta \sim 0.22$ and $i \sim 56^o$. The black contours show the 1-σ, 2-σ, and 3-σ levels of confidence interval, scaled to match the errors of β and inclination estimated from bootstraping. The area inside the green box indicates the region where the corresponding Vsini values are within the observed range of 180 - 245 $\mathrm{km\,s^{-1}}$.

3.4.2 α Oph

We also start with the standard gravity darkening model (β=0.25) for α Oph. We assume mass = 2.10$M_\odot$ (see §3.5) and distance = 14.68 pc (Gatewood, 2005) in the model. The metallicity $[Fe/H]$ of α Oph is -0.16 (Erspamer & North, 2003), thus a Kurucz grid with metallicity of -0.2 is applied. Figure 3.9 shows the best-fit standard model of α Oph. The best-fit parameters are listed in Table 3.4. The associated errors of the parameters are also obtained using the bootstrap procedure described in §3.4.1. The squared-visibilities, closure phases and triple amplitudes of the model are compared with the data in Figures 3.10, 3.11 and 3.12, respectively. The model shows that the photosphere of α Oph is also elongated and has two bright polar areas and a dark equator. Its radius at the equator is $\sim$ 20% larger than at the poles. It is seen nearly equator-on with an inclination of $87.70^o \pm 0.43^o$. The model also shows that α Oph is rotating at 88.5% of its break-up speed and the poles are $\sim$ 1840K hotter than the equator.

In the standard model, the ${\chi_\nu}^2$ of the closure phase only reaches 1.33 (Table 3.4), suggesting that we may need extra degrees of freedom to improve the fit. Therefore, following our approach for α Cep, we extend the standard model of α Oph to a free β. However, although we have searched the parameter space extensively, we cannot find a unique β-free model for α Oph due to the same reason that we encountered in imaging. As we mentioned in §4.2.3, this issue stems from the near equator-on and symmetric brightness distribution of α Oph, causing the closure phases to be mostly 0^o or $\pm 180^o$ (as shown in Fig.3.11) and hence lack of enough non-zero signatures to constrain the model when β is free.

Figure 3.13 shows the χ^2_ν space of inclination and β for α Oph. Unlike the single peak of α Cep, the peak of α Oph has a ridge spreading over a large range of inclination and β, indicating the inclination and β are highly degenerate and suggesting it is difficult to constrain a unique β-free model. Nevertheless, the corresponding $V\sin i$ values around the largest peak at $\beta \sim 0.08$ fall outside the observed range of 210 - 240 $\mathrm{km\,s^{-1}}$(enclosed by the green box in Figure 3.13), suggesting the peak is not real but only due to the degeneracy of β and inclination. Therefore, we can rule out the largest peak around $\beta \sim 0.08$. Also, the gravity darkening evolution models of Claret (2000) show that the value of β should be much larger than 0.15 for a $\sim 2\mathrm{M}_\odot$ star with average T_{eff} higher than 7500K, like α Oph. The second peak around $\beta \sim 0.15$ in Fig.3.13, however, is not consistent with the models of Claret (2000) although is inside the Vsini range. Thus, in this study we still prefer the other peak around the standard $\beta = 0.25$ model for α Oph. To break down the degeneracy and constrain the value of β more accurately, we will need more observations with higher resolution, especially in the visible where limb-darkening and gravity darkening are more prominent.

Table 3.4. Best-fit and physical parameters of α Oph

Model Parameters	Standard ($\beta = 0.25$)
Inclination (degs)	87.70 ± 0.43
Position Angle (degs)	-53.88 ± 1.23
T_{pol} (K)	9300 ± 150
R_{pol} ($R_\odot$)	2.390 ± 0.014
T_{eq} (K)	7460 ± 100
R_{eq} ($R_\odot$)	2.871 ± 0.020
ω	0.885 ± 0.011
β	0.25 (fixed)
Model V Magnitude[a]	2.086
Model H Magnitude[b]	1.66
Model v sin i (km/s)	237
Total χ^2_ν	0.91
CP χ^2_ν	1.33
Vis^2 χ^2_ν	0.72
T3amp χ^2_ν	0.81
Other Physical Parameters	
True $T_{eff}(K)$	8250 ± 100
True Luminosity ($L_\odot$)	30.2 ± 1.3
Apparent $T_{eff}(K)$	7950
Apparent Luminosity ($L_\odot$)	24.3
Mass ($M_\odot$)[c]	2.10 ± 0.02
Age (Gyrs)[c]	0.77 ± 0.03
$[Fe/H]$[d]	-0.16
Distance (pc)[e]	14.68

[a] V magnitude from literature: 2.086 ± 0.003 (Perryman et al., 1997)

[b] H magnitude from literature: 1.66 ± 0.03 (weighted average of fluxes from: Alonso et al., 1998; Cohen et al., 1999; Cutri et al., 2003)

[c] Based on the Y^2 stellar evolution model (Demarque et al., 2004).

[d] Erspamer & North (2003)

[e] Gatewood (2005)

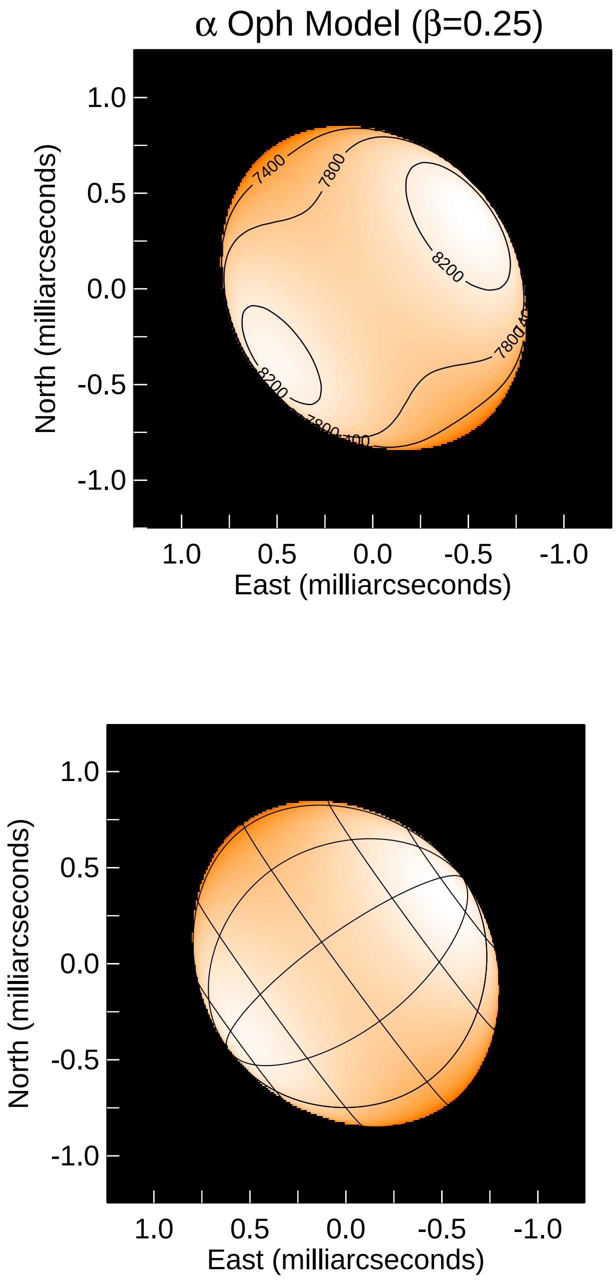

Figure 3.9 The best-fit standard gravity darkening model of α Oph. The contours in the left panel indicate the local brightness temperatures on the surface of the star. The right panel shows the latitude and longitude of α Oph to help visualize its geometry. The resolution of the data is 0.52 milliarcsec. The total χ_ν^2 of the model is 0.91.

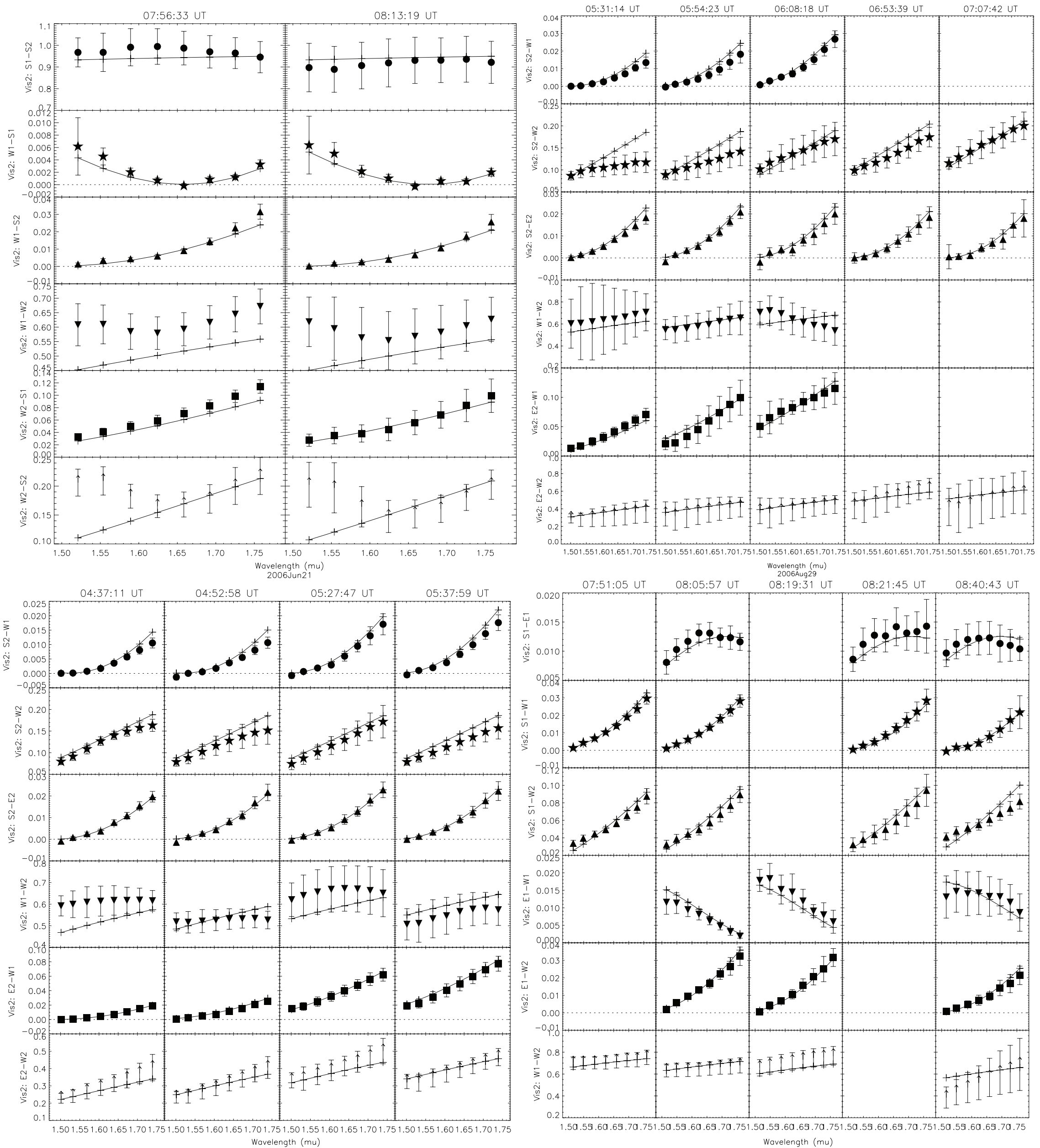

Figure 3.10 α Oph squared-visibility model (standard $\beta = 0.25$, solid lines) vs. data (filled points with error bars). Four out of eight nights (2006Jun21, 2006Aug29, 31, and 2007May12) are shown here. Each row stands for a different baseline, while the columns indicate different times of observation. The eight data points in each panel indicate the eight spectral channels of MIRC across the H band. The total χ_ν^2 is 0.72 for the squared-visibility only. (Please refer to the electronic edition if the type size is too small.)

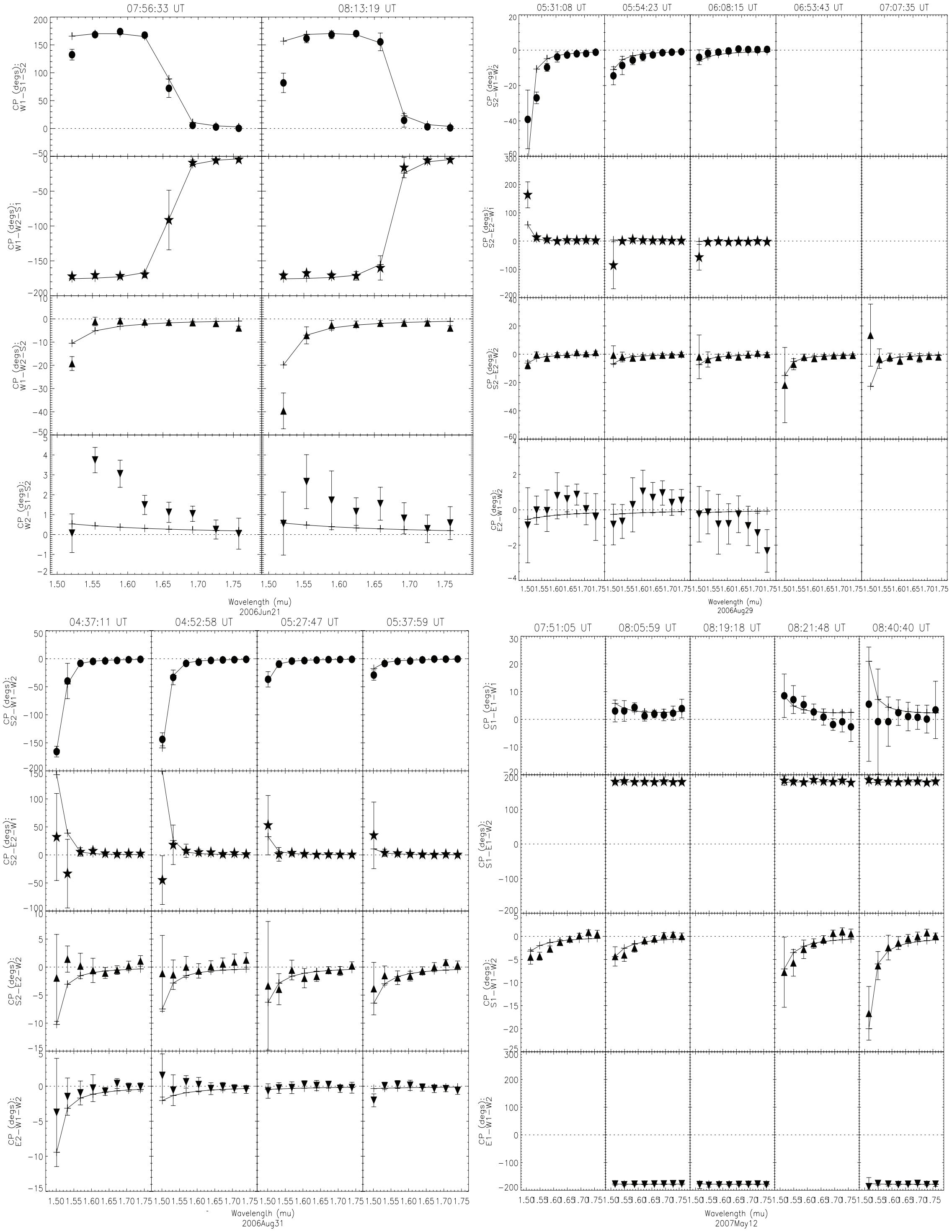

Figure 3.11 Closure phases of α Oph . Similar to Fig.3.10 but showing the closure phase for α Oph. Each row stands for a different telescope triangle. The total χ^2_ν for closure phase is 1.33.

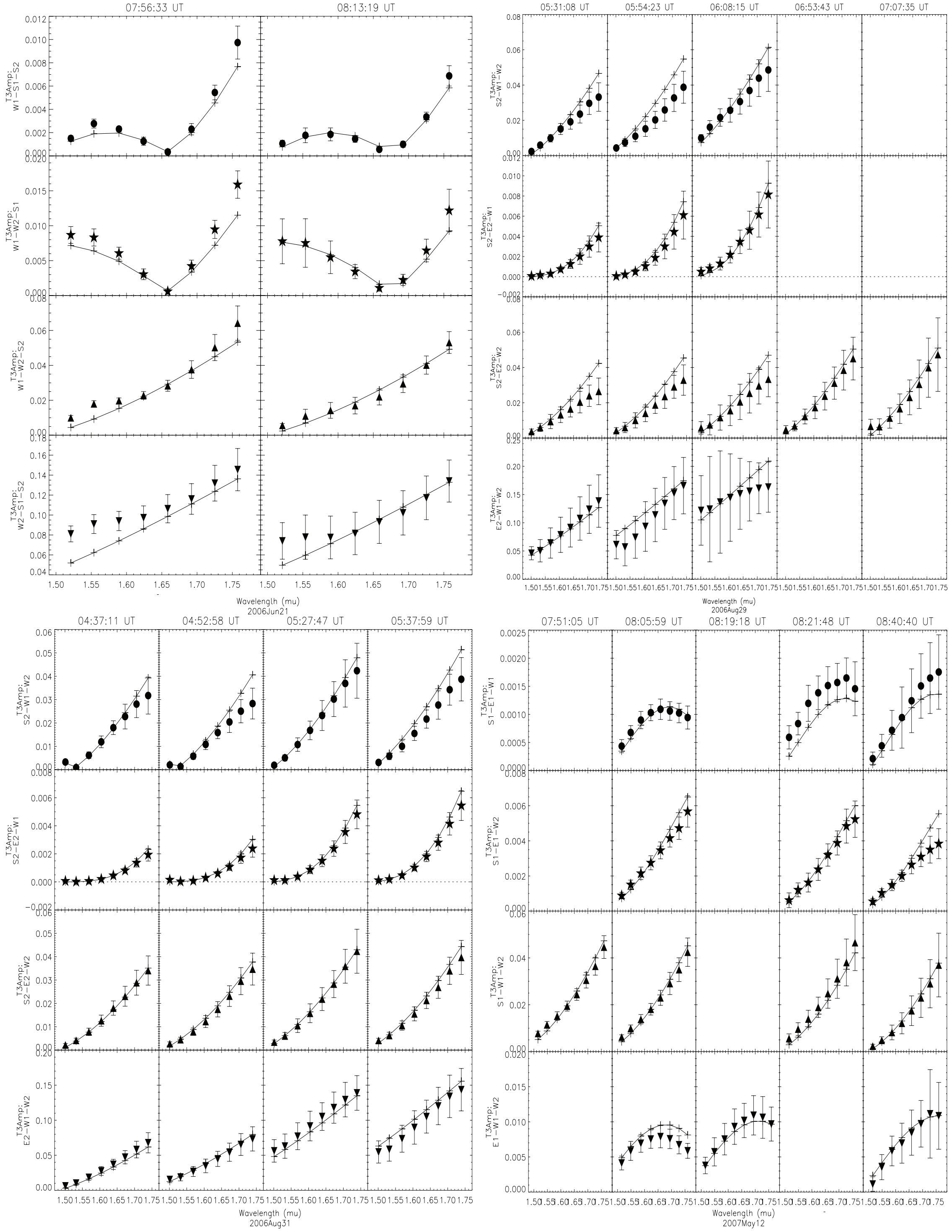

Figure 3.12 Triple amplitudes of α Oph . Similar to Fig.3.10 but showing the triple amplitudes for α Oph. The total χ^2_ν for triple amplitude is 0.81.

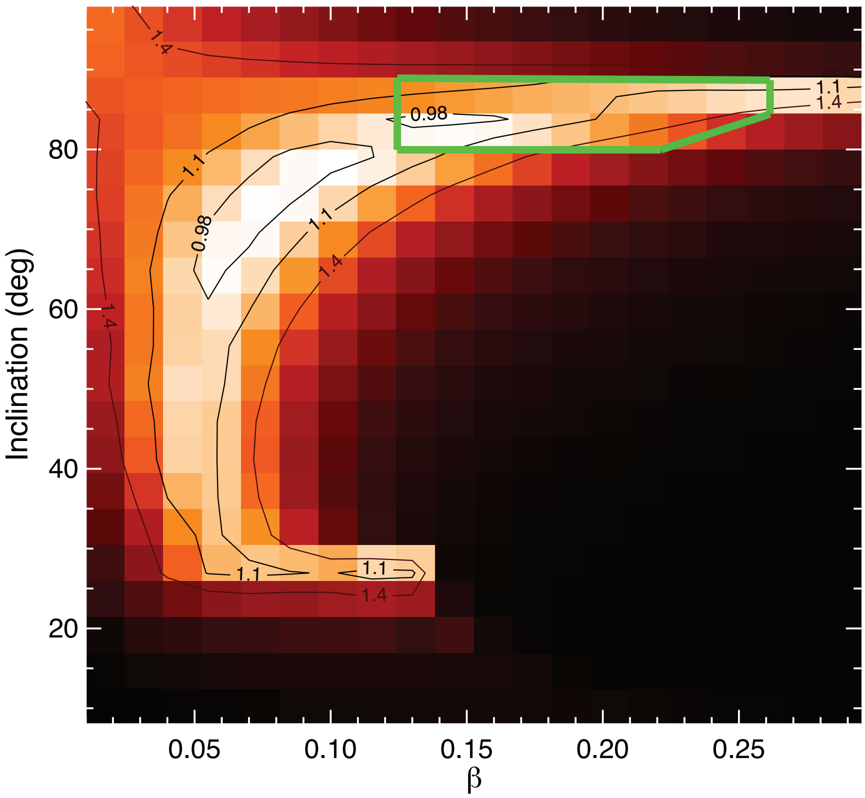

Figure 3.13 The χ_{ν}^{2} surface of β and inclination for α Oph. The corresponding probability is high throughout a large range of inclination and β, suggesting high degeneracy between the two parameters. The map also indicates the inclination at $\beta = 0.25$ (i.e., the standard model) is well constrained and is nearly equator-on. Since the probability is dominated by the degeneracy effects of β and inclination, we overplot the χ_{ν}^{2} contours on the map instead of confidence intervals. The region enclosed in the green box has V*sin*i values inside the observed range of 210-240 $\mathrm{km\,s^{-1}}$. The rest of the areas in the map fall outside the observed V*sin*i range and thus can be ruled out, even though they may fit the data better.

3.4.3 Altair

We have also modeled Altair with both the standard gravity darkening model and the β-free model. We assume mass = 1.791$M_\odot$ (Peterson et al., 2006) and distance = 5.14 pc (Perryman et al., 1997) in the model. The metallicity $[Fe/H]$ of Altair is -0.2 (Erspamer & North, 2003). The left panel of Figure 3.14 shows the best-fit standard model of Altair. The best-fit parameters are listed in Table 3.5. The associated errors of the parameters are also obtained using the bootstrap procedure described previously. The squared-visibilities, closure phases and triple amplitudes of the model are compared with the data in Figures 3.15, 3.16 and 3.17, respectively. Our model confirms that the photosphere of Altair is elongated and has two bright polar areas and a dark equator. Our best-fit parameters agree well with the best-fit parameters of Peterson et al. (2006). The radius at the equator is $\sim$ 22% larger than at the poles, and it has a medium inclination of $62.7^o \pm 1.5^o$. The model also shows that Altair is rotating at 90.2% of its break-up speed and the poles are $\sim$ 1900K hotter than the equator. However, our best-fit model has an overall reduced χ^2_ν of 1.79, indicating a need of extra degrees of freedom. Therefore, we also explored the β-free model for Altair.

The new best-fit prefers a non-standard β of 0.190, and the χ^2_ν of the fit is significantly improved (see Table 3.5). The new model is shown in the right panel of Figure 3.14. In addition to a lower β, the new model prefers a lower inclination, a cooler polar temperature, and a faster rotation rate than the standard model.

Table 3.5. Best-fit parameters for Altair

Parameters	β Fixed	β Free
Inclination (degs)	62.68 ± 1.44	57.18 ± 1.91
Position Angle (degs)	-61.72 ± 0.87	-61.76 ± 0.82
T_{pol} (K)	8714 ± 157	8450 ± 144
R_{pol} ($R_\odot$)	1.661 ± 0.0037	1.634 ± 0.011
T_{eq} (K)	6850 ± 116	6864 ± 152
R_{eq} ($R_\odot$)	2.022 ± 0.0087	2.0288 ± 0.0067
ω	0.9016 ± 0.0048	0.9230 ± 0.0063
β	0.25 (fixed)	0.190 ± 0.012
Model V Magnitude	0.7650	0.7650
Model H Magnitude	0.2245	0.2195
Model v *sini* (km/s)	241	240
Total χ^2_ν	1.79	1.37
CP χ^2_ν [c]	2.08	1.73
Vis^2 χ^2_ν[c]	1.48	1.10
T3amp χ^2_ν [c]	2.14	1.58
Other Physical Parameters		
True $T_{eff}(K)$	7574	
True Luminosity ($L_\odot$)	10.4	
Apparent $T_{eff}(K)$	7550	
Apparent Luminosity ($L_\odot$)[c]	10.1	
Mass ($M_\odot$)[d]	1.66 ± 0.04	
Age (Gyrs)	1.1 ± 0.1	
$[Fe/H]$[e]	-0.2	
Distance (pc)[d]	5.14	

[a] V magnitude from literatures (weighted average): 0.765 ± 0.015

[b] H magnitude from literatures (weighted average): 0.235 ± 0.043

[c] Based on the Y^2 stellar evolution model (Demarque et al., 2004).

[d] Erspamer & North (2003)

[e] Perryman et al. (1997)

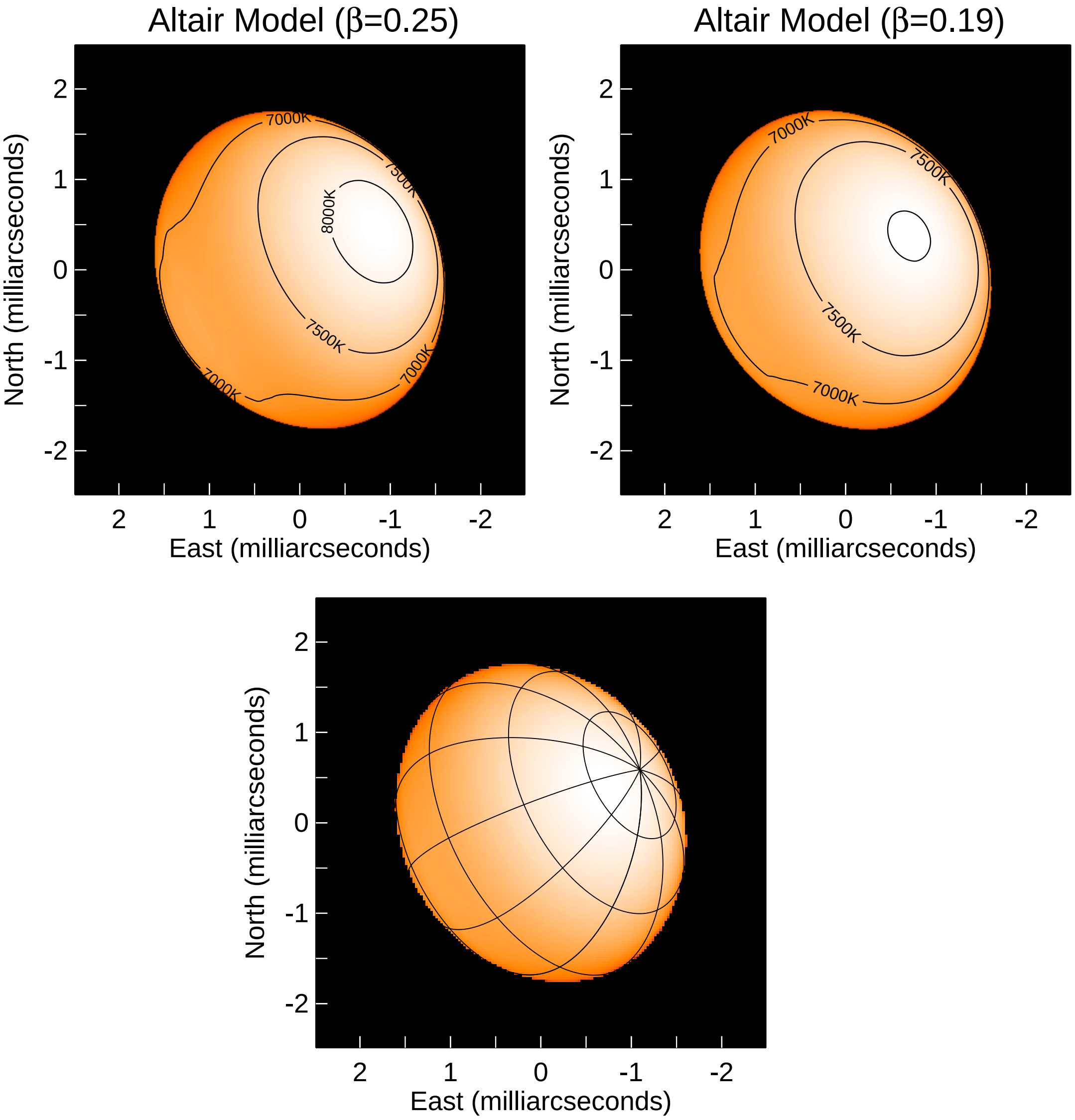
Altair Model (β=0.25)

Altair Model (β=0.19)

Figure 3.14 Altair gravity darkening models. The left panel shows the standard model (β=0.25); the right panel shows the β=0.19 model; and the bottom panel shows the latitude and longitude of Altair to illustrate its geometry.

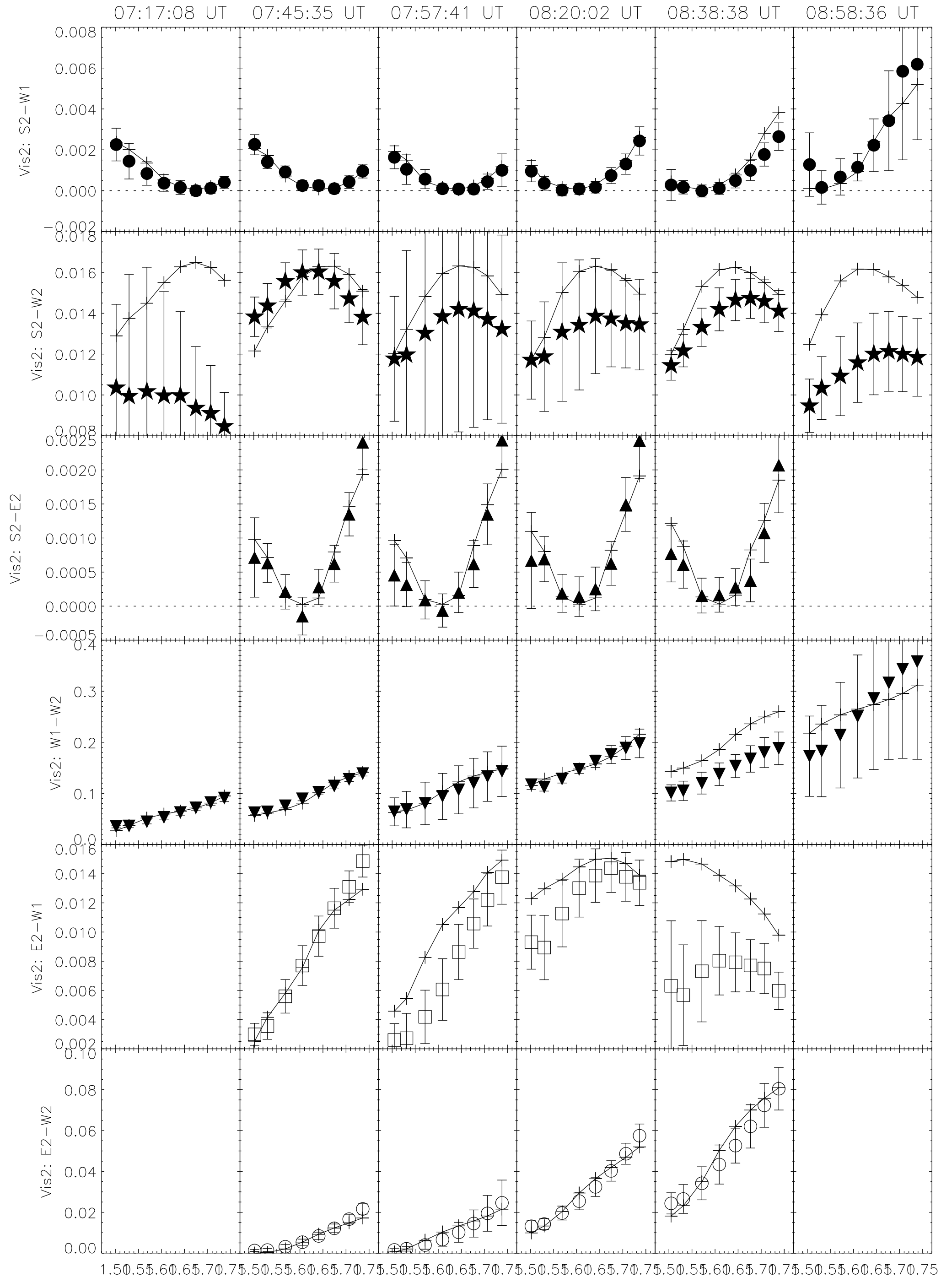

Figure 3.15 Altair squared-visibilities from the β=0.19 model (solid lines) vs. data (filled points with error bars) . Two nights of data (2006Aug31 and 2006Sep01) are all shown in the plot. Each row stands for a di?erent baseline, while the columns indicate di?erent times of observation. The eight data points in each panel indicate the eight spectral channels of MIRC across the H band. (Please refer to the electronic edition if the type size is too small.)

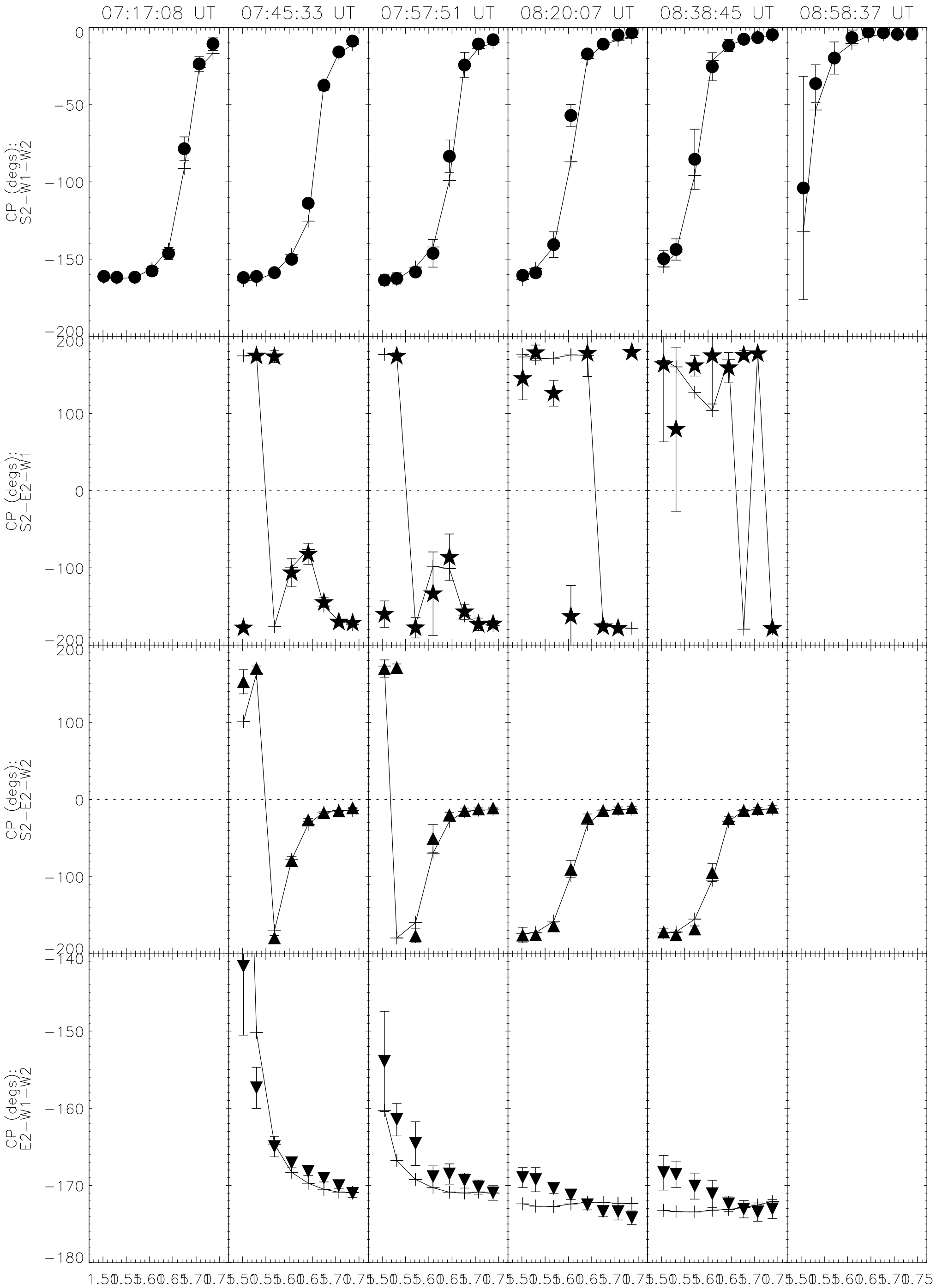

Figure 3.16 Closure phases of Altair. Similar to Fig.3.15, but showing the closure phases of Altair.

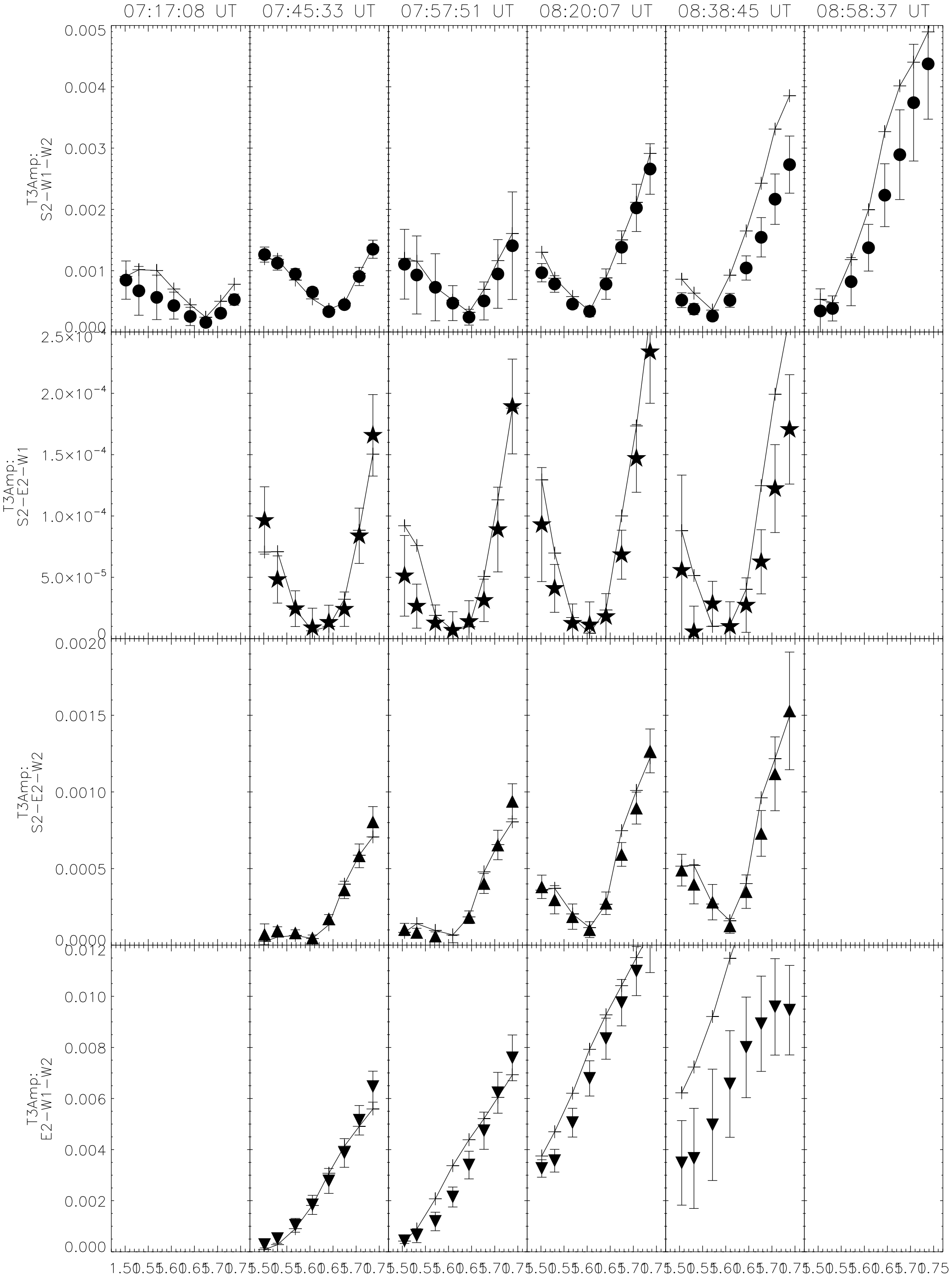

Figure 3.17 Triple amplitudes of Altair. Similar to Fig.3.15, but showing the triple amplitude of Altair.

3.5 Physical properties and comparison with stellar evolution tracks

In addition to the model parameters, we also calculate the true and apparent effective temperatures and luminosities for the three stars in Table 3.3, 3.4, & 3.5. The true luminosity is estimated by integrating local $\sigma T_{eff}(\theta)^4$ (where σ is the Stefan-Boltsman constant) over the stellar surface, and the true T$_{eff}$ is estimated from the total luminosity and the total surface area of the star. The apparent luminosity is obtained from $L = 4\pi d^2 F_{bol}$, where the bolometric flux F_{bol} is calculated by integrating the specific intensity over the whole spectrum and the projected angular area of the star. The apparent temperature is obtained from $\sigma T_{eff}^4 = \pi d^2 F_{bol}/A_{proj}$, where A_{proj} is the projected area.

The true T$_{eff}$ and luminosity of α Cep are very close to its apparent values due to its medium inclination (see Table 3.3). Its true T$_{eff}$ from the β-free model is 7510 ± 160K, close to although slightly cooler than the ∼7700K estimate of VB06 and Gray et al. (2003), as well as the 7740K estimate of Malagnini & Morossi (1990). Its true luminosity is 18.1 ± 1.8 L$_\odot$, consistent with the 17 L$_\odot$ estimate from Malagnini & Morossi (1990) and the 17.3 L$_\odot$ estimate of Simon & Landsman (1997)

The deviation of α Oph's true T$_{eff}$ and luminosity from its apparent values is very significant because of its near equator-on inclination. Its true T$_{eff}$ from the standard model is estimated to be 8250±100K. Its apparent T$_{eff}$, on the other hand, is 7950K based on the model, consistent with the apparent value of 7883 ± 63 K calculated by Blackwell & Lynas-Gray (1998) and the value of 8030 ± 160 K by Malagnini &

Morossi (1990). Its apparent luminosity is 24.3 $L_\odot$, in agreement with the 25.1 $L_\odot$ value of Malagnini & Morossi (1990) but smaller than its true luminosity of 30.2 ± 1.3 $L_\odot$.

Because of its medium inclination, Altair's true T_{eff} and luminosity are also very close to its apparent values, as shown in Table 3.5. Our estimated true temperature from the β-free model is 7574K, consistent with the value of 7588K of Blackwell et al. (1979) and 7680K of van Belle et al. (2001). Our estimated true luminosity of Altair is 10.4$L_\odot$, in agreement with the 10.6 $L_\odot$ of Peterson et al. (2006) and the 9.6 ± 1.2$L_\odot$ of Malagnini & Morossi (1990).

Because rapid rotators are hotter at the poles and cooler at the equators, their apparent temperatures are therefore dependent on their inclinations, which can easily introduce large biases to the observed values. To investigate this effect, we plot in Figure 3.18 the differences between the true and apparent values of T_{eff}s and luminosities as a function of inclination, scaled with their true values. The plots show that when a star is inclined by $\sim 54^o$, its apparent T_{eff} and luminosity seen by the observers will be equal to their true values, just as the cases of α Cep and Altair, and similar to the result of Gillich et al. (2008). When the star is seen pole on, such as Vega (Aufdenberg et al., 2006; Peterson et al., 2006), its apparent temperature can exceed the true value by $\sim 5\%$, and the luminosity can exceed by $\sim 40 - 50\%$ or even larger depending on the speed of the rotation, which explains the reason that Vega's luminosity was largely overestimated for a long time until recent studies of Aufdenberg et al. (2006) and Peterson et al. (2006). On the other hand, when a rapid rotator is equator-on, as the case of α Oph, its apparent temperature and luminosity

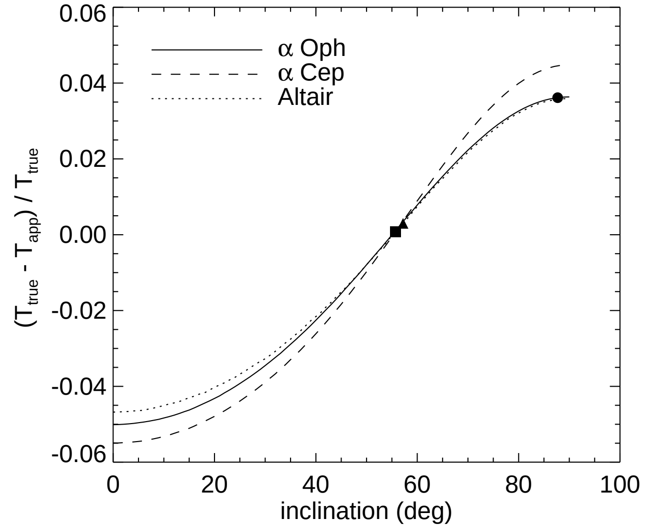

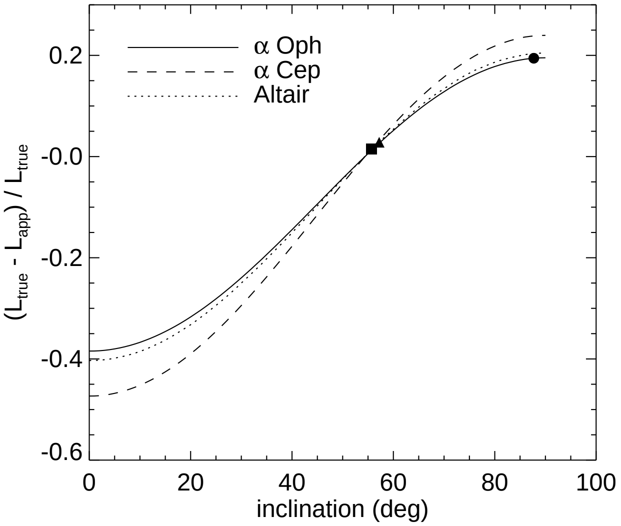

Figure 3.18 Effects of inclination to the apparent T$_{eff}$ and luminosity. The two plots show the deviation of the apparent T$_{eff}$ and luminosity from their true values at various inclinations respectively. The solid line indicates the standard model ($\beta = 0.25$) of α Oph. The dashed line indicates the $\beta = 0.216$ model of α Cep, and the dotted line indicates the $\beta = 0.19$ model of Altair. The apparent T$_{eff}$ and luminosity equal their true values at inclination of $\sim 54^o$. α Cep (filled square) and Altair (filled triangle) are seen very close to this zero-difference value, but α Oph (filled dot) is almost at the high end due to its large inclination.

can be underestimated by $\sim 4\%$ and $\sim 20\%$ respectively. The rotation speed of the star also affects the differences between its true and apparent values - the faster the star rotates, the larger the difference we see.

Our estimates of the true T_{eff}s and luminosities of the three stars also allow us to understand their current evolutionary status better. In Figure 3.19, 3.20, and 3.21, we plot the H-R diagram and the corresponding Y^2 stellar evolution tracks and isochrones (Demarque et al., 2004) for α Cep , α Oph, and Altair, respectively. Their possible ranges of locations on the H-R diagram (also called "inclination curve", Gillich et al., 2008) are also shown in the plots. Figure 3.19 shows that α Cep appears to be an A9 type star on the H-R diagram based on its apparent temperature and luminosity (filled triangle). However, it is classified as an A8V star by Gray et al. (2003), earlier than that inferred from the H-R diagram. Similarly, Figure 3.21 shows that Altair appears to be roughly an A8.5 type star, while it is classified as an A7 star (Gliese & Jahreiss, 1991), earlier than that from our figure as well. Furthermore, also in Figure 3.20, α Oph appears roughly as an A6.5 type star. Its apparent spectral type from Gray et al. (2001) is A5IV, also earlier than that inferred from the figure. We infer that this is because the spectra of the two stars are dominated by spectral lines from the hotter and brighter polar regions, causing their overall spectral classification to be biased toward the types of their poles which appear earlier than other regions of the stars. Therefore, for the case of an equator-on star, such as α Oph, although its apparent effective temperature is lower than its true temperature due to the inclination, its spectral type derived from spectroscopy can compensate this effect and make it look closer to its true spectral type. However, for a pole-on star such as Vega, this bias can not be compensated, and the spectral types derived from both spectroscopy and apparent temperature will appear earlier than its true type. This phenomenon indicates that the spectral types of rapid rotators are not only biased by their inclinations, but also by the spectral lines of their polar regions.

Using the Y^2 models, we estimate that α Cep has a mass of $1.92\pm0.04\mathrm{M}_\odot$, slightly smaller than the estimate of VB06. Its age is estimated to be 0.99 ± 0.07 Gyrs. We also estimate that α Oph has a mass of $2.10\pm0.02\mathrm{M}_\odot$, and an age of 0.77 ± 0.03 Gyrs. Its apparent position in the H-R diagram, however, indicates a lower mass of $1.99\mathrm{M}_\odot$, which is again consistent with the $2.0\mathrm{M}_\odot$ estimate of Malagnini & Morossi (1990) and Augensen & Heintz (1992). However, this value is much lower than the $2.84\mathrm{M}_\odot$ value of Gatewood (2005) and the $4.9\mathrm{M}_\odot$ of Kamper et al. (1989). To address the differences, we derive the mass range of α Oph using our new method of estimating mass in the next section (§3.6), and conclude the result of Gatewood (2005) and Kamper et al. (1989) can be ruled out. In addition, we also estimate that Altair has a mass of 1.66 ± 0.04 $\mathrm{M}_\odot$ and an age of 1.1 ± 0.1 Gyr. The estimated masses and ages of these three stars are included in Tables 3.3, 3.4, and 3.5, respectively.

We note that the Y^2 models are for non-rotating stars, whereas all the three stars presented above are rapid rotators. The fact that rotation may extend the main-sequence lifetime (Kiziloglu & Civelek, 1996; Maeder & Meynet, 2000) implies that our age estimates may not be accurate and needs further investigation. We also note that the masses of α Cep , α Oph , and Altair are all estimated based on non-α-enhanced Y^2 models. Studies have shown that rapid rotation can change the abundance of a star (e.g., Pinsonneault, 1997) and enhance the α-rich elements

(Yoon et al., 2008), resulting in very different estimates of its mass and age. Hence to derive the masses of these stars more accurately, detailed abundance studies are required to determine if they are α-enhanced and what abundance to use for their evolutionary models.

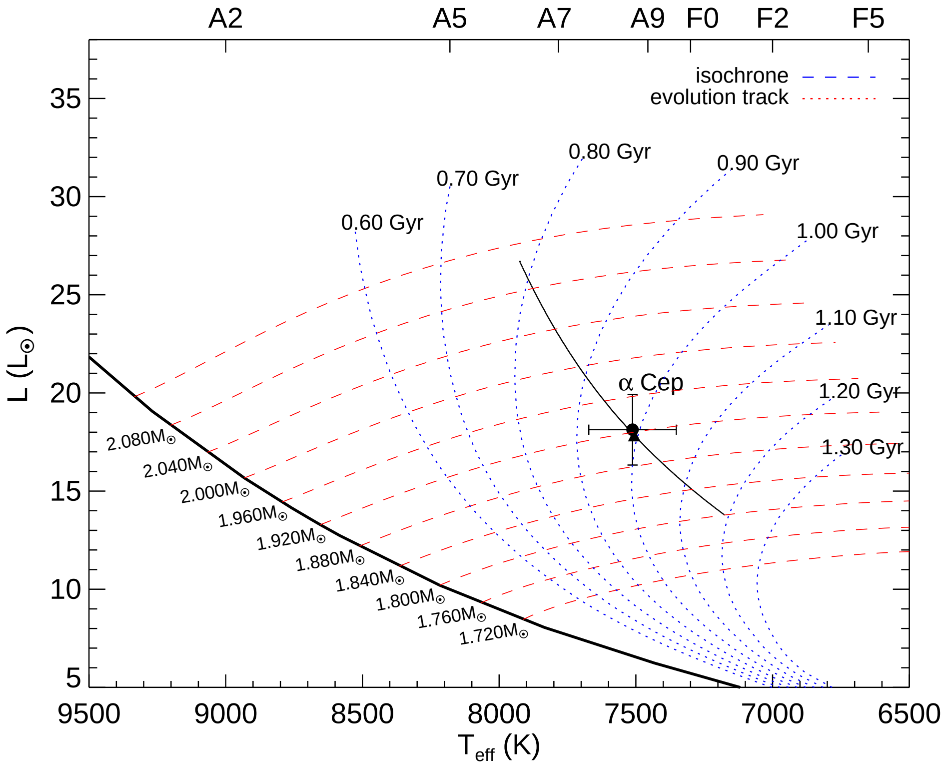

Figure 3.19 Position of α Cep on the HR diagram. The Y^2 stellar models with Z$\sim$ 0.02 are also shown in the figure. The dashed red lines indicate the evolutionary tracks and the dotted blue lines indicate the isochrones. The filled dot with error bars indicates the true T$_{eff}$ and luminosity of the α Cep, while the filled triangle indicates its apparent T$_{eff}$ and luminosity which are dependent on its inclination. The solid lines that go through the points show the position of α Cep on the H-R diagram as a function of inclination (also called "inclination curves", Gillich et al., 2008). These curves are more or less parallel to the Zero-Age Main Sequence indicated by the thick solid line at the bottom left of each plot, consistent with those of Gillich et al. (2008). For a 90^o inclination, the positions of the stars will be at the lower end of the curve; and for a 0^o inclination, the stars will be at the higher end of the curves. These plots suggest the inclination of a star can significantly change its apparent location on the H-R diagram.

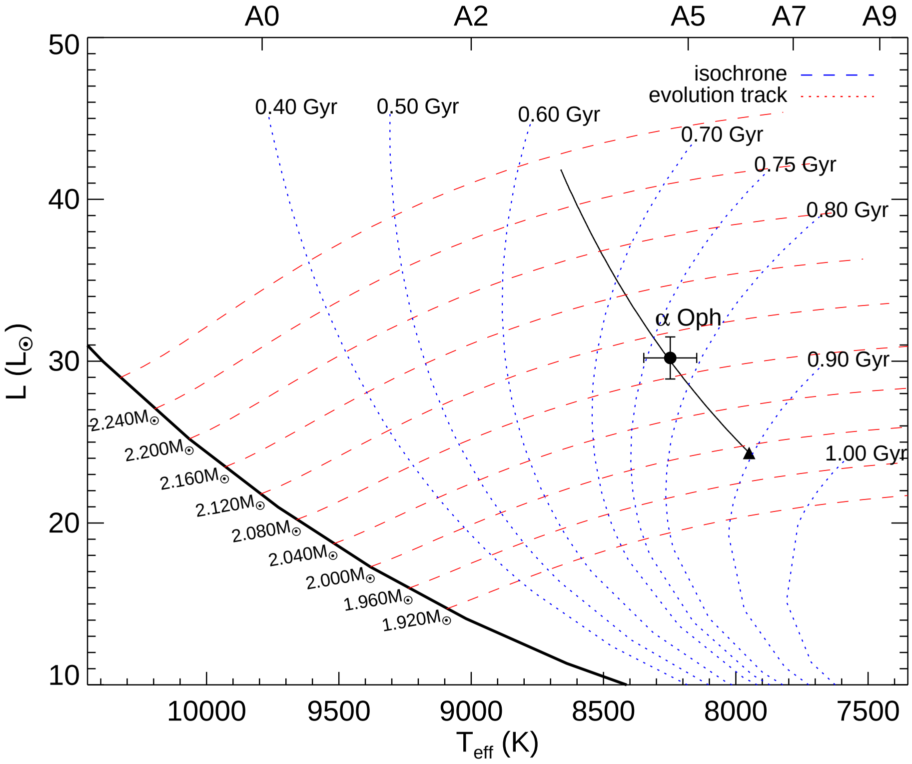

Figure 3.20 Position of α Oph on the HR diagram. The Y^2 stellar models with $Z \sim 0.014$ are also shown. Similar to Fig.3.19, the dashed red lines indicate the evolutionary tracks and the dotted blue lines indicate the isochrones. The filled dot with error bars indicates the true T$_{eff}$ and luminosity of α Oph, while the filled triangle indicates its apparent T$_{eff}$ and luminosity which are dependent on the inclination.

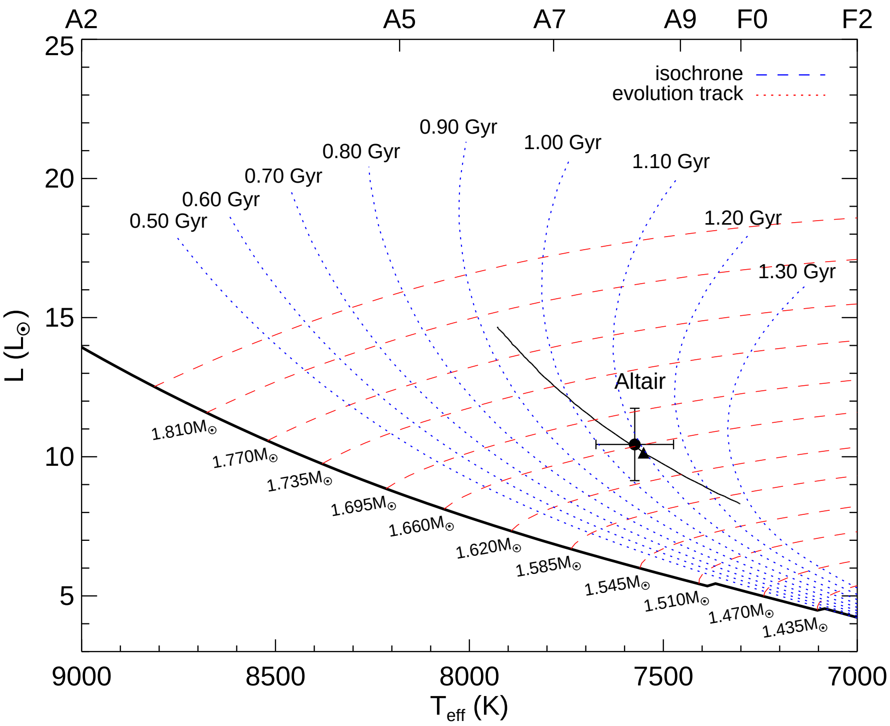

Figure 3.21 Position of Altair on the HR diagram. The Y^2 stellar models with $Z \sim 0.014$ are also shown. Similar to Fig.3.19, the dashed red lines indicate the evolutionary tracks and the dotted blue lines indicate the isochrones. The filled dot with error bars indicates the true T_{eff} and luminosity of Altair, while the filled triangle indicates its apparent T_{eff} and luminosity which are dependent on the inclination.

3.6 A new method to estimate the mass of a star

Mass is the most fundamental property of stars. The determination of stellar masses mostly relies on orbital measurements of binary systems (e.g., Zhao et al., 2007), stellar evolution models together with measurements of other stellar properties (e.g., van Belle et al., 2006), and asteroseismology together with measurements of stellar radii (e.g., Creevey et al., 2007). Here we propose a new method to estimate the mass of a star based on our modeling of rapid rotators.

Since we can determine the inclination, equatorial radius and the fractional rotation speed of a rapid rotator from our model, we therefore can combine the model of a rapid rotator with its mass to estimate the equatorial velocity and the Vsin i value. We can also reverse the process, taking a precise measurement of Vsin i and a best-fit rotator model to determine the mass of a star. This approach is most suitable for radiative rapid rotators which can be interpreted by the standard gravity darkening model, and also non-fully-radiative rotators if a more sophisticated fluid model is constructed (e.g., Jackson et al., 2004; MacGregor et al., 2007; Espinosa Lara & Rieutord, 2007). For stars with less accurate models, we can also use this method to roughly estimate their masses. The precision of Vsin i is also crucial for a precise mass estimate. As a preliminary test, we first apply this method to α Cep and α Oph.

The $Vsin$i range of α Cep (180 $\mathrm{km\,s^{-1}}$- 245 $\mathrm{km\,s^{-1}}$) corresponds to a large mass range of 1.3$M_\odot$ to 2.4$M_\odot$ based on the β-free model in §3.4.1. The mass of α Cep determined from stellar models, on the other hand, is $1.92 \pm 0.04 M_\odot$ (see §3.5), well within the mass range given by $Vsin$i. Similarly, the $Vsin$i range of α Oph (210

$\mathrm{km\,s^{-1}}$- 240 $\mathrm{km\,s^{-1}}$) gives a mass range of $1.7\mathrm{M}_\odot$ to $2.2\mathrm{M}_\odot$ when combined with the model in §3.4.2. Its mass determined from stellar models, $2.1 \pm 0.02\mathrm{M}_\odot$ (see §3.5), is also within the range. By contrast, the study of Gatewood (2005) and Kamper et al. (1989) gave a mass of $2.84\mathrm{M}_\odot$ and $4.9\mathrm{M}_\odot$ to α Oph respectively, far outside the range given by $V sin$i, and hence can be ruled out. Since α Oph is also a known astrometric binary, it is the ideal target to further test this new method by comparing its mass with that determined from the astrometric orbit. We are currently pursuing this study (Oppenheimer et al.2008, private communication) and will also present it in a future work.

3.7 Discussion

Although the β-free model of α Cep is consistent with the synthesized image (Fig.3.2) in basic features such as the bright pole and the dark equator, we also notice that the equator of the image is darker and cooler than that of the model - a phenomenon seen in a previous study of Altair (Monnier et al., 2007). The existence of the darker-than-expected equator on both stars implies that the extra gravity darkening may be real. However, it can also be due to a systematic effect of the imaging program. To confirm this conclusion we will need further studies such as model-independent latitudinal temperature profiles.

Our models show that all three stars have polar temperatures well above 8000K and equatorial temperatures below 7500K, which means, according to the stellar atmospheric grid of Kurucz (1979), the polar areas of α Cep, α Oph, and Altair are radiative and their equators can be convective, especially for α Cep and Altair as their equatorial temperatures are below 7000K. Since the existence of convection tends to lower the value of the average gravity darkening coefficient β of the whole star (Claret, 1998), it may be the cause of $\beta < 0.25$ in the β-free model of α Cep and Altair. The unusually strong chromosphere activity of α Cep and Altair among A stars (Walter et al., 1995; Simon & Landsman, 1997) also provides evidence to the convective layers since the chromosphere is directly linked to magneto-convection. This suggests that although A stars are generally considered to have no chromospheres due to their very thin or lack of convective layers (Simon et al., 2002), rapid rotators may have exceptions at their equators due to gravity darkening. This is also consistent with the conclusion from the hydrodynamic model of Espinosa Lara & Rieutord (2007). This effect may also shed some light on the searches for the onset of chromosphere and the transition from radiative to convective envelopes among early type stars (e.g., Simon et al., 2002).

Since convection also tends to smear out the temperature differences between the hot and cool regions of the stellar surface and make their intensity contrast lower, other mechanisms such as differential rotation (e.g., Espinosa Lara & Rieutord, 2007) may also exist in the equators of these stars in order to make the equator darker and cooler as in the image. For instance, a faster differentially spinning equator will have stronger gravity darkening, thus will appear darker than that of the standard model. However, the darker equator, if it is real, can also be caused by a very different form of gravity darkening law. To further address this issue, we will need detailed line profile studies and images at visible since gravity darkening is more prominent in the visible than in the H band.

The 87.70^o inclination of α Oph differs from its orbital inclination by about 27^o ($i \sim 115^o$, Kamper et al., 1989; Augensen & Heintz, 1992; Gatewood, 2005), indicating the spin of α Oph is not coplanar with its orbit. Even more interesting, the orbit of the binary is highly eccentric ($e \sim 0.8$, Kamper et al. 1989 and Gatewood 2005; $e = 0.57$, Augensen & Heintz 1992), implying the non-coplanarity and the high eccentricity of the system may be related to each other through interactions of the two stars with their disks in their early formation stages.

3.8 Conclusion

We have modeled the surface brightness distributions of α Cep , α Oph , and Altair using the gravity darkening model. We have also reconstructed an aperture synthesis image for α Cep, but no reliable image for α Oph is available due to its lack of closure phase signatures caused by its nearly symmetric brightness distribution. The image of α Cep shows the star is oblate and its equator is darker than its poles, directly confirming the gravity-darkening phenomenon. The models show that all three stars are rotating close to their break-up speed. They all appear oblate and have large latitudinal temperature gradient due to gravity darkening. A standard gravity darkening model of β=0.25 is adopted for α Oph, and its inclination is determined to be 87.70^o. For α Cep, a $\beta = 0.216$ model fits the data better and also agrees better with the image. It has a medium inclination angle of 55.70^o. Altair also prefers a non-standard β of 0.19, and its inclination is 57.18^o.

Our models also allow us to calculate and compare the true T_{eff}s and luminosities of these stars with their apparent values. We show that α Oph has a true T_{eff} of

8250K and luminosity of 30.2 $L_\odot$, significantly larger than its apparent values due to its equator-on inclination. The true T_{eff}s and luminosities of α Cep and Altair, on the other hand, appear very close to their apparent values because of their medium inclination. The spectral classification of the three stars from literatures, however, suggests earlier spectral types for all of them than that inferred from their apparent T_{eff}s and luminosities. We infer that this is because the spectra of rapid rotators are dominated by lines from their hotter and brighter polar regions which appear much earlier in spectral type than the other regions of the stars, causing their overall spectral classification to be biased toward their polar areas.

The temperatures and luminosities in turn allow us to make rough estimates of the masses of all three stars through stellar evolution models. The mass of α Cep is estimated to be 1.92$M_\odot$, the mass of α Oph is 2.10$M_\odot$, and that of Altair is 1.66 $M_\odot$. However, due to possible abundance anomaly caused by rapid rotation, the exact masses of the two stars still have to be scrutinized when a detailed abundance analysis is available.

Our gravity darkening models also allow us to propose a new method to estimate the masses of rapid rotators together with precise measurements of $V sin i$. We have tested this method on α Cep and α Oph and found our mass estimate from the stellar models are within the range. The star α Oph will be a good target to further test this method as it is also an astrometric binary.

Our models show that the equatorial temperatures of α Oph and especially α Cep and Altair are low enough to meet the onset conditions of convection, implying that convections in the equatorial region can be a reason of the unusually high chromosphere activities of α Cep and Altair. Although the α Cep model agrees with its image in general, the image shows extra darkening at the equator which is not expected by our gravity darkening model but is consistent with the previous result of Altair. This effect, if is real, is most likely caused by differential rotation of the star. But to further confirm the conclusion, detailed high resolution line profile analysis and images at visible are needed.

3.9 Future work

With the modeling of α Cep, α Oph, and Altiar in this chapter, along with other two previously studied rapid rotators, Vega and Regulus (Aufdenberg et al., 2006; McAlister et al., 2005), we now have five rapid rotators studied, ranging from B7 to A7. We have also observed a few more rapid rotators, so one of the the next steps will be to continue to increase the database of modeled rapid rotators.

As mentioned above, detailed high resolution line profile analysis and images at visible are needed to characterize the temperature profile of rapid rotators, and to investigate possible effects of differential rotation. Direct fit to a temperature profile that is independent to the gravity darkening model is also necessary to study the real temperature structure of these stars. For the case of α Oph, higher resolution observations at shorter wavelengths such as visible are strongly needed to break model degeneracies and characterize its gravity darkening. In addition, test of more sophisticated non-Roche models such as those of MacGregor et al. (2007) is also an important direction to pursue.

Chapter 4

Binaries

Abstract:[1] In this chapter we present interferometric studies of two binary systems: λ Virginis and β Lyrae. λ Virginis is a well-known double-lined spectroscopic Am binary with the interesting property that both stars are very similar in abundance but one is sharp-lined and the other is broad-lined. We present combined interferometric and spectroscopic studies of λ Vir. The small scale of the λ Vir orbit ($\sim$ 20 mas) is well resolved by the Infrared Optical Telescope Array (IOTA), allowing us to determine its elements as well as the physical properties of the components to high accuracy. The masses of the two stars are determined to be 1.897 $M_\odot$ and 1.721 $M_\odot$, with 0.7% and 1.5% errors respectively, and the two stars are found to have the same temperature of 8280 ± 200 K. The accurately determined properties of λ Vir allow comparisons between observations and current stellar evolution models, and reasonable matches are found. The best-fit stellar model gives λ Vir a subsolar metallicity of Z=0.0097, and an age of 935 Myr. Although currently atomic diffusion is considered to be the most plausible cause of the Am phenomenon, the issue is still being actively debated in the literature. With the present study of the properties and evolutionary status of λ Vir, this system is an ideal candidate for further de-

---

[1] This chapter is based on Zhao et al. (2007) and Zhao et al. (2008)

tailed abundance analyses that might shed more light on the source of the chemical anomalies in these A stars.

β Lyrae is a well known interacting and eclipsing binary. We present the first resolved images of β Lyrae, obtained with the CHARA Array interferometer and the MIRC combiner in the H band. The images clearly show the mass donor and the thick disk surrounding the mass gainer at all six epochs of observation. The donor is brighter and generally appears elongated in the images, the first direct detection of photospheric tidal distortion due to Roche-lobe filling. We also confirm expectations that the disk component is more elongated than the donor and is relatively fainter at this wavelength. Image analysis and model fitting for each epoch were used for calculating the first astrometric orbital solution for β Lyrae, yielding precise values for the orbital inclination and position angle. The derived semi-major axis also allows us to estimate the distance of β Lyrae; however, systematic differences between the models and the images limit the accuracy of our distance estimate to about 15%. To address these issues, we will need a more physical, self-consistent model to account for all epochs as well as the multi-wavelength information from the eclipsing light curves.

4.1 The metallic-lined A binary λ Vir

4.1.1 Introduction

Am stars were first recognized by Titus & Morgan (1940) as a group of stars for which spectral classification is ambiguous. The Ca II K lines correspond to earlier types than derived from the Balmer lines, which in turn give earlier types than the metallic lines. Am stars generally have deficient CNO abundances (e.g., Roby & Lambert, 1990; Sadakane & Okyudo, 1989, etc.), while their iron peak and rare earth elements are generally overabundant (van't Veer-Menneret et al., 1988; Cayrel et al., 1991). Statistical studies (Abt, 1961a; Abt & Morrell, 1995; Abt, 2000a) suggest that virtually all Am stars are binaries with projected equatorial rotational velocities less than 120 $\mathrm{km\,s^{-1}}$, and it is the slow rotation that causes the abundance anomalies of Am stars. It is now widely believed that atomic diffusion in slowly rotating stars (e.g., Am and Ap stars) will occur in an outer convection zone so that some elements will be depleted in the atmosphere while others will become overabundant, which partly explains the chemical peculiarity of these stars (Michaud, 1980; Richer et al., 1998). Recent progress has been made on atomic diffusion models (Richer et al., 2000), and Michaud et al. (2005) have shown an example study of *o* Leo indicating that these models can produce abundance anomalies that are consistent with observations. However, the masses they adopted from Griffin (2002) have much larger error bars (more than 20 times larger) than the original determinations of Hummel et al. (2001) and no explanation was given on such a large difference. This implies that if the values from Griffin (2002) were wrong, the studies of Michaud et al. (2005) would be affected and their conclusions might be changed as well. Very recently, Böhm-Vitense (2006) studied the interaction between Am stars and the interstellar medium, and suggested that the Am phenomenon may be due at least in part to accretion of interstellar material rather than the more popular explanation in terms of atomic diffusion processes. This study challenges the most popular explanation of the Am phenomenon and makes this puzzle more interesting yet still unclear. Although Am stars have been studied intensively since their discovery, only a few of them have well determined properties. Therefore, in order to address these problems, more precise and accurate measurements of Am stars are required so that more detailed studies can be conducted to help improve our understanding of the role of atomic diffusion and, eventually, the cause of the abundance anomalies in Am stars.

λ Virginis (HD 125337, HIP 69974, HR 5359; $V = 4.523$ mag, $H = 4.282$ mag) was first reported to be a double-lined spectroscopic binary by Campbell et al. (1911). The two components were classified as metallic-lined A (Am) stars (Cowley et al., 1969; Levato, 1975). Early spectroscopic studies estimated its orbital parameters and found a period of 206 days with very low eccentricity (~ 0.079) (Colacevich, 1941; Abt, 1961a; Stickland, 1975, 1990). Chemical abundance studies (Colacevich, 1941; Stickland, 1975) suggested the interesting property of λ Vir that both stars are very similar in abundance despite their different rotation velocities with the primary being broad-lined (with $v \sin i = 35~\mathrm{km\,s^{-1}}$) and the secondary sharp-lined (with $v \sin i = 16~\mathrm{km\,s^{-1}}$). The differing rotation rates and the unusual metallic-lined nature of the system, as well as the similarity in the abundance of the two components give us a unique opportunity to test stellar models and study its evolutionary status.

In this chapter, we report the combined interferometric and spectroscopic study of λ Vir and the testing of stellar evolution models. The observations span several orbital periods, providing enough orbital coverage and allowing us to deduce the orbital and physical properties of the system precisely. After describing the observations in §4.1.2, we discuss the bandwidth smearing effects for interferometric visibilities and closure phases, followed by the orbit determination in §4.1.6. We determine its physical properties in §4.1.7, and compare the resulting properties with stellar models in §4.1.8, both sections are based on the work of Zhao et al. (2007). Finally, we give our conclusions and summary in §4.1.9.

4.1.2 Observations

Spectroscopic observations and reductions

The spectroscopic observations of λ Vir were conducted at the Harvard-Smithsonian Center for Astrophysics (CfA) between 1982 July and 1991 February, mostly with an echelle spectrograph on the 1.5-m Wyeth reflector at the Oak Ridge Observatory (Harvard, Massachusetts). A single echelle order was recorded with an intensified Reticon diode array giving a spectral coverage of about 45 Å at a central wavelength of 5188.5 Å. The main spectral feature in this region is the Mg I b triplet, although there are numerous other metallic lines as well. The resolving power is $\lambda/\Delta\lambda \approx 35{,}000$. Occasional observations were made also with nearly identical instruments on the 1.5-m Tillinghast reflector at the F. L. Whipple Observatory (Mt. Hopkins, Arizona) and the Multiple Mirror Telescope (also on Mt. Hopkins, Arizona), prior to its conversion to a monolithic mirror. A total of 130 spectra were collected, with signal-to-noise ratios (SNRs) ranging from 20 to about 50 per resolution element of 8.5 $\mathrm{km\,s^{-1}}$.

Radial velocities were derived using TODCOR (Zucker & Mazeh, 1994), a two-dimensional cross-correlation algorithm well suited to our relatively low SNR spectra. TODCOR uses two templates, one for each component of the binary, and significantly reduces systematics due to line blending that are often unavoidable in standard one-dimensional cross-correlation techniques (see, e.g., Latham et al., 1996). The templates were selected from a large library of synthetic spectra based on model atmospheres by R. L. Kurucz (available at http://cfaku5.cfa.harvard.edu), computed for us by Jon Morse (see also Nordström et al., 1994; Latham et al., 2002). These calculated spectra are available for a wide range of effective temperatures ($T_{\rm eff}$), projected rotational velocities ($v \sin i$), surface gravities ($\log g$) and metallicities. Experience has shown that radial velocities are largely insensitive to the surface gravity and metallicity adopted for the templates. Consequently, the optimum template for each star was determined from grids of cross-correlations over broad ranges in temperature and rotational velocity, seeking to maximize the average correlation weighted by the strength of each exposure (see Torres et al., 2002). For the surface gravity we adopted the value of $\log g = 4.0$ for both stars (see §4.1.8), and for the metallicity we initially adopted the solar composition. However, in view of the metallic-lined nature of the stars we repeated the procedure for a range of metallicities from [m/H] $= -1.0$ to [m/H] $= +0.5$ in steps of 0.5 dex. We found the best match to the observed spectra for [m/H] $= +0.5$, which is consistent with the enhanced surface abundances expected for these objects. At this metallicity the effective temperatures we derive are 8800 ± 200 K for both stars, and the rotational velocities are $v_1 \sin i = 36 \pm 1$ km s^{-1} and $v_2 \sin i = 10 \pm 2$ km s^{-1} for the primary and secondary, respectively. The rotational velocity estimates are fairly consistent with determinations by other authors: Stickland (1975) reported 35 km s^{-1} and 16 km s^{-1} (no uncertainties given), and Abt & Morrell (1995) estimated 31 km s^{-1} and 13 km s^{-1}, with uncertainties of about 8 km s^{-1}. Very rough values without uncertainties were estimated more recently by Shorlin et al. (2002) as $\sim$50 km s^{-1} and < 10 km s^{-1}. We discuss the temperature estimates in §4.1.7.

In addition to the radial velocities and stellar parameters, we derived the spectroscopic light ratio following Zucker & Mazeh (1994). The result, $\ell_2/\ell_1 = 0.58 \pm 0.02$, corresponds to the mean wavelength of our observations (5188.5 Å) and is not far from the visual band.

Due to the narrow wavelength coverage of the CfA spectra there is always the possibility of systematic errors in the velocities, resulting from lines of the stars moving in and out of the spectral window with orbital phase (Latham et al., 1996). Occasionally these errors are significant, and experience has shown that this must be checked on a case-by-case basis (see, e.g., Torres et al., 1997, 2000). For this we performed numerical simulations in which we generated artificial composite spectra by adding together synthetic spectra for the two components, with Doppler shifts appropriate for each actual time of observation, computed from a preliminary orbital solution. The light ratio adopted was that derived above. We then processed these simulated spectra with TODCOR in the same manner as the real spectra, and compared the input and output velocities. Although the differences for λ Vir were well under 1 $\mathrm{km\,s^{-1}}$, they are systematic in nature and we therefore applied them as corrections to the raw velocities for completeness. The final velocities including these corrections are given in Table 4.1. Similar corrections were derived for the light ratio, and are already accounted for in the value reported above.

The stability of the zero-point of the velocity system was monitored by means of exposures of the dusk and dawn sky, and small run-to-run corrections were applied in the manner described by Latham et al. (1992). These corrections are also included in

Table 4.1. The accuracy of the CfA velocity system, which is within about 0.14 km s^{-1} of the reference frame defined by minor planets in the solar system, is documented in the previous citation and also by Stefanik et al. (1999) and Latham et al. (2002).

Table 4.1. Radial Velocity of λVir

HJD	Orbital Phase	RV_1 ($\mathrm{km\,s^{-1}}$)	RV_2 ($\mathrm{km\,s^{-1}}$)
45156.5547	0.72	-31.80	18.58
46576.6328	0.59	-19.43	5.80
46576.6758	0.59	-20.03	5.50
46576.6797	0.59	-19.24	5.70
46597.6406	0.69	-30.60	16.41
46597.6562	0.69	-30.60	16.34
46597.6641	0.69	-31.93	17.30
46611.5703	0.76	-33.75	19.10
46613.5664	0.77	-32.03	19.33
46633.6016	0.86	-26.78	13.07
46635.5430	0.87	-27.06	11.62
46636.5430	0.88	-28.03	10.66
46640.5586	0.90	-23.66	9.12
46809.9688	0.72	-32.51	18.19
46819.9570	0.77	-34.08	19.31
46896.7656	0.14	14.56	-30.78
46918.7227	0.24	17.31	-34.79
46924.6719	0.27	16.75	-33.91
46938.6758	0.34	12.25	-28.73
46953.6094	0.41	1.66	-20.67
47197.9453	0.59	-19.45	6.86
47206.0508	0.63	-25.53	11.80
47218.9141	0.70	-30.68	18.07
47222.8750	0.71	-32.75	16.99
47226.8438	0.73	-30.44	20.05
47320.7148	0.19	17.45	-34.27
47568.8828	0.39	5.82	-23.65
47569.9688	0.39	5.08	-22.15
47570.9414	0.40	2.87	-22.46
47574.9297	0.42	0.86	-20.01
47575.9141	0.42	-0.60	-19.07
47583.8047	0.46	-6.53	-13.33
47585.9062	0.47	-6.35	-11.88
47586.8359	0.48	-6.70	-11.02
47587.8633	0.48	-9.53	-10.34
47598.8789	0.53	-14.02	-2.58
47602.8516	0.55	-15.38	0.74
47607.8242	0.58	-18.86	4.20
47608.7930	0.58	-21.07	4.90
47612.8398	0.60	-21.97	8.06
47613.7578	0.61	-23.18	8.32
47628.7344	0.68	-29.95	16.34
47640.7031	0.74	-32.58	18.24
47641.8555	0.74	-30.13	19.15
47642.7695	0.75	-33.43	18.76
47643.7383	0.75	-32.53	18.59
47644.7266	0.76	-33.16	18.78
47661.7305	0.84	-30.64	15.75
47662.6680	0.84	-30.49	15.06
47664.7305	0.85	-30.27	14.10
47665.6602	0.86	-26.94	14.82
47674.5586	0.90	-24.69	8.50
47675.6406	0.91	-24.16	7.88
47676.6641	0.91	-21.57	7.61
47688.5938	0.97	-14.10	-2.76
47689.7031	0.97	-12.11	-3.75
47693.6289	0.99	-11.58	-8.51
47698.6328	0.02	-7.05	-12.13
47702.6523	0.04	-3.51	-15.23

Table 4.1—Continued

HJD	Orbital Phase	RV_1 (km s^{-1})	RV_2 (km s^{-1})
47723.5664	0.14	11.06	-31.07
47730.5547	0.17	14.62	-33.99
47763.5078	0.33	12.28	-29.11
47879.9688	0.89	-24.54	9.80
47894.9492	0.97	-14.83	-2.20
47895.9453	0.97	-12.76	-3.57
47898.9492	0.99	-12.30	-6.20
47900.9531	0.99	-10.97	-9.37
47904.9727	0.01	-6.57	-12.07
47908.9570	0.03	-5.09	-15.27
47910.9453	0.04	-3.03	-16.64
47922.9492	0.10	7.00	-27.02
47928.8906	0.13	10.71	-30.08
47930.9648	0.14	13.31	-30.51
47931.9258	0.14	14.32	-31.36
47933.9453	0.15	12.59	-32.76
47934.9492	0.16	15.58	-33.16
47935.8750	0.16	15.39	-33.56
47939.8906	0.18	15.06	-34.87
47942.8984	0.20	16.54	-35.06
47952.8672	0.25	16.34	-35.10
47955.8984	0.26	16.30	-34.90
47957.8320	0.27	14.77	-35.07
47958.9414	0.28	16.70	-34.97
47959.8477	0.28	15.94	-33.16
47960.8672	0.28	15.77	-33.39
47963.8711	0.30	14.87	-33.14
47969.7930	0.33	13.14	-30.06
47989.7422	0.42	-1.21	-17.35
47990.7617	0.43	-2.36	-17.36
47991.7852	0.43	-3.27	-16.77
47994.7852	0.45	-3.84	-14.83
47998.7109	0.47	-5.63	-11.45
47999.7344	0.47	-5.93	-10.69
48000.7148	0.48	-6.97	-10.60
48001.7500	0.48	-10.20	-9.33
48021.6758	0.58	-19.67	3.84
48023.7617	0.59	-23.76	5.77
48026.6797	0.60	-22.28	7.47
48027.6562	0.61	-21.28	8.32
48042.6328	0.68	-29.91	16.44
48044.7461	0.69	-29.98	17.49
48050.6172	0.72	-32.79	18.73
48052.5742	0.73	-33.89	18.41
48054.5898	0.74	-32.81	19.02
48055.6211	0.74	-34.69	18.90
48057.6484	0.75	-34.80	18.49
48058.6992	0.76	-34.14	19.76
48059.6445	0.76	-35.64	17.99
48060.5586	0.77	-32.41	19.65
48069.5781	0.81	-31.88	17.72
48078.6055	0.85	-28.72	14.35
48079.6523	0.86	-26.86	15.33
48082.5820	0.87	-26.60	12.51
48084.5625	0.88	-26.50	10.60
48087.5898	0.90	-25.65	8.99
48088.5781	0.90	-22.51	8.12
48100.5391	0.96	-14.22	-1.31
48101.5391	0.97	-14.20	-3.01

Table 4.1—Continued

HJD	Orbital Phase	RV_1 ($\mathrm{km\,s^{-1}}$)	RV_2 ($\mathrm{km\,s^{-1}}$)
48102.5781	0.97	-11.95	-3.36
48104.5508	0.98	-11.71	-6.25
48105.5273	0.98	-10.52	-6.74
48106.5273	0.99	-11.12	-7.38
48108.5312	1.00	-8.76	-8.89
48116.5391	0.04	-0.66	-15.99
48280.9727	0.83	-31.12	16.27
48281.9727	0.84	-30.50	15.95
48283.9688	0.85	-30.04	15.62
48289.9531	0.88	-26.94	11.90
48290.0078	0.88	-28.96	11.94
48291.8945	0.89	-26.25	11.06

Interferometric Observations and Data Reduction

The interferometric observations of λ Vir were carried out using the Infrared Optical Telescope Array (IOTA) (Traub et al., 2003) also at the F. L. Whipple Observatory. IOTA is a three 0.45m-telescope interferometer array that is movable along its L-shaped southeast and northeast arms, providing several different array configurations and having baselines up to 38m. Light from each telescope is focused into a single-mode fiber and the beams from 3 fibers are split and combined by the "pair-wise" beam combiner IONIC-3 (Berger et al., 2003) to form six fringes. Fringes are temporally scanned by piezo scanners in the delay lines, and are then detected by a PICNIC camera (Pedretti et al., 2004). This detection scheme leads to high sensitivities of IOTA (~7th magnitude at H band) (Monnier et al., 2004), and allows for precise measurements of visibilities and closure phases.

The observations reported here were taken in the H band ($\lambda_0 = 1.647\mu m$, $\Delta\lambda = 0.30\mu m$) between 2003 February and 2005 June, spanning four orbital periods (853 days) and covering a broad range of orbital phases, and different array configurations were applied to obtain good uv coverage. The observations were carried out following the standard procedures (e.g., Monnier et al., 2004), and the observation log is listed in Table 4.2. In short, λ Vir was observed in conjunction with nearby unresolved calibrators (HD 126035, HD 129502, HD 158352) to calibrate the varying system visibilities and closure phases caused by the instrumental response and the effect of atmospheric seeing. Each single observation typically consists of 200 scans within ~4 min, followed by calibration measurements of the background and individual response of each telescope. Two different piezo scan modes were used for different observing runs (see Table 4.2), mode one before 2003 June 17th (Telescope A fixed, Telescope B scan range: 50.8 μm, Telescope C scan range: 25.4 μm), and mode two thereafter (Telescope A fixed, Telescope B scan range: 25.4 μm, Telescope C scan range: -25.4 μm). The effect of different scanning modes is discussed later in the §4.1.5.

Reduction of the squared-visibilities (V^2) and the closure phases was carried out using established IDL routines described by Monnier et al. (2004, 2006). In short, we measure the power spectrum of each interferogram which is proportional to the broad-band V^2 (see Coude du Foresto et al., 1997, for an outline of the method), and correct for intensity fluctuations as well as bias terms that stem from read noise, background noise, etc. The variable flux ratios of each baseline are calibrated using a flux transfer matrix (Monnier et al., 2006). Measurement errors are obtained from the scatter of the data and are then combined with calibration errors. The calibration error, established statistically from the data fitting procedures (see §4), is $\sim 2\%$ for V^2, corresponding to 1% error in the visibility. In order to measure the closure phases, a real-time fringe-tracking algorithm (Pedretti et al., 2005) was applied to ensure that the interferograms are detected simultaneously in nearly all baselines (at least two are detected if fringes in the third baseline is weak). The closure phases are then obtained by calculating and averaging the bi-spectrum (triple product) in complex space, with the frequencies of each triple product closed, i.e., $\nu_{AB} + \nu_{BC} + \nu_{CA} = 0$ (Baldwin et al., 1996). The instrumental closure phase offset ($\leq 0.5°$, Monnier et al., 2006) is calibrated by using unresolved calibrators listed in the observation log. The calibration errors of the closure phases are dominated by fluctuations that result from

Table 4.2. IOTA Observing Log of λ Vir.

Date[a] (UT)	Interferometer Configuration[b]	Calibrator Names
2003 Feb 16,17	A35 B05 C10	HD 126035 (G7 III, 0.78 ± 0.24 mas)[c]
		HD 129502 (F2 III, 1.20 ± 0.22 mas)
2003 Feb 20-23	A25 B05 C10	HD 126035
2003 Mar 21	A35 B07 C25	HD 126035
2003 Mar 22	A35 B07 C10	HD 126035
		HD158352 (A8 V, 0.44 ± 0.10 mas)
2003 Mar 23, 24	A35 B15 C10	HD 126035; HD 158352
2003 Jun 12, 14-16	A35 B15 C10	HD 126035
2003 Jun 17	A35 B15 C10	HD 126035
2004 Mar 16-21	A35 B15 C10	HD 126035
2004 Apr 13	A35 B15 C10	HD 129502
2004 Apr 14	A35 B15 C10	HD 126035; HD 129502
2004 Apr 20	A35 B15 C10	HD 126035; HD 158352
2004 Apr 24,25	A35 B15 C10	HD 126035
2004 May 28	A35 B15 C10	HD 126035
2004 May 30	A35 B15 C10	HD 126035; HD 129502; HD 158352
2004 Jun 01	A35 B15 C10	HD 126035; HD 158352
2004 Jun 02-07	A35 B15 C10	HD 126035
2005 Jun 14-18	A35 B15 C10	HD 126035

[a] Scan Mode 1 before 2003 Jun 16: A: fixed, B: $\Delta X = 50.8\ \mu m$, C: $\Delta X = 25.4\ \mu m$;
Scan Mode 2 after 2003 Jun 16: A: fixed, B: $\Delta X = 25.4\ \mu m$, C: $\Delta X = -25.4\ \mu m$.

[b] Configuration refers to the location of telescopes A, B, C on the NE, SE and NE arms respectively; see Traub et al. (2003) for more details.

[c] Uniform disk (UD) diameters of the calibrators are generally estimated using *getCal*, an SED-fitting routine maintained and distributed by the Michelson Science Center (http://msc.caltech.edu).

extra optical path differences (OPDs) caused by the atmospheric piston fluctuations. We will discuss this effect in §4.1.5 and estimate errors for the closure phases in §4.1.4.

4.1.3 Bandwidth Smearing Effect of V^2

Interferometric measurements use a finite range of bandwidth. The resulting fringe packets thus suffer a modulation in the amplitude due to the overlap of fringes with different wavelengths, especially at the edges of the packets. For binary stars, the observed interferogram results from the interference of two fringe packets with an interferometric delay of $\vec{B} \cdot \vec{\rho}$ due to the binary separation (where $\vec{B}$ is the projected baseline vector (B_x, B_y) in meters and $\vec{\rho}$ is the angular separation $(a,\ b)$ of the binary in units of radians). Because the two fringe packets are modulated by bandwidth smearing, the resulting observed interferogram is also affected by this, causing significant systematic errors to the measured visibilities and closure phases. This effect is pronounced for broad band filters such as the H-band filter of the IOTA PICNIC camera. Our preliminary binary modelling indicated a poor fit to the squared-visibilities and the closure phases, evidenced by a large reduced χ^2 (χ^2_ν). Therefore, before we determined the orbit of λ Vir, we first investigated the influence of bandwidth smearing on our data.

The standard monochromatic squared-visibility of a binary can be written as

$$V^2 = \frac{|V_1|^2 + r^2|V_2|^2 + 2r \cdot |V_1| \cdot |V_2| \cdot \cos \frac{2\pi}{\lambda} \vec{B} \cdot \vec{\rho}}{(1+r)^2}, \tag{4.1}$$

where r is the flux ratio, and V_1, V_2 are the visibilities of the primary and the secondary respectively (Boden, 1999). For the case of IOTA IONIC-3, where we measure the power-spectrum of the interferogram to determine the broad-band squared-visibility[2](see e.g., Coude du Foresto et al., 1997), we integrate the squared-visibility

---

[2] This is equivalent to integrating the squared-visibility over the full wavelength range to get the broad-band value.

over the whole bandpass and subtract Equation 4.1 from it to obtain the difference between the polychromatic and the monochromatic squared-visibilities:

$$\Delta V^2 = V_{BS}^2 - V^2 = \frac{2r \cdot |V_1| \cdot |V_2| \cdot \cos(2\pi\delta) \cdot (\exp\frac{-\delta^2}{2f^2} - 1)}{(1+r)^2}, \tag{4.2}$$

where

$$f = \frac{\lambda \cdot \beta}{\Delta\lambda \cdot \sqrt{8 \ln 2}}. \tag{4.3}$$

We used a gaussian envelope function, $\exp\frac{-\delta^2}{2f^2}$, to approximate the modulation of the interferogram, where $\delta = \frac{\vec{B} \cdot \vec{\rho}}{\lambda} = \frac{B_x a + B_y b}{\lambda}$ is the phase difference of the two components in unit of wavelength, β is the introduced bandpass coefficient, and f is the corresponding bandwidth smearing coefficient which is also 1 σ of the envelope function of the interferogram. The exact value of f depends on the bandpass shape and windowing function. For example, for a "top-hat" bandpass approximation, $f \simeq 4.0$; for a Gaussian bandpass approximation with FWHM=$\Delta\lambda$, $f \simeq 2.6$. We applied Equation 4.2 to our squared-visibility model with f being a free parameter. The new best-fit is significantly improved ($\chi_\nu^2 \sim 1.3$) compared to the preliminary result ($\chi_\nu^2 \sim 1.9$), giving f a value of 3.4 which is consistent with the fact that the bandpass of IOTA is between a "top-hat" and a Gaussian function. Fig. 4.1 shows the best-fit squared-visibility models before and after applying the bandwidth smearing correction. The data are plotted versus interferometric delay $\vec{B} \cdot \vec{\rho}$ (i.e., projected baseline × angular separation of the binary) in unit of wavelength. The corresponding normalized residuals (i.e., normalized by their errors) are shown in the left panels for the 3 baselines respectively. As can be seen, the visibility amplitudes around ±1.0 and ±1.5 wavelengths in baseline AB (the top panel) are reduced a large amount from the original sinusoidal V^2 model because of the bandwidth smearing effect and the applied correction improved the fit significantly. Baselines AC and BC are shorter than baseline AB, and therefore provide measurements with delay differences < 1 wavelength and suffer less amplitude reduction than baseline AB.

A group of data around 1 wavelength in baseline AC from two different observations (2003Feb17 and 2004Apr) have large normalized residuals (> 5) even after removing all known calibration errors. The orbital phases of these two epochs are $\sim$0.1 and $\sim$0.20–0.25, respectively. Inspection of these data revealed unusually high variations in the system visibilities on this baseline, indicating the poor fit at these epochs is likely due to calibration problems rather than errors in our determined orbital parameters.

4.1.4 Bandwidth Smearing Effect of Closure Phase and OPD Fluctuations

Our preliminary best-fit on closure phases also showed large residuals, leading to even larger χ^2_ν (~ 3) than that of the squared-visibilities. This can also be the result of the bias induced by bandwidth smearing. However, unlike the case for the visibilities, this bias in the closure phases does not have a particularly simple analytical expression. One can only simulate this bias numerically, making it more difficult to look into the influence of bandwidth smearing. In our approach, we simulate the observational data of λ Vir by generating 3 interferograms for the 3 IOTA baselines at different epochs. The different piezo scan modes are also taken into account. We then put the 3 interferograms into the IOTA data reduction pipeline (§4.1.2) to reproduce the

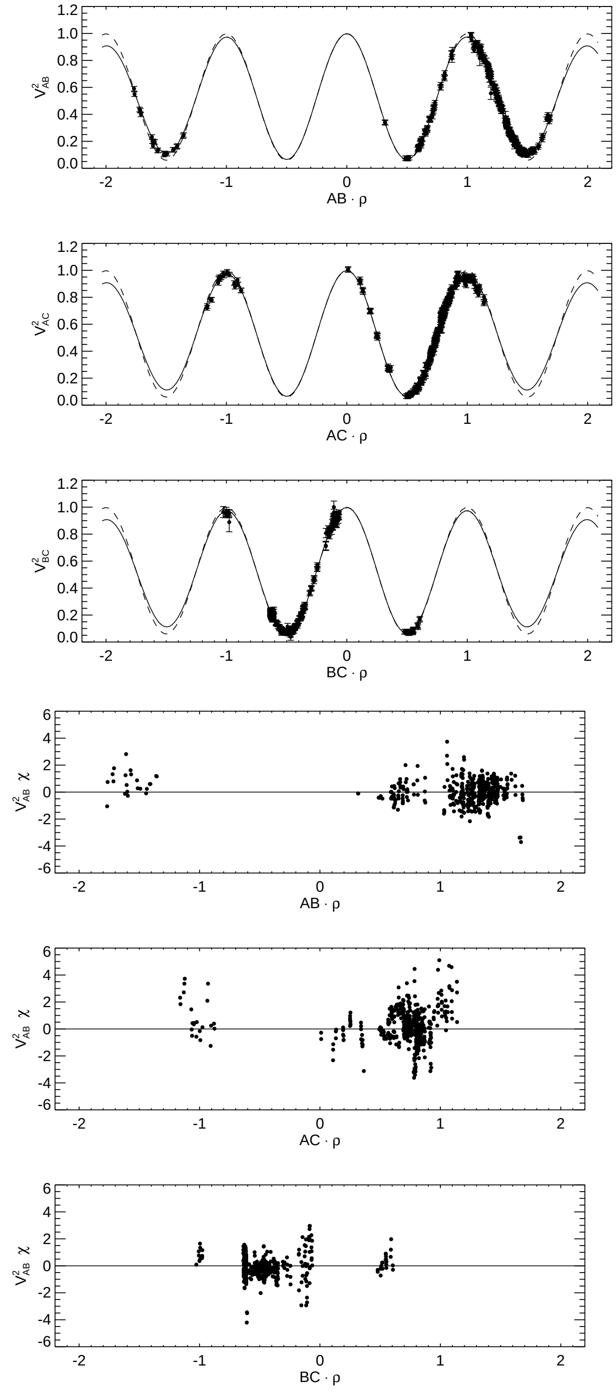

Figure 4.1 V^2 for 3 IOTA baselines vs. interferometric delay ($\vec{B} \cdot \vec{\rho}$) in units of wavelength. The dashed lines indicate the original squared-visibility model with no bandwidth smearing correction, while the solid lines show the models corrected for bandwidth smearing. V^2 data are overplotted with error-bars of 1-σ. The corresponding normalized residuals for the corrected model (i.e., residual/error) are shown in the right panels for the 3 baselines respectively.

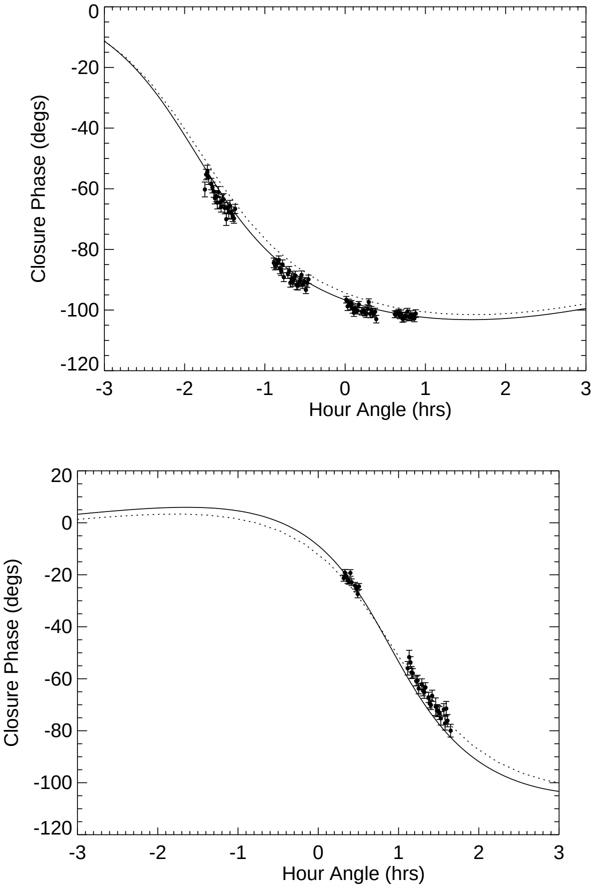

Figure 4.2 Preliminary closure phase model vs. hour angle. Two typical dates of data with different scan modes (left: 2003Mar24, scan mode 1; right: 2005Jun16, scan mode 2) are selected to represent the whole data set. The solid lines show the original closure phase model, while the dotted lines show the model with bandwidth smearing taken into account. The difference between the two models is about 5 degrees in both panels. Closure phases data are indicated as filled dots with 1-σ measurement errors.

“measured” closure phases as in real observations. We adopted the same bandpass function and bandwidth smearing coefficient from the visibility modelling (§4.1.3). By varying the width of the interferogram envelope function, we simulated the closure phases for both the monochromatic and the polychromatic cases.

Fig. 4.2 shows the bandwidth-smearing corrected (dotted line) and the original uncorrected (solid line) closure phase models for two typical observations (2003Mar24

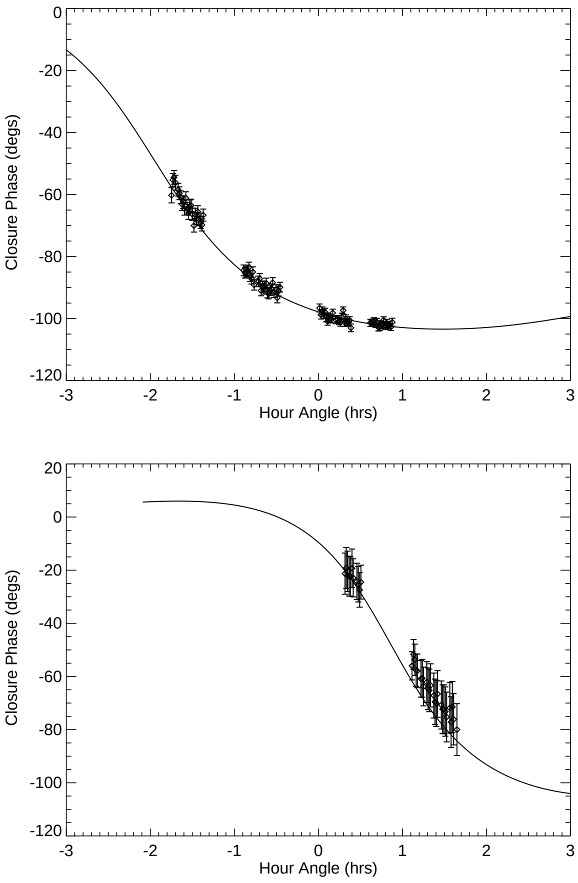

Figure 4.3 Closure phase model and data with new estimated errors. The two panels indicate the same dates as in Fig. 4.2. The new 1-σ errors in the left panel are smaller than those in the right one due to smaller closure phase fluctuations in scan mode 1. The good fit of the data within the errors suggests the robustness of our error estimation.

& 2005Jun16). These two observations represent two different a scanning modes, mode 1 for 2003Mar24 (left panel) and mode 2 for the latter one (right panel). Fig. 4.2 indicates that bandwidth smearing can change the closure phases by ~ 5 degrees at these two epochs. Although the fit is improved in the right panel by the simulated bandwidth smearing model, the one in the left is worse than the original fit. In fact, the original model deviates from the measured closure phases by up to 10 degrees in the whole data set, and the simulated bandwidth smearing cannot reduce these deviations significantly, implying other biases may exist in the closure phase measurements.

Another source of error in the closure phases stems from the offsets of the fringe phases due to extra OPDs induced by the atmospheric piston fluctuations. Further investigations (see §4.1.5) suggest that this effect does dominate the errors of our closure phase measurements. To reduce the influence of this effect on our fits, we estimate the errors of the closure phases based on their uncertainties obtained from the simulations of closure phase fluctuations caused by extra OPDs. The details of the simulation and the corresponding closure phase behaviors are discussed in §4.1.5. Fig. 4.3 shows the best-fit closure phase model for the two typical observations, overplotted with the observed data and the estimated errors. The errors in the first epoch (left panel) are much smaller than those in the second epoch due to their differing scan modes. The best fit leads to a χ^2_ν of 1.2 with 476 degrees of freedom for the closure phases (previously $\chi^2_\nu \sim 3$), which is significantly reduced as a result of the reliable error estimation.

4.1.5 OPD fluctuations and closure phase errors

Because fringes are obtained by piezo scanning, the measured interferograms are thus temporal sequences that span several atmospheric coherence times. In our data reduction pipeline, fringe scans are divided into segments of equal time according to the atmospheric coherence time (Baldwin et al., 1996) to allow best signal-to-noise ratio for averaging the closure phase. More specifically, the complex visibility of each short time segment is calculated individually for the 3 baselines. The triple product of each segment is thus obtained from a complex multiplication of the three visibilities.

Lastly, the (complex) triple products from each segment are averaged together with those from the other segments to form a single estimate of the complex triple product for each scan. The closure phase is of course derived as the phase argument of the final complex triple product (see Monnier, 1999).

Fig. 4.4 shows an example of this method. The simulated fringes are divided into segments of 16 pixels in the pipeline, corresponding to 10–20 milli-seconds in time (depending on the scan rate). With zero atmospheric delays, the fringe envelopes are aligned in time and the calculation of the triple product is straightforward (and the resulting bias on the closure phase has already been discussed in §4.1.4). As the atmospheric piston fluctuates and causes OPD fluctuations, the fringe envelopes may not coincide exactly in time and thus we must consider this additional complication on the closure phase estimator. Because the "phase" of the fringes within the coherence envelope may not be constant with optical path difference, due to both source structure and also due to dispersion in beam combining optics, we intuitively can see that OPD fluctuations will corrupt the measurement process. We note that this effect does not exist for the monochromatic (i.e., very narrow bandwidth) case and we later (see Eq.4.4) derive a more quantitiative bandwidth condition.

In order to investigate the influence of this effect, it is instructive to consider the case of a binary star and we have performed simulations in this section using the parameters of the λ Vir system (see —s4.1.6). We have simulated OPD fluctuations above each telescope, ensuring the OPDs are closed in triangle (i.e., $OPD_{AB} + OPD_{BC} + OPD_{CA} = 0$). The resulting closure phases are then calculated using the IOTA data reduction pipeline (described above and also in §4.1.2). Fig. 4.5

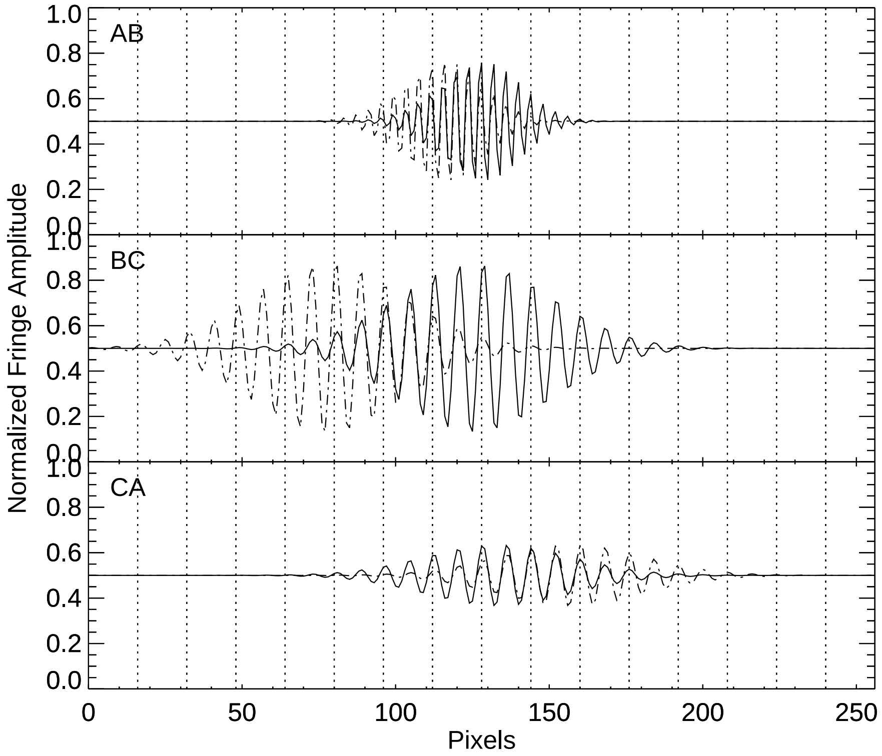

Figure 4.4 Simulated λ Vir fringes for IOTA baseline AB, BC, and CA, respectively. The solid lines indicate normalized fringes with zero phase shift while the dotted-dashed lines show an example of fringes with phase shifts of 3, -6, and 3 wavelengths, respectively. The vertical dotted lines divide the fringes into segments of 16 pixels.

shows 20 simulated closure phase curves for each of the two representative epochs, 2003Mar24 for piezo scan mode 1 and 2005Jun16 for mode 2. The closure phases fluctuate in both panels due to the fluctuations of extra OPDs which were assumed to follow a normal distribution with 1-σ deviation of 1.2 wavelengths (determined below). As can be seen in Fig. 4.5, the flucutating OPDs introduce sometimes very large errors in the closure phase (up to $\sim 10^\circ$ in the left panel and $\sim 30^\circ$ in the right) which depend on both hour angle (i.e., projected binary separation) and scan mode (which affects the interferograms). These errors are many times larger than those seen from bandwidth smearing calculated without OPD fluctuations in Fig. 4.2, sug-

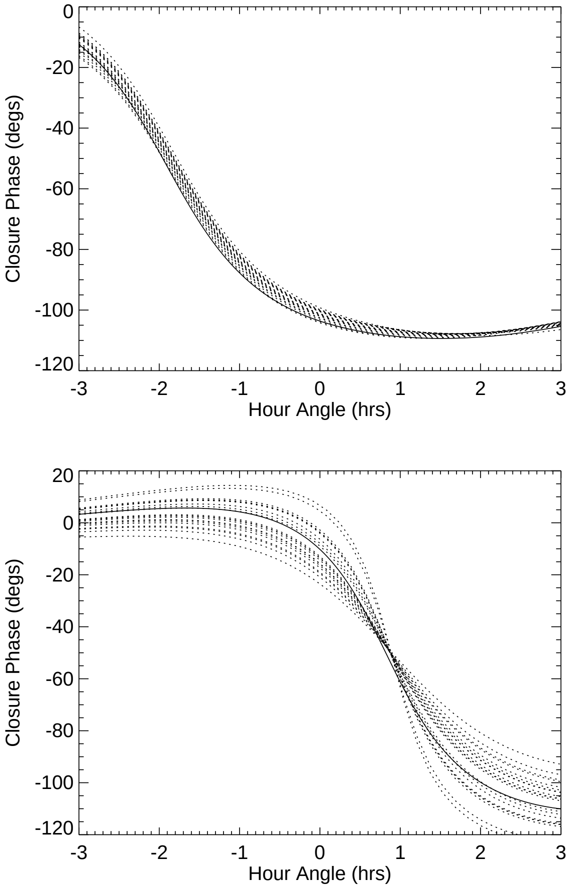

Figure 4.5 Closure phase fluctuations due to additional OPDs, caused by the varying atmospheric piston. The dotted lines indicate simulated closure phases with different OPDs. The closure phase models with no bandwidth smearing correction and zero OPD fluctuations are plotted as solid line for reference. As in Fig. 4.2, two dates with different scan modes (left: 2003Mar24, scan mode 1; right: 2005Jun16, scan mode 2) are selected to represent the entire data.

gesting the errors from these fluctuations are dominant errors in our closure phase measurements.

We have reduced the influence of this disturbing effect on our closure phase modeling in §4.1.4 by simulating the closure phase fluctuations for all of our data. From the scatter of simulated closure phases, we provide an estimate of the closure phase errors to the model fitting process. The standard deviation of the simulated OPD fluctuations was determined iteratively in model fitting procedures in order to reduce the χ^2_ν to close to unity. We found that just a small uncorrected atmospheric OPD fluctuation of $\pm$ 2 μm was enough to explain our observed closure phase errors, and this level of OPD error is similar to actual residuals reported at IOTA by Pedretti et al. (2005).

Quite unexpectedly, we discovered that the closure phase simulations showed "null points" where OPD fluctuations had no effect on the measured closure phases (e.g., see null fluctuation point in the right panel of Fig.4.5, but not in the left panel). To look into this in more detail, we simulated the closure phase fluctuations for both scan modes at all observed epochs. Fig.4.6 shows two typical epochs and the comparison of the two modes at each epoch. As we can see, the fluctuations of the two modes behave differently. Both of them have null points but the locations of the nulls are different. This is because fringes are scanned from different sides in different modes. For example, in our case, one mode scans fringe AC from the left hand side while the other scans from the right hand side, which causes the segments of fringe AC in the two modes to be scanned at different coherence times, thus introducing different errors to the triple products and causing the closure phases to fluctuate differently. For the case of a binary star, it is easy to prove that when any two of the 3 interferometric delays between components ($\vec{B} \cdot \vec{\rho}$) are equal to $\pm\frac{n}{2}$ wavelengths, the closure phase will be immune to OPD fluctuations and therefore has a null. The behaviors of other nulls may be related to their scan mode and are not yet clear. Note that these results are restricted to models of binary stars, but presumably apply in general to objects with any resolved asymmetric structure affected by bandwidth smearing.

We can use our empirical study of binary stars to motivate a scaling relation for estimating when bandwidth smearing corrupts the closure phase measurement process. In our simulations of IOTA, we found strong effects when the source structure (scale: ρ) fills approximately $\sim \frac{1}{5}$ of the field-of-view defined by bandwidth-smearing. Thus, we find that bandwidth-smearing has a much stronger and more corruptive effect on closure phases than on visibility amplitudes. We can express this mathematically as a condition to meet in order to assure good closure phase measurement:

$$\frac{\vec{B} \cdot \vec{\rho}}{\lambda} < \frac{1}{5} \frac{\lambda}{\Delta\lambda}, \tag{4.4}$$

where $\vec{B} \cdot \vec{\rho}$ is the previously defined interferometric delay; $\vec{B}$ is the projected baseline vector (B_x, B_y) in unit of meters and $\vec{\rho}$ is the binary angular separation (a, b) in unit of radian (for cases other than a binary, this represents the typical scale of source structure).

In order to avoid these closure phase fluctuations, one could consider using a closure phase estimator that is not affected by the fringe phase shift, e.g., an estimator that does not divide fringes into coherence segements. However, this estimator is likely to be very noisy unless the entire interferogram is scanned within a coherence time – drastically reducing signal-to-noise ratio for faint objects. Since all of these problems actually stem from bandwidth smearing, we conclude that using narrow bandwidth is a better approach and is of importance for precision work.

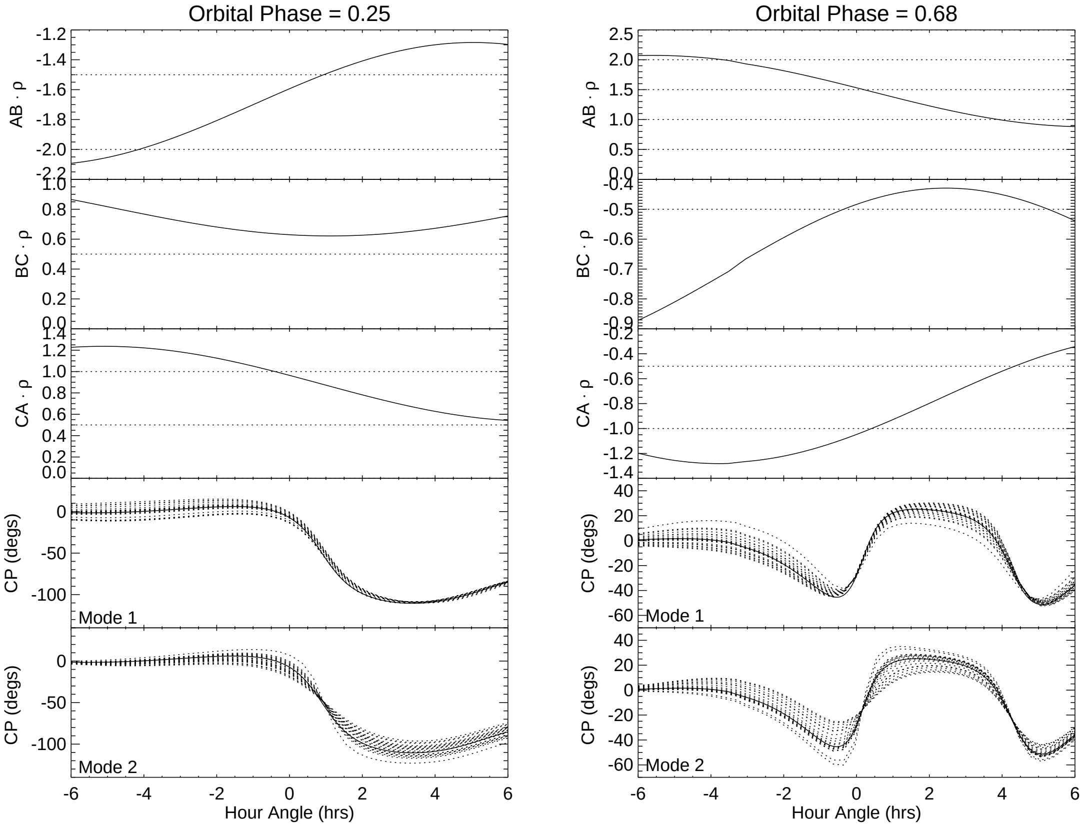

Figure 4.6 Comparison of closure phase fluctuations between the two scan modes. We show two typical epochs at different orbital phases, the left plot is for phase 0.25, while the right is for 0.68. The interferometric delay ($\vec{B} \cdot \vec{\rho}$, in units of wavelength) of the three baselines are plotted as solid lines in the top three panels of each plot. The dotted lines indicate phases of $\pm\frac{n}{2}$ wavelengths, corresponding to $\pm n\pi$ in radian. The two bottom panels show the corresponding closure phases for scan mode 1 and 2 respectively. The solid lines indicate the model closure phase with zero OPD fluctuation and no bandwidth smearing correction, while the dotted lines indicate the simulated closure phase fluctuations.

4.1.6 The final orbit of λ Vir

With the bandwidth smearing effects addressed as described above, we proceed in this section with a simultaneous Keplerian orbital fit to the radial velocities, the squared visibilities, and the closure phases for λ Vir. This allows us to determine the full set of orbital elements, for which the closure phases remove the ambiguity in the position angle of the ascending node (Ω) that is usually inherent in the visibility measurements. The inclination angle i is determined from the interferometric data, and consequently the masses M_1 and M_2 can be found from the spectroscopic values of $M_1 \sin^3 i$ and $M_2 \sin^3 i$. Since neither of the λ Vir components are resolved by IOTA, we take the sizes of the two components into account by using a uniform stellar disk model (Boden, 1999). The applied diameters, 0.40 mas for the primary and 0.30 mas for the secondary, are consistent with the values determined in §4.1.8. The overall χ^2 of the measurements is minimized using standard non-linear least-squares techniques, in our case the Levenberg-Marquardt algorithm, and the errors of the best-fit parameters are estimated using the bootstrap method (Press, 1992).

The calibration error of the squared-visibilities is obtained from the fitting procedures, leading to a value of $\Delta V^2 = 0.017$ that corresponds to a 1.7% error for an unresolved source ($V^2 = 1$). Closure phase errors are determined in the previous section (§4.1.4). The statistical weights (or errors) of the radial velocity data are established from the model fitting procedures as well. In particular, we start with initial values and iterate the χ^2 minimization for the primary and the secondary radial velocities until the estimated weights converge. The resulting error for the primary, $1.34\ \mathrm{km\,s^{-1}}$, is larger than that of the secondary, $0.50\ \mathrm{km\,s^{-1}}$, due to the fact that the primary is broad-lined and the secondary is sharp-lined. Fig. 4.7 shows the radial velocity models, plotted versus orbital phase. In the fit we allowed for a possible offset between the primary and secondary velocities that could originate from a template mismatch in the cross-correlations due to the metallic-lined nature of the stars (see §4.1.2). We found a small but statistically significant offset of 0.70 ± 0.13 $\mathrm{km\,s^{-1}}$, which has been accounted for in plotting the secondary velocities. The corresponding best-fit residuals are given in the right panels. It is noticeable that the primary has much larger residuals than the secondary. We searched carefully for the presence of a third star that might be responsible for fluctuations in the orbit. However, neither the spectroscopic or interferometric data, nor the *Hipparcos* data and other available online catalogs (such as 2MASS) indicate any such evidence. Keck aperture masking was also used on this source and no wider companions ($\rho < 0.5''$) were observed at $2\mu m$ (Monnier 2005, private communication). These investigations indicate the absence of a third companion within the detection limits, and even if it exists, it would have negligible influence on the λ Vir orbit. The temperature and luminosity of the primary star are typical of δ Sct variables, which have pulsation periods usually less than 0.3 days. Our velocity sampling is not well suited to discover periodicities as short as this. However, it is unlikely that oscillations of this kind contribute significantly to the velocity residuals we see in Fig. 4. Instead, the pattern suggests a much longer-period variation (quite apparent in the figure, at least between phase 0.0 and 0.5). Indeed, a periodogram analysis of the residuals shows significant power at a period very close to half the orbital period. We believe the source of these residuals is template mismatch, caused by the anomalous abundances of the stars. The primary is more vulnerable to these effects due to its broader lines. The dependence with phase comes from the unavoidable fact that different spectral lines shift in and out of our spectral window as the stars orbit each other.

The preliminary orbital parameters are shown in the third column of Table 4.3. As can be seen in the table, the χ^2_ν of the squared-visibilities and closure phases are still larger than unity. In fact, these large χ^2_νs are due to the systematic bias in the closure phases caused by the bandwidth smearing effect mentioned previously, which tends to change the flux ratio and cannot be eliminated by the new estimated errors. In order to reduce this bias and other uncertainties in the closure phases, we conservatively give small weight to the closure phases in the fit such that the orbital parameters primarily come from the squared-visibilities and the radial velocities. The weight for the closure phases is determined iteratively in the fit until the deweighting of closure phases does not change the flux ratio any more. Fig. 4.8 depicts the best-fit visual orbit of λ Vir, and the final best-fit parameters are listed in the fourth column of Table 4.3. The de-weighting of the closure phases also improved the χ^2_ν of the visibilities, as well as the overall fit. The value of the flux ratio increased a significant amount due to the elimination of the closure phase bias. For reference, we also list the parameters from Stickland (1975) in the table. Due to the measurement uncertainties of Stickland (1975) and the near-equal masses of the two components, the primary and secondary components were reversed, resulting in a 180° difference in ω compared to our value. We have corrected this in Table 4.3.

Table 4.3. Orbital and Binary Parameters of λ Vir.

Parameter	Stickland1975[a]	Preliminary fit[b]	Best Fit[c]
H-band Flux ratio		0.5749 ± 0.0021	0.6055 ± 0.0056
Period (days)	206.64 ± 0.05	206.7323 ± 0.0061	206.7321 ± 0.0040
T_0 (MJD)	40253.1 ± 15.5	53070.28 ± 0.50	53070.30 ± 0.32
Eccentricity	0.079 ± 0.021	0.0603 ± 0.0031	0.0610 ± 0.0036
ω (degrees)	273.3 ± 26.8	272.10 ± 0.71	272.28 ± 0.46
Ω (degrees)		196.57 ± 0.16	196.40 ± 0.22
i (degrees)		109.97 ± 0.15	109.86 ± 0.24
a (mas)		19.768 ± 0.072	19.759 ± 0.079
K_1 (km/s)	29.51 ± 0.89	24.78 ± 0.17	24.78 ± 0.17
K_2 (km/s)	24.85 ± 0.65	27.308 ± 0.067	27.308 ± 0.067
ΔRV (km/s)		-0.69 ±0.13	-0.70 ± 0.13
γ (km/s)	-6.40 ± 0.41	-8.053 ±0.045	-8.053 ± 0.045
f coefficient[d]		3.47 ± 0.18	3.08 ± 0.14
RV χ^2/dof		1.02	1.02
V^2 χ^2/dof		1.40	1.03
CP χ^2/dof		1.21	0.12
Total χ^2/dof		1.21	0.89

[a] Due to measurement uncertainties in Stickland's work the primary and secondary components are reversed, resulting in a value of ω that differs from ours by 180°. This has been corrected in the table.

[b] Preliminary orbit fit using bandwidth smearing corrected V^2 model and re-estimated closure phase errors (see §4.1.6).

[c] Closure phases are de-weighted in the best-fit to eliminate biases and uncertainties, especially those in the flux ratio.

[d] The introduced bandwidth smearing coefficient (see §4.1.3).

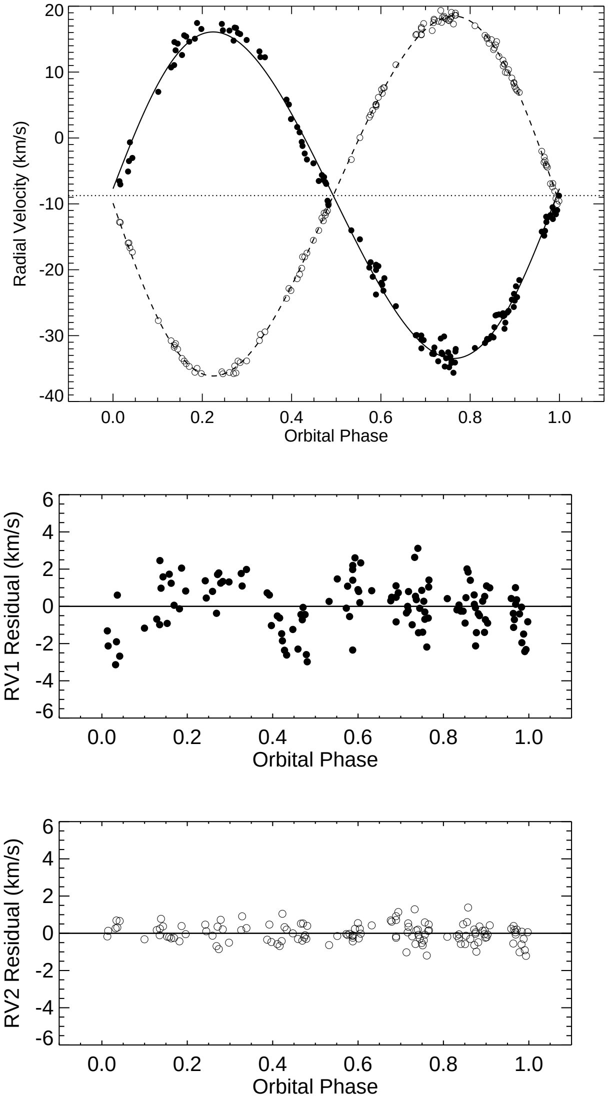

Figure 4.7 Best-fit radial velocity model vs. orbital phase. The data are shown with filled circles for the primary and open circles for the secondary respectively. The best-fit radial velocity curves are also shown (primary: solid line, secondary: dashed line). The dotted line indicates the systemic velocity of the primary. Secondary velocities have been corrected for the offset described in the text. Velocity residuals are given in the right panels. The larger values for the primary are caused by the larger rotational broadening of its spectral lines, and possibly also by template mismatch due to the anomalous abundances (see text).

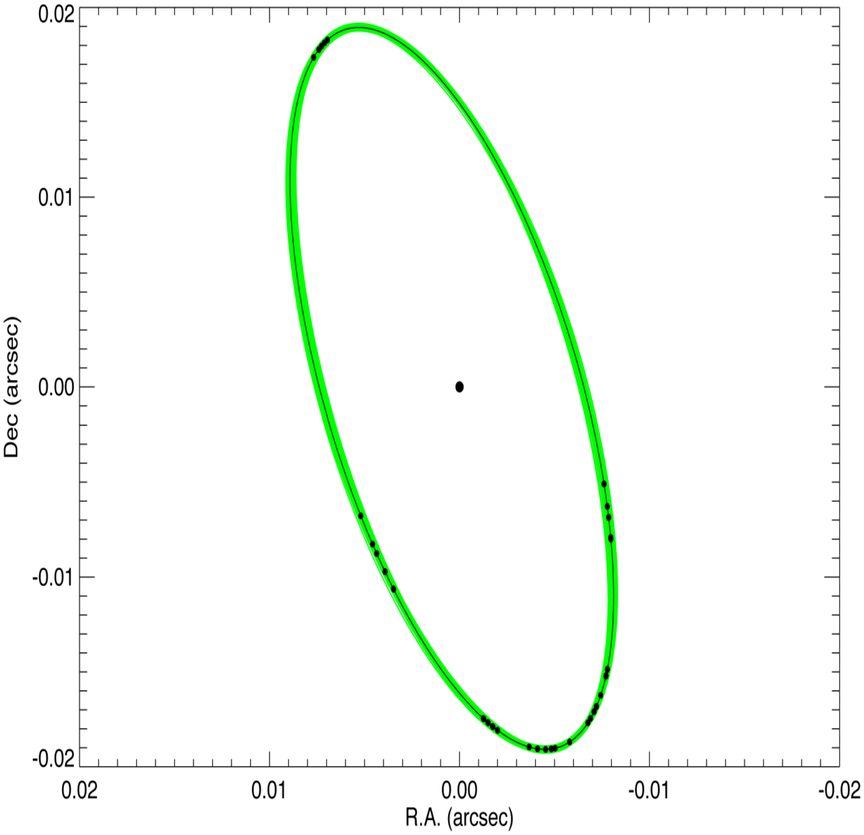

Figure 4.8 The best-fit visual orbit of λ Vir. The primary is shown by the central dot. The solid line indicates the best-fit orbit, and the overplotted filled dots show the epochs of interferometric observations. The shaded area around the orbit indicates the 1-σ uncertainties of the orbit.

4.1.7 Physical parameters

The combination of the astrometric and spectroscopic information provided by our orbital solution yields precise estimates of the absolute masses of the components of λ Vir, with relative errors of only 0.7% for the primary and 1.5% for the secondary. These are listed in Table 4.4 along with other physical parameters described below. We use these in the next section to compare against recent stellar evolution models and assess the evolutionary state of the system.

The system bolometric flux and luminosities are determined through spectral energy distribution (SED) modelling. Zhao et al. (2007) constructed two-component SED models using both Kurucz and Pickles model templates (Kurucz et al., 1974; Pickles, 1998) and applied them to a substantial amount of archive photometric measurements in the Johnson, Strömgren, Geneva and 2MASS systems, as well as spectrophotometric measurements from Breger (1976), Burnashev (1985), and Glushneva et al. (1998). However, the Burnashev (1985) and Glushneva et al. (1998) spectrophotometry are not consistent with photometry at wavelengths longer than 420nm, and the Burnashev (1985) data also have bad normalizations that do not agree with other data. Therefore, we only take the spectrophotometry of Breger (1976) into account in our fitting. The component light ratios determined from spectroscopy and interferometry in §4.1.2 are also used to constrain the models. After extensive tests of model templates, we found that the Pickles templates are not appropriate for λ Vir because of its metallic-lined nature. The Kurucz model with [m/H] = +0.5 best fits the data. Fig. 4.9 depicts the resulting best-fit Kurucz model, as well as the corresponding SEDs for both the primary and the secondary, overplotted with the input flux measurements and the model net flux for corresponding bandpasses. The best-fit model calls for two A1V stars with no need of extinction correction. The resulting system bolometric flux is $3.794 \times 10^{-7} \pm 0.014 \times 10^{-7}$ erg cm^{-2} s^{-1}. With the distance determined below, the luminosities for the primary and the secondary are 20.84 ± 0.25 L$_\odot$ and 12.58 ± 0.16 L$_\odot$ respectively.

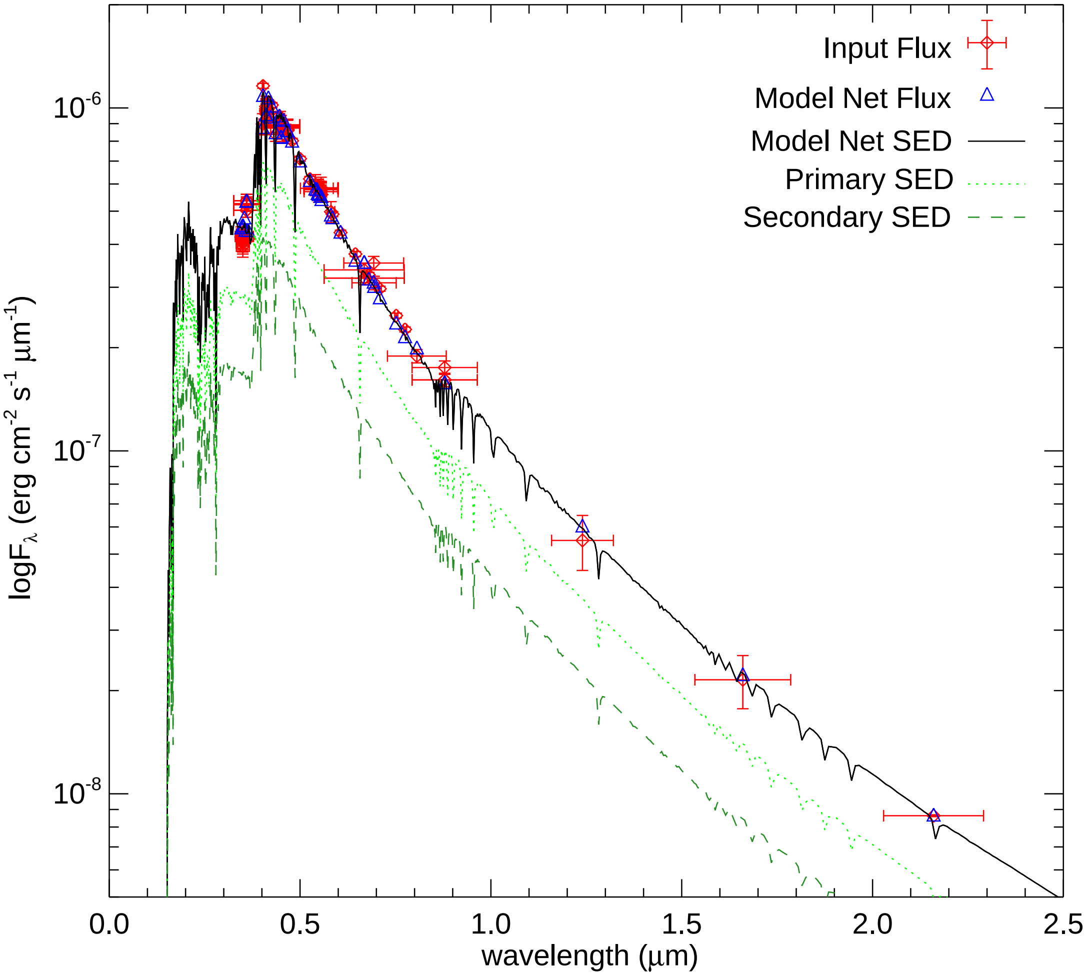

Figure 4.9 SED models of λ Vir. The net SED model is shown by the solid line, overplotted with input flux and the bandpass integrated model flux. The bandpass of input fluxes are shown by the horizontal error-bars. The SED for the primary is shown by the dotted line and the secondary by the dashed line. The models correspond to two A1V stars. (Zhao et al. (2007))

The effective temperature estimates in §4.1.2 are strongly correlated with the metallicity adopted for λ Vir, in the sense that higher metallicities lead to higher temperatures. Consequently, because the composition in the surface layers of λ Vir is enhanced compared to normal A stars, our temperatures are likely to be overestimated. We therefore made use of extensive photometric measurements available for the object in the Johnson, Strömgren, and Geneva systems (Mermilliod et al., 1997) as well as 2MASS, to derive the mean effective temperature based on a large number of color/temperature calibrations (Popper, 1980; Moon & Dworetsky, 1985; Blackwell et al., 1990; Gray, 1992; Napiwotzki et al., 1993; Balona, 1994; Smalley & Dworetsky, 1995; Kunzli et al., 1997; Cox, 2000). In addition we made an estimate by the infrared flux method (Blackwell et al., 1990) based on the bolometric flux determined from the SED, the flux from the 2MASS K_s band, and the corresponding integrated flux from the Kurucz model. The various estimates are in good agreement, showing a scatter of about 120 K and yielding an average of $T_{\rm eff} = 8280 \pm 200$ K, where the uncertainty is a conservative estimate to account also for the possibility of systematics errors in the calibrations. To the extent that the abundance enhancement of the two stars is similar (which appears to be the case, as reported by Stickland, 1975), our spectroscopic analysis in §4.1.2 indicates no significant difference in temperature between the stars. Reddening estimates based on Geneva and Strömgren photometry give negligible values using calibrations by Crawford (1979) and Kunzli et al. (1997), consistent with the relatively close distance to the object.

The orbital parallax of the system is $\pi_{\rm orb} = 18.81 \pm 0.10$ mas, corresponding to a distance of 53.16 ± 0.29 pc. The trigonometric parallax listed in the *Hipparcos* catalog is $\pi_{\rm HIP} = 17.47 \pm 0.94$ mas, which is slightly lower than ours (a 1.4σ or 7% effect) most likely because it does not account for the perturbation from the orbital motion. The original *Hipparcos* observations are available in the form of 'abscissa residuals', which are the one-dimensional residuals (along the scan direction of the satellite) from the usual 5-parameter solutions yielding the position, proper motion, and parallax as reported in the Catalogue (ESA 1997). We have re-reduced these measurements by expanding the model to account for the orbital motion constrained using our own solution, and we have solved for the semimajor axis of the photocenter ($a_{\rm phot}$) as well as corrections to the position and proper motion of the barycenter and a correction to the parallax. The formalism for this solution follows closely that described by van Leeuwen & Evans (1998) and Pourbaix & Jorissen (2000), and a recent example of a similar application is given by Torres (2006). The revised *Hipparcos* parallax we obtain is $\pi'_{\rm HIP} = 18.55 \pm 0.84$ mas, which is now in much better agreement with $\pi_{\rm orb}$ (within 0.3 σ). The motion of the center of light of the binary is clearly detected by *Hipparcos*, albeit with much lower precision than the relative semimajor axis, and amounts to $a_{\rm phot} = 3.84 \pm 0.63$ mas[3].

This value along with the relative semimajor axis and the mass ratio allow us to obtain an independent estimate of the light ratio in the *Hipparcos* passband (H_p), which is $\ell_2/\ell_1 = 0.39 \pm 0.06$. This is significantly lower than the spectroscopic and interferometric value in §4.1.2. There is no evidence from either the spectroscopy or the interferometry of any photometric variability in λ Vir that might explain the

---

[3] For completeness we list here the remaining parameters adjusted in this fit: $\Delta\alpha\cos\delta = -0.19 \pm 0.77$ mas, $\Delta\delta = +0.03 \pm 0.47$ mas, $\Delta\mu_\alpha \cos\delta = +1.48 \pm 0.81$ mas yr^{-1}, and $\Delta\mu_\delta = +0.47 \pm 0.58$ mas yr^{-1}. These should be added with their sign to the catalog values of the position and proper motion to yield the revised values.

difference, in agreement with the small scatter observed in the brightness measurements from *Hipparcos* ($\sigma_{H_p} = 0.006$ mag; Esa, 1997). The small amplitude of the photocentric motion compared to the median error of an individual abscissa residual (2.3 mas) may be cause for some concern about possible systematics in the *Hipparcos* light ratio, although we have no independent evidence for such an effect. On the other hand, in view of the metallic-lined nature of the stars we cannot entirely rule out the possibility of a bias in the spectroscopic value of ℓ_2/ℓ_1 of a similar nature as the effect in the temperatures mentioned above. However, the brightness ratio is a differential measurement and therefore we would not expect the effect to be large. Since both light ratio estimates are close to the visual band and the stars are of similar temperature, for the purpose of the modelling in the next section we have chosen as a compromise to adopt the weighted average of the spectroscopic and *Hipparcos* values. That average is $\ell_2/\ell_1 = 0.56 \pm 0.10$. The larger uncertainty accounts for the individual weights as well as the difference in the values themselves.

The absolute visual magnitudes of the components follow from this value along with the orbital parallax and the apparent system magnitude of $V = 4.52 \pm 0.01$ (Mermilliod et al., 1997), and are included in Table 4.4. Although we have derived a very precise flux ratio in the H band from the interferometric observations, a total H-band magnitude for the system is unavailable (the star is bright enough that it saturated the 2MASS detector), and so the individual magnitudes cannot be computed directly.

Table 4.4. Physical Parameters of λ Vir.

Physical Parameter	Primary Component	Secondary Component
Mass ($M_\odot$)[a]	1.897 ± 0.016	1.721 ± 0.023
π_{orb} (mas)[a]	18.81 ± 0.10	
$\pi'_{\rm HIP}$(mas)[b]	18.55 ± 0.84	
System distance (pc)[a]	53.16 ± 0.29	
Semimajor axis (AU)[c]	1.0504 ± 0.0071	
Visible light ratio	0.56 ± 0.10	
H band flux ratio[c]	0.6055 ± 0.0056	
V Magnitude (mag)	5.003 ± 0.070	5.63 ± 0.12
Bolometric flux (10^{-7} erg cm^{-2} s^{-1})	2.366 ± 0.010	1.428 ± 0.089
Total bolometric flux (10^{-7} erg cm^{-2} s^{-1})	3.794 ± 0.014	
Luminosity ($L_\odot$)	20.84 ± 0.25	12.58 ± 0.16
T_{eff} (K)	8280 ± 200	8280 ± 200
$v \sin i$ (km s^{-1})	36 ± 1	10 ± 2

[a] Parameters that are determined directly from the best-fit orbital parameters.

[b] Revised *Hipparcos* parallax accounting for orbital motion.

[c] From table 4.3

4.1.8 Comparison with stellar evolution models

The accurately measured masses, absolute visual magnitudes, and effective temperatures of the components of λ Vir, as well as the flux ratio in the H band, allow a comparison with current models of stellar evolution. For their ease of use we have chosen here the Yonsei-Yale series of calculations by Yi et al. (2001) and Demarque et al. (2004). The color/temperature transformations and bolometric corrections adopted are those of Lejeune et al. (1998), and the passband of the H filter in those calculations is sufficiently close to that used at IOTA for our purposes. Unfortunately the actual bulk composition of λ Vir is difficult or impossible to determine observationally because of the metallic-lined nature of both stars. Therefore, we have explored a range of interior metallicities in the models to identify the values that are consistent with the observations.

Initially we considered only the masses, absolute magnitudes, and effective temperatures of the two stars as constraints. By interpolation we computed a fine grid of isochrones for a large number of age and metallicity combinations, and compared each model with the 6 measurements under the assumption that the stars are coeval and have the same interior composition. The result is shown in Fig. 4.10, where each filled circle represents an age/metallicity combination that agrees with the observations for both stars within the errors. The best agreement occurs near the center of the region (larger filled circles), at a metallicity near $Z = 0.01$ and an age of about 900 Myr. Next we added the constraint on the flux ratio in H, requiring that in addition to matching the masses, magnitudes, and temperatures, the models reproduce the observed magnitude difference in H. The combinations that also satisfy this last constraint cover a smaller area of the diagram, and are indicated with open circles in Fig. 4.10. The best overall match is achieved for a metallicity of $Z = 0.0097$ (corresponding to [Fe/H] $= -0.29$, assuming no enhancement of the alpha elements) and an age t of 935 Myr, at which the models agree with all observables well within the errors (typically to better than 0.4σ).

The comparison of the masses, absolute magnitudes, and temperatures with the models is shown graphically in Fig. 4.11. The solid lines in the top panel represent evolutionary tracks computed for the exact masses we measured for each star, and the dotted lines indicate the uncertainty associated with the mass errors ($\pm 1\sigma$). The 935-Myr isochrone is shown as a dashed line, and indicates that the components of λ Vir are indeed consistent with having the same age, as expected. Fig. 4.11b shows the best-fit model isochrone and the observations in the mass-luminosity diagram.

The constraint on the flux ratio is illustrated in Fig. 4.12, where we have chosen to represent the predicted magnitude difference from the model (solid line) as a function of the primary mass, with the secondary mass being determined at each point along the curve from the measured mass ratio ($q \equiv M_2/M_1$). The dotted lines represent the uncertainty in the location of this curve ($\pm 1\sigma$) resulting from the error in q. The measurement is in good agreement with the predictions.

The estimated radii of the stars from the best fitting model are $R_1 = 2.35\ \mathrm{R}_\odot$ and $R_2 = 1.84\ \mathrm{R}_\odot$ for the primary and secondary, respectively, and the corresponding angular diameters at the distance of λ Vir are $\phi_1 = 0.41$ mas and $\phi_2 = 0.32$ mas. These are not far from the values adopted for the orbital solution described in §4.1.6. The surface gravities are $\log g_1 = 3.97$ and $\log g_2 = 4.14$, which are close to the value of $\log g = 4.0$ adopted for both components in §4.1.2.

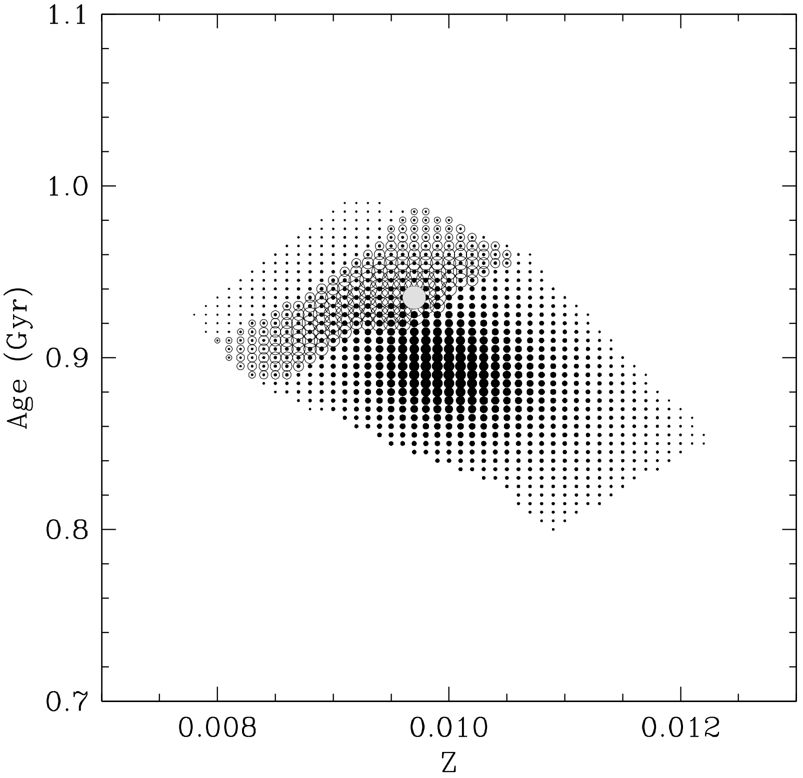

Figure 4.10 Determination of the age and metallicity of λ Vir by comparison with stellar evolution models by Yi et al. (2001) and Demarque et al. (2004). Filled circles show all age/metallicity combinations that yield an isochrone matching the measured values of the mass, effective temperature, and absolute visual magnitude of both stars (assumed to be coeval) within the observational errors (Table 4.4). Larger filled circles indicate a better match. Open circles indicate age/metallicity combinations that in addition satisfy the measured flux ratio in the H band, within its uncertainty. The size of the open circles is again proportional to the goodness of fit. The best overall match to the observations is indicated with the large grey circle, and corresponds to $Z = 0.0097$ (or [Fe/H] $= -0.29$) and an age of 935 Myr. (Zhao et al. (2007))

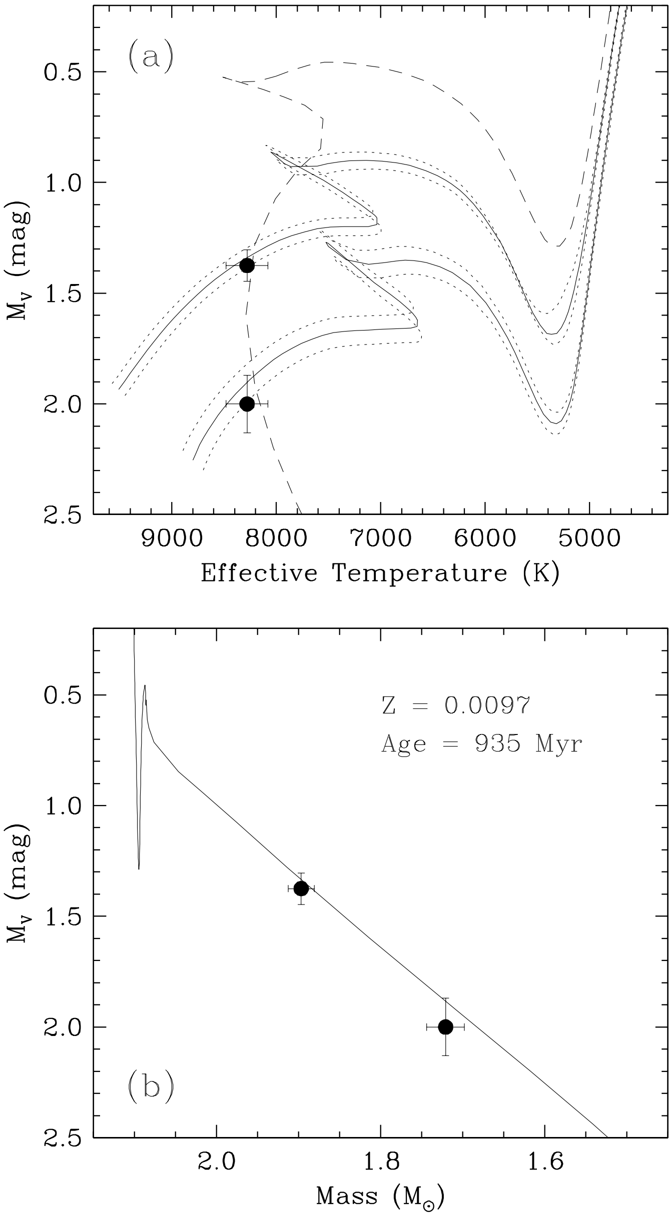

Figure 4.11 Comparison of stellar evolution models. Comparison between the measurements for λ Vir and the best matching stellar evolution models by Yi et al. (2001) and Demarque et al. (2004), for a metallicity of $Z = 0.0097$ (or $[\mathrm{Fe/H}] = -0.29$) and an age of 935 Myr. (a) Evolutionary tracks in the absolute magnitude/effective temperature diagram for the exact masses measured for each star (solid lines). The uncertainty in the location of the tracks stemming from the mass errors ($\pm 1\sigma$) is represented with the dotted lines. The 935-Myr isochrone is shown by the dashed line. (b) Best-fitting isochrone in the mass-luminosity diagram. (Zhao et al. (2007))

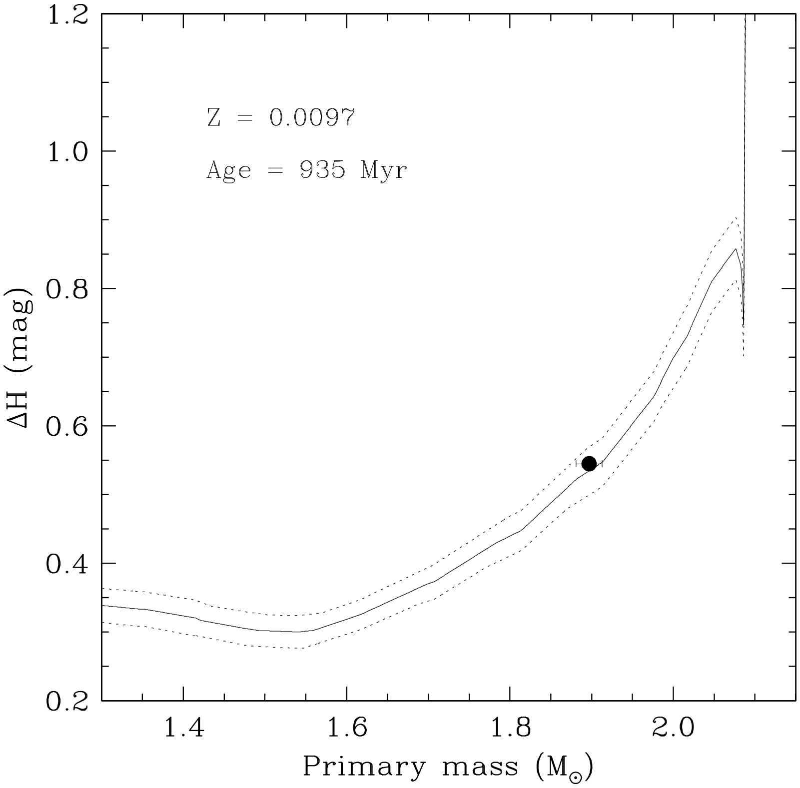

Figure 4.12 Predicted magnitude difference in the H band from the best-fitting model isochrone for λ Vir, compared with our accurate measurement from IOTA (vertical error bar smaller than the size of the point). The solid line is the prediction for the exact mass ratio q we measure. At each point along this line the secondary mass is computed from the primary mass and q, and the magnitude difference read off from the isochrone. The dotted lines represent the uncertainty in the prediction resulting from the error in q. (Zhao et al. (2007))

4.1.9 Summary and conclusion

By combining the interferometric and radial velocity data, we have determined the 3-dimensional orbital of λ Vir to high precision. We studied the effects of bandwidth smearing on squared-visibilities and closure phases. The calibration problems in the closure phases due to these effects are larger than expected, suggesting the necessity of using narrow bandwidth for precision work.

Our precise determination of the λ Vir orbit allows us to study its physical properties accurately. We determined the masses of the two components with accuracies of 0.7% and 1.5% for the primary and the secondary respectively. We studied the SED of λ Vir with archival photometric and spectrophotometric data. The Kurucz model templates with [m/H] = +0.5 fit the data best, yielding a solution with two A1V type stars. The temperatures of the system are derived from various methods, leading to a value of 8280±200 K for both stars. Other properties of λ Vir, such as distance, bolometric flux, luminosity, radii, motion of the photocenter, are also determined. The accurately determined properties allow a comparison with current stellar evolution models. The model that matches best yields a subsolar metallicity of $Z = 0.0097$ and an age of 935 Myr, indicating the evolution of λ Vir is similar to normal A stars despite their surface abundance anomalies.

The origin of the abundance anomalies of Am stars has been a puzzle for a quite some time. It is widely believed that when stars are slow rotators, atomic diffusion will play an important role in the outer convection zones, causing abnormal abundances and therefore the Am phenomenon. However, different views have also been presented (Böhm-Vitense, 2006). Although Am stars have been studied intensively, only a few of them have well determined properties. With its accurately determined physical properties and well known evolution status, as well as its possibly differing rotation rates (which may lead to different diffusion efficiencies), λ Vir is an ideal candidate for follow up studies such as detailed abundance analyses and atomic diffusion modelling that can shed light on our understanding of the causes of the Am phenomenon.

4.2 The interacting and eclipsing binary β Lyrae

4.2.1 Introduction

Interacting binaries are unique testbeds for many important astrophysical processes, such as mass and momentum transfer, accretion, tidal interaction, etc. These processes provide information on the evolution and properties of many types of objects, including low-mass black holes and neutron stars (in low-mass X-ray binaries), symbiotic binaries, cataclysmic variables, novae, etc. Although these types of objects are widely studied by indirect methods such as spectroscopy, radial velocity, and sometimes eclipse mapping, very few of them have been directly resolved because they are very close to each other and far away from us. Thus, directly imaging interacting binaries, although very challenging, will undoubtedly help us to improve our understanding of these objects.

The star β Lyrae (Sheliak, HD 174638, HR 7106, $V = 3.52$, H=3.35) is a well known interacting and eclipsing binary that has been widely studied since its discovery in 1784 (Goodricke, 1785). According to the current picture (Harmanec, 2002), the system consists of a B6-8 II Roche-lobe filling mass-losing star, which is generally denoted as the donor or the primary, and an early B type mass-gaining star that is generally denoted as the gainer or the secondary. The donor, which was initially more massive than the gainer, has a current mass of about 3 $M_{\odot}$, while the gainer has a mass of about 13 $M_{\odot}$. The artist's view of the system is shown in Figure 4.13. It is thought that the gainer is completely embedded in a thick accretion disk with bipolar jet-like structures perpendicular to the disk, which creates a light-scattering halo above its poles. The orbit of the system is highly circular (Harmanec & Scholz, 1993), and is very close to edge-on (Linnell, 2000). Recent RV study on the ephemeris of the system gives a period of $12.^{d}94$ (Ak et al., 2007). The period is increasing at a rate of ~ 19 sec per year due to the high mass transfer rate, $2 \times 10^{-5} \mathrm{M}_{\odot}\ \mathrm{yr}^{-1}$, of the system.

The primary eclipse of the light curve (i.e., at phase 0) corresponds to the eclipse of the donor. In the *UBV* bands, the surface of the donor is brighter than that of the gainer, and therefore the primary minimum is deeper than the secondary minimum. At longer wavelengths, however, the studies of Jameson & Longmore (1976) and Zeilik et al. (1982) suggest that the relative depth of the secondary minimum in the light curve gradually deepens and becomes deeper than the primary minimum at wavelengths longer than $3.6\mu m$.

Light curve studies and theoretical models have shown that, at the distance of 296pc (van Leeuwen, 2007), the estimated separation of the binary is only 0.92 milliarcsecond (hereafter *mas*, $58.5\,\mathrm{R}_{\odot}$). The angular diameter of the donor is $\sim$0.46 mas ($29.4\,\mathrm{R}_{\odot}$), and the disk surrounding the gainer is only ~ 1 mas across (e.g., Linnell, 2000; Harmanec, 2002). The goal of directly imaging β Lyr, therefore, requires the angular resolution only achievable by today's long-baseline interferometers. Recently, Schmitt et al. (2008) used the NPOI interferometer to image successfully the Hα emission of β Lyr, an update to the pioneering work of Harmanec et al. (1996). Also, radio work using MERLIN found a nebula surrounding the secondary but could not resolve its bipolar shape (Umana et al., 2000). Despite recent progress, the individual objects of the system have not been resolved yet, putting even a simple astrometric

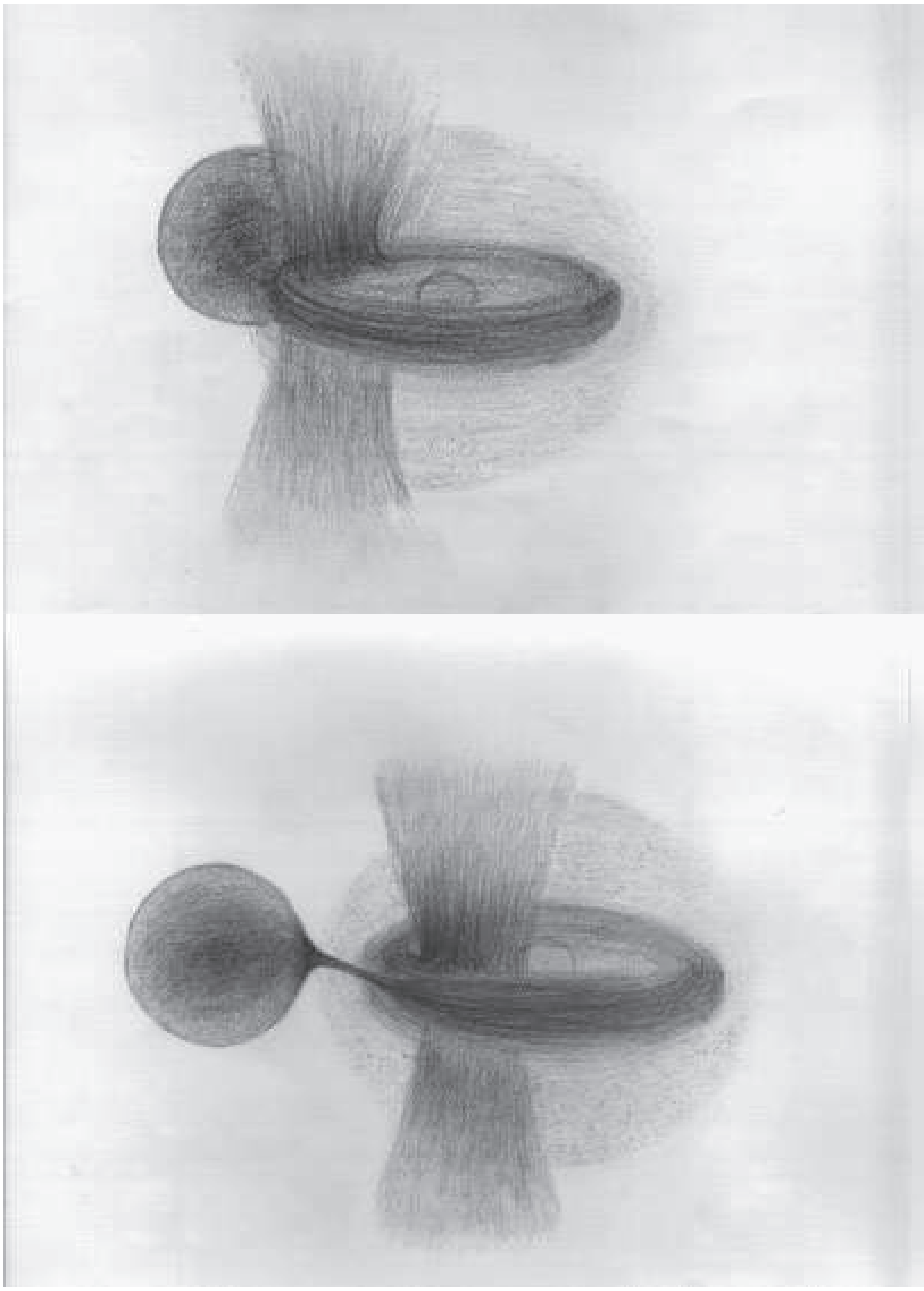

Figure 4.13 Artist's view of the probable appearance of β Lyr system with various components of its circumstellar matter: gas stream, accretion disk, jet-like structures and scattering halo/stellar wind above the polar regions of the mass-accreting star. A view at elongation and at a phase shortly after the primary mid-eclipse are shown. All relative dimensions are drawn in scale. The position of the massaccreting star is indicated, although the star is in fact hidden from view inside the disk (Figure from Harmanec (2002))

orbit beyond our reach.

In this study, we present the first resolved images of the β Lyr system at multiple phases, obtained with the CHARA Array and the MIRC combiner. We give a brief introduction to our observations and data reduction in §4.2.2. We present our aperture synthesis images with simple models in §4.2.3. In §4.2.4 we discuss our astrometric orbit of β Lyr and we give the outlook for future work in §4.2.5.

4.2.2 Observations and data reduction

Our observations were conducted at the Georgia State University (GSU) Center for High Angular Resolution Astronomy (CHARA) interferometer array along with the MIRC instrument. More details about CHARA and MIRC can be found in §2.6.1 and §2.6.2. We observed β Lyr on 6 nights in 2006 and 2007 using an array configuration optimized for good imaging (equal Fourier coverage in all directions) and following standard observing procedures (Monnier et al., 2007, M. Zhao et al. 2009, in press). A typical baseline coverage of our observations is shown in Figure 4.14. In short, we observed our target along with two or three calibrators on each night and a complete observing log is listed in Table 4.5.

The data reduction process follows the pipeline outlined by Monnier et al. (2007). In brief, after frame co-adding, background subtraction and Fourier transform of the raw data, fringe amplitudes and phases are used to form squared-visibilities and triple products. Photometric calibrations are estimated using shutter matrix measurements and partial beam chopping. Finally, calibrators with known sizes (see Table 4.5) are used to calibrate the drifts in overall system response before obtaining final calibrated

Table 4.5. Observation logs for β Lyr

Date (UT)	Mean MJD	Telescopes	N$_{blk}$	Calibrators
2006Oct16	54024.17	W1-W2-S2-E2	1	29 Peg, υ And
2007Jul03	54284.25	W1-W2-S1-E1	3	γ Lyr, υ Peg, υ And
2007Jul04	54285.26	W1-W2-S1-E1	3	γ Lyr, υ Peg, υ And
2007Jul07	54288.22	W1-W2-S1-E1	3	γ Lyr, υ Peg, σ Cyg
2007Jul09	54290.25	W1-W2-S1-E1	3	γ Lyr, υ Peg
2007Jul12	54293.26	W1-W2-S1-E1	3	γ Lyr, σ Cyg

[a] N$_{blk}$: number of data blocks

[b] Calibrator Diameters (milli-arcsec): 29 Peg = 1.017 ± 0.027, υ And = 1.098 ± 0.007 , σ Cyg = 0.542 ± 0.021 (A. Merand 2008, private communication); γ Lyr = 0.74 ±0.10 (Leggett et al., 1986); υ Peg = 1.01 ± 0.04 (Blackwell & Lynas-Gray, 1994)

squared-visibilites and complex triple amplitudes.

4.2.3 Synthesis imaging and modeling

For imaging with optical interferometry data, we employed two independent applications: "Markov-Chain Imager for Optical Interferometry (MACIM)" (Ireland et al., 2006) and the Maximum-Entropy-based BSMEM (Buscher, 1994). Further description and a detailed comparison of these algorithms on simulated data appear in Lawson et al. (2004, 2006). Both of these algorithms benefit from use of prior information, generally based on lower resolution data. For β Lyr we began each image reconstruction with a two-component Gaussian model which mainly acts to limit the field-of-view of the image. The final images do not resemble the priors except in general extent, i.e., the final positions, relative sizes, and relative brightnesses are not dependent on the priors. The final reconstructed images from both methods are shown in Figure 4.15. The MACIM and BSMEM images are consistent with each other, although they use very different algorithms, giving confidence to the image

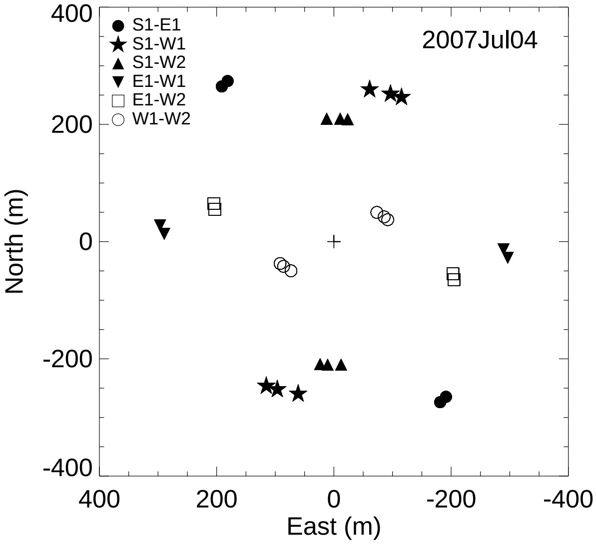

Figure 4.14 Telescope spatial coverage of β Lyr on UT 2007Jul04, using the W1-W2-S1-E1 configuration of CHARA. The symbols stand for different baselines. The longest projected baseline in this observation is 328.5m, corresponding to a resolution of 0.52 milli-arcseconds in the H band. The actual UV coverage is similar to this spatial coverage but each point spreads over 8 wavelength channels.

fidelity. Any differences, such as the more Gaussian shapes for BSMEM compared to the more "flat-top" profiles for MACIM, illustrate the limitations of our dataset. We present here results from both algorithms in lieu of image "error bars" which are notoriously difficult to define in aperture synthesis imaging.

The six epochs span all phases of the orbit, changing from middle primary eclipse (phase=0.035) to nearly maximum elongation (phase=0.210 and 0.828), and secondary eclipse (phase=0.438). The system is well resolved into two separate components at phases close to the maximum elongation. Since the primary eclipse is still the deeper one in the H-band (Jameson & Longmore 1976), we can conclude that the object with higher surface brightness is the mass donor star (i.e., the component moving from left to right in the 2007 July sequence). The donor is partially resolved and appears elongated at all epochs except at phase 0.035 when it is blocked by the disk, directly confirming its Roche-lobe filling picture. The thick disk surrounding the gainer is also resolved and appears elongated. At the first epoch (phase = 0.035), we see mostly the emission from the disk superposed with a small amount of light from the poles of the donor.

We can extract further information by constructing a simple two-component model to determine the separation and position angle for each epoch. We assume the donor and gainer can be modeled as uniform ellipses. Other models, such as two truncated gaussian ellipses, a rain-drop-shaped Roche-lobe filling star with a truncated gaussian disk, etc., were also considered and gave equivalent results due to limited resolution. Therefore, for simplicity and to minimize the degrees of freedom of the model, uniform ellipses are adopted. The free parameters in the models are: the semi-major and semi-minor axes of the two components, their individual position angles, the separation and position angle of the system, and the flux ratio of the donor and the disk. We used ephemeris data from Ak et al. (2007) to fix which component was in front during modeling. Due to degeneracies in the separation and the dimensions of the blocked component when the two are overlapping with each other, the size of the blocked component is fixed to the average from the two separated epochs, 2007Jul04 and 2007Jul12. The best-fit models for all epochs are presented in the third column of Figure 4.15 and the resulting positions and total flux ratios from the models are listed in Table 4.6, along with the results obtained from the image centroids where separating the two components is possible. Errors of the positions are estimated from the χ^2 surfaces of each parameter where $\Delta\chi^2 = 1$, or from the scatter in fits within each night, whichever is bigger.

The models confirm that the smaller and more circular component, i.e., the donor, has higher surface brightness and total flux than the more elongated disk around the gainer. The ellipse size of the donor from the models, when averaged over all the epochs, is 0.62 ± 0.16 mas along the major axis, and 0.52 ± 0.14 mas along the minor axis, which confirmed the images that the donor is elongated, but slightly larger than that from the theoretical models (Harmanec, 2002). The averaged size of the disk surrounding the gainer is 1.04 ± 0.11 mas along the major axis, consistent with the size of the images of the first epoch as well as theoretical models (Harmanec, 2002) and the Hα disk of Schmitt et al. (2008). The minor axis of the disk is 0.63 ± 0.07 mas, larger than that expected in theoretical models (Bisikalo et al., 2000; Linnell, 2000), implying this extended structure is perhaps from the electron scattering and/or free-free emission from the halo above the poles of the gainer (Jameson & Longmore, 1976; Zeilik et al., 1982).

We also compared the flux ratios from our models with those obtained from H band light curves. The light curves from literatures[4] give a value of $\frac{f_1+f2}{f_p} = 1.86$, where f_1, f_2 and f_p are the fluxes of the donor, the disk of the gainer and the flux at the primary eclipse. Because the donor is not completely eclipsed by the disk at primary eclipse (Linnell, 2000), $f_p = f_2 + af_1$, where a is the fraction of the donor flux that goes through. Therefore we can infer that $\frac{f_1}{f_2} > 0.86$, consistent with our flux ratios derived from the models at phase 0.210 and 0.828, i.e., 1.16 and 1.32.

---

[4] The light curve of Zeilik et al. (1982) at the H band gives a -0.61 mag difference between the total magnitude of the system and the magnitude at primary eclipse. Interpolating the J and K band light curves of Jameson & Longmore (1976) we can obtain an H band magnitude difference of -0.74. Taking the average of the two we get a difference of 0.675 mag, corresponding to a $\frac{f_1+f_2}{f_p}$ value of 1.86.

Table 4.6. Orbital positions of β Lyr

		MACIM		BSMEM		Model		
Date	Phase	Sep. (mas)	P.A. (deg)	Sep. (mas)	P.A. (deg)	Sep. (mas)	P.A. (deg)	Flux ratio (donor/gainer)
2007Jul03	0.132	0.811	255.4	0.853	253.7	0.701 ± 0.091	256.3 ± 4.0	1.01 ± 0.11
2007Jul04	0.210	0.891	253.3	0.886	254.4	0.852 ± 0.045	254.2 ± 2.1	$1.16^{+0.20}_{-0.15}$
2007Jul07	0.438	–	–	–	–	0.338 ± 0.105	250.8 ± 7.3	3.51 ± 1.27
2007Jul09	0.595	–	–	0.675	73.9	0.454 ± 0.042	77.9 ± 1.4	2.43 ± 0.28
2007Jul12	0.828	0.842	72.3	0.783	69.6	0.754 ± 0.063	73.2 ± 0.8	$1.32^{+0.67}_{-0.27}$

[a] Some positions are omitted for images whose centroids cannot be separated.

In addition, taking the average of the two values, $\frac{f_1}{f_2} = 1.24$, we get $a = 0.165$, suggesting that 16.5% of flux from the donor goes through at the primary eclipse. This also implies that the donor contributes $\sim$ 17% of total flux at the primary eclipses, consistent with the 20% value of Linnell (2000).

The goodness of fit of the models (included in each panel of Figure 4.15) are in general similar to that of the images. Nevertheless, discrepancies exist between the models and the images. For instance, the components' separations from the models are slightly smaller than the images. The gainer disk appears bigger in the models than in the images. These properties demonstrate the complexity of β Lyr and suggest that the disk may be asymmetric. They also highlight the deficiencies in our models and underscore the need for a self-consistent model that treats the radiative transfer properly and accounts for all epochs simultaneously.

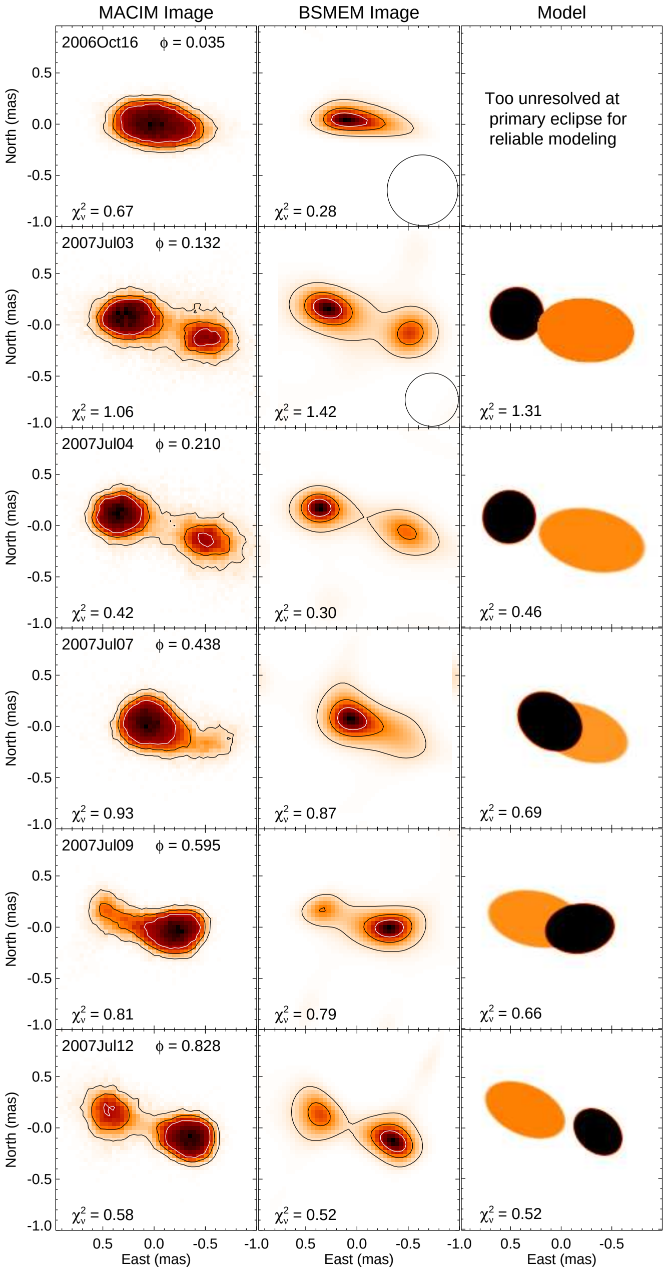

Figure 4.15 Reconstructed images and two-component models of β Lyr . The left, middle and right columns show the MACIM, BSMEM and model images respectively. Darker colors indicate higher intensity. The darker component is the donor. The contours in the images correspond to 0.3, 0.6, 0.9 of the peak intensity. Observing dates and corresponding phases (from the ephemeris in Ak et al. 2007) are labeled in the first column. The best-fit χ^2/DOF of each image is labeled in the bottom left corner. The resolution of the reconstructed images is 0.69 mas for the first epoch and 0.52 mas for the other 5 epochs, and the corresponding beams are shown in the first and second epochs in the middle panels respectively. Due to lack of enough resolution and the complexity of the radiative transfer at the first epoch when the star is behind the disk, no reliable model is available for our limited data.

4.2.4 The orbit of β Lyr

Despite the deficiencies in our simplified models, the positions of each component's center of light are well-constrained, especially near the maximum elongation of the orbit. Thus, the above results, along with the elements obtained from RV and light curve studies allow us to calculate the astrometric orbit of β Lyr for the first time. We adopt $P = 12.^d9414$ and $T_{mini} = JD2454283.0430$ (on 2007Jul01) from the recent ephemeris[5] (Ak et al., 2007), and $e = 0$ (Harmanec, 2002). The best-fit orbit using the model positions is shown in Figure 4.16. The resultant inclination, position angle of the ascending node (Ω) and semi-major axis are listed in Table 4.7. Other orbital solutions using positions from the images are also listed in the table. Errors of orbital elements are estimated using Monte-Carlo simulations. The 3 sets of inclination and Ω in Table 4.7 are consistent with each other and suggest a retrograde orbit (i.e., position angle decreasing with time). Our estimate on Ω is roughly consistent with the 248.8^o value in Schmitt et al. (2008), and is almost perpendicular to the orientation of the jet (163.5^o) implied by Hoffman et al. (1998).

We can also estimate the distance of β Lyr using orbital parallax (see Table 4.7) by combining its angular semi-major axis with the linear $a \sin i$ value, $57.87 \pm 0.62\,R_\odot$[6]. The distance from our models, 314±17 pc, is larger than that from the images, 278±24 pc and 274±34 pc, but they are all consistent within errors with the *Hipparcos*

---

[5] T_{mini} (phase 0) is the epoch of primary minimum light.

[6] We obtain the semimajor axis by combining the semiamplitude of the gainer K_1 (41.4 ± 1.3 km s^{-1}, Harmanec & Scholz 1993; 42.1 ± 1.3 km s^{-1} [error assumed], Bisikalo et al. 2000; 35.4 ± 2.7 km s^{-1} [from their Fig. 5], Ak et al. 2007; yielding a weighted average of 41.1 ± 2.7 km s^{-1}) with that for the donor K_2 (185.27 ± 0.20 km s^{-1}, Ak et al. 2007). We derive $q = M_2/M_1 = 0.222 \pm 0.013, a \sin i = 57.87 \pm 0.62\,R_\odot$, $M_1 \sin^3 i = 12.73 \pm 0.27\ M_\odot$, and $M_2 \sin^3 i = 2.82 \pm 0.18\ M_\odot$

Table 4.7. Parameters of β Lyr

	MACIM	BSMEM	Model
Inclination (deg)	92.10 ± 1.24	91.96 ± 1.65	92.25 ± 0.82
Ω (deg)	253.22 ± 1.97	251.87 ± 1.83	254.39 ± 0.83
semi-major axis (mas)	0.976 ± 0.083	0.993 ± 0.122	0.865 ± 0.048
Distance (pc)	276 ± 23	271 ± 33	312 ± 17

distance, 296±16 pc (van Leeuwen, 2007). Finally, using the newly estimated $M \sin^3 i$ for both components (see footnote 6) together with the inclination from the models, we get mass of the gainer = $12.76 \pm 0.27 \mathrm{M}_\odot$ and mass of the donor= $2.83 \pm 0.18 \mathrm{M}_\odot$.

4.2.5 Future work

We have only presented simple two-component models in this work since we mostly focus on the orbital positions of β Lyr. We have already discussed problematic discrepancies between the models and the images and also some internal inconsistencies between the model epochs. The systematic difference in component separations between the images compared to the model fits poses the most severe problem, limiting the accuracy of our distance estimates to $\sim 15\%$. To address these issues and better understand other physical properties of β Lyrae, a more physical, self-consistent model is required that treats the radiative transfer and the sizes of the two components properly, accounts for all epochs simultaneously, and incorporates the multi-wavelength information from eclipsing light curves.

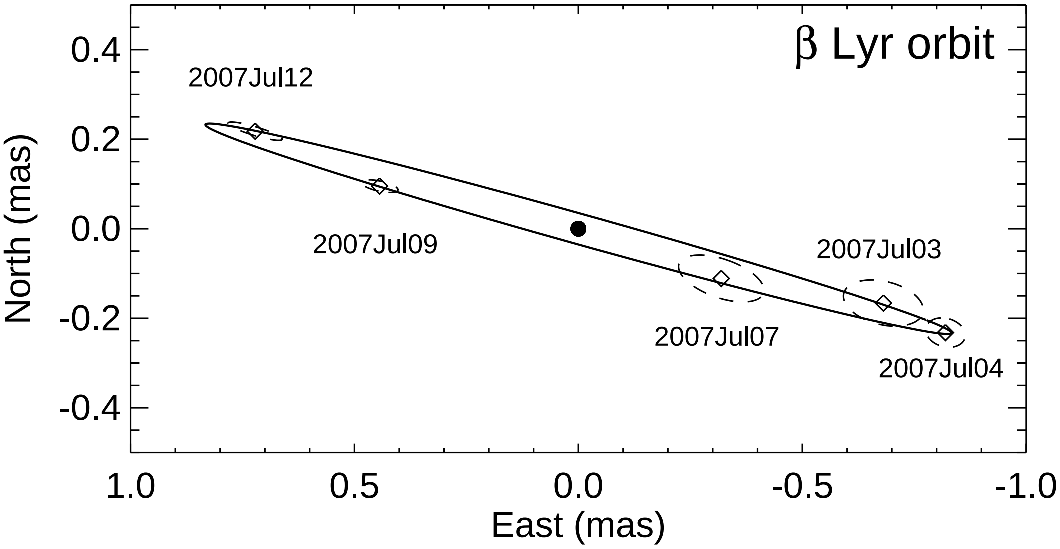

Figure 4.16 The best fit relative orbit of β Lyr (*solid line*). The donor is indicated as a filled dot in the center. Positions of each epoch are shown by the open dots, surrounded by their error ellipses in dashed lines. The upper part of the ellipse is located towards the observer.

Chapter 5

Hot Jupiters

Abstract:[1] Direct detection of light from hot Jupiters has recently been achieved by measurements from the Spitzer Space Telescope, the Hubble Space Telescope, and ground-based telescopes, opening the era of characterizing exoplanetary atmospheres. Most of the detections, however, are for transiting hot Jupiters, and information on non-transiting hot Jupiters are still not enough to break model degeneracies and provide detailed conclusions. More detections that can measure the astrometric orbits and flux variations of non-transiting hot Jupiters, especially in the near-IR, are necessary. One promising way to reach this goal is to use precision closure phase measurements obtained with ground-based long baseline optical interferometers. We present our preliminary closure phase studies toward detecting nearby hot Jupiter systems using CHARA-MIRC, including closure phase simulations and test observations. Our preliminary observations show that we can reach $\sim 0.4\sigma$ and $\sim 0.6\sigma$ of the required signal levels for detections for the short and long triangles of CHARA respectively, the best precision of closure phases to date. We conduct closure phase studies to improve our calibration, and test our new calibration and data analysis schemes on the high contrast binary ϵ Per. Several other improvements are also

---

[1] This chapter is partly based on (Zhao et al., 2008)

being employed to increase the signal-to-noise of observations. With all these improvements, our goal of directly detecting light from hot Jupiters will be feasible to achieve.

5.1 Introduction

The discovery of a planet around a nearby star 51 Peg in 1995 opened a window into new worlds outside the solar system (Mayor & Queloz 1995). Since then, more than 350[2] so-called exoplanets have been discovered, revolutionizing our knowledge of the nature and origin of them. Among those discovered planets, the vast majority of them were detected by indirect methods such as radial velocity (RV) and transit. The RV method detects the tiny wobble of the host star caused by its orbiting planets through spectroscopy, while the transit method detects the dip of the light curve of the host star caused by its planet passing in front of it. Only a few systems were discovered by other methods, including microlensing (e.g., Bond et al., 2004), pulsar timing (e.g., Peale, 1994), and direct imaging (e.g., Kalas et al., 2008). During the past 3 years, the Spitzer Space Telescope, the Hubble Space Telescope, and several ground-based telescopes have made breakthrough and directly detected light from ~10 transiting exoplanets at their secondary transits (Deming et al., 2005, 2006; Charbonneau et al., 2005; Harrington et al., 2006; Knutson et al., 2007b, 2008; Harrington et al., 2007; Swain et al., 2008; Sing & López-Morales, 2009; de Mooij & Snellen, 2009), opening the era of exoplanet spectroscopy and characterization of exoplanetary atmospheres. Most recently, a planet orbiting an early type A star with

---

[2] Data from The Extrasolar Planets Encyclopaedi: http://exoplanet.eu

a debris disk, Fomalhaut, was directly imaged by the Hubble Space Telescope (Kalas et al., 2008), and a system with 3 planets, HR 8799, was imaged by Gemini and Keck (Marois et al., 2008), setting a milestone for direct imaging .

To characterize and understand the structures and atmospheres of exoplanets, the most direct way is to detect their thermal emission. However, this is a very challenging task because of the planets' close angular distances and extremely high brightness contrast to their host stars. Since RV and transit can only detect planets with periods shorter than ∼10 years, our knowledge of planets are mostly limited to the inner part of those systems. Due to this bias, a large population of the discovered planets are close-in (< 0.1AU) giant planets with masses similar to that of Jupiter. Because of their close-in orbit, these planets generally have temperatures higher than 1000K, and are thus also known as "hot Jupiters". Hot Jupiters are best suited for direct detection and characterization because of their relatively high brightness ratios to their host stars at convenient bands (e.g., J, H, K, and mid-infrared), and also because of their well-studied atmospheric models. Theoretical models have predicted many features in the atmospheres of hot Jupiters. They are predicted to have molecular bands such as H_2O, CO, CO_2, and CH_4. Clouds are also predicted to exist at high altitude of these planets. These clouds can absorb shorter wavelength radiation from deeper layers of the atmospheres and re-emit the energy in longer wavelengths, turning some near-IR emission into absorption, which is thus also known as "thermal inversion" (Burrows et al., 2005; Burrows et al., 2008). In addition, due to their close-in orbits, hot Jupiters are tidally locked to their host stars, leading to a constant day side that experiences intense stellar irradiation and a cold night side that remains in perpetual shadow (Guillot et al., 1996). Theoretical models show that the temperature difference between the day and night sides can be very high, which can induce atmospheric circulation and strong zonal winds to redistribute heat from the day side to the night side.

Many of these features have already been confirmed by recent detections of thermal emission at secondary transit using the Spitzer Space Telescope and the Hubble Space Telescope. For instance, emitted spectra at secondary eclipse have shown the presence of water, carbon dioxide, and carbon monoxide (e.g., Grillmair et al. 2007, Richardson et al. 2007, Swain et al. 2008, Charbonneau et al. 2008). Recent light curve study of the hot Jupiter HD 189733b at 8 μm have demonstrated temperature variation between the day and night sides and found that the hottest region lies 30^o east of the substellar point, indicating clear evidence for strong winds in the atmosphere (Knutson et al., 2007b). Studies have also suggested the existence of hot stratosphere and thermal inversion on the dayside of some hot Jupiters (e.g., HD 209458b and HD 149026b), while other planets such as HD 189733b (Charbonneau et al., 2008; Grillmair et al., 2008) do not have such a layer, implying fundamental atmospheric differences between these planets and have led to sub-classification of hot Jupiters (Burrows et al. 2008, Fortney et al. 2008).

Although recent secondary transit detections have been amazingly successful in characterizing hot Jupiters, they still have some limitations. Transiting light curve measurement can constrain the inclination of a planet. When combined with RV data, it can determine a planet's most fundamental property - mass. However, without transit, determining the masses of hot Jupiters are much more difficult due to the degeneracy of $M\sin i$. Also, while transit provides an extremely powerful tool to directly study the atmosphere of hot Jupiters without spatially resolving the planetary system, it is more difficult to separate the light of a non-transiting hot Jupiter for a direct detection. Although there are so far two direct detections of the day-and-night flux variation of non-transiting hot Jupiters by the Spitzer telescope (Harrington et al. 2006, Cowan et al. 2006), the lack of absolute flux calibration in those detections still leaves many model degeneracies (Burrows et al. 2008). In addition, the Spitzer measurements of non-transiting hot Jupiters are all limited to mid-IR, while many important molecular feathers (such as H_2O, CO and CO_2) and the bulk of hot Jupiter's energy exist in the near-IR. Without information in these shorter wavelengths, our understanding of these hot Jupiters are very limited and we cannot estimate the global energy budget of them to see whether they have internal source of heat or not, just as the cases of the giant planets in our solar system. Furthermore, although there are more than 50 transiting planets discovered to date, non-transiting hot Jupiters are still the majority of the hot Jupiter population. Thus, characterizing non-transiting planets is also of great importance for a thorough understanding of hot Jupiters. In order to solve these problems, we require a technique that can resolve the planetary systems ($\sim$3 milliarcsec) while providing high contrast measurements ($>10^4$:1) in the near-IR. Precision closure phase from ground-based long baseline interferometers are extremely well suited for this purpose.

In this chapter we report our studies toward direct detection of hot Jupiters using precision closure phase measurement. In §5.2 we give a brief introduction of our method. We list our best candidates in §5.3, and simulate closure phases and differential closure phases for them in §5.4. We talk about our observations of υ And and present preliminary study of our data in §5.5. We present our closure phase calibration study in §5.6 and report our preliminary results of the test binary ϵ Per in §5.7. Finally, we conclude and discuss the future work in §5.8.

5.2 Precision closure phases, differential closure phases, and differential phases

Among the methods used to detect light from hot Jupiters, a promising way is to use ground-based long baseline optical/IR interferometers along with precision closure phase measurements. This method is very well studied and have been widely applied to modern optical/IR interferometers (see, e.g., Segransan et al., 2000; Joergens & Quirrenbach, 2004; Monnier, 2003).

As we have already mentioned in §2.3, closure phase is immune to any phase shifts induced by the atmosphere as well as many other systematic errors. Hence it is a good quantity for stable and precise measurements (Monnier, 2003). Closure phase is very sensitive to asymmetric structures and can sense the structures of star-planet systems as analogs of high-contrast binaries. The detection of closure phase of a hot Jupiter will not only allow us to extract the planet-to-star flux ratio, but also allow us to determine their full orbital parameters, including the inclination angle which can help us to estimate the mass of a planet when combined with RV, and to break other model degeneracies such as the heat re-distribution factor (Burrows et al., 2008).

Another interferometric method of detecting hot Jupiters is to use differential closure phase, i.e., the difference between closure phases at two different wavelengths. Hot Jupiters and their host stars' brightness contrast varies at different wavelengths (Sudarsky et al., 2003; Burrows et al., 2008) (see Figure 5.1). The difference between two wavelengths can cause a slight shift to the system's photo-center, inducing a phase shift to the observed fringes and closure phases (e.g., Vasisht & Colavita, 2004). Since closure phases are usually obtained at multiple wavelengths simultaneously, such as those from the 8 channels of MIRC (see §2.6.2), the calibration may benefit from the differential measurement of two wavelength channels since they may be stable to systematic errors such as drifts of the optics. Therefore, differential closure phase is also potentially a very stable quantity for precision measurements. In addition, the difference between two wavelengths may also boost the closure phase signal in some cases as shown later in §5.4, making the detection easier to achieve.

Based on the same principle of differential closure phase, we can also apply differential measurement for the phase from two telescopes at different wavelengths, which is also known as the differential phase. Differential phase is also immune to the atmospheric turbulence because even though the individual phases are corrupted by the atmospheric turbulence, the turbulence changes the phases in the same way for different wavelengths and can thus be eliminated by the differential measurement. Differential phase can also yield the flux ratio and orbital parameters of hot Jupiter systems and, in addition, also provides valuable spectral information about the planet atmospheres. Furthermore, because differential phase can be added together coherently, it may be relatively easier to get better signal-to-noise than closure phase. Therefore, differential phase is also a potential quantity for characterization

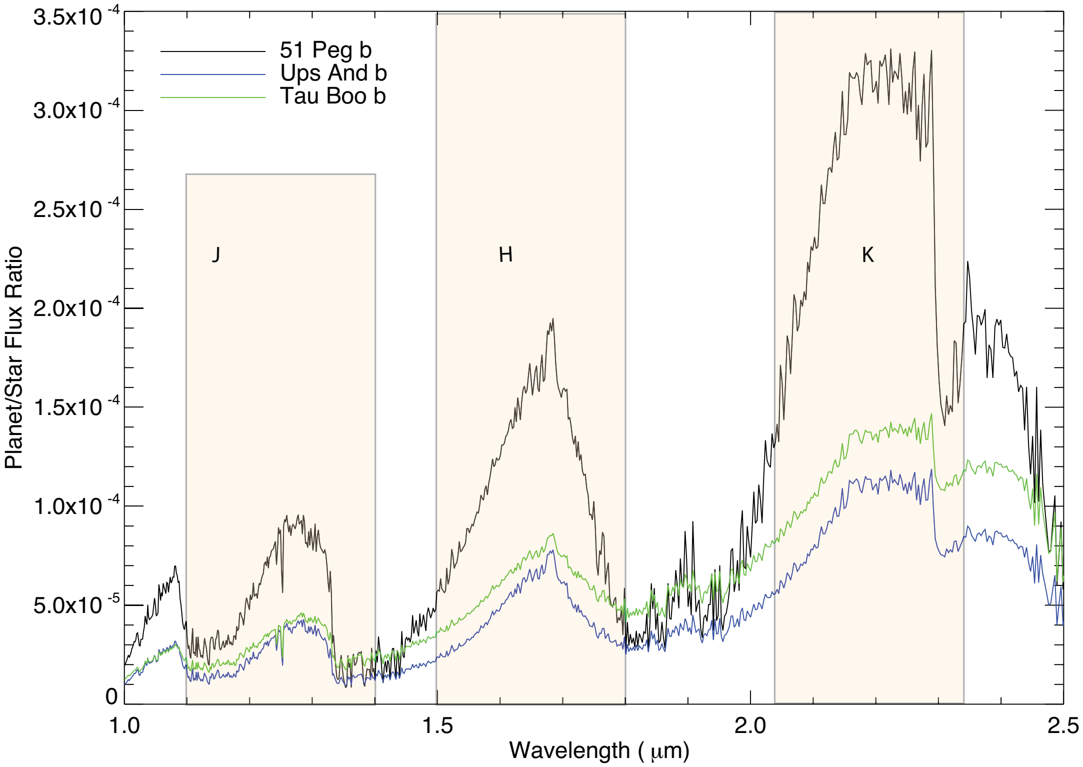

Figure 5.1 Planet to star flux ratios of υ And b, 51 Peg b, and τ Boo b in the near-IR, taken from Sudarsky et al. (2003). The flux ratio of 51 Peg b is ~ 2.5 times higher than that of υ And b and τ Boo b.

of hot Jupiters.

5.3 Hot Jupiter candidates for MIRC

Since the MIRC combiner (see §2.6.2) is specially designed for stable closure phase measurements, we use the CHARA array and MIRC to conduct our study. Among our list of nearby hot Jupiter candidates chosen for CHARA-MIRC, υ And b, τ Boo b and 51 Peg b are currently most favorable due to the high brightness of their host stars. Table 5.1 lists their properties and orbital parameters. In this chapter, we mostly focus on υ And since it is the brightest candidate.

The star υ And is an F8V star located 13.5 pc away from the Sun. Butler et al. (1997) first discovered its hot Jupiter υ And b in 1997, which has a period of 4.6 days and is orbiting at 0.059 AU. The follow-up observations of Butler et al. (1999) found two more companions in the system, υ And c and υ And d. υ And c is orbiting at 0.83 AU to the host star and has a period of 241 days, while υ And d is orbiting at 2.5 AU and has a period of 1267 days (Butler et al., 1999). The system is non-coplanar. The middle and the outer planets have a relative inclination of 15^o-20^o, and the overall inclination of the system is low but should be $>13^o$-19^o (Laughlin & Adams, 1999; Stepinski et al., 2000). In 2006, Harrington et al. (2006) directly detected light from the hot Jupiter υ And b using Spitzer MIPS at $24\mu m$, in which they saw the day-night flux variations of the planet over five epochs of the whole 4.6-day orbital period, and provided a lower limit to the flux ratio. Since then, atmospheric models have been applied to interpret these data. However, as Burrows et al. (2008) pointed out, due to the lack of absolute flux level and information in other wavelengths, there are too many degrees of freedom to draw strong conclusions on the planetary and atmospheric properties. Astrometric orbit of the planet (which

Table 5.1 Hot Jupiter systems for CHARA-MIRC [a]

Planet Name	Dist. pc	H_* mag	K_* mag	Period day	e	Semimajor axis AU (mas)	T_0 JD	Diameter_* mas
υ And b	13.5	2.957	2.859	4.6170	0.034	0.059 (4.42)	2450088.64	1.098
τ Boo b	15.6	3.546	3.507	3.3128	0.018	0.049 (3.13)	2451653.968	0.9
51 Peg b	15.4	4.234	3.911	4.2310	0.01	0.051 (3.31)	2450203.947	0.7

---

[a] References: (Marcy et al., 1997; Drake et al., 1998; Butler et al., 1999; Henry et al., 2000; Burrows et al., 2000)

can provide sin$i$) and observations at other wavelengths are thus strongly required to its break model degeneracies.

τ Boo is a F6IV type star located at 15.6 pc from us. It is also a binary star system, with a cooler M type star orbiting in a highly eccentric orbit (e=0.91, semi-major axis = 225 AU or 14.39 arcsec) (Patience et al., 2002). τ Boo b is a hot Jupiter orbiting at 0.05 AU from the host star τ Boo (Butler et al., 1997), and has an inclination of about 40^o (Leigh et al., 2003). Cameron et al. (1999) claimed a tentative detection of starlight reflected from the planet. However, this detection was not able to be confirmed, and other studies could only give an upper limit (Leigh et al., 2003).

51 Peg b is the first planet found to be orbiting around a sun-like (Mayor & Queloz, 1995). Its host star 51 Pegasi is a G5V star located 15.4 pc from the Sun. The discovery of 51 Peg b opened a window to a new type of planets, i.e., hot Jupiters. 51 Peg b is orbiting at 0.051 AU from the star and has a period of 4.23 days and a mass of ~0.5 M_j (Mayor & Queloz, 1995; Marcy et al., 1997; Trilling, 2000). Bundy & Marcy (2000) have looked for transit of the planet but no evidence were found.

5.4 Closure phase and differential phase simulations

Because exoplanet-hosting stars and their closest hot Jupiters are similar to high contrast close binaries, we simulate closure phase signals using binary model (Zhao et al., 2007) for υ And, τ Boo, and 51 Peg. The simulations assume using CHARA-MIRC at the H band. The orbital properties of the three systems are listed in Table 5.1. The diameter of star υ And is newly measured to be 1.098 ± 0.007 mas using the FLOUR instrument at CHARA (Mérand 2007, private communication). The infrared flux ratios of the planets are adopted from the models of Sudarsky et al. (2003), which are shown in Figure 5.1. Since the inclination (i) and the position angle of the ascending node (Ω) are unknown for these systems, we assume inclination=45^o and Ω=45^o for our first set of models. Figure 5.2 shows the resulting closure phase simulations. The left column shows the results for the short baselines of CHARA, while the right column shows the results for the longest baselines. The closure phases vary at different channels. Due to higher resolution of the long baselines in the right column, the host stars are more resolved than at the short baselines and thus the closure phase signals are stronger. In the left column, υ And b shows an average signal level of $\sim 0.01^o$ at the highest signal channels. Its peak signal is $\sim$$0.02^o$, smaller than that of 51 Peg b due to its lower flux ratio, and is close to that of τ Boo b. However, if we use the longest telescope triangle S1-E1-W1 instead, as shown in the left column, the average signal of υ And at the shortest wavelength (dash-dotted line) increases to $\sim 0.08^o$, and its peak reaches 0.18^o, almost 10 times higher than the shorter triangle in the left column. This is because at the longest baselines of CHARA, the photosphere of the host star υ And starts to be resolved, which essentially lowers the fringe visibility of the host star and increases the planet-star flux ratio of the system. The peak signals of 51 Peg b and τ Boo b also become higher at this triangle but not as much as that of υ And because their host stars are not fully resolved yet.

Figure 5.3 shows the simulations of closure phases for inclination=0^o and $\Omega = 60^o$. The peak signals of υ And b is 0.17^o, close to that of Figure 5.2. Similarly, the peak signal of 51 Peg b and τ boo b are 0.038^o and 0.023^o respectively, close to the values in Figure 5.2 as well. Although the orbital inclination and Ω of the three hot Jupiters are arbitrarily chosen in Figure 5.2 and Figure 5.3, our simulations with various i and Ω indicate that we can always get similar signal levels for the three hot Jupiters by using proper telescope triangles and/or observing at a different time. These simulations also suggest that in order to detect the peak signals of υ And b, our closure phase precision needs to be better than $\sim 0.17^o$ for the long triangles of CHARA and better than $\sim 0.02^o$ for the short triangles. For 51 Peg b and τ Boo b the precision needs to be better than 0.04^o and 0.02^o respectively.

In addition to closure phases, we also show the simulated differential closure phases between several channels in Figure 5.4 for the longest triangle S1-E1-W1. The peak differential closure phase levels of 51 Peg b and τ Boo b (top right and bottom panel) are both close to their peak closure phase signals in Figures 5.2 & 5.3 due to less differences between different wavelength channels. However, for the case of υ And b (top left panel), due to the different signs of closure phases between the shortest wavelength channel and other channels at certain hour angles (see top right panel of Fig. 5.2), its differential closure phase signal is higher and reaches

$\sim \pm 0.25^o$ at the peak and the trough, an increase of $\sim 28\%$ compared to the peak of its closure phases. For other sets of i and Ω values, there is also similar boost of signal, although the increase may be smaller. This suggests the differential closure phase is potentially a better quantity for our work, but more investigations are still needed.

Furthermore, as mentioned in §5.2, differential phase is another potential observable for detecting the signal from hot Jupiters. We therefore simulate the differential phase for the three candidates. Specifically, we first simulate complex visibilities for the 8 individual wavelength channels of MIRC for each candidate, and use the two channels at the edge (i.e., at $1.52\mu m$ & $1.76\mu m$) to interpolate the phases for the middle channels to calibrate the OPD drift caused by atmospheric pistons. The differential phase for a certain channel is then calculated by subtracting the interpolated phase. Figure 5.5 shows the results at 1.66 μm, the central channel of MIRC, using CHARA's longest baseline S1-E1 (331m). The signals are weaker than that of closure phases in Figures 5.2 & 5.3, suggesting higher precision is required for detection. More investigation and application of differential phase will be conducted in a future work.

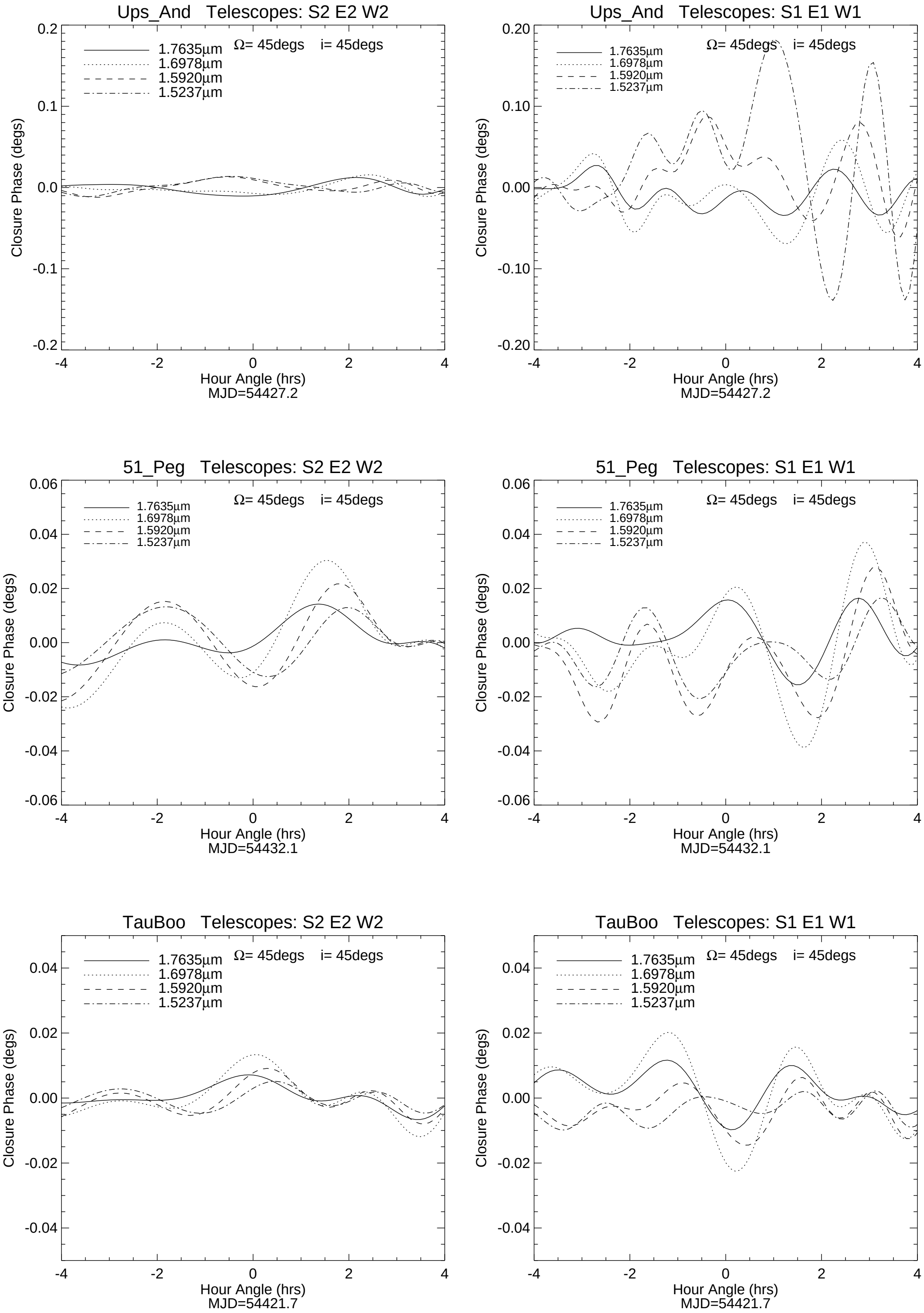

Figure 5.2 Closure phase simulation A. Simulations for υ And b, 51 Peg b and τ Boo b. Four out of eight wavelength channels of MIRC are shown here. We assume $i = 45^o$ and $\Omega = 45^o$ in these simulations. The left hand side panels use short baseline triangles of CHARA, while the right hand side panels use long triangles.

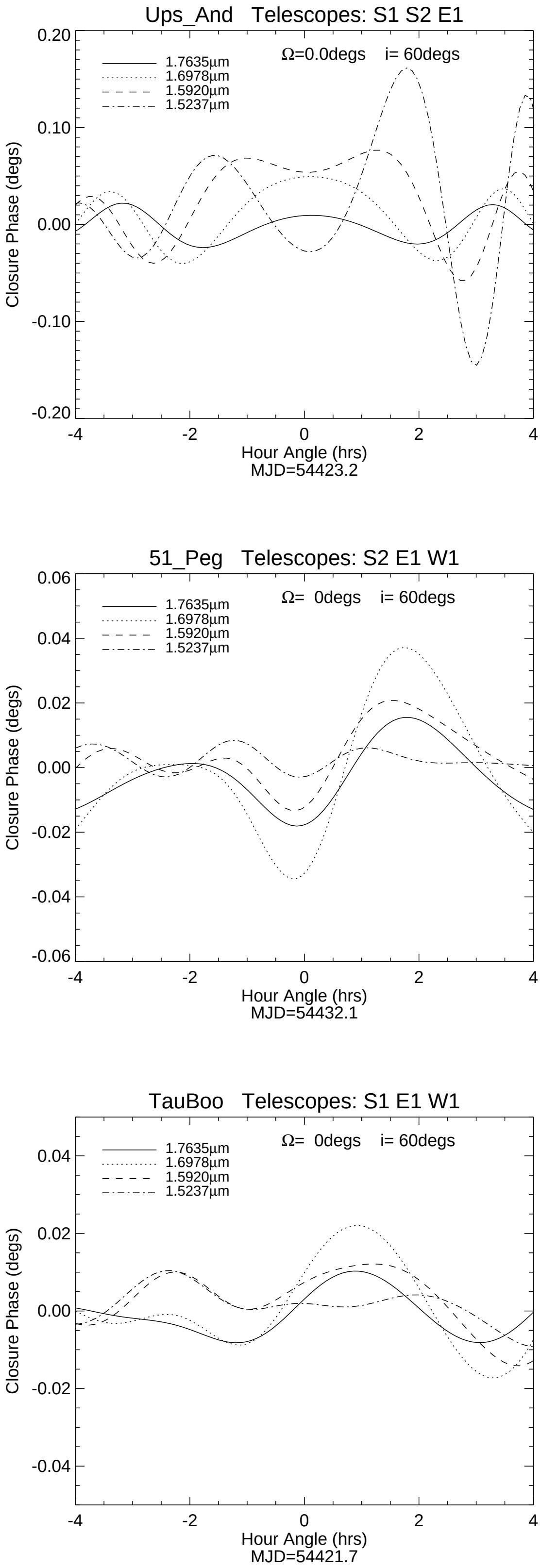

Figure 5.3 Closure phase simulation B. Simulations for υ And b, 51 Peg b and τ Boo b, assuming $i = 0^o$ and $\Omega = 60^o$. Four out of eight wavelength channels of MIRC are shown here.

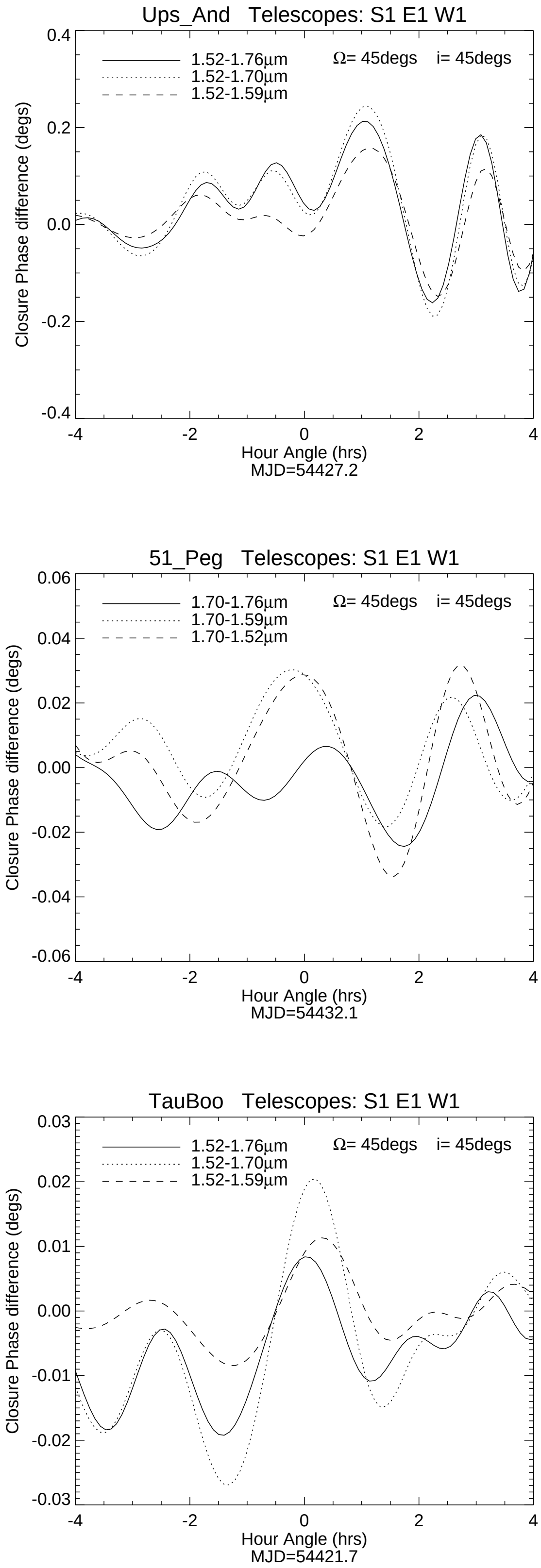

Figure 5.4 Differential closure phases simulation for υ And b, 51 Peg b and τ Boo b. The three different lines show the results of selected wavelength pairs. The i and Ω values are the same as Figure 5.2.

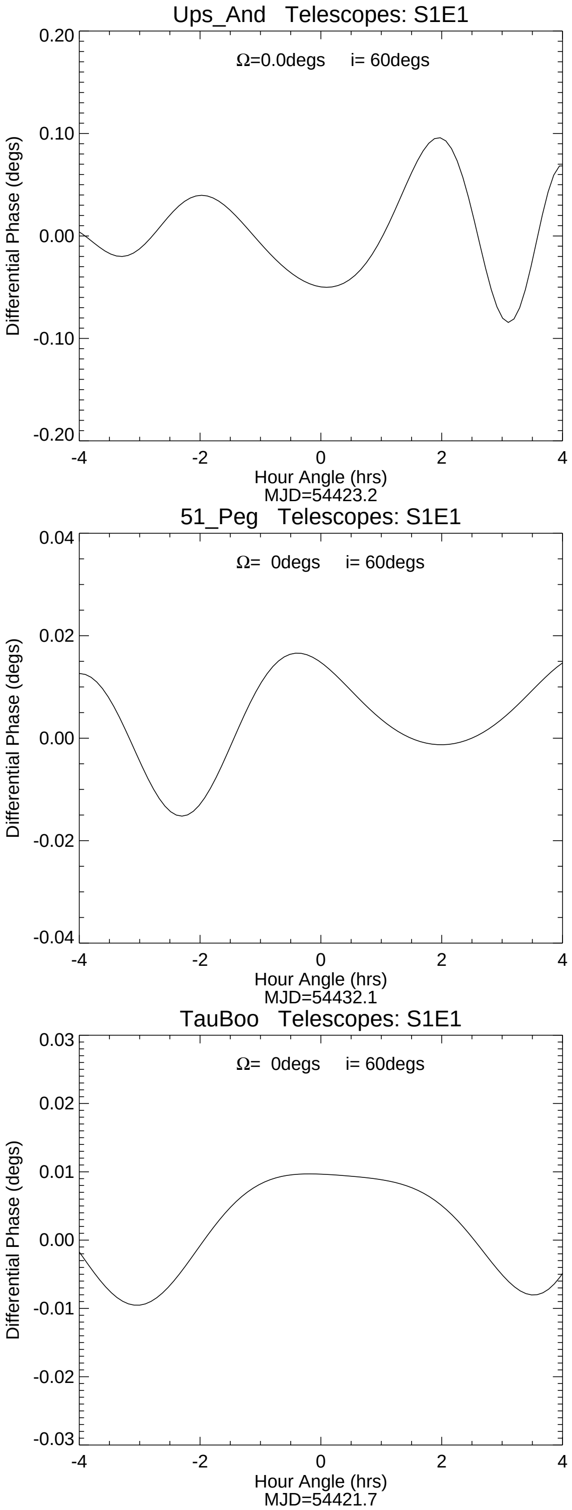

Figure 5.5 Differential phase simulation for the central channel (1.66 μm). Differential phases for υ And b, 51 Peg b and τ Boo b are shown from top to bottom respectively, using the longest baseline S1-E1 of CHARA. The differential phases are calculated by subtracting the phase interpolated from the two edge channels from the real "measured" phase to calibrate the OPD.

5.5 Observations of υ And

We conducted our observations of υ And using CHARA-MIRC on several nights in August 2007 and November 2007, using both the inner array (telescope S2-E2-W1-W2) and the outer array (telescope S1-E1-W1-W2) of CHARA and following the standard observing procedures (Monnier et al., 2007). The highest resolution obtained by the inner array was 0.7 mas, and that of the outer array was 0.5 mas. The data reduction process follows the pipeline outlined by Monnier et al. (2007) as well, which can also be found in previous chapters (§3 & §4.2).

We show some reduced closure phases from 2 nights in November 2007 in Figure 5.6. The errors of the November data in the plots average down as $\sqrt{N}$, suggesting that the measurements are stable and immune from systematic errors like the changes in the seeing. We can see in the top plot that the error of the 60-file averaged data (Δt =320 sec) on Nov14 is only 0.161^o for 1.4 hours of observation. The error of that on Nov16 is even smaller, only 0.126^o in 1.7 hours. This suggests that the error of the data on Nov14 can reach 0.066^o when averaged over the whole 1.4 hours. Similarly, the final error of the Nov16 data can reach 0.045^o once averaged over the 1.7 hours of observation. Compared to the peak signal of υ And b, 0.02^o, in the simulations in last section (§5.4), these values correspond to $\sim 0.3\sigma$ and $\sim 0.44\sigma$ of the peak signal for the short triangles.

The closure phases obtained with the longest triangle S1-E1-W1 are shown in the bottom plots of Figure 5.7. As expected, the closure phase signal are much noisier than those of the shorter baselines because υ And is starting to be resolved at long baselines, leading to low visibilities and low signal-to-noise data. The 60-file averaged data (Δt =320 sec) give an error of 0.822^o on Nov22 (top panel). The final error reaches 0.03^o when averaged over the whole 1.7 hours of observation, corresponding to 0.6σ of the possible peak signal, 0.17^o, of the longest triangle shown in Figures 5.2 and 5.3. However, the Aug12 data (bottom panel) give a much larger error compared to that of Nov 22 although its seeing condition was actually slightly better. The errors of the Aug 12 data also average down slightly slower than $\sqrt{N}$, implying there may be some systematic drifts in the data that are not well calibrated. These scatters may be partly caused by different observation schemes used between the two nights, in which we frequently move the fibers of MIRC to peak the flux of each beam in the November observations while in August we observed continuously and allowed the fiber flux to drift, causing the signal-to-noise to decrease with time. The drift of flux may have also caused additional spectra tilts across the 8 channels of MIRC, which may not be well calibrated for the data of Aug 12, and therefore, added extra noise to the closure phases.

Although the data shown above represent the general quality of our data, we also notice some closure phase drifts in certain nights and channels, as shown in Figure 5.8. These drift can be due to the spectra tilt of the beams, dispersion effects across different channels, and/or polarization, etc. To further investigate these issues, more calibration studies are therefore needed.

The above results show that within about 2 hrs, we can reach 0.6σ of the peak signal under decent condition using the longest telescope triangle. This suggests we still need a factor of ∼2 more signal-to -noise in in order to make a 1σ detection. The most straightforward way to increase the signal to noise is to increase the integration time. However, as we can see from Figures 5.2 and 5.3 in last section, the closure phases change very fast with time, making it difficult to integrate for a long time as closure phases will be averaged out otherwise. Fortunately, as most of the known hot Jupiter systems have very well known orbital parameters from RV, we can take the advantage of their known properties (i.e., e, P, T_0, semi-major axis), hold them fixed in the fit, and only solve for the unknown parameters (i.e., inclination and Ω). This approach allows us to observe the target for a long time within each night and also allows us to combine as many nights of data as possible together for a joint solution along with the RV data to reach the required precision. We will test this method with ϵ Per in §5.7.

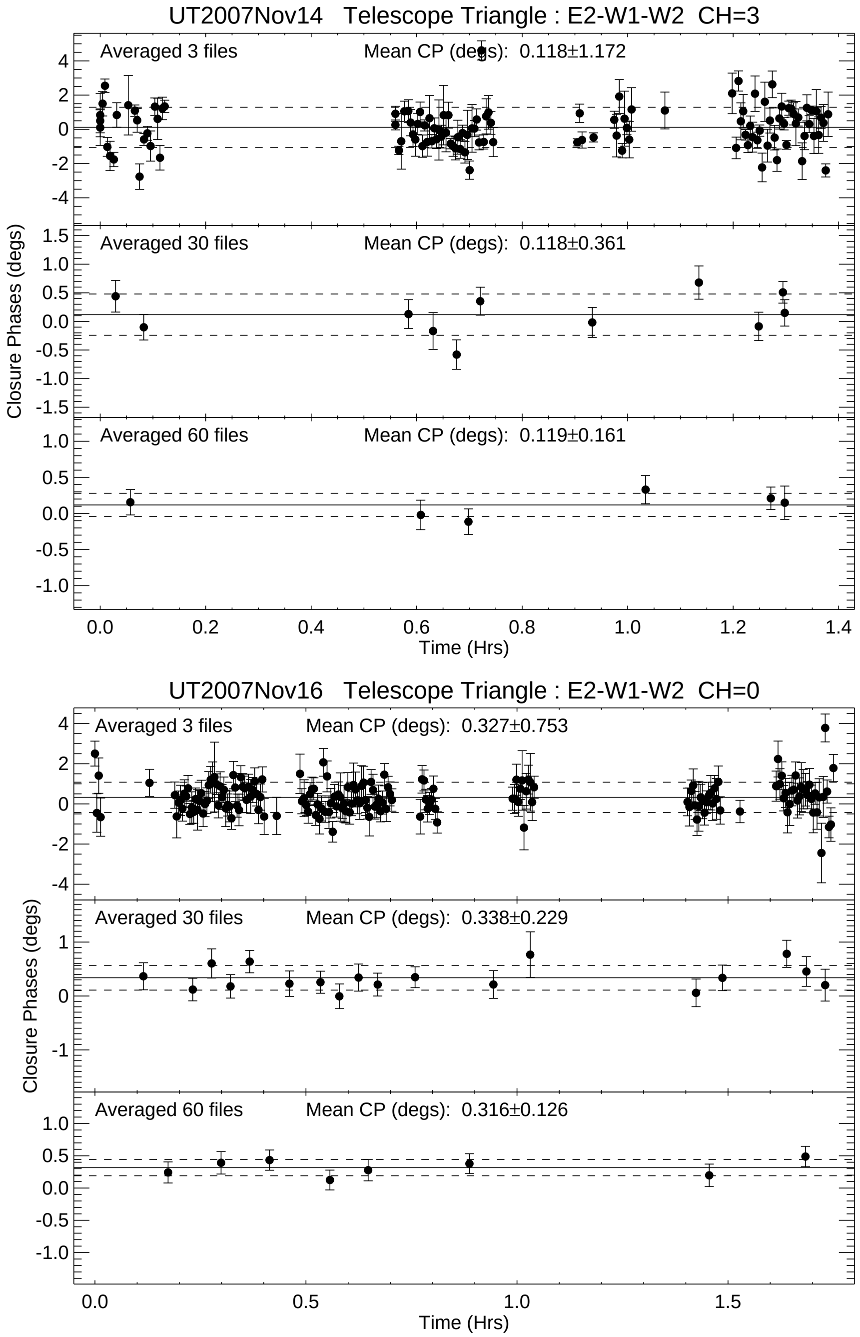

Figure 5.6 Preliminary results on υ And using inner triangle E2-W1-W2 of CHARA. The resolution of this triangle is 0.7 mas. Every single point in the top panel of each plot is an average of 3 files, corresponding to an integration time of 16 sec, while the points in the middle and bottom panel are average of 30 files and 60 files, corresponding to 160 sec and 320 sec of integration time respectively. The solid lines indicate the averaged closure phases for each panel, while the dashed lines indicate 1-σ deviation from the average. MIRC wavelength channel numbers are indicated at the top of each plot. Channel 0 and 3 correspond to 1.76μm and 1.66 μm respectively.

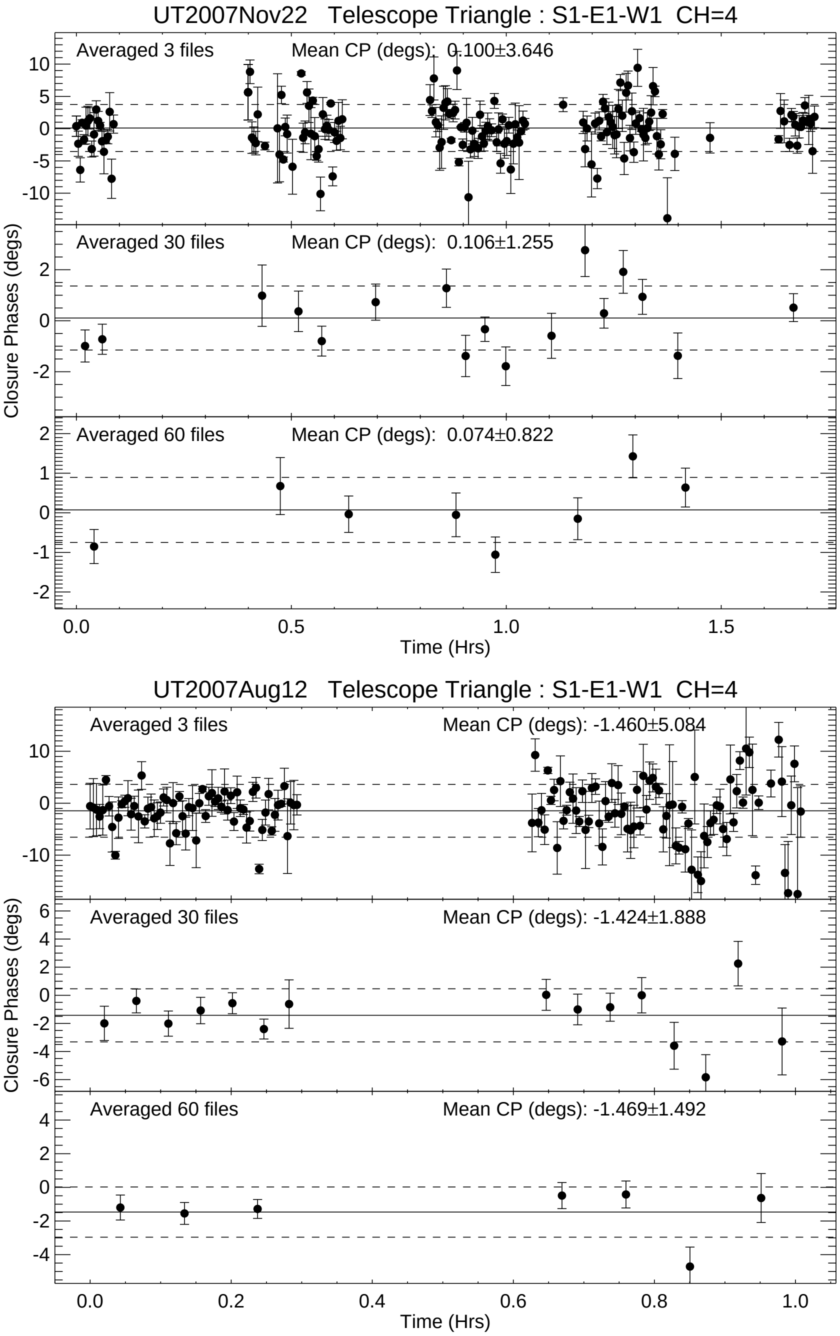

Figure 5.7 Preliminary results of υ And using the outer array (S1-E1-W1) of CHARA. The resolution is 0.5 mas. The arrangement of the panels, line styles, symbols and notations are similar to that of Figure 5.6.

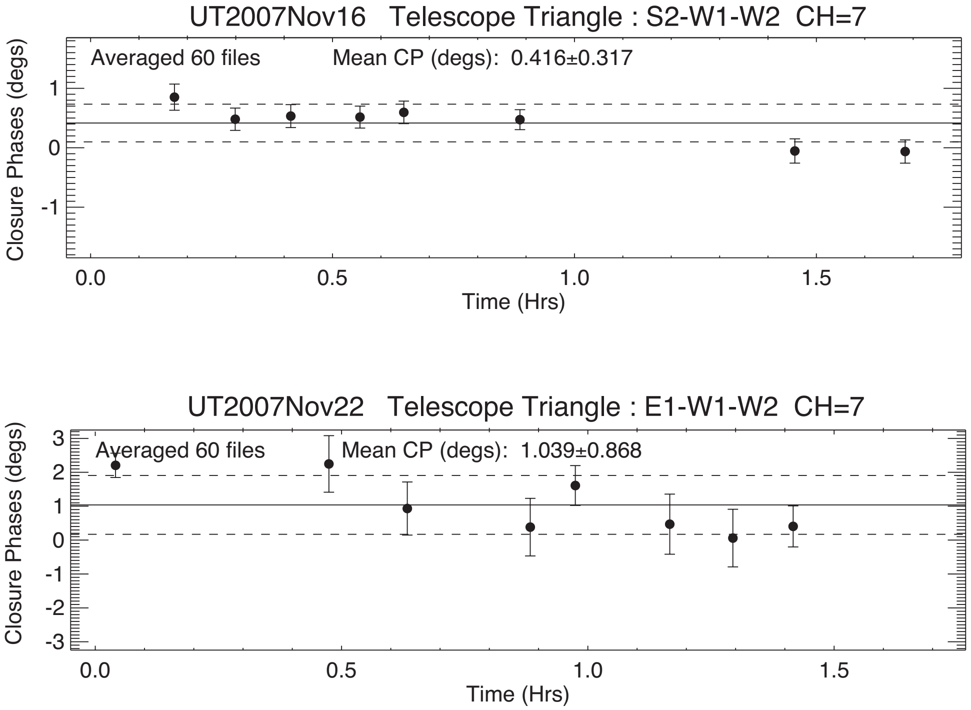

Figure 5.8 Closure phase drifts in υ And data. The 60-file averaged data (Δt =320 sec) from 2007 Nov 16 and Nov 22. The data show clear drifts in the closure phases.

5.6 Closure phase calibration studies

We first investigate the cause of the closure phase drifts. Since some mirrors in the CHARA system have different coatings and were recoated at different time, polarization may be introduced in the beam train which can cause the phases to change while the telescope is rotating and tracking a star. Therefore, we first look for correlations between closure phases and the hour angle, azimuth angle, and altitude of the targets. Figure 5.9 plots closure phases of six calibrators obtained in 2008 August (Algenib, 38 Tau, γ Lyr, γ Tri, ζ Peg, ζ Per) versus hour angle. There is a clear trend of closure phase change as a function of hour angle in the figure. The slope of the trend also changes as a function of wavelength. Since the hour angle of a target is also a function of its azimuth and altitude, we investigate their relation with closure phase in Figure 5.10 and 5.11. The closure phases also show some trend with azimuth in Figure 5.10. However, the correlation is much stronger with altitude in Figure 5.11, and the closure phase drift reaches 10 degrees from 60^o to 85^o of altitude. The dependence of closure phase on azimuth and especially on altitude is so strong that it greatly affects our calibration. To better understand this correlation and calibrate this effect, we therefore fit the closure phase as a function of both azimuth and altitude.

In Figure 5.12 we fit closure phases of six calibrators together as a plane function of azimuth and altitude. Closure phase also shows strong correlation with the plane function and the fit is better than previous plots (Figs. 5.10 & 5.11). We also attempt to include quadratic effects in the fit in Figure 5.13 and 5.14. We first use sin and cos functions in Figure 5.13 since phase changes caused by azimuth wrap around when the azimuth is more than 180^o. The fit to plane functions with sin and cos as basis is much better than the previous plane fit as indicated by the reduced χ^2s labeled in the plots. The fit is even better in quadratic form in Figure 5.14, and most of the data points can be very well modeled by a quadratic function.

Since these fits allow us to empirically model the closure phase drifts of multiple nights of data together very well. We therefore can use these best-fit functions to predict the zero points and calibrate our closure phases. We test this new calibration scheme first on a calibrator ζ Per. ζ Per is a B1Ib type star and has a diameter of only 0.67 ± 0.03 mas[3]. This means ζ Per is not resolved in our observation and the closure phase should be constantly 0^o. However, as we can see in the left panel of Figure 5.15, its closure phase has large drifts from shorter wavelengths to longer wavelengths, and the biggest difference reaches as high as 10^o. We apply the new calibration scheme by fitting a quadratic function to all of the calibrators within that observation run (8 nights, 6 calibrators, including ζ Per itself) and subtract the predicted zero closure phases from the measured values of ζ Per. After we applied the new calibration scheme, as shown in the right panel of Figure 5.15, these drifts are calibrated out and the closure phases are mostly around 0^o as they are supposed to be.

---

[3] Obtained from getCal: http://nexsciweb.ipac.caltech.edu/gcWeb/gcWeb.jsp

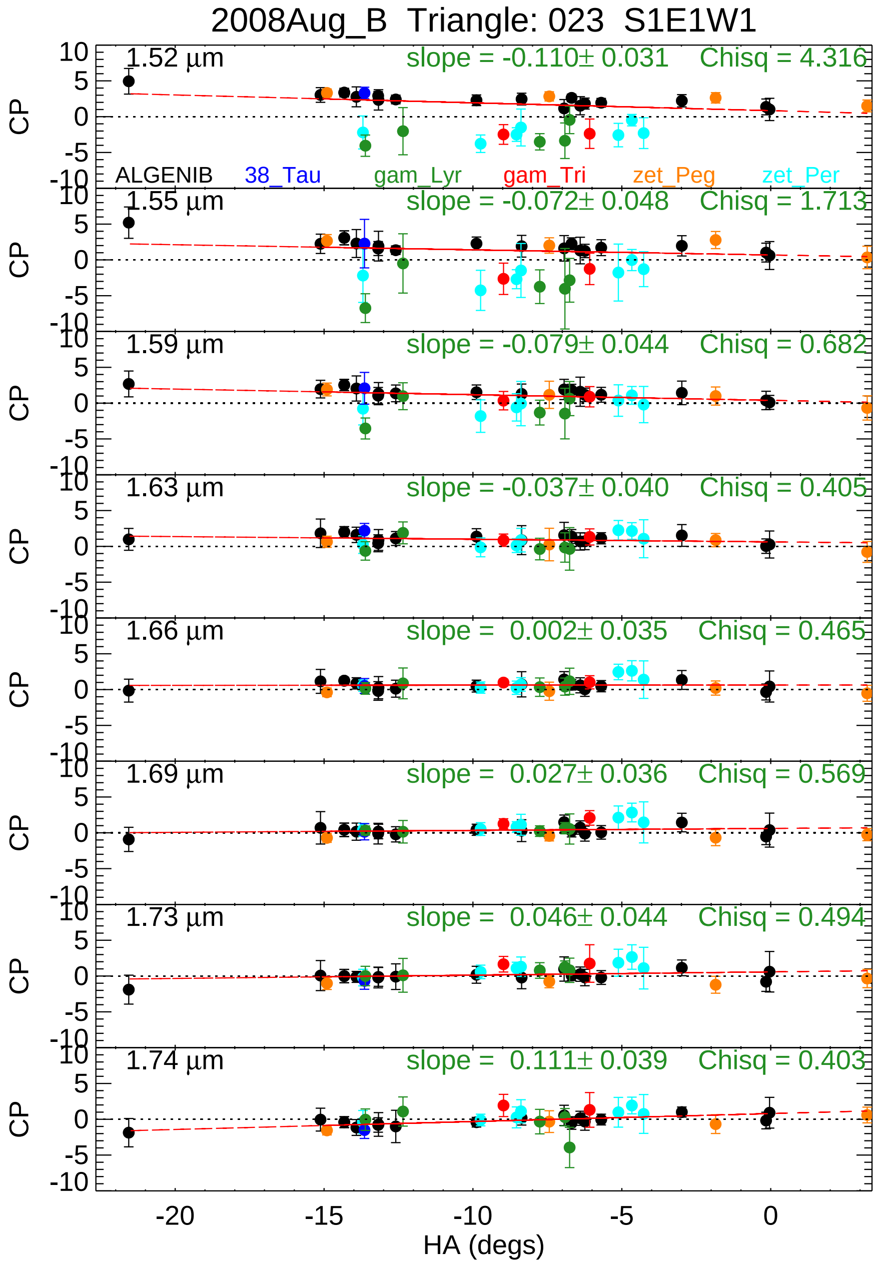

Figure 5.9 Closure phase vs. H.A. for six calibrators in 2008 August. The 8 panels show the data of 8 wavelength channels of MIRC. The data were taken with telescope S1-E1-W1. The red line shows the linear fit of closure phase as a function of hour angle. Different colors stand for different targets. The slope of the linear fit and the reduced χ^2 are also labeled in each panel.

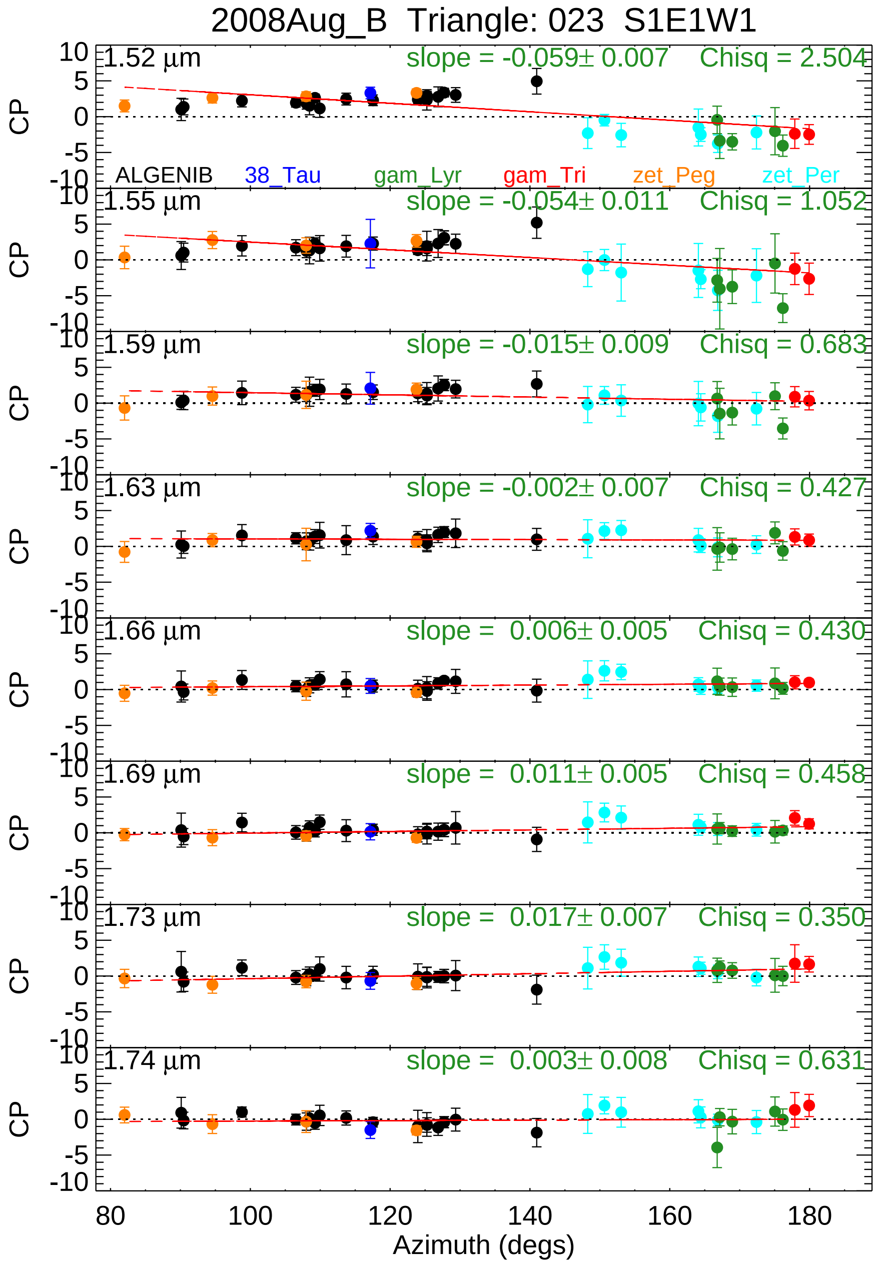

Figure 5.10 Closure phase vs. Azimuth for six calibrators in 2008 August. The 8 panels show the data of 8 wavelength channels of MIRC. The data were taken with telescope S1-E1-W1. The red line shows the linear fit of closure phase as a function of azimuth. Different colors indicate different targets. The slope of the linear fit and the reduced χ^2 are also labeled in each panel

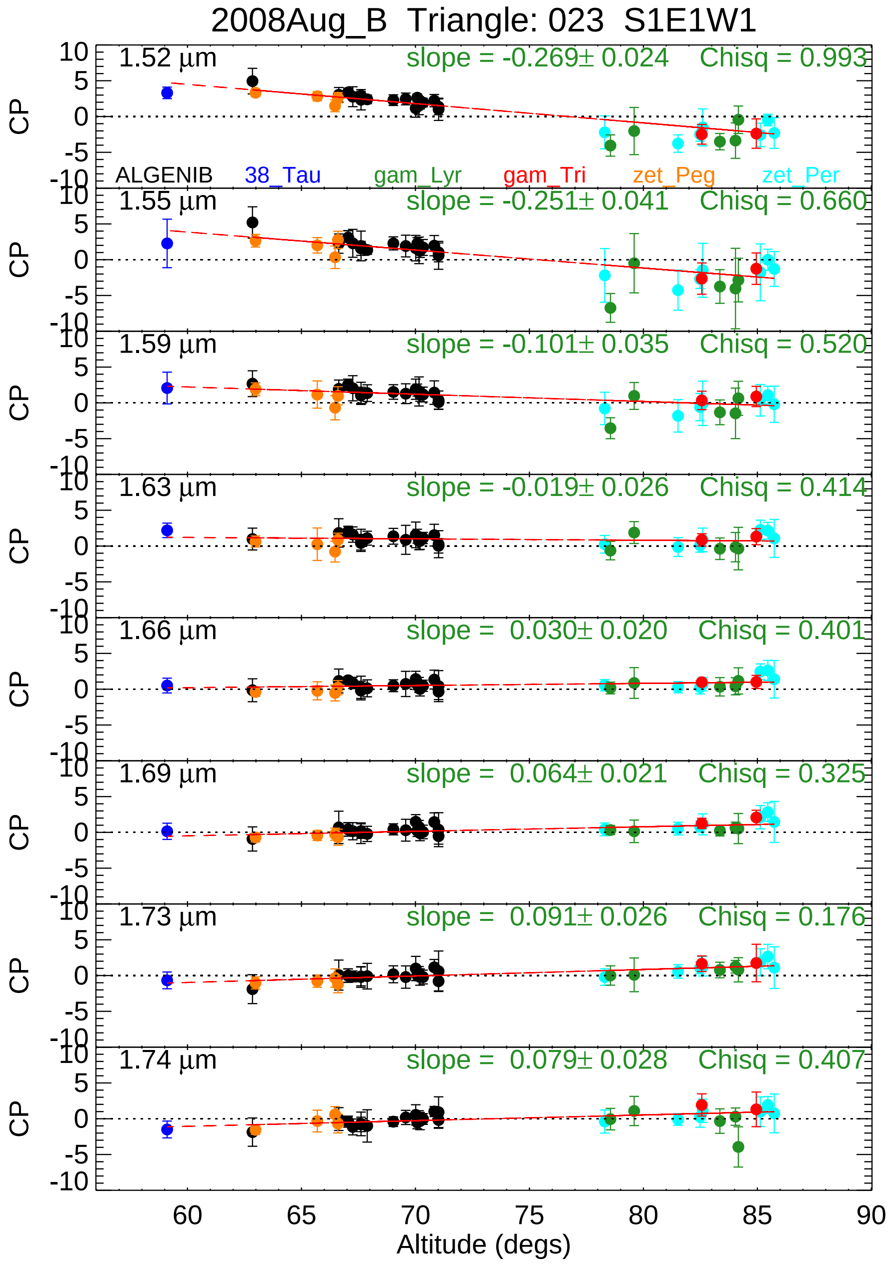

Figure 5.11 Closure phase vs. Altitude for six calibrators in 2008 August. The red line shows the linear fit of closure phase as a function of altitude. The parameters of the fits are shown in each panel.

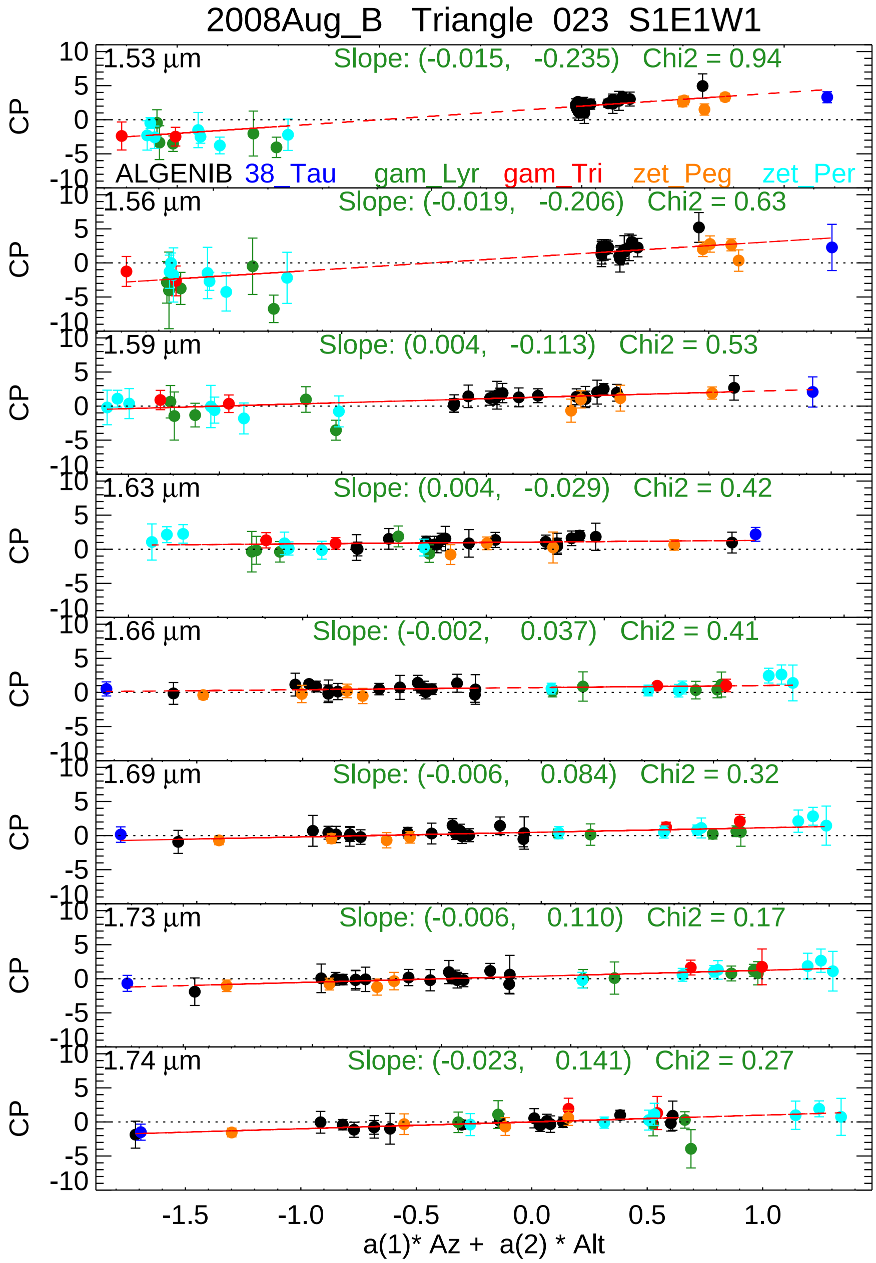

Figure 5.12 Closure phase as a function of azimuth and altitude using plane fit A. The arrangement and notations are similar to those of Figures 5.9, 5.10 and 5.11, except that the red line is a fit to the plane function: $a_0 + a_1 \cdot Az + a_2 \cdot Alt$. The best fit parameters a_1 and a_2 and the reduced χ^2 are shown in each panel.

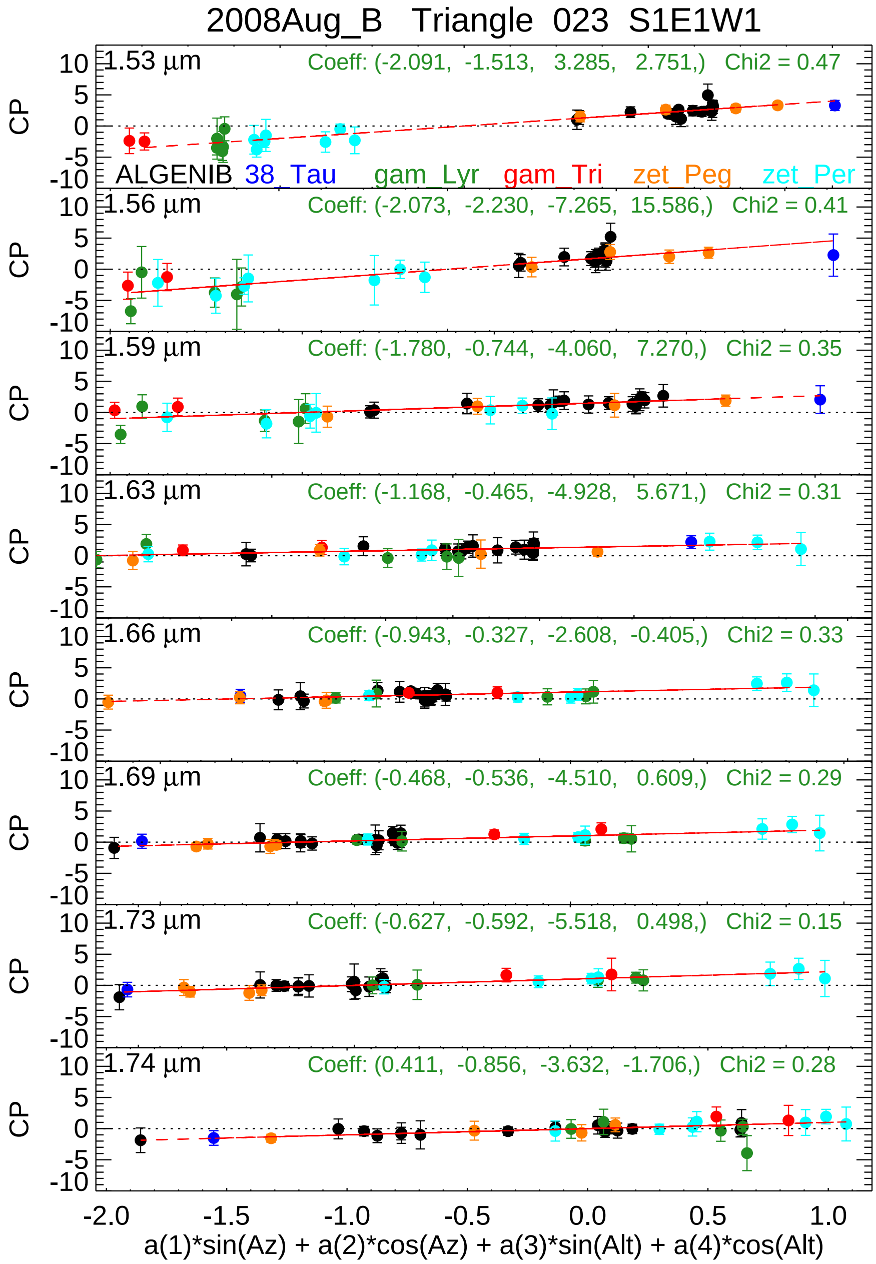

Figure 5.13 Closure phase as a function of azimuth and altitude using plane fit B. The arrangement and notations are similar to those of Figures 5.9, 5.10 and 5.11, except that the red line is a fit to the plane function: $a_0 + a_1 \cdot \sin(Az) + a_2 \cdot \cos(Az) + a_3 \cdot \sin(Alt) + a_4 \cdot \cos(Alt)$. The best fit parameters and the reduced χ^2 are shown in each panel.

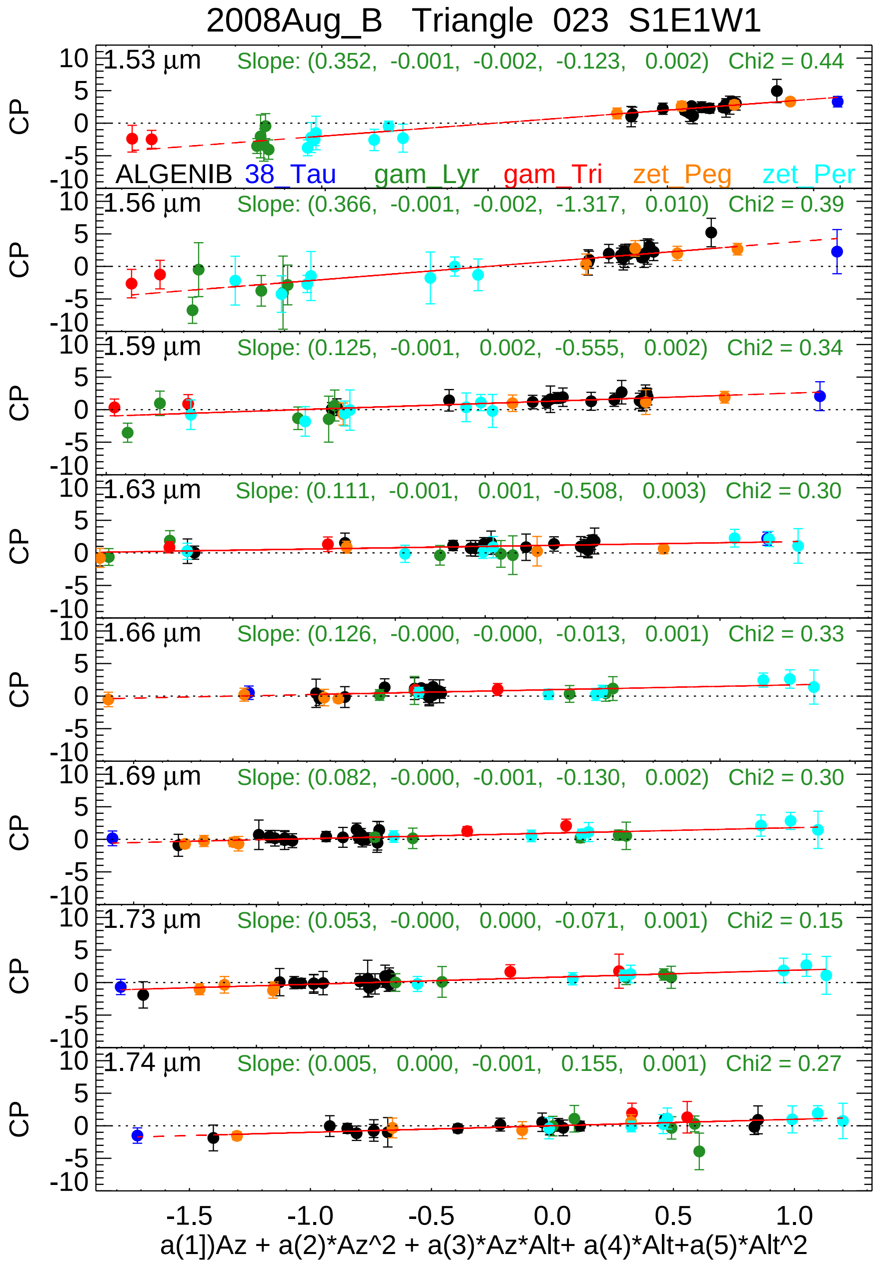

Figure 5.14 Closure phase as a function of azimuth and altitude using quadratic fit. The arrangement and notations are similar to those of Figures 5.9, 5.10 and 5.11, except that the red line is a fit to the plane function: $a_0 + a_1 \cdot Az + a_2 \cdot Az^2 + a_3 \cdot Az \cdot Alt + a_4 \cdot Alt + a_5 \cdot Alt^2$. The best fit parameters and the reduced χ^2 are shown in each panel.

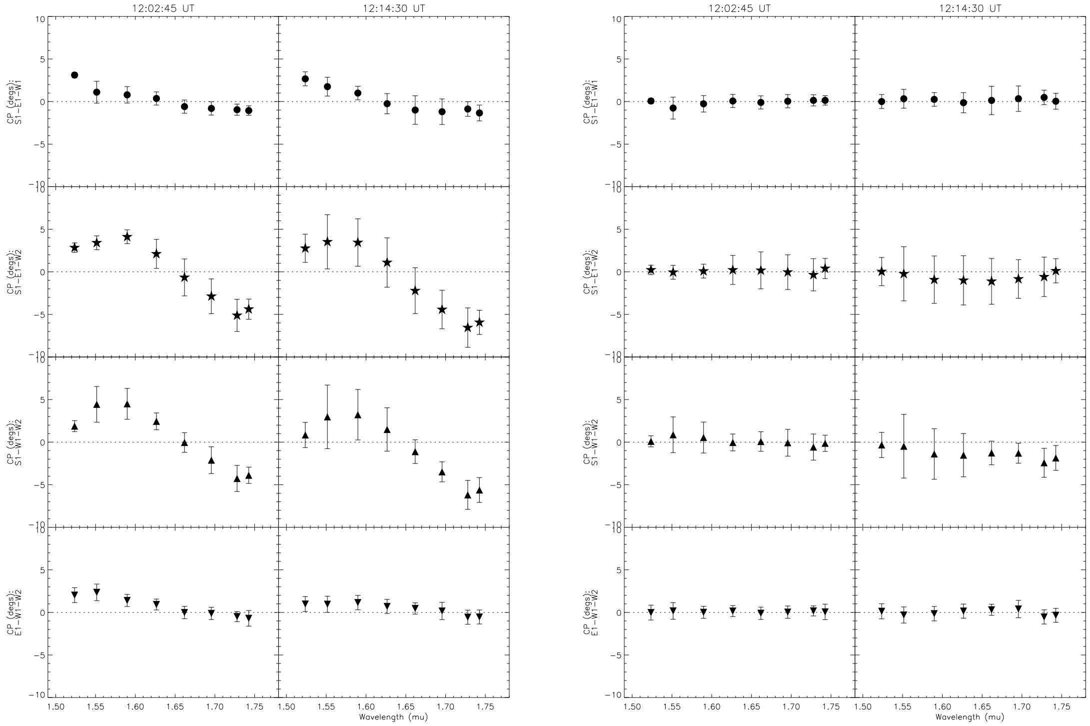

Figure 5.15 The closure phases of ζ Per before and after the new calibration scheme. The left panel shows the closure phases before the new calibration, while the right panel shows that after the new calibration. All of the calibrators, including ζ Per itself, are included in the quadratic fit used in the new scheme. The two columns in each panel shows closure phases taken at different time. The four rows shows the four independent closed triangles using telescope S1-E1-W1-W2 of CHARA. The eight points in each panel indicate the eight wavelength channels of MIRC.

5.7 Test observation of ϵ Per

To test the data analysis scheme we mentioned in §5.5, as well as the new closure phase calibration scheme that we discussed in last section, we observed the high contrast binary ϵ Per.

ϵ Per (45 Per, HD 24760, V= 2.9, H= 3.6, K = 3.7, d = 165.0 pc) is a bright single-line spectroscopic binary with a period of 14 days. The primary was classified as B0.5 V by Johnson & Morgan (1953) and has an estimated mass of 13.5 $M_\odot$(Libich et al., 2006). With a mass function of 0.003, we can estimate the mass of the secondary to be approximately 0.85 $M_\odot$ for an edge-on orbit. In this case, the brightness ratio would be approximately 300:1 at the *H* band, and the semi-major axis would be about 1-2 mas. With a primary diameter of about 0.4 mas (from getCal), and an *H* magnitude of 3.6, ϵ Per is an ideal high contrast binary for our study of closure phases.

We observed ϵ Per in a total of six nights in August, November and December of 2008, using telescopes S1-E1-W1-W2 of CHARA-MIRC. After data reduction following the standard procedure described in previous chapters, we searched for the companion by holding the period, T_0, eccentricity and ω fixed and allow the flux ratio, semi-major axis, inclination, and Ω to change as free parameters. The fixed parameters we adopt are listed in Table 5.2. The diameter of the primary is estimated by fitting the visibilities using a uniform disk (UD) model, which gives us a slightly larger size of 0.5 mas. The size of the secondary is roughly estimated by assuming the star has a diameter of 1 $R_\odot$, corresponding to a angular size of 0.08 mas at a distance of 165 pc. Although the estimate of the secondary diameter may not be very accurate, it would not affect our search for the companion since the companion is too small to be resolved.

We first search for the companion using the data calibrated with the old closure phase calibration scheme. Figure 5.16 shows the χ^2 surfaces of Ω vs. inclination and semi-major axis vs. inclination. There are several local minimums in the χ^2 surfaces and the brightest peaks ($\chi^2_\nu = 1.58$) suggest that the companion is most likely at $i = 86^o \pm 44^o$ and $\Omega = 53^o \pm 63^o$, and have a semi-major axis of 1.12 ± 0.35 mas and an H band flux ratio of $(100 \pm 61) : 1$. The errors of the parameters are obtained by bootstrapping different nights of data.

We then re-calibrated the closure phase data using the new scheme discussed in last section to calibrate the closure phase drifts at different azimuth and altitude. Specifically, we fit the closure phase drifts for every wavelength channel with all calibrators to get the zero closure phase points. Similar to that of Figure 5.14, quadratic functions are also adopted in the fit. ϵ Per is also included in the quadratic fit because the drifts of its closure phases are strong functions of azimuth and altitude, largely dominating the signal of the companion which can be treated as tiny perturbations to zero closure phases. We then subtract the derived zero closure phase points from the un-calibrated closure phases of ϵ Per to obtain the calibrated values. Figures 5.17 and 5.18 show the closure phases of ϵ Per before and after using the new calibration scheme. Figure 5.17 shows that the old closure phase data have large drifts and deviations from zero. These drifts and deviations are mostly calibrated in the new closure phases, as shown in Figure 5.18. We then re-search for the companion using the new closure phase data. Figure 5.19 shows the new χ^2 spaces of ϵ Per. The

Table 5.2. ϵ Per parameters

Eccentricity[a]	Period[a]	T_0[a]	ω[a]	$D_{primary}$	$D_{secondary}$
	days	MJD	^{o}	mas	mas
0.5549	14.069	47767.043	105.8	0.50	0.08

[a] Parameters from Libich et al. (2006)

local minimums in the new plots become brighter compared to the previous ones in Figure 5.17. Apparently, the large drifts in the old closure phase data have biased our previous search to the middle bottom region of the χ^2 space (see Figure 5.17). The peaks of the new χ^2 surfaces are now located at a higher Ω of $259^o \pm 66^o$, a higher semi-major axis of 1.54 ± 0.13, and an inclination of $90^o \pm 7^o$ (errors are also obtained from bootstrap). The H band flux ratio of the peaks is now (316 ± 113) :1, consistent with our estimate based on the masses of the two stars. The reduced χ^2 of the peaks is 0.31, much lower than that of the previous result (1.58), and indicating the new calibration has eliminated large systematics of the data. However, the fact that the differences between other local minimums and the highest peaks are much smaller in the new χ^2 surfaces also implies that we do not have enough signal-to-noise to claim a detection of the companion yet. More observations and further calibration studies are still needed to look for the companion and test our method.

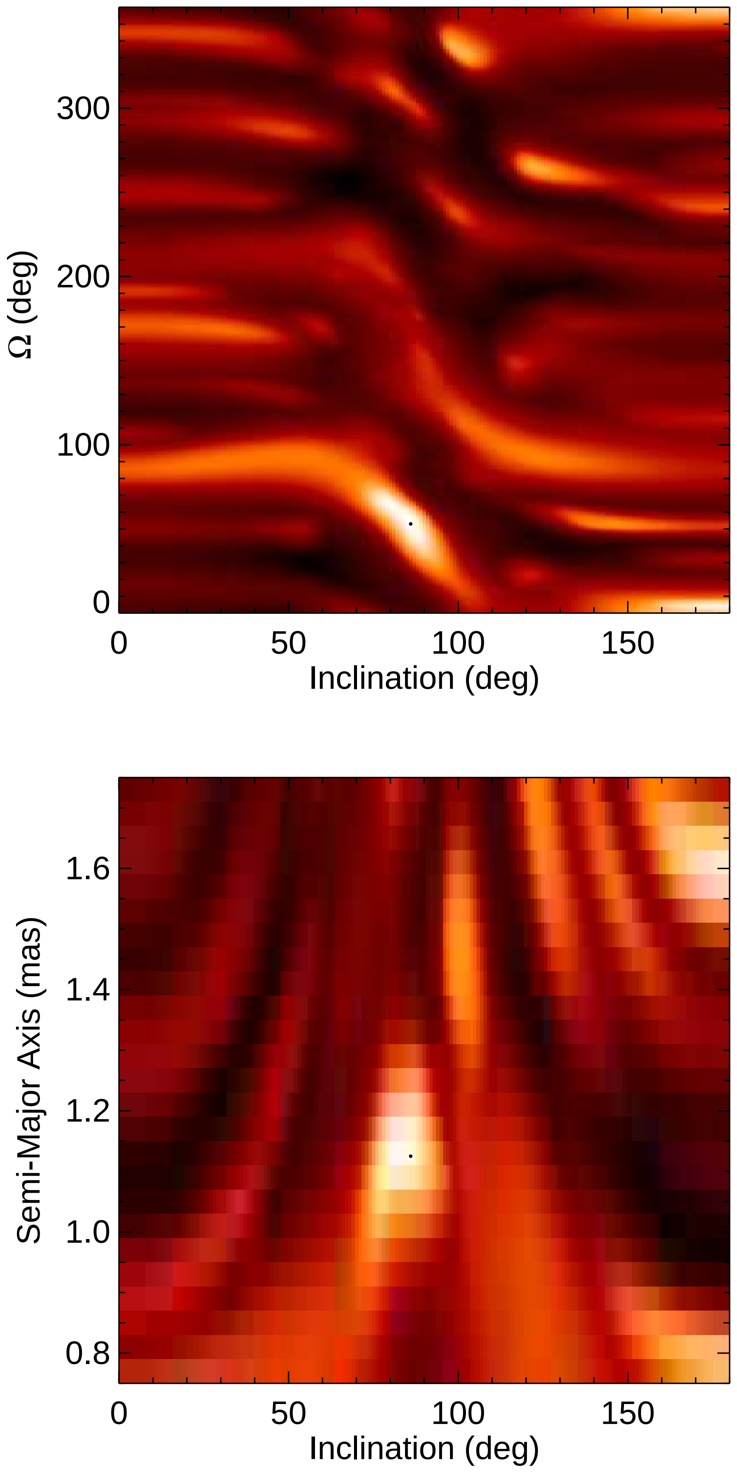

Figure 5.16 The χ^2 surface of ϵ Per. The top panel shows the the χ^2 surface of Ω and inclination, while the bottom one shows the χ^2 surface of semi-major axis and inclination. Bright areas indicate low χ^2 and high probability. The black dot at the brightest peak indicates the best result.

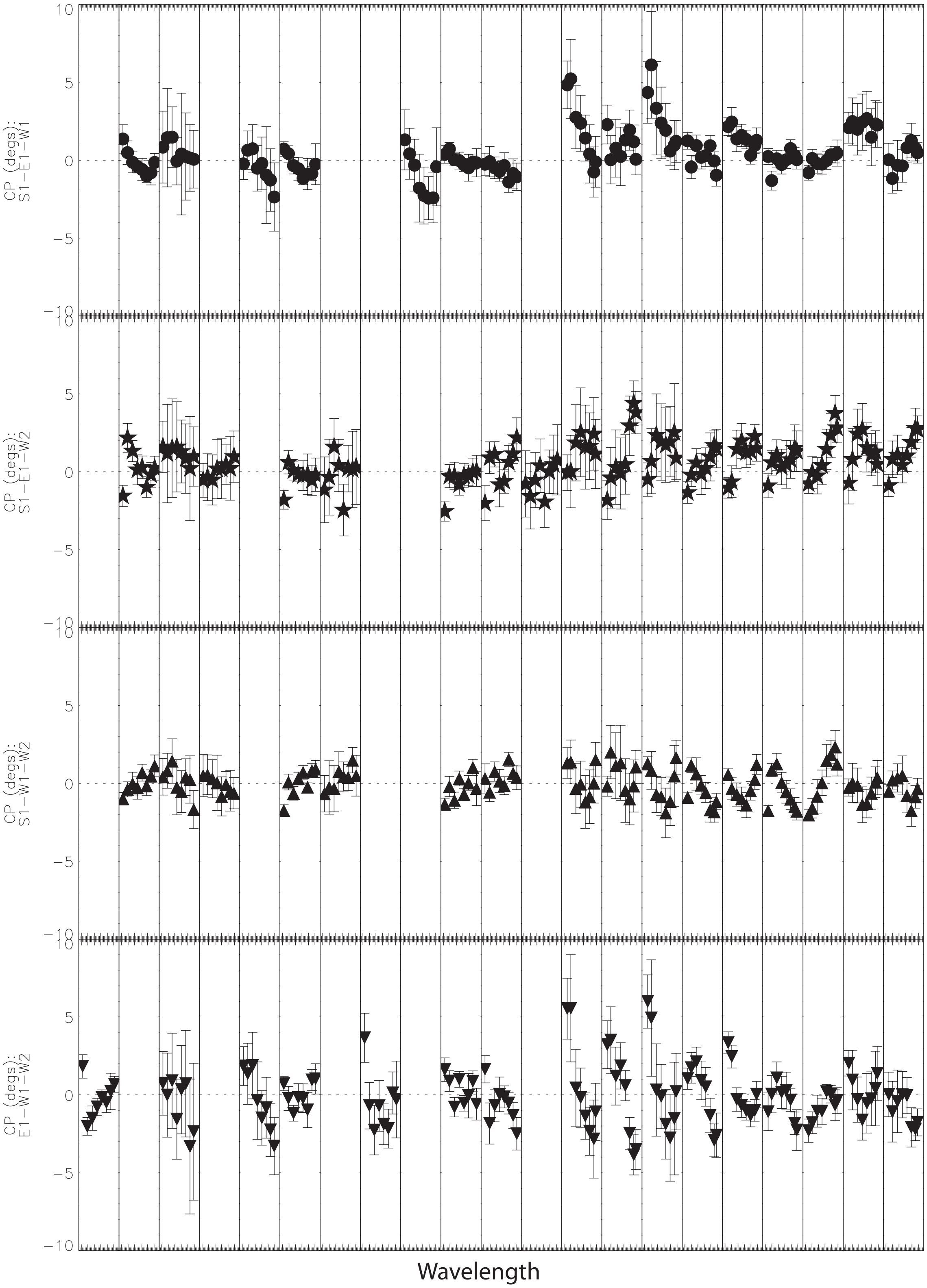

Figure 5.17 ϵ Per closure phase before new calibration scheme. Each column stands for closure phases at different times. The eight points within each panel indicate the closure phases for the eight wavelength channels of MIRC. The four rows stand for the four telescope triangles we use.

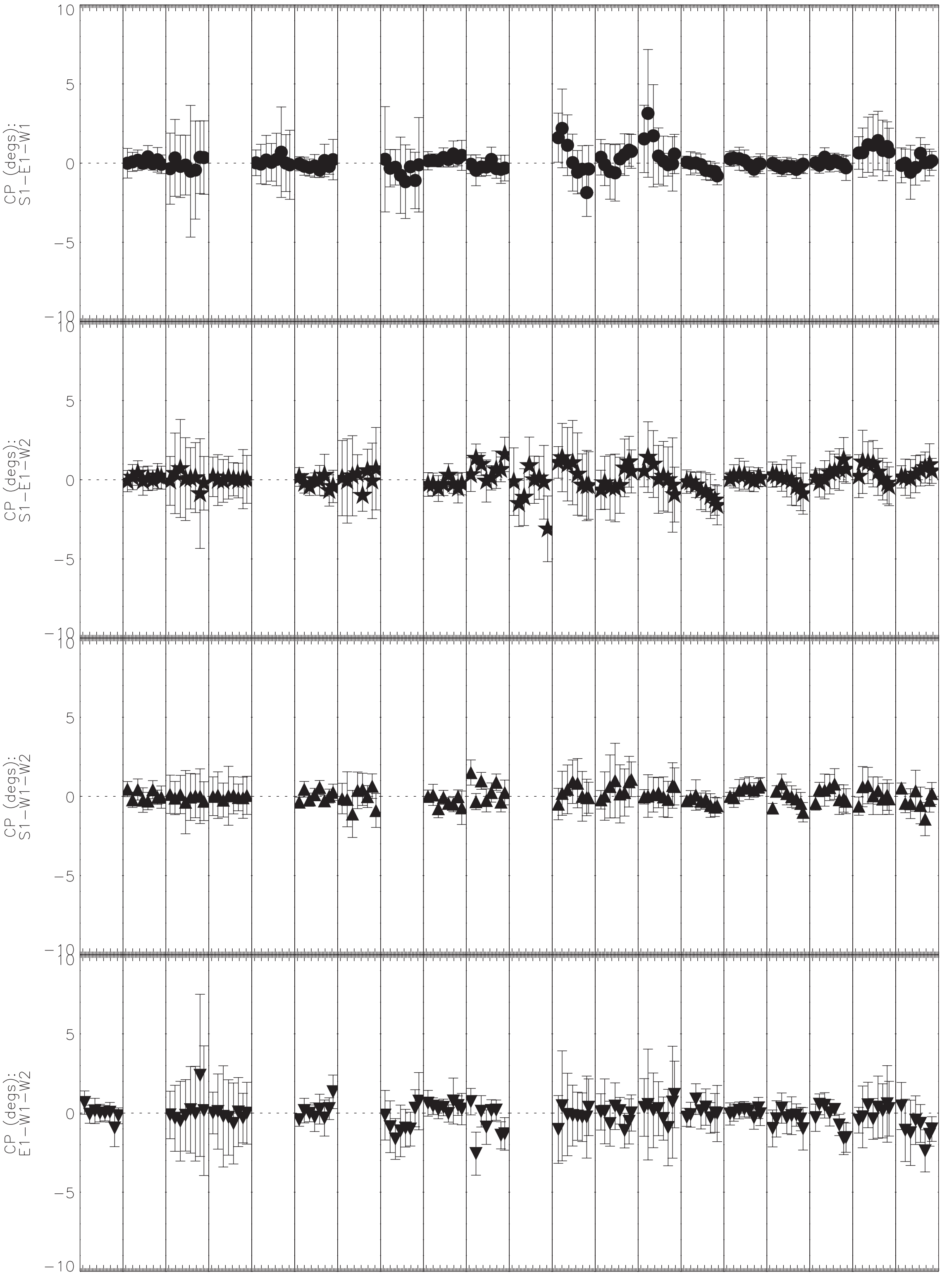

Figure 5.18 ϵ Per closure phase after the new calibration scheme. Each column stands for closure phases at different times. The eight points within each panel indicate the closure phases for the eight wavelength channels of MIRC. The four rows stand for the four telescope triangles we use.

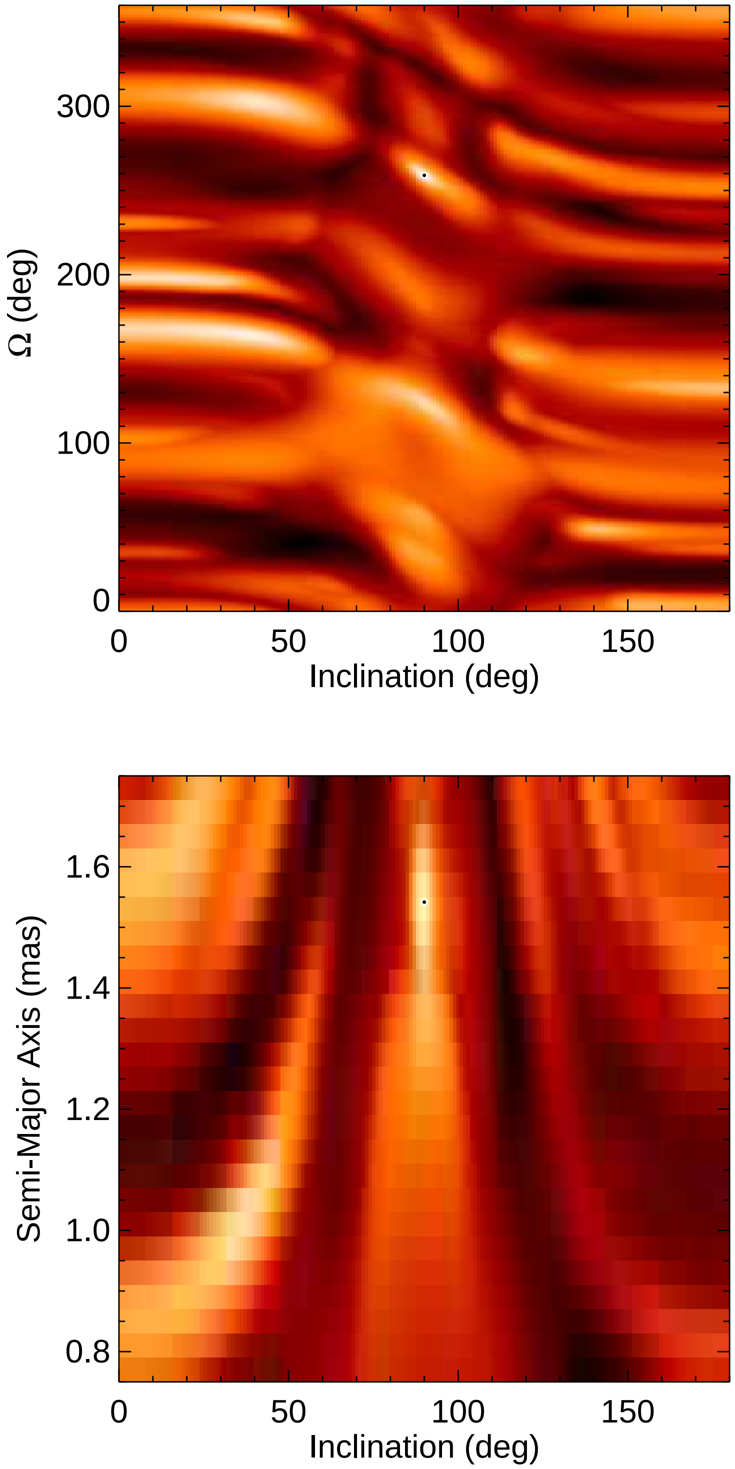

Figure 5.19 The χ^2 surface of the newly calibrated ϵ Per data, after applying the new calibration scheme. The top panel shows the the χ^2 surface of Ω and inclination, while the bottom one shows the χ^2 surface of semi-major axis and inclination. Bright areas indicate low χ^2 and high probability. The black dot at the brightest peak indicates the best result.

5.8 Conclusions and future work

We have simulated the closure phases and differential closure phases for the 3 best hot Jupiter candidates for CHRAR-MIRC. Currently υ And is the best system for CHARA-MIRC because of its highest brightness. Our simulations show that in order to detect the signal from υ And b, the closure phase precision has to be better than 0.17^o, and the differential closure phase precision has to be better than 0.25^o for the long triangles of CHARA. For the short triangles, the closure phase precision has to be better than 0.02^o. We have demonstrated that our closure phase precisions are currently at $\sim 0.6\sigma$ and $\sim 0.4\sigma$ level for the long triangle and the short triangle respectively. This suggests the signal-to-noise of the data has to be 5-7 times of the current value in order to reach a 3σ detection of υ And b, and 9-12 times for a 5-σ detection. To reach this goal, we can take the advantage of the accurately known orbital parameters of hot Jupiter systems and only search for the unknown parameters (i.e., inclination, Ω, flux ratio, and if necessary, day-night flux variation) in our analysis. This approach will not be affected by the fast changing closure phases within one night and thus allow us to observe the target for a long time. It also allows us to combine many nights of data together for a joint search of the hot Jupiter, which will greatly increase the overall signal-to-noise of our data.

We have also investigated the closure phase drifts in our data, and have found that the drifts have strong correlations with azimuth and altitude, implying that this effect may stem from polarization and other systematic effects such as atmospheric dispersion. The closure phase drifts can be well modeled as quadratic plane functions of azimuth and altitude. As shown by our test on the calibrator ζ Per, these functions can be used to predict the zero closure phase points and can be applied to real data as a new calibration scheme.

We have tested our data analysis scheme and calibration scheme on the high contrast binary ϵ Per. We have found possible existence of the companion, but will also need more data and further investigations to confirm the results.

Future work should include further calibration studies to better understand polarization and dispersion effects so that we can better calibrate the closure phase drifts. Simulations of the MIRC system may also be necessary to study systematic errors. More observations are strongly needed to increase the overall signal-to-noise of ϵ Per data so that the effectiveness of our data analysis method can be validated. More data are also needed for υ And. In addition, differential closure phase may be better in calibrating systematic effects. Also as shown in §5.4, υ And have stronger differential closure phase signal at certain baselines and channels than its closure phases. Thus differential closure phase can be used as another quantity to detect the planet.

In addition to the data analysis and calibration studies, there are also other active efforts to help improve the signal-to-noise of our observations, including the CHAMP fringe tracker for MIRC (Berger et al., 2008) which can help track and stabilize the fringes to increase the coherent time for data collection, a photometric channel for MIRC beams (Che 2009, private communication) which can help improve the flux calibration and increase the data taking efficiency, and other improvements to the CHARA beams. With all these improvements, we are expecting to get ~10 times of more signal-to-noise in future observations, and the goal of detecting light from hot

Jupiters, especially from υ And b will be feasible.

Chapter 6

Summary and Future Work

We have studied three different categories of objects in this thesis using long-baseline near-IR imaging interferometry, including rapid rotators, binaries, and efforts on detecting hot Jupiters. For rapid rotators, we have made one of the first images of main sequence stars other than the Sun and have modeled the surface brightness distributions of α Cep , α Oph , and Altair. We confirmed the gravity-darkening phenomenon, both from imaging and modeling, and also found deficiencies in the standard model. Our modeling allowed us to investigate the effects of rotation to the locations of rapid rotators on the HR diagram. Based on our modeling, we proposed a method to combine interferometric and spectroscopic measurements to weigh stars in a new way.

With the three rapid rotators in this thesis and the other two previously studied objects, Vega and Regulus (Aufdenberg et al., 2006; McAlister et al., 2005), we now have five rapid rotators modeled in total, ranging from B7 to A7, giving us for the first time a decent sample to calibrate the luminosity and effective temperature of the upper main sequence. In addition to these five rapid rotators, we have also observed a few more objects, so the next step will be to continue increasing the database of rapid rotators to provide an even bigger sample.

To further investigate the deficiencies of the standard gravity darkening model, we also need detailed high resolution line profile analysis and images at visible to characterize the temperature profile of rapid rotators, and to investigate possible effects of differential rotation. Direct fit to a temperature profile that is independent to the gravity darkening model is also necessary to study the real temperature structure of these stars. For the case of α Oph, because of its symmetric geometry, higher resolution observations at shorter wavelengths such as visible are strongly needed to break model degeneracies and characterize its gravity darkening. At last, test of more sophisticated non-Roche models such as those of MacGregor et al. (2007) is also an important direction to pursue in the future.

For binary stars, we have determined the orbital elements and the masses of the metalic-lined A binary λ Vir and the eclipsing and interacting binary β Lyr by combing interferometric and spectroscopic measurements. Most importantly, we have made the first resolved images of β Lyr , the closest binary system by far, revealing the faces of its components for the first time within more than 200 years. We have also presented simple two-component models for β Lyr in this thesis. However, discrepancies were also found between different models and between models and images. To address these issues and better understand other physical properties of β Lyr, a more physical, self-consistent model is required that treats the radiative transfer and the sizes of the two components properly, accounts for all epochs simultaneously, and incorporates the multi-wavelength information from eclipsing light curves. For λ Vir, we compared our observations with stellar evolution models and found it has subsolar metallicity, indicating the evolution of λ Vir is similar to that of normal A stars despite their surface abundance anomalies. With its accurately determined physical properties and well known evolution status, λ Vir serves as an ideal candidate for follow up studies such as detailed abundance analyses and atomic diffusion modelling that can shed light on our understanding of the causes of the Am phenomenon. In addition to the study of λ Vir, we have also investigated the bandwidth smearing effects of closure phases for the first time and have made an empirical criteria to determine when bandwidth smearing is important for closure phases.

We have also presented the first detailed study of precision closure phases toward directly detecting thermal emission from hot Jupiters, including simulations and test observations, and have demonstrated the best closure phase precision to date. We have also found for the first time a closure phase-boosting effect that can largely increase the closure phase signal when the host star is resolved by the array. On the other hand, we have also found systematics in our data which greatly affect the precision of our measurements. Investigation of these systematics has provided a new calibration scheme, allowing us to calibrate the azimuth-and-altitude-dependent drift of closure phase to some extent. However, further investigations of systematic errors and improvements to the calibration schemes are still needed to increase our precision to the required level, including test of dispersion effects and modeling polarization. More observations are still strongly needed to increase the overall signal-to-noise of our data and to validate the new calibration method. Future simulations of the MIRC system may also be necessary to study systematic errors. In addition to the precision closure phase method, differential phase and differential closure phase are also potentially very stable observables for high precision measurements. More studies are needed to explore the potential of these two observables and to apply them to exoplanet work. Together with other efforts that are being pursued to improve the signal-to-noise of our measurements, these methods can provide us a unique way to characterize the atmospheres of non-transiting hot Jupiters in the future.

Appendices

Appendix A

CHARA Observing Planning Tool

As we have discussed in §2.6.1, CHARA has six telescopes separated by distances ranging from 30m to 331m. To compensate the large optical path differences among different light beams that come into the telescopes, CHARA uses two systems, a 44m movable delay line system and a POP system. The POPs have five different fixed optical delay intervals, ranging from 0m to 143.1m. Because of this, using a certain POP will limit the observable area on the sky. Figure A.1 shows the sky coverage of CHARA, from using 2 telescopes only to all 6 telescopes. Using more telescopes gives less observable sky area. For instance, using 6 telescopes limits the observable sky to a area with only ∼2 hours of R.A. across and 10^o of Declination for POP 111235. Because each telescope has 5 possible POP setups, there are 7776 possible POP choices in total if we use all 6 telescopes, and 1024 choices if we use 4 telescopes, making it very difficult to choose the optimal POPs for a certain group of targets. Therefore, we've made an observing planning tool for MIRC and CHARA users to configure the array and organize their observations.

The software is available at http://www.astro.lsa.umich.edu/∼mingzhao/mirc_plan.zip. We present some screenshot of the tool in Figure A.2 and give some brief instructions on how to use the tool in the following sections.

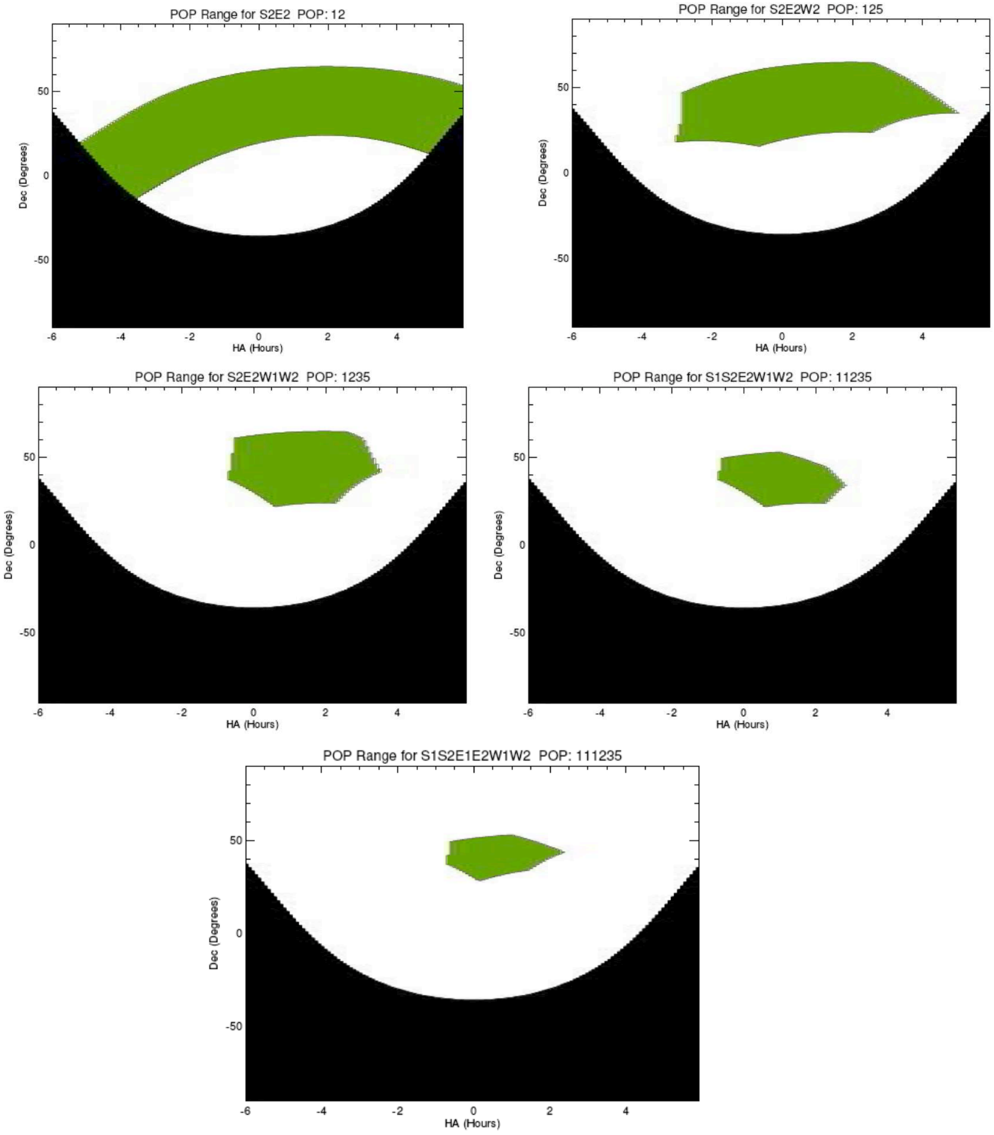

Figure A.1 An example of CHARA sky coverage for various telescope combinations and POP configurations. Green areas indicate observable areas on the sky, while dark areas means unreachable places by the telescopes.

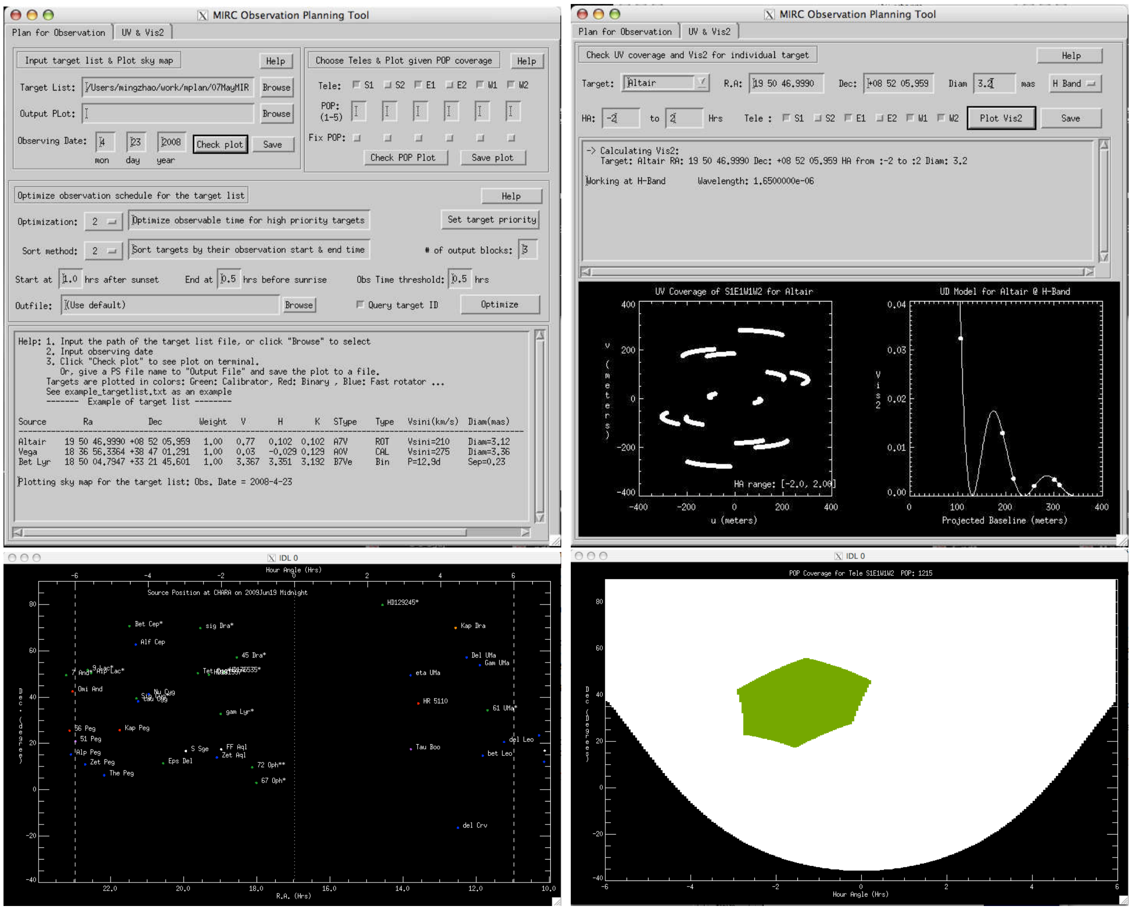

Target List: /Users/mingzhao/work/mplan/07MayMIR

Output PLot:

Observing Date: 4 (mon) 23 (day) 2008 (year)

Tele: ☑ S1 ☐ S2 ☑ E1 ☐ E2 ☑ W1 ☑ W2

POP: (1-5)

Fix POP: ☐ ☐ ☐ ☐ ☐ ☐

Optimization: 2 Optimize observable time for high priority targets

Sort method: 2 Sort targets by their observation start & end time

\# of output blocks: 3

Start at 1.0 hrs after sunset End at 0.5 hrs before sunrise Obs Time threshold: 0.5 hrs

Outfile: (Use default) ☐ Query target ID

```
Help: 1. Input the path of the target list file, or click "Browse" to select
      2. Input observing date
      3. Click "Check plot" to see plot on terminal.
         Or, give a PS file name to "Output File" and save the plot to a file.
      Targets are plotted in colors: Green: Calibrator, Red: Binary , Blue: Fast rotator ...
      See example_targetlist.txt as an example
      -------  Example of target list --------

Source      Ra            Dec           Weight  V      H      K     SType  Type  Vsini(km/s)  Diam(mas)
---------------------------------------------------------------------------------------------------------
Altair   19 50 46.9990 +08 52 05.959  1.00   0.77   0.102  0.102 A7V    ROT   Vsini=210    Diam=3.12
Vega     18 36 56.3364 +38 47 01.291  1.00   0.03   -0.029 0.129 A0V    CAL   Vsini=275    Diam=3.36
Bet Lyr  18 50 04.7947 +33 21 45.601  1.00   3.367  3.351  3.192 B7Ve   Bin   P=12.9d      Sep=0.23

Plotting sky map for the target list: Obs. Date = 2008-4-23
```

Target: Altair R.A: 19 50 46.9990 Dec: +08 52 05.959 Diam 3.2 mas H Band

HA: -2 to 2 Hrs Tele : ☑ S1 ☐ S2 ☑ E1 ☐ E2 ☑ W1 ☑ W2

```
-> Calculating Vis2:
   Target: Altair RA: 19 50 46.9990 Dec: +08 52 05.959 HA from :-2 to :2 Diam: 3.2

Working at H-Band      Wavelength: 1.6500000e-06
```

Figure A.2 Screenshots of the Observation Planning Tool.

A.1 Introduction to the software

The MIRC Planning Tool is divided into four parts. The first three parts work together to collect the target list, provide a sky chart for the targets, visualize the sky coverage of different POP combinations for all telescope configurations, and help to optimize the POP configuration based on the priority of the targets. They also output a detailed observing schedule that can be used directly by observers. These three parts are arranged in the same page of the GUI as three separate sections, as shown in the top left panel of Figure A.2. The bottom of the first page of the GUI gives information of any actions. Sky charts and POP coverage plots generated by the software will be shown in separate pop-up windows, as indicated by the two bottom panels of Figure A.2.

The fourth part of the software is arranged on the second page, which can be accessed by pressing down the second tab at the top of the GUI. This part of the software can help observers to look at the UV coverage of the observations and predict the squared visibilities of a given target. The screenshot is shown in the top right panel of Figure A.2.

Here we give a brief instruction on how to use the software. There are also HELP buttons in each tool box to give brief instructions about the function of each panel and how to use them. To run the program, one needs to use the up-to-date IDL Astrolib, which can be found from the internet. After downloading the Astrolib, one needs to put the directory path into the !path variable. For example:

```
!path=!path+“:”+expand_path(’+’+’∼/work/mplan:’),
```

where ’∼/work/mplan’ is the full path of the mircplan directory.

Before starting the program, one also needs to make a list that contains all the information about the targets and calibrators. To do this, one can use the file example_targetlist.txt as an example. One has to follow the format of the example strictly, otherwise the program may give wrong output due to mis-reading the target list. It is better to fill in all information to the target list, although the minimum requirements are: Source, R.A., Dec., Weight, V, H, and K.

Currently, the program works in the mirc_plan directory only. To start the program, enter IDL and type: @mircplan

Below is a common procedure to run the program:

1. Make a target list file according to example_targetlist.txt

2. Input the path of the target list in the first box (upper left box).

3. Input observing time (default is current date)

4. Check the sky plot

5. Goto the second tool box (the right side one) and assign telescopes.

6. Goto the third tool box and set target priority if the priorities are not set previously in the file. Normally this does not need to be changed.

7. Click Optimize and check the output files. Usually, one needs to go through the best POPs and choose the one that has the best hour angle coverage. Note: CHARA has a zenith hole of 8^o-10^o, which has to be taken into account when picking the optimal POPs.

8. If need to check POP coverage, go to the second box, assign POPs under the check box of each telescope, and click to check the pop coverage plot.

9. If you want to fix some certain pops for optimization, for example, if you

want to fix S1 to POP 2, E1 to POP 3, just type in the pop numbers for those telescopes and check the corresponding FIX POP boxes. Then go to the third tool and optimize.

10. In the second tab, UV & Vis2, all information need to be filled in order to run the program.

Appendix B

Calibrators

To calibrate the systematic visibilities of science targets, one has to observe calibrators adjacent to the targets every night. Unresolved bright stars close to the targets on the sky are the best calibrators for this purpose. However, because of the high resolution of the CHARA baselines and the limited sensitivity of MIRC (currently H<4.5 mag), it is not easy to find ideal calibrators, especially those near science targets. Therefore, we have carefully selected a list of targets that are good for MIRC and other combiners at CHARA in Table B.1 below.

Table B.1. List of calibrators for MIRC and the CHARA array

Source		R.A.			Dec		V	H	K	Vsini	Diameter	Spectral	Reference^b
	(hr)	(min)	(sec)	(^{o})	(')	(")				(km/s)	(mas)	Type ^{a}	
Gam Peg	0	13	14.1528	+15	11	0.945	2.83	3.638	3.77	5	0.42±0.09	B2IV	1
87 Peg	0	9	2.4247	+18	12	43.067	5.565	3.476	3.321		1.066±0.014	G9III	3
37 And	0	56	45.2115	+38	29	57.641	3.867	3.652	3.636	80	0.789±0.007	A5V	2
HD 3989	0	42	48.964	+45	55	46.306	7.07	3.71	3.49		1.414±0.015	K5III	3
Zet Cas	0	36	58.2846	+53	53	48.874	3.666	4.248	4.247	10	0.30±0.09	B2IV	1
Kap Cas	0	32	59.9917	+62	55	54.418	4.189	4.148	4.013	55	0.39±0.05	B1Ia	1
Chi Cet	1	49	35.1027	-10	41	11.077	4.664	3.47	3.872	65	0.82±0.10	F3III	1
Ups And	1	36	47.8428	+41	24	19.652	2.7	2.957	2.859	11	1.098±0.007	F8V	2
49 And	1	30	6.1025	+47	0	26.185	5.269	3.42	3.12	10	1.121±0.015	G9III	3
HD 9022	1	30	18.3082	+59	46	55.377	6.904	3.43	3.2		1.028±0.014	K3III	3
Eps Cas	1	54	23.7255	+63	40	12.365	3.342	3.934	3.963	30	∼0.6	B3III	9
Gam Tri	2	17	18.8673	+33	50	49.897	4	3.862	3.958	254	0.522±0.033	A1Vnn	4
50 Cas	2	3	26.1053	+72	25	16.66	3.948	3.898	3.921	90	0.5	A2V	9
94 Cet	3	12	46.4365	-1	11	45.964	5.06	3.768	3.748	7	0.77±0.06	F8V	1
HD 20791	3	21	6.8033	+3	40	32.233	5.69	3.58	3.54	-	0.907±0.012	G8.5III	3
Zet Per	3	54	7.9215	+31	53	1.088	2.883	2.621	2.603	55	0.67±0.03	B1Ib	1
Eps Per	3	57	51.2307	+40	0	36.773	2.901	3.595	3.713	130	0.36±0.07	B0.5V	1
HD 20762	3	23	32.8041	+58	43	19.276	6.591	3.51	3.27		0.876±0.012	K0II-III	3
HD 22427	3	39	32.6332	+59	26	43.561	6.9	3.65	3.38		0.907±0.013	K2III-IV	3
tau Ori	5	17	36.3899	-6	50	39.874	3.59	3.887	3.875	40	0.45	B5III	9
kap Ori	5	17	36.3899	-6	50	39.874	2.049	2.686	2.679	80	0.45±0.03	B0Iab	8
Eps Ori	5	36	12.8135	-1	12	6.911	1.7	2.408	2.273	85	0.69±0.04	B0Ia	8
Gam Ori	5	25	7.8631	+6	20	58.928	1.64	2.357	2.375	55	0.72±0.04	B2III	8
Eta Aur	5	6	30.8928	+41	14	4.108	3.152	3.761	3.857	125	0.374±0.079	B3V	4
tet Gem	6	52	47.3382	+33	57	40.514	3.6	3.229	3.163	130	0.82±0.03	A3III	8
24 CMa	7	3	1.4726	-23	49	59.847	3	3.275	3.342	55	0.26±0.20	B3Ia	1
32 Hya	9	31	58.9281	-1	11	4.79	4.555	4.187	4.146	70	0.59±0.17	A3V	1
Tet Hya	9	14	21.859	+2	18	51.409	3.88	4.04	3.943	100	0.59±0.12	B9.5V	1
24 Uma	9	34	28.8597	+69	49	49.234	4.565	2.735	2.68	10	1.41±0.20	G4III	1
48 Leo	10	34	48.0147	+6	57	13.496	5.081	3.008	2.977	10	1.35±0.15	G8.5III	1
eta Leo	10	7	19.9523	+16	45	45.592	3.511	3.499	3.299	23	0.67±0.07	A0Ib	1
lam Uma	10	17	5.7915	+ 42	54	51.714	3.442	3.459	3.418	35	0.81±0.26	A2IV	1
Phi Leo	11	16	39.7009	-3	39	5.764	4.467	4.186	4.126	254	0.56	A7IVn	9
tet Leo	11	14	14.405	+15	25	46.453	3.3	3.19	3.082	24	0.86±0.22	A2V	1
61 Uma	11	41	3.015	+34	12	5.888	5.3	3.648	3.588	8	0.88±0.06	G8V	1
BET Uma	11	1	50.4768	+56	22	56.736	2.346	2.359	2.285	32	1.27±0.29	A1V	1

Table B.1—Continued

Source		R.A.			Dec		V	H	K	Vsini	Diameter	Spectral	Reference^{b}
	(hr)	(min)	(sec)	(^{o})	(’)	(”)				(km/s)	(mas)	Type ^{a}	
gam Crv	12	15	48.3702	-17	32	30.946	2.59	2.975	2.945	30	0.75±0.06	B8III	8
HD104356	12	1	1.7	-1	46	5.4	6.329	3.482	3.349		0.938±0.013	G8III	3
HD112413	12	56	1.6674	+ 38	19	6.167	2.9	3.131	3.145	29	0.66±0.11	alpha2 CVn	1
70 Vir	13	28	25.809	+13	46	43.634	5	3.457	3.5	3	0.94±0.10	G5V	1
HD114889	13	13	12.4043	18	43	37.228	6.11	3.44	3.175		1.048±0.015	G8III	3
bet Com	13	11	52.393	+27	52	41.459	4.26	2.992	2.923	10	1.18±0.08	G0V	1
9 Lib	14	50	52.7131	-16	2	30.401	2.753	2.439	2.44	102	1.23±0.18	A3IV	1
HD129245	14	33	38.3	+79	39	37.5	6.28	3.48	3.23		1.15±0.02	K3III	3
32 Ser	15	49	37.2084	-3	25	48.748	3.548	3.759	3.702	80	0.67±0.22	A0V	1
eps Ser	15	50	48.9661	+4	28	39.829	3.713	3.44	3.425	47	0.8±0.15	A2m	1
HD139087	15	35	53.3678	+ 11	15	56.361	6.051	3.263	3.208		1.009±0.013	K0III	3
gam Ser	15	56	27.183	+15	39	41.821	3.85	2.875	2.703	10	1.29±0.10	F6IV	1
HD133392	15	3	6.0551	+35	12	20.864	5.521	3.356	3.257		1.048±0.015	G8III	3
Zet Oph	16	37	9.5378	-10	34	1.524	2.578	2.667	2.684	341	0.51±0.05	Be	5
HD162113	17	49	19.0434	+1	57	41.089	6.458	3.129	3.619		0.90±0.012	K0III	3
94 Her	17	58	30.1494	+30	11	21.396	4.411	2.823	2.771	30	1.02±0.24	F2II	1
Del UMi	17	32	13.0005	+86	35	11.258	4.348	4.331	4.258	180	0.46	A1Vn	9
67 Oph	18	0	38.7157	+2	55	53.643	3.974	3.975	4.001	40	0.49±0.11	B5Ib	1
72 Oph	18	7	20.9842	+9	33	49.85	3.722	3.426	3.412	75	0.74±0.03	A4IVs	8
HD173667	18	45	39.7254	+20	32	46.708	4.2	3.286	3.19	12	0.98±0.04	F6V	7
110 Her	18	45	39.7254	+20	32	46.708	4.2	3.286	3.19	12	0.98±0.04	F6V	8
gam Lyr	18	58	56.6227	+32	41	22.407	3.24	3.227	3.122	71	0.74±0.1	B9III	8
HD175535	18	53	13.5455	+50	42	29.597	4.92	3.134	2.73	10	1.35±0.31	G7IIIa	1
45 Dra	18	32	34.5226	+57	2	44.157	4.781	2.93	2.704	17	1.35±0.25	F7Ib	1
HD 176598	18	56	25.7187	+65	15	29.101	5.632	3.63	3.4		0.924±0.012	K1III	3
Lam Aql	19	6	14.9384	-4	52	57.195	3.427	3.477	3.564	155	0.64±0.16	B5Vn	1
Alf Sge	19	40	5.7918	+18	0	50.006	4.392	2.746	2.616	10	1.31±0.05	G1II	6
HD 181597	19	18	37.8714	+49	34	10.042	6.326	3.79	3.65		0.878±0.012	K1III	3
HR 7420	19	29	42.3591	+51	43	47.204	3.769	3.691	3.598	220	0.72	A5Vn	9
sig Dra	19	32	21.5908	+69	39	40.232	4.7	3.039	2.78	8	1.28±0.08	K0V	1
Eps Aqr	20	47	40.5515	-9	29	44.793	3.77	3.671	3.737	130	0.71±0.18	A1.5V	8
Tau Aql	20	4	8.3152	+7	16	40.677	5.521	3.307	3.197	-	1.097±0.014	K0III	3
Eps Del	20	33	12.7712	+11	18	11.746	4.032	4.55	4.381	50	0.38	B6 III	9
24 Vul	20	16	47.0859	+24	40	15.966	5.306	3.186	3.014	10	1.08±0.015	G8III	3
Sig Cyg	21	17	24.9529	+39	23	40.853	4.256	3.864	3.683	30	0.542±0.021	B9 Iab	2
Gam Aqr	22	21	39.3754	-1	23	14.393	3.847	4.053	4.021	80	0.52	A0V	9

Table B.1—Continued

Source	R.A.			Dec			V	H	K	Vsini	Diameter	Spectral Type [a]	Reference[b]
	(hr)	(min)	(sec)	(^{o})	(')	(")				(km/s)	(mas)		
Tet Peg	22	10	11.9852	+6	11	52.314	3.5	3.39	3.377	144	0.80±0.17	A1Va	1
zet Peg	22	41	27.7208	+10	49	52.912	3.4	3.527	3.566	210	0.65±0.14	B8.5V	8
ksi Peg	22	46	41.581	+12	10	22.396	4.2	3.078	2.961	9	1.10±0.06	F7V	1
HD214995	22	41	57.4557	+14	30	59.014	5.927	3.52	3.21	-	0.971±0.013	K0III	3
51 Peg	22	57	27.9805	+20	46	7.796	5.5	4.234	3.911	-	0.71±0.05	G2.5IVa	8
29 Peg	22	9	59.2441	+33	10	41.606	4.292	3.299	3.117	-	1.017±0.027	F5III	2
Alp Lac	22	31	17.501	+50	16	56.969	3.777	3.867	3.851	150	0.66±0.16	A1V	1
9 Lac	22	37	22.4177	+51	32	42.442	4.654	3.693		90	0.65±0.08	A8IV	1
Iot Psc	23	39	57.0409	+5	37	34.65	4.13	2.988	2.946	3	1.19±0.06	F7V	1
ups Peg	23	25	22.7841	+23	24	14.764	4.4	3.23	3.033	85	1.01±0.04	F8IV	6
7 And	23	12	33.0034	+49	24	22.346	4.54	3.76	3.791	65	0.663±0.024	F0V	4

[a] Spectral types, coordinates, and the V, H, K magnitudes are from the SIMBAD database, operated at CDS, Strasbourg, France

[b] References: 1. from getCal: http://nexsciweb.ipac.caltech.edu/gcWeb/gcWeb.jsp ; 2. Private communication, (Mérand 2008); 3. Mérand et al. (2005) ; 4. van Belle et al. (2008) ; 5. Hanbury Brown et al. (1974); 6. Blackwell & Lynas-Gray (1994); 7. Blackwell & Lynas-Gray (1997) ; 8. CHARM Catalog (Richichi et al., 2005) 9. Pasinetti Fracassini et al. (2001)

References

Abt, H. A. 1961, *ApJS*, 6, 37

Abt, H. A., & Morrell, N. I. 1995, *ApJS*, 99, 135

Abt, H. A. 2000, *ApJ*, 544, 933

Abt, H. A., Levato, H., & Grosso, M. 2002, *ApJ*, 573, 359

Ak, H., Chadima, P., Harmanec, P., et al. 2007, *A&A*, 463, 233

Alonso, A., Arribas, S., & Martinez-Roger, C. 1996, *A&A*, 313, 873

Alonso, A., Arribas, S., & Martinez-Roger, C. 1998, *A&AS*, 131, 209

Andersen, J. 1991, *A&A Rev.*, 3, 91

Aufdenberg, J. P., et al. 2006, *ApJ*, 645, 664

Augensen, H. J. & Heintz, W. D. 1992, *PASP*, 104, 314

Baines, E. K., van Belle, G. T., ten Brummelaar, T. A., McAlister, H. A., Swain, M., Turner, N. H., Sturmann, L., & Sturmann, J. 2007, *ApJ*, 661, L195

Baines, E. K., McAlister, H. A., ten Brummelaar, T. A., Turner, N. H., Sturmann, J., Sturmann, L., Goldfinger, P. J., & Ridgway, S. T. 2008, *ApJ*, 680, 728

Baines, E. K., McAlister, H. A., ten Brummelaar, T. A., Sturmann, J., Sturmann, L., Turner, N. H., & Ridgway, S. T. 2009, arXiv:0906.2702

Baade, W. 1926, Astronomische Nachrichten, 228, 359

Baldwin, J. E., Beckett, M. G., Boysen, R. C., Burns, D., et al. 1996, *A&A*, 306, L13+

Balona, L. A. 1994, *MNRAS*, 268, 119

Barman, T. S., Hauschildt, P. H., & Allard, F. 2005, *ApJ*, 632, 1132

Barnes, T. G., Evans, D. S., & Moffett, T. J. 1978, *MNRAS*, 183, 285

Berger, J.-P., et al. 2003, Proceedings of the SPIE, 4838, 1099

Berger, D. H., et al. 2006, *ApJ*, 644, 475

Berger, D. H., et al. 2008, *Proc. SPIE*, 7013, Bernacca, P. L. & Perinotto, M. 1973, A catalogue of stellar rotational velocities. (Contributi dell'Osservatorio Astrofisico dell'Universita di Padova in Asiago, Padova: Cleup, 1970-1973)

Bisikalo, D. V., Harmanec, P., Boyarchuk, A. A., Kuznetsov, O. A., & Hadrava, P. 2000, *A&A*, 353, 1009

Blackwell, D. E., Petford, A. D., Arribas, S., Haddock, D. J., & Selby, M. J. 1990, *A&A*, 232, 396

Blackwell, D. E. & Lynas-Gray, A. E. 1994, *A&A*, 282, 899

Blackwell, D. E., & Lynas-Gray, A. E. 1997, NASA STI/Recon Technical Report N, 98, 69702

—. 1998, *A&AS*, 129, 505

Blackwell, D. E., Petford, A. D., & Shallis, M. J. 1980, *A&A*, 82, 249

Blackwell, D. E., Shallis, M. J., & Selby, M. J. 1979, *MNRAS*, 188, 847

Boden, A. F. 1999, in Principles of Long Baseline Interferometry, Edited by Peter R. Lawson, 9–29

Boden, A. F., Torres, G., & Hummel, C. A. 2005, *ApJ*, 627, 464

Boden, A. F., Torres, G., & Latham, D. W. 2006, *ApJ*, 644, 1193

Boden, A. F., Akeson, R. L., Sargent, A. I., Carpenter, J. M., Ciardi, D. R., Bary, J. S., & Skrutskie, M. F. 2009, *ApJ*, 696, L111

Boccaletti, A., Moutou, C., Mouillet, D., Lagrange, A.-M., & Augereau, J.-C. 2001, *A&A*, 367, 371

Böhm-Vitense, E. 2006, *PASP*, 118, 419

Bond, I. A., et al. 2004, *ApJ*, 606, L155

Born, M. 1999, Principles of optics: 7th (expanded) edition by Born, M., 1999.,

Breger, M. 1976, *ApJS*, 32, 7

Briggs, D. S., Schwab, F. R., & Sramek, R. A. 1999, Synthesis Imaging in Radio Astronomy II, 180, 127

Burns, D., et al. 1997, *MNRAS*, 290, L11

Burrows, A., Dessart, L., Livne, E., Ott, C. D., & Murphy, J. 2007, *ApJ*, 664, 416

Burrows, A., Budaj, J., & Hubeny, I. 2008, *ApJ*, 678, 1436

Burrows, A., Marley, M., Hubbard, W. B., Lunine, J. I., Guillot, T., Saumon, D., Freedman, R., Sudarsky, D., & Sharp, C. 1997, *ApJ*, 491, 856

Burrows, A., Hubeny, I., & Sudarsky, D. 2005, *ApJ*, 625, L135

Burrows, A., Guillot, T., Hubbard, W. B., Marley, M. S., Saumon, D., Lunine, J. I., & Sudarsky, D. 2000, *ApJ*, 534, L97

Burrows, A., Hubeny, I., Budaj, J., Knutson, H. A., & Charbonneau, D. 2007, *ApJ*, 668, L171

Butler, R. P., Marcy, G. W., Fischer, D. A., Brown, T. M., Contos, A. R., Korzennik, S. G., Nisenson, P., & Noyes, R. W. 1999, *ApJ*, 526, 916

Butler, R. P., Marcy, G. W., Williams, E., Hauser, H., & Shirts, P. 1997, *ApJ*, 474, L115

Budaj, J. 1996, *A&A*, 313, 523

Budaj, J. 1997, *A&A*, 326, 655

Bundy, K. A., & Marcy, G. W. 2000, *PASP*, 112, 1421

Burnashev, V. I. 1985, Abastumanskaia Astrofizicheskaia Observatoriia Biulleten, 59, 83

Buscher, D. F., 1994, Proc. SPIE 2200, 260

Cameron, A. C., Horne, K., Penny, A., & James, D. 1999, *Nature*, 402, 751

Campbell, W. W., Moore, J. H., Wright, W. H., & Duncan, J. C. 1911, Lick Observatory Bulletin, 6, 140

Cassisi, S. 2009, American Institute of Physics Conference Series, 1111, 55

Cayrel, R., Burkhart, C., & van't Veer, C. 1991, in IAU Symp. 145: Evolution of Stars: the Photospheric Abundance Connection, 99–+

Charbonneau, D., Allen, L. E., Megeath, S. T., Torres, G., Alonso, R., Brown, T. M., Gilliland, R. L., Latham, D. W., Mandushev, G., O'Donovan, F. T., & Sozzetti, A. 2005, *ApJ*, 626, 523

Charbonneau, D., Knutson, H. A., Barman, T., Allen, L. E., Mayor, M., Megeath, S. T., Queloz, D., & Udry, S. 2008, *ApJ*, 686, 1341

Clark, B. G. 1980, *A&A*, 89, 377

Claret, A. 2004, *A&A*, 424, 919

Claret, A. & Cunha, N. C. S. 1997, *A&A*, 318, 187

Claret, A. 1998, *A&AS*, 131, 395

—. 2000, *A&A*, 359, 289

Cohen, M., Walker, R. G., Carter, B., Hammersley, P., Kidger, M., & Noguchi, K. 1999, *AJ*, 117, 1864

Colacevich, A. 1941, Oss. Mem. Arcetri, 58, 28

Cornwell, T. J., & Wilkinson, P. N. 1981, *MNRAS*, 196, 1067

Cornwell, T., Braun, R., & Briggs, D. S. 1999, Synthesis Imaging in Radio Astronomy II, 180, 151

Coude du Foresto, V., Ridgway, S., & Mariotti, J.-M. 1997, *A&AS*, 121, 379

Cowley, A., Cowley, C., Jaschek, M., & Jaschek, C. 1969, *AJ*, 74, 375

Cox, A. N. 2000, *S&T*, 100, 388

Crawford, D. L. 1979, *AJ*, 84, 1858

Creevey, O. L., Monteiro, M. J. P. F. G., Metcalfe, T. S., Brown, T. M., Jiménez-Reyes, S. J., & Belmonte, J. A. 2007, *ApJ*, 659, 616

Cutri, R. M., et al. 2003, 2MASS All Sky Catalog of point sources.

Cunha, M. S., et al. 2007, *A&A Rev.*, 14, 217

Danchi, W. C., Bester, M., Degiacomi, C. G., Greenhill, L. J., & Townes, C. H. 1994, *AJ*, 107, 1469

Demarque, P., Woo, J.-H., Kim, Y.-C., & Yi, S. K. 2004, *ApJS*, 155, 667

Domiciano de Souza, A., Kervella, P., Jankov, S., Abe, L., Vakili, F., di Folco, E., & Paresce, F. 2003, *A&A*, 407, L47

Deming, D., Harrington, J., Seager, S., & Richardson, L. J. 2006, *ApJ*, 644, 560

Deming, D., Seager, S., Richardson, L. J., & Harrington, J. 2005, *Nature*, 434, 740

de Mooij, E. J. W., & Snellen, I. A. G. 2009, *A&A*, 493, L35

Drake, S. A., Pravdo, S. H., Angelini, L., & Stern, R. A. 1998, *AJ*, 115, 2122

Esa, . 1997, VizieR Online Data Catalog, 1239, 0

Erspamer, D. & North, P. 2003, *A&A*, 398, 1121

Espinosa Lara, F. & Rieutord, M. 2007, *A&A*, 470, 1013

Frémat, Y., Zorec, J., Hubert, A.-M., & Floquet, M. 2005, *A&A*, 440, 305

Gatewood, G. 2005, *AJ*, 130, 809

Gliese, W., & Jahreiss, H. 1991, NASA STI/Recon Technical Report A, 92, 33932

Gies, D. R., et al. 2007, *ApJ*, 654, 527

Gillich, A., Deupree, R. G., Lovekin, C. C., Short, C. I., & Toqué, N. 2008, *ApJ*, 683, 441

Glushneva, I. N., Doroshenko, V. T., Fetisova, T. S., Khruzina, T. S., Kolotilov, E. A., Mossakovskaya, L. V., Ovchinnikov, S. L., & Voloshina, I. B. 1998, VizieR Online Data Catalog, 3208, 0

Goodricke, J. 1785, Phil. Trans. Roy. Soc., 75

Gray, D. F. 1992, Science, 257, 1978

Gray, R. O., Corbally, C. J., Garrison, R. F., McFadden, M. T., & Robinson, P. E. 2003, *AJ*, 126, 2048

Gray, R. O., Napier, M. G., & Winkler, L. I. 2001, *AJ*, 121, 2148

Griffin, R. E. 2002, *AJ*, 123, 988

Grillmair, C. J., et al. 2008, *Nature*, 456, 767

Guillot, T., Burrows, A., Hubbard, W. B., Lunine, J. I., & Saumon, D. 1996, *ApJ*, 459, L35

Hanbury Brown, R., Davis, J., & Allen, L. R. 1974, *MNRAS*, 167, 121

Harmanec, P. 2002, Astronomische Nachrichten, 323, 87

Harmanec, P., Morand, F., et al. 1996, *A&A*, 312, 879

Harmanec, P., & Scholz, G. 1993, *A&A*, 279, 131

Harrington, J., Hansen, B. M., Luszcz, S. H., Seager, S., Deming, D., Menou, K., Cho, J. Y.-K., & Richardson, L. J. 2006, Science, 314, 623

Harrington, J., Luszcz, S., Seager, S., Deming, D., & Richardson, L. J. 2007, *Nature*, 447, 691

Hanbury Brown, R., Davis, J., Lake, R. J. W., & Thompson, R. J. 1974, *MNRAS*, 167, 475

Henry, G. W., Baliunas, S. L., Donahue, R. A., Fekel, F. C., & Soon, W. 2000, *ApJ*, 531, 415

Henyey, L. G., Wilets, L., Böhm, K. H., Lelevier, R., & Levee, R. D. 1959, *ApJ*, 129, 628

Hillenbrand, L. A., & White, R. J. 2004, *ApJ*, 604, 741

Högbom, J. A. 1974, *A&AS*, 15, 417

Hoffman, J. L., Nordsieck, K. H., & Fox, G. K. 1998, *AJ*, 115, 1576

Hofmann, K.-H., Scholz, M., & Wood, P. R. 1998, *A&A*, 339, 846

Hummel, C. A., Carquillat, J.-M., Ginestet, N., Griffin, R. F., Boden, A. F., Hajian, A. R., Mozurkewich, D., & Nordgren, T. E. 2001, *AJ*, 121, 1623

Hut, P. 1981, *A&A*, 99, 126

Ireland, M. J., Monnier, J. D., & Thureau, N. 2006, in Proceedings of the SPIE, Volume 6268, pp. 62681T (2006).

Ireland, M. J., et al. 2008, in Proceedings of the SPIE, 7013, 63I

Johnson, H. L., & Morgan, W. W. 1953, *ApJ*, 117, 313

Jackson, S., MacGregor, K. B., & Skumanich, A. 2004, *ApJ*, 606, 1196

Jameson, R. F., & Longmore, A. J. 1976, *MNRAS*, 174, 217

Joergens, V., & Quirrenbach, A. 2004, *Proc. SPIE*, 5491, 551

Kalas, P., et al. 2008, Science, 322, 1345

Kamper, K. W., Legget, D., & McCarthy, Jr., D. W. 1989, *AJ*, 98, 686

Kervella, P. & Domiciano de Souza, A. 2006, *A&A*, 453, 1059

Kiziloglu, N. & Civelek, R. 1996, *A&A*, 307, 88

Knutson, H. A., et al. 2007, *Nature*, 447, 183

Knutson, H. A., Charbonneau, D., Allen, L. E., Burrows, A., & Megeath, S. T. 2008, *ApJ*, 673, 526

Kurucz, R. L., Peytremann, E., & Avrett, E. H. 1974, Blanketed model atmospheres for early-type stars (Washington : Smithsonian Institution : for sale by the Supt. of Docs., U.S. Govt. Print. Off., 1974.), 37–+

Kurucz, R. L. 1979, *ApJS*, 40, 1

—. 1993, VizieR Online Data Catalog, 6039, 0

Kunzli, M., North, P., Kurucz, R. L., & Nicolet, B. 1997, *A&AS*, 122, 51

Lebreton, Y. 2000, *ARA&A*, 38, 35

Latham, D. W., Mathieu, R. D., Milone, A. A. E., & Davis, R. J. 1992, in IAU Symp. 151: Evolutionary Processes in Interacting Binary Stars, ed. Y. Kondo, R. Sistero, & R. S. Polidan, 471–+

Latham, D. W., Nordstroem, B., Andersen, J., Torres, G., Stefanik, R. P., Thaller, M., & Bester, M. J. 1996, *A&A*, 314, 864

Latham, D. W., Stefanik, R. P., Torres, G., Davis, R. J., Mazeh, T., Carney, B. W., Laird, J. B., & Morse, J. A. 2002, *AJ*, 124, 1144

Principles of Long Baseline Stellar Interferometry, Ed. by Lawson, P. R., 2000

Lawson, P. R., et al. 2004, Proc. SPIE, 5491, 886

Lawson, P. R., et al. 2006, Proc. SPIE, 6268, 62681U

Leigh, C., Cameron, A. C., Horne, K., Penny, A., & James, D. 2003, *MNRAS*, 344, 1271

Lejeune, T., Cuisinier, F., & Buser, R. 1998, *A&AS*, 130, 65

Levato, A. 1975, *A&AS*, 19, 91

Leggett, S. K., et al. 1986, *A&A*, 159, 217

Libich, J., et al. 2006, *A&A*, 446, 583

Linnell, A. P. 2000, *MNRAS*, 319, 255

Lippincott, S. L. & Wagman, N. E. 1966, *AJ*, 71, 122

Laughlin, G., & Adams, F. C. 1999, *ApJ*, 526, 881

Lucy, L. B. 1967, Zeitschrift fur Astrophysik, 65, 89

MacFadyen, A. I. & Woosley, S. E. 1999, *ApJ*, 524, 262

MacFadyen, A. I., Woosley, S. E., & Heger, A. 2001, *ApJ*, 550, 410

MacGregor, K. B., Jackson, S., Skumanich, A., & Metcalfe, T. S. 2007, *ApJ*, 663, 560

Maeder, A. & Meynet, G. 2000, *ARA&A*, 38, 143

Maeder, A., Meynet, G., & Ekström, S. 2007, in Astronomical Society of the Pacific Conference Series, Vol. 374, 13–+

Malagnini, M. L. & Morossi, C. 1990, *A&AS*, 85, 1015

Marois, C., Macintosh, B., Barman, T., Zuckerman, B., Song, I., Patience, J., Lafrenière, D., & Doyon, R. 2008, Science, 322, 1348

Marcy, G. W., Butler, R. P., Williams, E., Bildsten, L., Graham, J. R., Ghez, A. M., & Jernigan, J. G. 1997, *ApJ*, 481, 926

Mason, B. D., et al. 1999, *AJ*, 117, 1890

Mayor, M., & Queloz, D. 1995, *Nature*, 378, 355

McAlister, H. A. & Hartkopf, W. I. 1984, Catalog of interferometric measurements of binary stars

McAlister, H. A., et al. 2005, *ApJ*, 628, 439

Mérand, A., Bordé, P., & Coudé Du Foresto, V. 2005, *A&A*, 433, 1155

Mérand, A., Bordé, P., & Coudé Du Foresto, V. 2005, *A&A*, 433, 1155

—. 2006, *A&A*, 447, 783

Mermilliod, J.-C., Mermilliod, M., & Hauck, B. 1997, *A&AS*, 124, 349

Meynet, G. & Maeder, A. 2000, *A&A*, 361, 101

Michaud, G. 1980, *AJ*, 85, 589

Michaud, G., Richer, J., & Richard, O. 2005, *ApJ*, 623, 442

Millan-Gabet, R., Schloerb, F. P., Traub, W. A., Malbet, F., Berger, J. P., & Bregman, J. D. 1999, *ApJ*, 513, L131

Monnier, J. D. 1999, Ph.D. Thesis

Monnier, J. D. 1999, in Principles of Long Baseline Interferometry, Edited by Peter R. Lawson, 203–226

Monnier, J. D., Tuthill, P. G., & Danchi, W. C. 1999, *ApJ*, 525, L97

Monnier, J. D., Tuthill, P. G., & Danchi, W. C. 2000, *ApJ*, 545, 957

Monnier, J. D., Danchi, W. C., Hale, D. S., Tuthill, P. G., & Townes, C. H. 2000, *ApJ*, 543, 868

Monnier, J. D., Danchi, W. C., Hale, D. S., Lipman, E. A., Tuthill, P. G., & Townes, C. H. 2000, *ApJ*, 543, 861

Monnier, J. D., & Millan-Gabet, R. 2002, *ApJ*, 579, 694

Monnier, J. D. 2003, Reports on Progress in Physics, 66, 789

Monnier, J. D., et al. 2004, *ApJ*, 602, L57

Monnier, J. D., Berger, J.-P., Millan-Gabet, R., & Ten Brummelaar, T. A. 2004, in Proceedings of SPIE Volume 5491. p.1370, ed. W. A. Traub, 1370–+

Monnier, J. D., et al. 2006, in Proceedings of the SPIE, Volume 6268, pp. 62681P (2006).

Monnier, J. D., et al. 2006, *ApJ*, 647, 444

Monnier, J. D., et al. 2007, Science, 317, 342

Monnier, J. D., Tannirkulam, A., Tuthill, P. G., Ireland, M., Cohen, R., Danchi, W. C., & Baron, F. 2008, *ApJ*, 681, L97

Moon, T. T. & Dworetsky, M. M. 1985, *MNRAS*, 217, 305

Mourard, D., et al. 2008, in Proceedings of the SPIE, 7013, 62M

Napiwotzki, R., Schoenberner, D., & Wenske, V. 1993, *A&A*, 268, 653

Narayan, R. & Nityananda, R. 1986, *ARA&A*, 24, 127

Nordström, B., Latham, D. W., Morse, J. A., Milone, A. A. E., Kurucz, R. L., Andersen, J., & Stefanik, R. P. 1994, *A&A*, 287, 338

Ohishi, N., Nordgren, T. E., & Hutter, D. J. 2004, *ApJ*, 612, 463

Palla, F., & Stahler, S. W. 2001, *ApJ*, 553, 299

Pasinetti Fracassini, L. E., Pastori, L., Covino, S., & Pozzi, A. 2001, *A&A*, 367, 521

Patience, J., et al. 2002, *ApJ*, 581, 654

Peale, S. J. 1994, *Ap&SS*, 212, 77

Pedretti, E., Millan-Gabet, R., Monnier, J. D., Traub, W. A., Carleton, N. P., Berger, J.-P., Lacasse, M. G., Schloerb, F. P., & Brewer, M. K. 2004, *PASP*, 116, 377

Pedretti, E., Traub, W. A., Monnier, J. D., Millan-Gabet, R., Carleton, N. P., Schloerb, F. P., Brewer, M. K., Berger, J.-P., Lacasse, M. G., & Ragland, S. 2005, *Appl. Opt.*, 44, 5173

Pedretti, E., Monnier, J. D., ten Brummelaar, T., & Thureau, N. 2009, New Astronomy Reviews, in press

Perryman, M. A. C., et al. 1997, *A&A*, 323, L49

Perrin, G., Ridgway, S. T., Coudé du Foresto, V., Mennesson, B., Traub, W. A., & Lacasse, M. G. 2004, *A&A*, 418, 675

Peterson, D. M., et al. 2006, *Nature*, 440, 896

Pickles, A. J. 1998, VizieR Online Data Catalog, 611, 863

Pinsonneault, M. 1997, *ARA&A*, 35, 557

Popper, D. M. 1980, *ARA&A*, 18, 115

Pott, J.-U., et al. 2008, arXiv:0811.2264

Pourbaix, D., & Jorissen, A. 2000, *A&AS*, 145, 161

Press, W. H. 1992, in Numerical Recipes in C. The Art of Scientific Computing; 2nd edition (Cambridge University Press)

Quirrenbach, A., Buscher, D. F., Mozurkewich, D., Hummel, C. A., & Armstrong, J. T. 1994, *A&A*, 283, L13

Quirrenbach, A. 2001, *ARA&A*, 39, 353

Raghavan, D., et al. 2009, *ApJ*, 690, 394

Richer, J., Michaud, G., Rogers, F., Iglesias, C., Turcotte, S., & LeBlanc, F. 1998, *ApJ*, 492, 833

Richer, J., Michaud, G., & Turcotte, S. 2000, *ApJ*, 529, 338

Richichi, A., Percheron, I., & Khristoforova, M. 2005, *A&A*, 431, 773

Roby, S. W. & Lambert, D. L. 1990, *ApJS*, 73, 67

Royer, F., Grenier, S., Baylac, M.-O., Gómez, A. E., & Zorec, J. 2002, *A&A*, 393, 897

Royer, F., Zorec, J., & Gómez, A. E. 2007, *A&A*, 463, 671

Sadakane, K. & Okyudo, M. 1989, *PASJ*, 41, 1055

Schmitt, H. R., et al. 2008, *ApJ*, submitted (ArXiv:0801.4772)

Shorlin, S. L. S., Wade, G. A., Donati, J.-F., Landstreet, J. D., Petit, P., Sigut, T. A. A., & Strasser, S. 2002, *A&A*, 392, 637

Schwarzschild, M. 1958, Ricerche Astronomiche, 5, 204

Simon, T., Ayres, T. R., Redfield, S., & Linsky, J. L. 2002, *ApJ*, 579, 800

Simon, T. & Landsman, W. B. 1997, *ApJ*, 483, 435

Sing, D. K., & López-Morales, M. 2009, *A&A*, 493, L31

Smalley, B. & Dworetsky, M. M. 1995, *A&A*, 293, 446

Stefanik, R. P., Latham, D. W., & Torres, G. 1999, in ASP Conf. Ser. 185: IAU Colloq. 170: Precise Stellar Radial Velocities, ed. J. B. Hearnshaw & C. D. Scarfe, 354–+

Segransan, D., Beuzit, J.-L., Delfosse, X., Forveille, T., Mayor, M., Perrier-Bellet, C., & Allard, F. 2000, *Proc. SPIE*, 4006, 269

Sudarsky, D., Burrows, A., & Hubeny, I. 2003, *ApJ*, 588, 1121

Stepinski, T. F., Malhotra, R., & Black, D. C. 2000, *ApJ*, 545, 1044

Stickland, D. J. 1975, in The Physics of Ap Stars, W.W. Weiss, H. Jenkner, H.J.Wood; Eds, 701–712

Stickland, D. J. 1990, The Observatory, 110, 43

Swain, M. R., Vasisht, G., & Tinetti, G. 2008, *Nature*, 452, 329

Talon, S., Zahn, J.-P., Maeder, A., & Meynet, G. 1997, *A&A*, 322, 209

Tannirkulam, A., et al. 2008, *ApJ*, 689, 513

ten Brummelaar, T. A., et al. 2005, *ApJ*, 628, 453

Thiébaut, E. 2008, in Preceedings of SPIE, Vol. 7013

Thureau, N. D., Ireland, M., Monnier, J. D., & Pedretti, E. 2006, in Proceedings of the SPIE, Volume 6268, pp. 62683C (2006).

Titus, J. & Morgan, W. W. 1940, *ApJ*, 92, 256

Thompson, A. R., Moran, J. M., & Swenson, G. W. 1986, New York, Wiley-Interscience, 1986, 554 p.,

Torres, G., Andersen, J., Nordström, B., & Latham, D. W. 2000, *AJ*, 119, 1942

Torres, G., Neuhäuser, R., & Guenther, E. W. 2002, *AJ*, 123, 1701

Torres, G., Stefanik, R. P., Andersen, J., Nordstrom, B., Latham, D. W., & Clausen, J. V. 1997, *AJ*, 114, 2764

Torres, G. 2006, *AJ*, 131, 1022

Traub, W. A., et al. 2003, Proceedings of the SPIE, 4838, 45

Trilling, D. E. 2000, *ApJ*, 537, L61

Tuthill, P. G., Monnier, J. D., & Danchi, W. C. 1999, *Nature*, 398, 487

Tuthill, P. G., Monnier, J. D., & Danchi, W. C. 2001, *Nature*, 409, 1012

Tycner, C., Jones, C. E., Sigut, T. A. A., Schmitt, H. R., Benson, J. A., Hutter, D. J., & Zavala, R. T. 2008, *ApJ*, 689, 461

Uesugi, A. & Fukuda, I. 1970, Catalogue of rotational velocities of the stars (Contributions from the Institute of Astrophysics and Kwasan Observatory, University of Kyoto, Kyoto: University, Kwasan Observatory, Institute of Astrophysics, 1970)

Uesugi, A., & Fukuda, I. 1982, Kyoto: University of Kyoto, Departement of Astronomy, 1982, Rev.ed.,

Umana, G., Maxted, P. F. L., Trigilio, C., Fender, R. P., Leone, F., & Yerli, S. K. 2000, *A&A*, 358, 229

van Belle, G. T., et al. 2006, *ApJ*, 637, 494

van Belle, G. T., Ciardi, D. R., Thompson, R. R., Akeson, R. L., & Lada, E. A. 2001, *ApJ*, 559, 1155

van Belle, G. T., et al. 2008, *ApJS*, 176, 276

van Leeuwen, F., & Evans, D. W. 1998, *A&AS*, 130, 157

van Leeuwen, F. 2007, Hipparcos, the New Reduction of the Raw Data (ASSL 350) (Dordrecht: Springer)

van't Veer-Menneret, C., Coupry, M. F., & Burkhart, C. 1988, *A&A*, 203, 123

Vasisht, G., & Colavita, M. M. 2004, *Proc. SPIE*, 5491, 567

von Zeipel, H. 1924a, *MNRAS*, 84, 665

—. 1924b, *MNRAS*, 84, 684

Wagman, N. E. 1946, *AJ*, 51, 209

Walter, F. M., Matthews, L. D., & Linsky, J. L. 1995, *ApJ*, 447, 353

Weigelt, G., Balega, Y., Bloecker, T., Fleischer, A. J., Osterbart, R., & Winters, J. M. 1998, *A&A*, 333, L51

Weiner, J., Hale, D. D. S., & Townes, C. H. 2003, *ApJ*, 589, 976

Wesselink, A. J. 1946, *Bull. Astron. Inst. Netherlands*, 10, 88

Yi, S., Demarque, P., Kim, Y.-C., Lee, Y.-W., Ree, C. H., Lejeune, T., & Barnes, S. 2001, *ApJS*, 136, 417

Yoon, J., Peterson, D. M., Zagarello, R. J., Armstrong, J. T., & Pauls, T. 2008, *ApJ*, 681, 570

Zahn, J.-P. 1977, *A&A*, 57, 383

Zahn, J.-P. 1989, *A&A*, 220, 112

Zeilik, M., Heckert, P., Henson, G., & Smith, P. 1982, *AJ*, 87, 1304

Zhao, M., et al. 2007, *ApJ*, 659, 626

Zhao, M., et al. 2008, *ApJ*, 684, L95

Zhao, M., Monnier, J. D., ten Brummelaar, T., Pedretti, E., & Thureau, N. D. 2008, *Proc. SPIE*, 7013,

Zhao, M., et al. 2009, *ApJ*, in press.

Zucker, S. & Mazeh, T. 1994, *ApJ*, 420, 806